UNIVERSITY OF OKLAHOMA

GRADUATE COLLEGE

EFFECTS OF EQUIVALENCE RATIO ON COMBUSTION CHARACTERISTICS OF LAMINAR PARTIALLY PREMIXED FLAMES OF PETROLEUM-BIOFUEL BLENDS

A DISSERTATION

SUBMITTED TO THE GRADUATE FACULTY

in partial fulfillment of the requirements for the

Degree of

DOCTOR OF PHILOSOPHY

By

VINAY N. SINGH
Norman, Oklahoma
2013

EFFECTS OF EQUIVALENCE RATIO ON COMBUSTION CHARACTERISTICS
OF LAMINAR PARTIALLY PREMIXED
FLAMES OF PETROLEUM-BIOFUEL BLENDS

A DISSERTATION APPROVED FOR THE
SCHOOL OF AEROSPACE AND MECHANICAL ENGINEERING

BY

_____
Dr. S.R. Gollahalli, Co-chair

_____
Dr. R.N. Parthasarathy, Co-chair

_____
Dr. Lance L. Lobban

_____
Dr. M. Cengiz Altan

_____
Dr. Wilson E. Merchan-Merchan

Acknowledgements

No study is done without assistance. Presenting this dissertation, I take the excellent opportunity to acknowledge all the guidance and help that I have received from all quarters.

It is a proud privilege to express my overwhelming senses of gratitude to my esteemed advisors, Dr. Subramanyam Gollahalli and Dr. Ramkumar Parthasarathy for their initiation, able guidance, constant encouragement and continuous supervision, without which it would not have been possible for me to complete this work. From the conception of this work, right up to its maturity, they have nurtured it with essentials, leaving no scope for deficiency.

My sincere thanks are due to all the Committee members starting from Dr. Wilson Merchan-Merchan, Dr. Cengiz Altan and Dr. Lance Lobban for their valuable support and guidance throughout my dissertation. I am extremely grateful to Dr. Akutlu for attending the first part of my dissertation with keen interest.

I would like to express my deep gratitude towards the Department of Energy & NSF EPSCOR for the financial support I received during my dissertation

I am greatly indebted to the Machine shop personnel Billy Mays and Greg Williams for their ever available guidance, invaluable suggestions & encouragement in the building of this project.

I would like to acknowledge the constant support, encouragement and affection given to me by my labmates Dr. Norman Love, Nikhil Dhamale, Pablo Barajas, Balasaheb

Dahifale, Diana Martinez, Cristian Aldana, Carloz Mendez, Victor Tran, Cory Morton, Maria Grisanti, Tanjir Ratul & friends without whom it wouldn't have been possible for me to give this dissertation the shape it has taken today.

Lastly & above all, like my own life, the formulation of this dissertation work has been possible only because of immense support, endless love & the confidence of my wife, Neha Singh and the blessings & inspirations that my parents have constantly showered upon me throughout my study as throughout my life.

Table of Contents

Chapter 5 Results and Discussion (Flame Structure)

Chapter 6 Computational Analysis

Chapter 7 Summary and Conclusions

List of Tables

List of Figures

Chapter 1 Introduction and Background

Chapter 2 Literature Review

Chapter 3 Experimental Setup and Method

Chapter 4 Results and Discussions (Global Properties)

Chapter 5 Results and Discussion (Flame Structure)

Chapter 6 Computational Analysis

Abstract

In order to provide energy independence and control pollutant emissions during combustion, alternative fuels are being developed. Biodiesel (fatty acid methyl esters) has received, and continues to receive, considerable attention for its potential use as an augmenting fuel to petroleum diesel. Its advantages include decreased net hydrocarbon, carbon monoxide, and particulate matter emissions, and fuel properties similar to petroleum diesel for ease of use in diesel engines. Its disadvantages include poorer cold flow characteristics, lower heating values, and mostly higher emissions of oxides of nitrogen. In addition, using pure biodiesel in an engine can clog fuel filters due to its poorer cold flow characteristics. Because biodiesel is a strong solvent, it will probably loosen debris in pipes and tanks, sometimes degrading rubber hoses. Biodiesel blends with diesel fuel are preferred in such conditions.

Biodiesel blends with petroleum diesel at a mixing ratio between 2 and 20 vol. % are widely offered as automotive fuels. The target for the future is to bring this ratio to a higher percentage, in order to increase the share of renewable energy in transport. Knowledge of the combustion and pollutant emission characteristics is important in the application of biofuels and their blends. There is, however, limited evidence on the effects of such blends on the combustion and emissions of diesel engines not originally designed to operate on biodiesel blends. Biofuels, such as canola methyl ester (CME) & soy methyl ester (SME), have considerable potential for use as fuels in internal combustion engines. In the current study to understand the effects of equivalence ratio on the combustion properties of petroleum-biofuel blends, partially-premixed laminar

flames of prevaporized blends were investigated. A laminar flame environment was chosen to simplify the fluid mechanics. The primary objective of this study was to clarify controversies and discrepancies in literature that existed and clearly define the cause(s) of soot and NO_x formation in biofuel blends on a chemical basis. The equivalence ratios were chosen to simulate the partial premixed to non-premixed flame combustion zones that exist in the far-injector regions in diesel engines. The documented combustion characteristics included inflame species concentration, inflame temperature, global emissions, global radiation, OH, and CH radicals, and soot volume fraction. To investigate the primary mechanism(s) which would contribute to soot and NO_x formation and their interactions for biofuel blends on a chemical basis alone was the goal of the project.

The fuel was vaporized by injecting into a hot air stream. The resulting flame was laminar whose characteristics were dependent on the chemistry of the fuel alone. Three blends of CME with petroleum-based diesel & three blends of SME with petroleum-based diesel were used with 25, 50 and 75% volume concentration of the biofuels respectively. The equivalence ratio was altered by changing the air flow rate. The measured radiative heat fraction significantly increased with increasing equivalence ratio (1.2 to 7). A decrease in the soot volume fraction was observed as the volume percentage of biofuel was increased in the blend. It was found that the NO_x emissions and the flame temperature decreased as the equivalence ratio was increased for all fuels tested. The biofuel flames produced the highest emission index of NO_x, which decreased as the volume percentage of biofuel was decreased in the fuel blend. In contrast, the CO emissions increased as the equivalence ratio was increased for all fuels

tested. CO emissions decreased as the volume percentage of biofuel was increased in the blend due to the presence of oxygen molecule in the biofuel, and consequently lower amount of soot was formed.

A high level of correlation between temperature, soot, and radiation was observed. As the equivalence ratio was increased, the soot content in the flames became larger, leading to larger flame radiation and lower flame temperatures. The biofuel flames behaved similar to petroleum fuel flames, and the quantitative variations are documented in the study. To determine the dominant route of soot and NOx formation in flames of the six biofuel blends, PLIF measurements of OH and CH radicals were carried out. Close to stoichiometry, flames from all fuels produced peak OH concentration fields and peak temperatures. Also, it was observed that residence time increased with NO_x concentration. These results indicated the dominance of the thermal (Zeldovich) mechanism for all fuels at this condition. The results of the OH concentration and the soot concentration for all fuels tested at near stoichiometry condition shows that, OH radical dominated the soot oxidation process.

Numerical analysis with surrogate fuels (n-heptane and methyl decanoate) was performed with FLUENT software to predict temperature and concentration fields to substantiate the experimental results. Experimental and the numerical model values for temperature profiles showed that n-heptane and biodiesel blend surrogate produced results within experimental uncertainties and meets the criteria for the formation of NO by the Zeldovich mechanism.

Chapter 1
Introduction

Background:

From 1970 to present, the domestic oil supplies in the United States have continued to fall, with the result that vast quantities of imported oil are required to make up for the deficit. Since 2000, oil prices have tripled, and we can expect more of the same in the years ahead. The main problem is that, even now, the annual demand for oil is four times greater than the volume of new oil reserves discovered. Based on a report published by the United States Energy Information Administration in January 2013, the world liquid fuels consumption grew by 0.9 million bbl/d (barrel a day) to reach 89.2 million bbl/d (Energy Information Administration, 2013) and by 2030, that demand is expected to climb to around 121 million bbl/d. This is troubling since a number of Industry experts now say that, global production probably will never exceed 100 million barrels a day due to future supply limitations.

As per the Annual Energy Review of 2012 by the United States Energy Information Administration, approximately 27 percent of the total energy consumed in the United States was used for transportation, as shown in Fig. 1. Transportation sector use of energy experienced tremendous growth overall; except for a few year-to-year declines, particularly in the early 1980s and in 2008 and 2009. From Fig. 2, throughout the 1949-to-2011 period, petroleum supplied most of the demand for transportation energy; in 2011, petroleum accounted for 94 percent of the transportation sector's total use of energy and is predicted to increase. The uncertainty surrounding the current and the future cost and the supply of fossil fuels, the high motivation for energy

independence and the need to reduce greenhouse emissions has caused governments, universities, and industries in many developed and developing countries to look for alternate forms of transportation energy. In recent years, hybrid, hydrogen, and exotic technologies have got great media coverage, but all these approaches requires a massive investment in the existing automotive and fuel system infrastructure.

In the meantime, there is one liquid fuel that is both renewable and can be used in a wide range of vehicles without any modifications to the engines. That fuel is biofuel. Biofuels have attracted considerable attention during the past decade because of relative abundance of feedstocks in all regions, and as renewable, biodegradable, and non-toxic fuels. It is known for its easy utilization in combustion engines existing fuel distribution infrastructure compatibility.

The 1973 oil export embargo imposed by the Arab members of OPEC (Organization of the Petroleum Exporting Countries) against the United States gave the first significant push on the production of biofuels in the country. Biofuel is a fuel composed of glyceride-free mono-alkyl esters of long-chain fatty acids converted from triglycerides such as biologically-based fats and oils (Sun et al. 2010). The alkyl ester generally takes the form of methyl ester, which is often classified as fatty acid methyl ester (FAME). Other alkyl esters, such as ethyl ester, have occasionally been used. A feedstock is the raw material from which oils and fats are derived. Rapeseed, soybean, cottonseed, linseed, and peanut are common vegetable-oil feedstocks. Other feedstocks could include sources such as waste cooking grease or beef tallow. In some cases it is possible for these unprocessed feedstocks to be used directly in an engine application. Complications, however, may arise with the direct use of these oils and fats within an

engine. They can cause severe injector coking, piston ring sticking, and engine deposits which will render the engine inoperable (Agarwal 2007). The process of converting the unmodified oil or fat into a suitable fuel i.e., the conversion of a triglyceride to an alkyl ester is called transesterification.

Transesterification

Transesterification is the process where a triglyceride is stripped of its fatty esters, by reacting it with an alcohol (usually methanol, but others may be used) in the presence of a catalyst (such as sodium or potassium hydroxide, but others may be used) (Ma et al. 1999). In addition to the fatty acid esters, glycerol is a by-product. The glyceride-free fatty acid esters are then termed "biofuel". A replication of the transesterification process provided in (Graboski et al. 1998) is shown in Fig. 3 for informational purposes. Note that R1 through R3 represent fatty acid chains of either the triglyceride or the methyl ester.

Advantages and disadvantages of biofuel

The widespread use of biofuel is based on the following positive attributes (Tyson 2004):

- Biofuel is renewable and non-petroleum-based;
- Biofuel can reduce greenhouse gas emissions;
- Biofuel is less toxic and is biodegradable;
- Biofuel can reduce tailpipe emissions of particulate matter (PM), carbon monoxide (CO), hydrocarbon (HC), and other air toxics;
- No or minor modifications are needed for the traditional compression ignition engine to use biofuel;

- Biofuel compression ignition engines are similar in operation as conventionally-fuelled diesel engines.

Biofuel also has some negative attributes:

- Lower heating value (LHV), less favorable cold flow properties, lower volatility, and higher viscosity (data shown in Table 1);
- Lower storage stability and material compatibility issue;
- Possibly higher oxides of nitrogen (NOx) emission;
- High manufacture cost because of transesterification and expensive feedstocks;

Canola Methyl Ester (CME)

Biofuel can be produced from animal fats, vegetable oil or recycled restaurant grease. Due to its important advantages, Canola biodiesel or CME was one of biofuels used for the study. It is already widespread in most parts of the world and can produce more oil per unit of seed as compared to other oilseeds. It has the lowest level of saturated fat and hence performs better in cold weather. Due to its low iodine value it is less prone to oxidation. It also helps sequester carbon in the soil.

Soy Methyl Ester (SME)

The other biofuel used in the study is Soy biodiesel or SME produced from soybean oil. Some of the advantages associated with SME are as follows: It is grown locally and has a much lower cloud point compared to other biodiesels available in the market and hence can be used at much lower temperatures. The byproduct of the soybean forms a high protein product, soybean meal (staple feedstuff for cattle and poultry)

Due to its disadvantages, biofuel blends with diesel fuel are preferred over pure biofuel. There is, however, limited evidence on the effects of such blends on the combustion and emissions of diesel engines not originally designed to operate on biofuel blends. Knowledge of the combustion characteristics is important in the application and further development of biofuels.

The earliest use of biofuel in the literature was as fuel for a diesel engine. When using any engine it is important to consider certain characteristics such as the fuel consumption rate, thermal and combustion efficiency, power output, and pollutants emitted. Compression ignition engines typically produce higher efficiencies and have lower fuel consumption rates than spark ignition engines. The tradeoff, however, is found in the relatively large amounts of PM and NO_x produced by the compression engine. The current project *does not* simulate the combustion environment of the diesel engine; rather, it simplifies the process by removing several variables (high pressure, droplet evaporation, injection timing), as is further discussed later in the dissertation.

Significance of soot

The source of production of soot is not well understood in the case of biodiesel or its blends. Soot particles are recognized as an important cause of health and respiratory problems. Over the past decade, several hundreds of studies have linked soot particles to increased risk of lung cancer, asthma and chronic bronchitis. Fine soot emissions (smaller than 2.5μm) have been linked to increased risk of heart attack and have been identified as the greatest contributor to cancer risk, given their ability to reach deep into the lungs. Recognizing the adverse health and environmental effects resulting from PM,

the Environmental Protection Agency (EPA) has been placing increasingly severe regulations on emissions from cars and aircraft jet engines for the past ten years. Stricter regulations on allowed levels of smoke visibility and on the size of soot particles from combustion devices are expected.

Soot particles are formed and destroyed during rich combustion of hydrocarbon fuels in many combustion devices: internal combustion engines, jet engines, coal power plant burners and others. The choice of hydrocarbon fuel mixture, oxidizer, and fuel flow rates, mixing patterns, temperatures, and pressure are design parameters that affect in a complex and non-linear fashion the characteristics of soot emitted from combustion devices, including particle size distribution and surface reactivity. While our understanding of soot formation and growth has improved in recent years, the prediction of soot emissions remains a complex task in case of biofuels and their blends. Soot formation involves a sequence of gas-phase reactions forming polycyclic aromatic hydrocarbons (PAH) followed by particle inception, particle/particle interactions, soot particle growth and oxidation by heterogeneous reactions with chemical species in the gas-phase. The interaction between turbulent transport and molecular diffusion as well as local flow conditions (e.g., chemical species concentrations and temperature) plays a key role in controlling soot concentrations.

Significance of NOx

NO_x is a regulated emission by the EPA because of its contribution to pollution, inherent health risks, and environmental hazards. NO_x has been shown to cause respiratory irritation, reduction of lung function, asthma attacks, permanent lung damage, or damage vegetation (Fernando et al. 2006). Additionally, NO_x is involved in

the formation of acid rain which can cause damage to man–made structures, increase the acidity of waterways and harm wildlife that occupy lakes or rivers. The two most common types of NO_x are nitric oxide (NO) and nitrogen dioxide (NO_2). In the presence of hot stagnant air and sunlight NO_x can convert to hazardous ground level ozone. Investigation on causes of NO_x formation and reduction of the pollutant through exhaust gas recirculation (EGR), catalytic converters, and modifications to injection timing has been a well-researched topic in diesel engines running on diesel fuel. As biodiesel fuels slowly become more popular and affordable they are being run in diesel engines. In general, when commercially available biodiesel fuels such as soy and canola methyl ester and their blends with diesel are run in the diesel engine they produce higher levels of NO_x.

An agreement of the cause of the increased pollutant has not been positively identified. In order to ensure the use of biodiesel and their blends in the future, causes of the increased pollutant emissions must be established. Presently, our capability to understand the production of soot and NO_x emissions in realistic combustion devices remains insufficient as the existing studies often rely on engine studies. It is largely due to the complexity of the engine studies, which require knowledge of many factors and their effect on soot production. Therefore, the study investigates the causes and fundamental formation processes in the soot and NO_x production in biodiesel fuel and their blends with the use of the laminar flame arrangement technique which provides a convenient venue to study the effects of *only* fuel composition and chemistry on the combustion properties.

Problem Discussion

Reported studies of exhaust emissions of diesel engines when operated on neat transesterified biofuels and their blends with diesel fuel showed a reduction in CO, smoke and PM, along with an increase in NO_x. But there were discrepancies related to the cause of soot and NO_x production. This is because of the complex nature of engine testing which requires knowledge of many components and their effect on the soot and NO_x formation. Love et al. (2009) studied the effect of only the chemical aspects of NOx formation in pure biodiesel fuels, eliminating physical variables and the study was a significant contributor in delineating the mechanism of the formation of NO_x. However, due to required modifications and to avoid maintenance and performance problems in existing combustors to fuel them with, biodiesel in its pure form, requires blending of biodiesels with petroleum diesel is preferred. Also, to better understand the fundamental mechanisms and interaction of soot forming and nitric oxide reactions in biodiesel blends, this study considered only the chemical aspects, eliminating physical variables that are encountered in the diesel engine. The study was approached through conventional experimental methods and laser diagnostics. Furthermore, a computational model was also used to numerically study the flames in laminar condition at fuel-rich conditions.

Given the many different possible reasons for increase in NO_x emissions, a detailed literature review was conducted in order to have a better understanding of CO and NO_x emissions, and fuel chemistry effects presented in the following chapter.

Organization of the Dissertation

This thesis consists of seven chapters and three appendices. An introduction to the problem, and the description of biofuel used in the study are given in Chapter 1. Chapter 2 presents the literature review, and discussion of the objectives. Chapter 3 details the experimental techniques and instrumentation used in the present investigation, and the methods to characterize the combustion properties of the tested fuels. Chapter 4 describes the results for the global flame properties. This includes flame appearance, flame length, emissions indices for NO and CO, and radiation parameters. Chapter 5 presents the results and discussion for the experimentally obtained data involving the internal structure of the flame. This includes measured flame temperatures, concentration profiles of stable species (CO, CO_2, and NO), soot volume fraction, and PLIF images of intermediate species respectively. Chapter 6 contains the numerical portion of the report: the governing equations, reaction models, grid parameters, grid independence measurements, and comparison of computational results with experimental. Finally, in Chapter 7 a general discussion of the dissertation is given followed by recommendations for future studies.

Table 1: Measured properties of diesel, B100 and B20 retrieved from the specified literature (Sun et al. 2010)

Property	Unit	Diesel	B100 (SME)	B20 (SME)
Carbon content	mass %	86.7	77.1	-
Hydrogen content	mass %	12.71	11.81	-
Oxygen content	mass %	-	10.97	-
Nitrogen content	mass %	0.0001-0.003	0.002-0.007	-
C/H Ratio (mass basis)	-	6.82	6.53	-
Saturates content	vol. %	63	-	-
Olefins content	vol. %	1.3	-	-
Aromatics content	vol. %	35.7	-	-
Sulfur content	mass %	0.041	<0.005	0.00205
Typical formula	-	$C_{14.09}H_{24.78}$	$C_{18.74}H_{34.43}O_2$	-
Average molecular weight	g/mol	193.89	291.62	-
Denity, 21 ^oC	g/ml	0.8537	0.8814	0.8577
Kinematic viscosity, 40 ^oC	mm^2/s	2.8271	4.2691	2.862
Cloud point	^oC	-20	(-5)-(-10)	-12
Cold filter	^oC	-25	(-5)-(-10)	-
Pour point	^oC	-35	(-5)-(-10)	-
Bulk modulus	Mpa	12.392*P + 1595.1	11.316*P + 1747.5	-
Speed of sound	m/s	4.5129*P + 1375.8	3.855*P + 1410	-
Cetane number	-	42.6	51.5	-
Acid Number	mg_{KOH}/g	-	0.38	0.14
Flash Point	^oC	67	141	-
Higher heating value	MJ/kg	45.339	39.871	-
Lower Heating value	MJ/kg	42.64	37.388	-

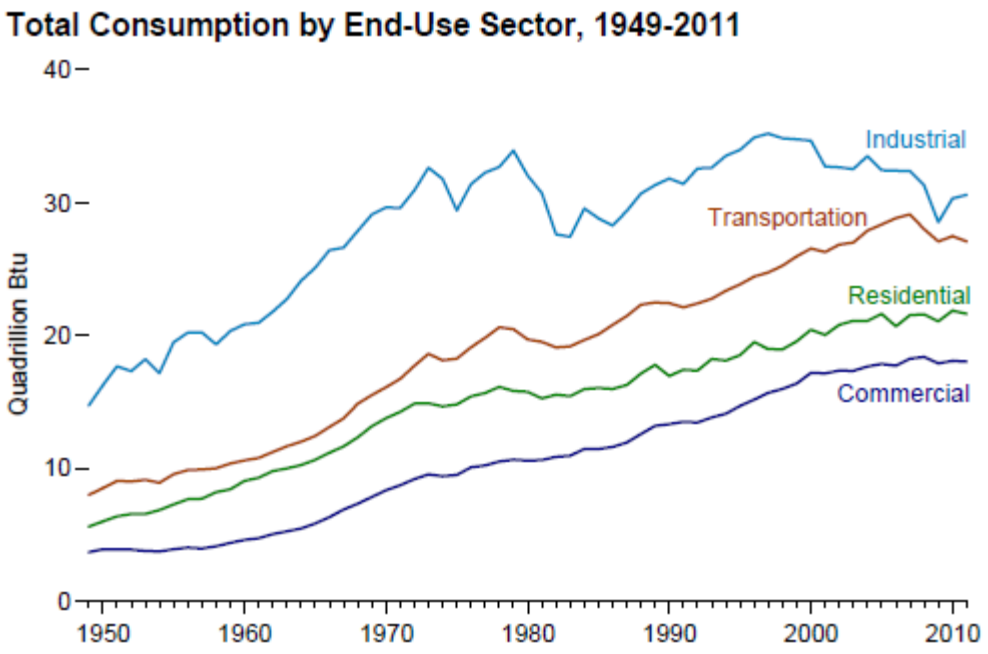

Fig. 1: Energy consumed in the United States over 61 year period {Annual Energy Review, EIA 2012}

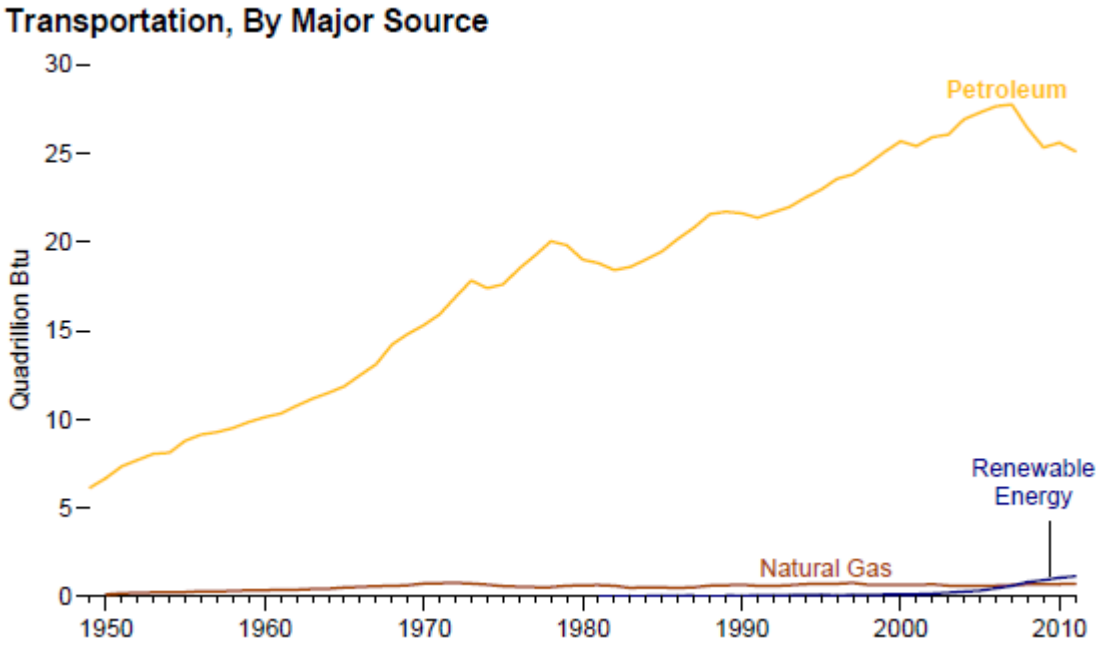

Fig. 2: Energy consumed in the Transportation Sector of United States over 61 year period{Annual Energy Review, EIA 2012}

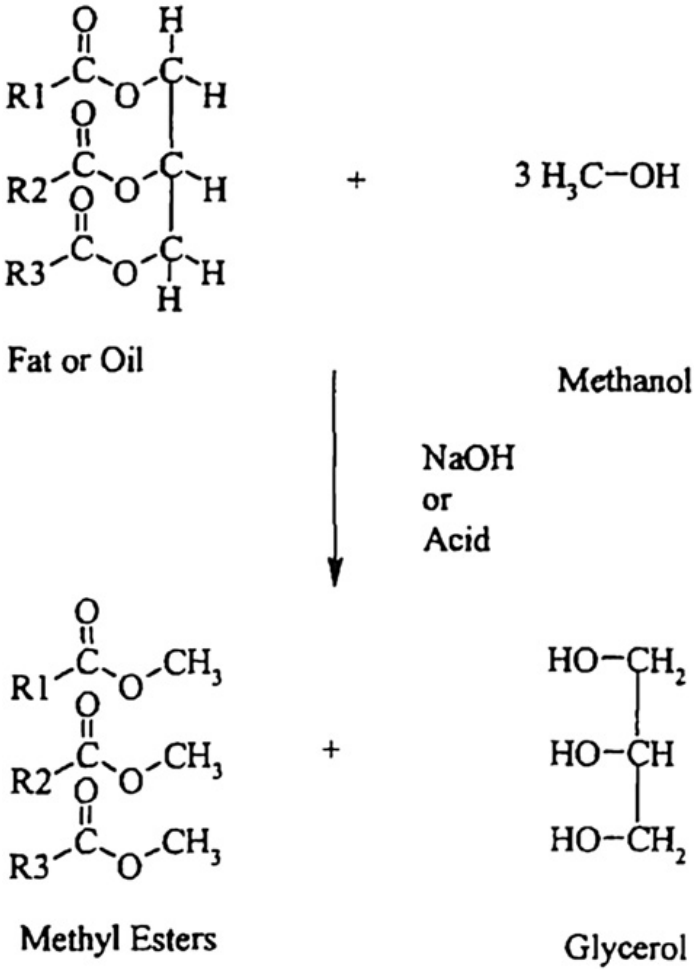

Fig. 3: A diagram representing the transesterification process, replicated from (Graboski et al. 1998). The general scheme of the process is to modify a triglyceride (a fat or oil which is a glyceride with three fatty acids, represented as R1, R2, and R3) into a fatty acid methyl ester.

Chapter 2
Literature Review

A brief summary of biodiesel effects on pollutant emissions is presented in this chapter. There has been an increased interest in reformulated and alternative fuels to control pollutant emissions during combustion and to provide energy independence. Biofuels derived from the transesterification of vegetable oils, animal fats, or waste cooking oils to form the corresponding fatty acid methyl esters are an attractive alternate energy source. These biofuels can be produced domestically and can be derived from renewable sources. In addition, they are carbon –neutral and low in sulfur content. Biodiesel differs than fossil diesel in chemical character, as it primarily consists of esters, compared to the paraffinic and aromatic character of fossil diesel (Graboski et al. 1998). As a result of the different chemical composition, biodiesel also exhibits different physical properties than fossil diesel, such as higher cetane number, lower heating value, higher viscosity and flash-point. The different properties may in turn affect the combustion and emissions in a diesel engine.

Several researchers have reported studies of exhaust emissions of diesel engines when operated on neat transesterified biofuels and their blends with diesel fuel. The results included a reduction in CO, smoke and PM, along with an increase in NO_x and fuel consumption. The rise in fuel consumption is caused by differences in fuel energy content. For the case of the increased NOx emissions from biodiesel, studies suggest that the NO_x emission levels increase is not determined by a change in a single fuel property, but rather is the result of a number of coupled mechanisms whose effects may tend to reinforce or cancel one another under different conditions, depending on specific

combustion and fuel characteristics (Mueller et al. 2009). A number of fuel properties (viscosity, heating value, density and cetane number), as well as engine operating conditions and technology have all been shown to play a role on biodiesel emission effects.

Engine studies on biofuel and blends

A report by EPA (2002) indicated that the use of B100 and B20 soy biofuel blend (20% biofuel by volume) produced 13% and 2% more NO_x, respectively, in heavy duty highway engines than the conventional diesel fuel. An average emission impact of biodiesel for heavy-duty highway engines has been shown in fig. 4. Canakci et al. (2003) used petroleum diesel, yellow grease biofuel and soybean oil biofuel in a four–cylinder turbocharged diesel engine, at steady state engine operating conditions. Although the use of both biofuels resulted in significant reductions in PM, CO, and unburned hydrocarbons, NO_x increased by 11% and 13% for the yellow grease methyl ester and soybean oil methyl ester respectively. Tat et al. (2003) reported that, there was approximately a 14% increase in NO_x with soybean biofuel relative to No.2 diesel fuel and a 1% increase in NO_x emission with yellow grease biofuel in the emissions of a turbocharged diesel engine. Graboski et al. (2003) studied the effect of the composition of 28 neat biofuels, four B20 blends, and diesel fuel on a four stroke six cylinders, direct injected (DI), turbocharged, and intercooled, 11.1 L, 345 bhp engine. They found that NO_x emissions were higher for the unsaturated fuels, for neat biofuels and biofuel blends, when compared to diesel fuel with the exception of highly saturated fuels such as methyl stearate.

Szybist et al. (2005) reported an increase in NO_x emissions with biofuels. Emissions studies were performed with biofuel, Fischer−Tropsch (FT) diesel and conventional diesel fuel, at a variety of static fuel injection timing conditions in a single-cylinder DI diesel engine with a mechanically controlled, in-line, pump-line-nozzle fuel injection system. Szybist et al. (2005) also investigated the effect of cetane number of biofuel blends on the emissions from a single cylinder air-cooled direct injection compression ignition engine. NO_x emissions were found to be higher and insensitive to ignition delay and highly dependent on the timing of the combustion process, initiated by the start of fuel injection. One of the studies (Labeckas et al. 2006) with a four-stroke, four-cylinder diesel engine showed the effects of rapeseed methyl ester (RME) on the exhaust emissions. The engine was operated on neat RME and its 5%, 10%, 20% and 35% blends with diesel fuel. An increase in NO_x emissions with increased engine speed was observed; the result was attributed to the increased mass percentage of oxygen in the biofuel.

Karabektas (2009) tested rapeseed methyl ester and petroleum diesel in a four-stroke, DI, naturally aspirated/ turbocharged diesel engine at full load conditions; the results showed that the production of NO_x and brake thermal efficiency in operations with biodiesel were higher than those in the operations with diesel fuel, whereas CO emissions and torque were lower. Lujan et al. (2009) tested four fuel compositions in an engine test cell. Results obtained from the study show that the emissions of NO_x increased with the increase in biodiesel content. On the other hand CO and HC emissions were reduced with the addition of biodiesel. Fontaras et al. (2010) performed a number of experiments with B10 biodiesel fuel of palm oil origin in a light-duty

common-rail Euro 3 engine. The results on the engine bench were compared with those from an Euro 3 common-rail light-duty vehicle driven on the chassis dynamometer, in order to include the effects of emission control systems. The measurements included in-cylinder pressure, pollutants emissions, and fuel consumption. The results showed that the use of both biodiesel blends resulted in a reduction in PM emissions; only marginal effects on NOx emissions over the certification test could be identified. Buyukkaya (2010) evaluated the performance and emissions of diesel engine that was fueled with neat rapeseed oil and its blends of 5%, 20% and 70% and petroleum diesel fuel. The results of this study were in agreement with those from previous studies; an increase in brake specific fuel consumption (BSFC), accompanied by a decrease in CO was observed. Muralidharan et al. (2011) carried out experiments on four stroke single cylinder multi fuel engine fuelled with waste cooking oil methyl ester and its blends with diesel. The experiments were conducted at a fixed compression ratio of 21, engine speed of 1500 rpm using fuel blends of 20%, 40%, 60% and 80% biodiesel with diesel. It was found that the NO_x emissions of biodiesel and its various blends were higher than that of diesel and a reduction in CO, HC and CO_2 was reported. Gumus et al. (2012) studied the effects of fuel injection pressure on the exhaust emissions and BSFC of a DI diesel engine fuelled with biodiesel-diesel blends. The experiments were performed at four different fuel injection pressures. They found that the BSFC, CO_2 and NOx emissions increased while HC and CO emissions decreased. As the fuel injection pressure was increased, the BSFC, and the emissions of HC and CO decreased while the emissions of NOx and CO_2 increased. They attributed the findings to the fuel properties and combustion characteristics of the biodiesel used. Ozener et al. (2012) compared the

combustion, performance and emission characteristics of petroleum diesel fuel and soy biodiesel and its blends (B10, B20, and B50). The experiments were performed in a single-cylinder DI diesel engine at steady state conditions. Their findings showed that biodiesel had a 2-9% increase in BSFC, due to the LHV of the biodiesel. They reported a significant reduction in CO (28-46%), and a slight increase in emissions of NOx (6.95-17.62%).

Flame studies on biofuel and blends

Jha et al. (2008) investigated the effect of component methyl esters of biodiesel on open air flame temperature distribution and the effect of blending biodiesel with diesel and oxygenated fuels like ethanol and methyl esters on open air flames. It was found that the oxygenated nature of the fuels contributed towards the increase in the flame temperature. Also, the effects of saturated hydrocarbon and unsaturated hydrocarbon chains on the in-flame temperature were investigated. The saturated methyl esters resulted in a greater flame temperature in comparison to unsaturated methyl esters. The study showed that shorter chained fatty acid methyl esters led to higher flame temperatures when compared to their longer chained counterparts.

Love et al. (2009) investigated laminar flames of pre-vaporized mixtures of fuels with air. Several liquid fuels were tested, including commercially available petroleum-based No. 2 diesel fuel, CME, kerosene, methanol, toluene, and selected alkanes. The measured radiant heat fraction values and the emission indices of NO and CO of both petroleum-derived and biofuels agreed well with those found in literature; thus, the feasibility of this method to rapidly characterize the combustion and emission properties of new liquids, such as biofuels, was demonstrated. Love et al. (2009) later employed

this experimental technique to investigate the effect of iodine number on NOx formation in laminar partially premixed flames of three vaporized biofuels: CME, SME and methyl stearate. The iodine numbers for the selected fuels varied over a wide range from 0.5 to 141. Key measurements included NOx concentrations and temperature fields. It was observed that the peak NOx concentration occurred in the near-burner region for all biofuels. Also, the peak NOx concentration significantly increased with the iodine number, indicating a strong correlation between the chemical structure of the fuel and NOx emission. The analysis of results indicated that the Zeldovich mechanism was not the dominant route in NOx production in fuel-rich biofuel flames; the Fenimore mechanism, appeared to play a significant role in the NOx production. Dhamale et al. (2010) performed experiments with turbulent SME flames and No. 2 diesel flames. The experiments were conducted at an initial equivalence ratio of 7 and three Reynolds numbers (based on the injector diameter and the bulk burner-exit velocity of the air/fuel mixture): 2700, 3600 and 4500. Three blends, B25, B50 and B75 of SME were studied. It was found that the radiative heat fraction measured in the SME flames was lower than the corresponding value in pure diesel flames and increased with Reynolds number. The global emission measurements indicated that the NOx emissions from the SME-diesel blend flames were lower than those from the pure diesel flame. At quarter and half flame height the temperature peaked near the edge of the flame, whereas the temperature peaked at the centerline at three-quarter flame height. In-flame NOx concentrations decreased with an increase in Reynolds number. Also, the peak NOx concentration in the diesel flame was higher than that measured in the SME flames. The CO emission index decreased with the increase in the SME

concentration in the fuel blend. Also, the CO emission index decreased with the increase in Reynolds number for all flames. The oxygenated nature of the biodiesel blends was the reason attributed to the decrease in CO content as the combustion process was aided by the presence of oxygen molecules. The presence of oxygen also reduced the soot content and thus reduced the radiative heat fraction.

In general, pollutant emission studies in engines and flames have shown that the use of the majority of biofuels and blends produced more NOx and less CO, PM, and unburned HC than the use of diesel fuel. Xue et al. (2011) conducted a detailed analysis of effect of biodiesel on engine power, economy and emissions by citing reports about biodiesel engine performances and emissions published since 2000. The review reported a substantial reduction in PM, HC and CO emissions and an increase in NOx emissions and fuel consumption accompanied by engine power loss with the use of biodiesel. It favors to reduce carbon deposits and wear of the key engine parts. The report concluded that blends with small portion of biodiesel are technically feasible as an alternative fuel to diesel to help control air pollution without significantly sacrificing engine power and economy.

Another review conducted by Giakoumis et al. in 2012 targeted the impacts of diesel-biodiesel blends on the emissions of compression ignition engines. The review included large amount of published data from four stroke engines during the last two decades. The analysis primarily focused on PM and NO_x. Other regulated pollutants CO and HC ere also presented in the review. A decreasing trend in PM, HC and CO and an increasing trend in NOx emissions is established when the biodiesel in the fuel blend ratio increases. The increased oxygen concentration in the fuel biodiesel blend has been

identified as the key contributor for reduced PM emissions relative to petroleum diesel operation. On the other hand, the increase in NO_x emission is attributed to higher iodine number for biodiesels produced from unsaturated feedstocks which contain higher proportion of unsaturated components relative to petroleum diesel.

The review conducted for this study focused on a small portion of literature present which contains enough information on the effects of biodiesel or biodiesel blends on emissions. Although inconsistent, most of the literature states that NO_x emissions has increased with the use of biodiesel or biodiesel blends in comparison with baseline petroleum diesel fuel. One of the reasons for the discrepancy is the number of factors that are responsible for the NO_x effects. Also these factors vary with operating conditions and engine technology. To provide a better picture on the effects of biodiesel and its blends on emissions numerous theories have been proposed wherein they relate to several engine parameters. However, the reasons behind the observed NO_x increase and soot formation from biodiesel blends have not been clearly delineated.

Objectives

The objective of this study was to clarify controversies and discrepancies in literature that existed and clearly define the cause(s) of soot and NO_x formation in biofuel blends on a chemical basis. The chemical aspect of the combustion of the fuels was decoupled from the physical. The variables measured included: inflame species concentration, inflame temperature, global emissions, global radiation, OH, and CH radicals, and soot volume fraction. To investigate the primary mechanism(s) which would contribute to soot and NO_x formation and their interactions for biofuel blends on a chemical basis alone was the goal of the project.

In order to achieve the objectives mentioned, the current study focused on simplifying the combustion process that exists in an engine, by removing variables such as high pressure, droplet evaporation and injection timing. The experiments were conducted in a laminar flow environment to attribute the measured combustion properties to the fuel chemistry alone. Fuels used in the study were premixed and prevaporized to avoid the vaporization effects. Three blends of CME; CME B25, CME B50 and CME B75 and three blends of SME; SME B25, SME B50 and SME B75 were used for the study.

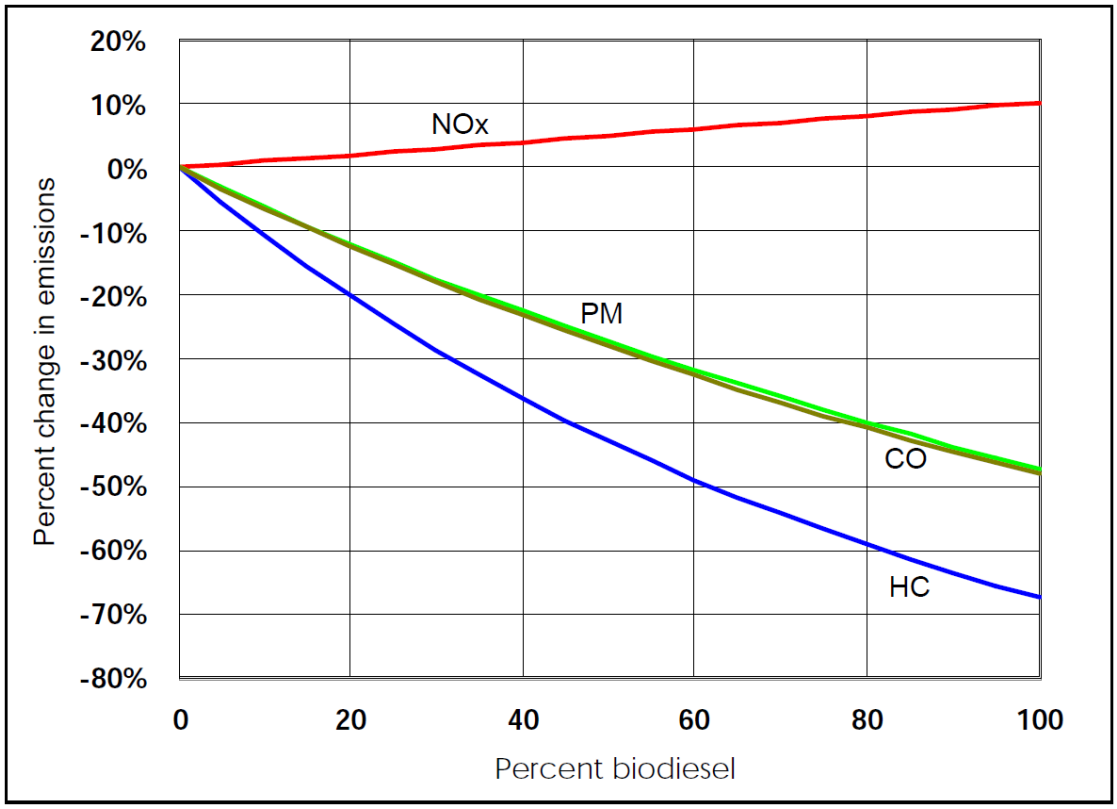

Fig. 4: Average emissions impacts of biodiesel for heavy-duty highway engines {EPA, 2002}

Chapter 3
Experimental set-up and method

This chapter describes the details of the experimental setup and its components along with the background for the measurement techniques. All experiments were conducted at the Combustion and Flame Dynamics Laboratory at the University of Oklahoma. A list of the instruments used (Table 3) is also presented in this chapter.

Combustion Chamber and Fuel Delivery System

The experiments were conducted in a vertical steel test chamber shown in Fig. 5 with a cross section of 76 x 76 cm^2 and a height of 100 cm. The walls of the chamber contained windows provided with removable slotted metal sheet covers measuring 96 cm x 25 cm to allow optical (laser, photography) and instrument (thermocouple, emissions probe) access. The top of the combustion chamber was connected to the atmosphere through an exhaust duct. The ambient pressure in the laboratory was maintained at slightly (20 Pa) above the atmospheric pressure, to provide a positive draft inside the test chamber and eliminate any leakage of the combustion products into the main laboratory facility. High temperature heating tape with a proportional temperature controller was used to heat the flow lines carrying air to the desired temperature of 400^oC (which was close to the final boiling point of the liquid fuels) to completely vaporize the liquid fuels, without any coking. The liquid fuel was injected with the help of a syringe pump into the heated carrier gas stream through a high temperature silica-based septum with a 50 cm^3 syringe and sent to a 9.5 mm inner diameter tube burner shown in Fig. 6. The volumetric flow rate of the carrier gas was monitored using a calibrated rotameter. The feed line temperature was monitored using

K-Type thermocouples. The vaporized fuel was ignited using a pilot flame, which was removed after ignition. The resulting flame was laminar whose characteristics at those conditions were dependent on the chemistry of the fuel alone.

A schematic diagram of the setup is presented in Fig. 7. The initial equivalence ratio was altered by changing the flow rate of the air using the calibrated rotameter, keeping the fuel flow rate constant. The equivalence ratios used in this study were 1.2, 2, 3 and 7. The test conditions are presented in Table 3 b.

Tested Fuels

Three blends of CME with petroleum-based diesel & three blends of SME with petroleum-based diesel were used. These included CME B25 (25% by volume of CME), CME B50 (50% by volume of CME), CME B75 (75% by volume of CME), SME B25 (25% by volume of SME), SME B50 (50% by volume of SME), and SME B75 (75% by volume of SME). The blends were prepared using a splash blending technique (Reid 2007) in 5 gallon amounts. The fuel with lower density was splash blended by adding the fuel with higher density and then stirred to ensure complete mixing of the fuels. To ensure that the properties of the fuel remained consistent throughout the blend, the fuel samples were stored in a transparent container and were observed for a period of one month to see if the two fuels separated. For each blend, one sample was sealed and the other was open to the environment. No separation was observed in both the sealed and open containers after a month. The fuels were found to be completely miscible. The molecular formula, chemical composition and physical properties of no. 2 diesel fuel, CME, SME and the blends are presented in Table 2.

A hydrometer from Fisher Scientific was used to determine the density of all the fuels tested. The fuel was poured into a graduated cylinder, and the hydrometer was gently lowered into the fuel until it floated freely. The point at which the surface of the liquid touched the stem of the hydrometer was noted. The hydrometer contained a scale inside the stem, so the specific gravity was read directly. An oxygen bomb calorimeter from PARR Instrument Company was used to measure the LHV. About 1g of fuel to be tested was weighed into a crucible, and placed inside the stainless steel container filled with 30 bar (435 PSI) of oxygen (Quality: technical oxygen 99.98%). The fuel sample was than ignited through a cotton thread connected to an ignition wire inside the stainless steel container and combusted. The viscosities of the fuels were measured using a falling ball viscometer from Gilmont. The Hoppler principle was used to measure the viscosity of fuels (Newtonian fluid) by measuring the time required for a ball to fall under gravity through the sample-filled tube. The average time of three tests was taken; the result was converted into a viscosity value using a simple formula. A decrease in the heating value and an increase in the oxygen percentage are observed as the volume percentage of CME & SME was increased in the blend.

Instrumentation:

Flame Visualization:

Visible flame images were acquired using an 8 mega pixel digital AF SLR camera (EOS Digital Rebel XT/EOS 350D). The images were obtained under similar lighting conditions with a dark background at 1/25 second shutter speed. Using appropriate software, the number of pixels was counted and converted into the length scale using a calibration reference.

The flame length was determined by counting the number of pixels from the tip of the burner to the farthest point of visible luminosity. This pixel count was then converted into a length scale using the calibration reference. Ten images per flame condition were taken at arbitrary time intervals and the resultant flame lengths were averaged.

Flame Radiation:

A wide view-angle (150 ^{o}) high sensitivity pyrheliometer was used to measure the radiation from the flame (). The pyrheliometer was located far enough (50 cm) from the burner, so that its view-angle covered the entire flame length and the flame could be assumed as a point source. The pyrheliometer had a linear voltage output with incident radiation flux, and a sensitivity of 23.65 W/m^2/mV. A data acquisition board along with suitable software was used to sample the measured radiative heat flux. Each test was run for time duration of 3 min. with a sampling rate of 1 Hz, allowing the heat flux to reach a steady value. The background radiation was subtracted from the total radiation measured to give the corrected radiation due to flame. The radiative fraction of heat released was computed using this value with the following equation

$$F = \frac{4\pi l^2 . q_{corrected}}{\dot{m} . LHV_{fuel}} \quad (1)$$

Since most of the radiation in these flames is emitted by burning soot, the radiative heat fraction provides a convenient indication of the soot content in these flames. A schematic diagram of this set-up is presented in Fig. 8.

Temperature profiles:

For flame temperature measurements, an in- house platinum-13% rhodium-platinum (R-type) thermocouple with a wire diameter of 0.12 mm and bead diameter of 0.25 mm was used. The thermocouple was mounted on a two dimensional linear traversing mechanism. Radial temperature profiles were measured at three axial locations, 25%, 50%, and 75% of the visible flame height. The temperature data was acquired through the use of LabVIEW 7.1 data acquisition software at a sample rate of 2 Hz over a 60 second time interval at each point. The data was then corrected for radiative and conductive losses; (the details are presented in appendix A). The setup for temperature measurements is illustrated in Fig. 9.

Global Emissions:

Emissions of pollutant species from the flame were measured by collecting gas samples through a 1 mm diameter tip, expanding to a 6 mm ID tube uncooled quartz probe placed at the top of a Pyrex flue gas collector. A schematic diagram of the set-up and the probe used for sampling the flue gases is shown in Figs. 10 & 11 respectively. The Pyrex flue gas collection funnel was placed 25 cm above the burner exit to collect the combustion products. Since the jet exit velocities were same for all conditions, the entrainment and dilution was similar at this location for all flames. Also, the temperature variation of the products was small. The flue gas collector and probe were aligned axially with the burner and the probe was placed above the flame. The gas samples were passed through a filter and ice-chilled water bath to remove particulates or moisture that might be present in the sample gas. A NOVA model 376WP portable flue gas analyzer was used to measure the concentration of NO, CO_2 and CO. The O_2, CO, and NO sensors were electrochemical 'fuel cell' type sensors which produced small electrical outputs proportional to the volumetric concentration of the gas being detected. The CO_2 sensor used a non-dispersive infrared (NDIR) to determine the concentration. The analyzer was calibrated with standard zero and reference gases before measurements were taken. The global emissions measurements were corrected to account for dilution of the product gases due to entrainment from ambient air. Therefore, the emission index was used to characterize the pollutant emissions (Turns 2000). The emission index expresses the amount of pollutant formed per unit mass of the fuel burnt:

$$EI_i = \left\{\frac{X_i}{X_{CO}+X_{CO_2}}\right\}\left\{\frac{N.MW_i}{MW_f}\right\} \quad (2)$$

Here X_i represents the mole fraction of species *i*, N is the number of carbon atoms in the mixture, and MW_i and MW_f are the molecular weight of species *i* and fuel respectively. It is assumed that all the carbon in the fuel is converted into CO or CO_2; the assumption is reasonable because the soot content in the flames was small.

In-Flame Species Concentration:

In-flame species concentrations (CO_2, O_2, and NO) were measured with custom made stainless steel gas sample probe, Fig. 12. The probe consisted of a short 1.75 mm inner diameter and 3.2 mm outer diameter stainless steel tube cemented with high temperature ceramic adhesive into a stainless steel 4.6 mm inner diameter 6.35 mm outer diameter holder. This probe could withstand the high temperatures produced by the flames which tended to soften quartz tubing. Additionally, the diameter of the sampling probe was large enough not to clog from soot accumulation on the inlet.

The sampling probe was mounted on a two-dimensional linear traversing mechanism. Measurements were taken with the probe placed perpendicular to the burner centerline. The probe was radially traversed at 2 mm intervals and at the same axial positions as the temperature measurements.

Soot Volume Fraction

A 5 mW Helium-Neon laser (λ = 632.8 nm) was used as a light source with a power detector that was placed opposite to the light source after passage through the flame. A schematic drawing of the setup used for soot volume fraction is presented Fig.13. The beam attenuation in the flame due to the presence of soot was obtained by measuring the intensity of light with and without the flame. The voltage readings from the power detector were digitally sampled using LabView (National Instruments Inc.) at the rate of 2 Hz for duration of 1 minute. The average of the collected power readings at each location was then used in the calculation of soot volume fraction using equation (3), which is derived from the application of Beer's Law as provided by Yagi and Iino (1962). Other authors have used this relationship to study the soot distributions in a diesel-air flame and combustion in a diesel engine.

$$f_v = \frac{-ln\left(\frac{I_0}{I_s}\right).\lambda}{k_\lambda.\delta} \tag{3}$$

In Eq. (3) I_s is the incident laser intensity, I_o the attenuated laser intensity, k_λ the spectral extinction coefficient based on the refractive indices of the soot, λ the laser wavelength, and δ the flame thickness. The spectral extinction coefficient was assumed to be that of diesel soot. The laser and power meter were moved in equal distances along the radial direction and traversed in the axial direction at the same locations where in-flame temperature and in-flame species concentrations had been recorded.

PLIF Instrumentation:

Planar Laser Induced Fluorescence (PLIF) has been used extensively to determine the relative population densities of intermediate radicals within a combustion test medium. For PLIF measurements, a wavelength-controlled narrowband light source (laser) is used to excite molecules of a desired species to a higher energy level. The incident photons absorbed at each point are re-emitted with a modified spectral distribution. The re-emitted photons, a form of molecular scattering and radiation termed fluorescence, are of interest for PLIF measurements. By capturing emitted fluorescence a non-intrusive method for measurement of various flow field properties, such as species concentration, with low temporal (5-20 ns) and spatial resolution can be accomplished.

The laser system used for the measurements included a Quanta-Ray GCR 200 pulsed Nd:YAG laser and Quanta- Ray MOPO-730 Optical Parametric Oscillator (OPO) with Frequency Doubler Option (FDO). The GCR 200 generated a laser beam at a wavelength of 355 nm, which pumped the OPO. The OPO was a coupled dual oscillator system including the power oscillator, which was seeded by the narrow output master oscillator. The gain in the OPO system was accomplished from the nonlinear interaction between the intense optical wave (laser) and crystal having a large nonlinear polarizability coefficient. Tuning of wavelengths of the passing laser was obtained by altering the angle of the OPO crystals made from Type I Beta Barium Borate (BBO) crystal. The tuning wavelengths range from 190 – 2000 nm (ultraviolet to infrared) when using the FDO.

PLIF measurements were acquired by using a laser and a Princeton Instruments Model PI-MAX3: 1024i ICCD camera which reduced effects of background noise or

stray light. The output beam of the OPO/FDO was directed with a highly reflective optical turning mirror onto a cylindrical lens creating a laser sheet. The laser sheet created a 2-D sheet of radical fluorescence which was directed into the testing section. Florescence images were then acquired at 90^{o} to the incident laser sheet. A schematic diagram of this setup can be seen in Fig. 14. The laser was tuned to the corresponding excitation wavelength of OH (283.5 nm) and later for CH (431 nm). OH was pumped at the Q_1 (6) transition in the OH $A^2\Sigma \leftarrow X^2\Pi$ system of the (1,0) band and the resulting fluorescence from the (1,1) band (315 nm) was collected. CH PLIF was done using the transition of (0,0) band near 431 nm of the $A^2\Delta \leftarrow X^2\Pi$ system. In case of CH the transition was highly diagonal hence the excitation and detection were done on the same band.

PLIF images were captured from a flame region panning from the injector exit to 5 cm above the burner. Images are presented as normalized signal intensities providing a qualitative representation. Signal intensities were normalized by dividing all readings by the maximum value detected by the ICCD for a fuel; this is further discussed in Chapter 5. A total of 40 images were acquired using Lightfield 4.1 data acquisition/imaging software and averaged.

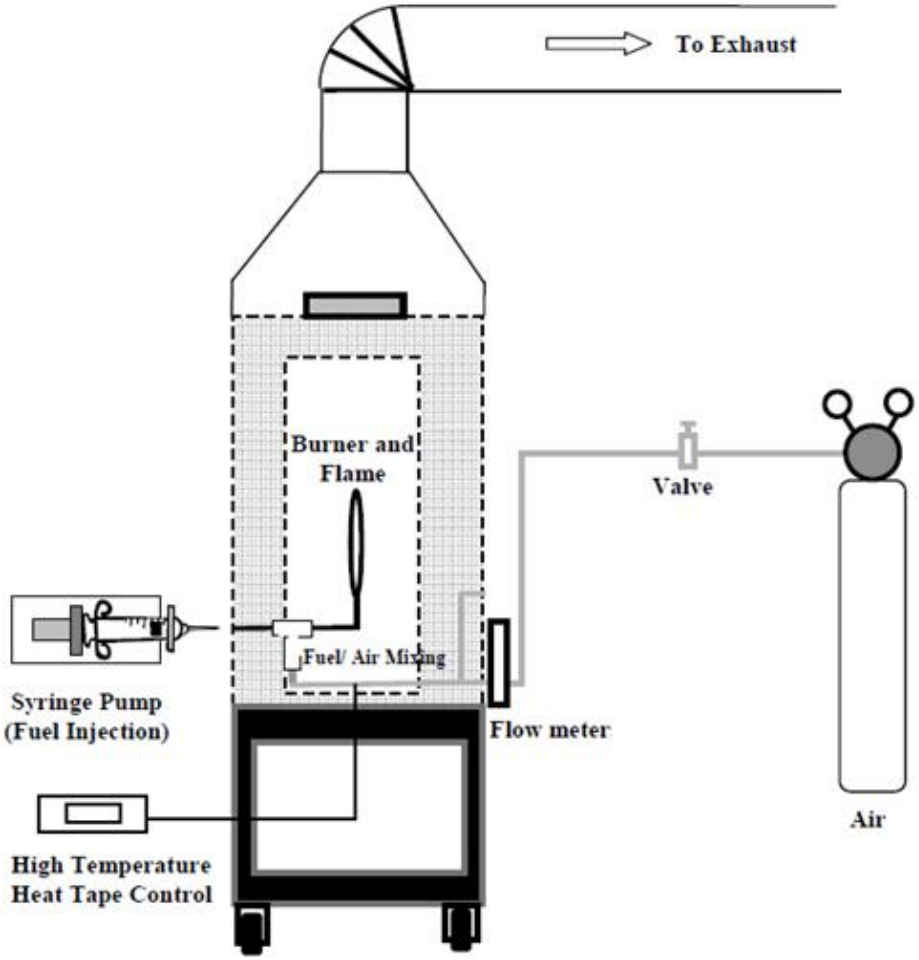

Fig. 5: Laboratory combustion chamber and Fuel supply train.

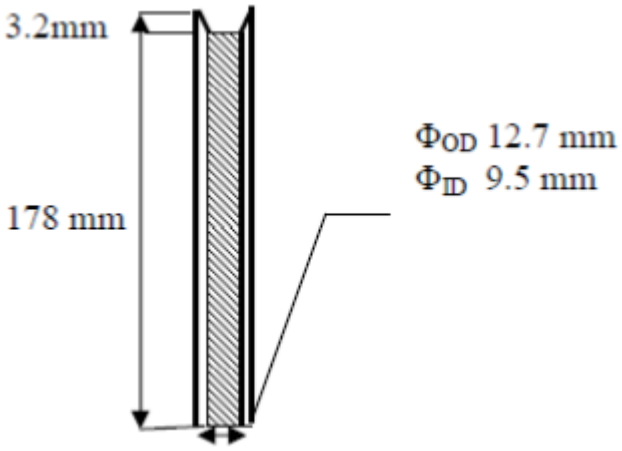

Fig. 6: Schematic diagram of tubular burner

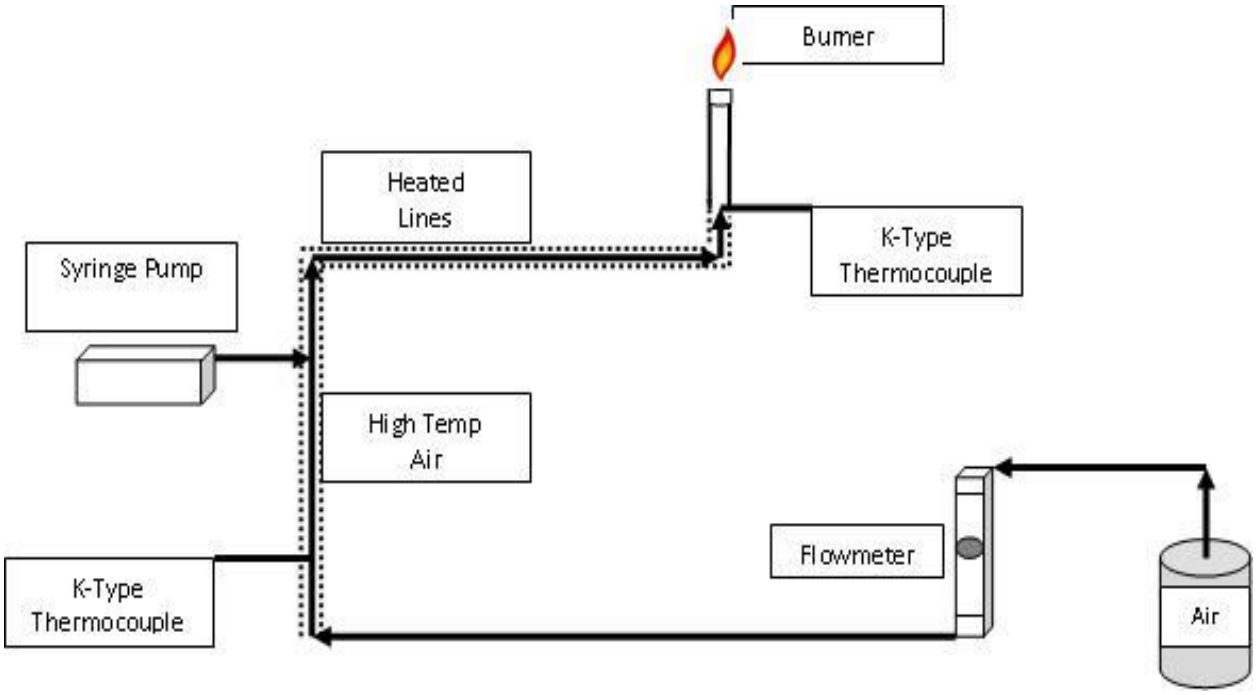

Fig. 7: Schematic Diagram of the experimental set-up.

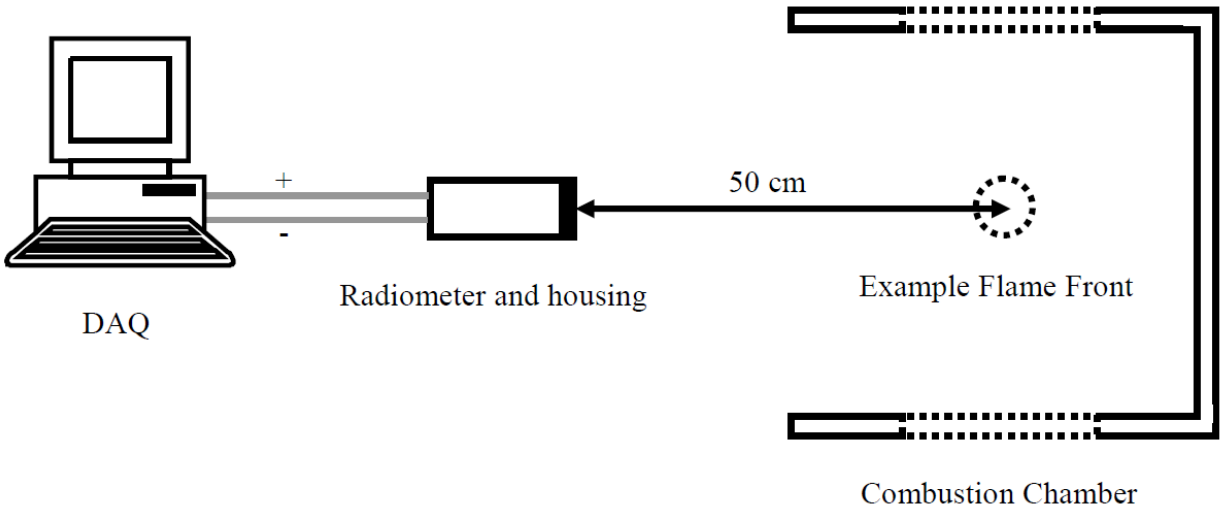

Fig. 8: Top view drawing of global radiation set-up.

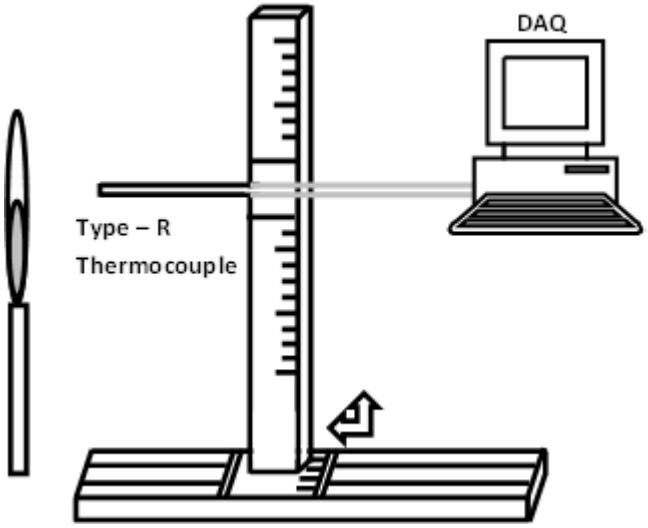

Fig. 9: Schematic drawing of the thermocouple and traverse used for temperature measurements.

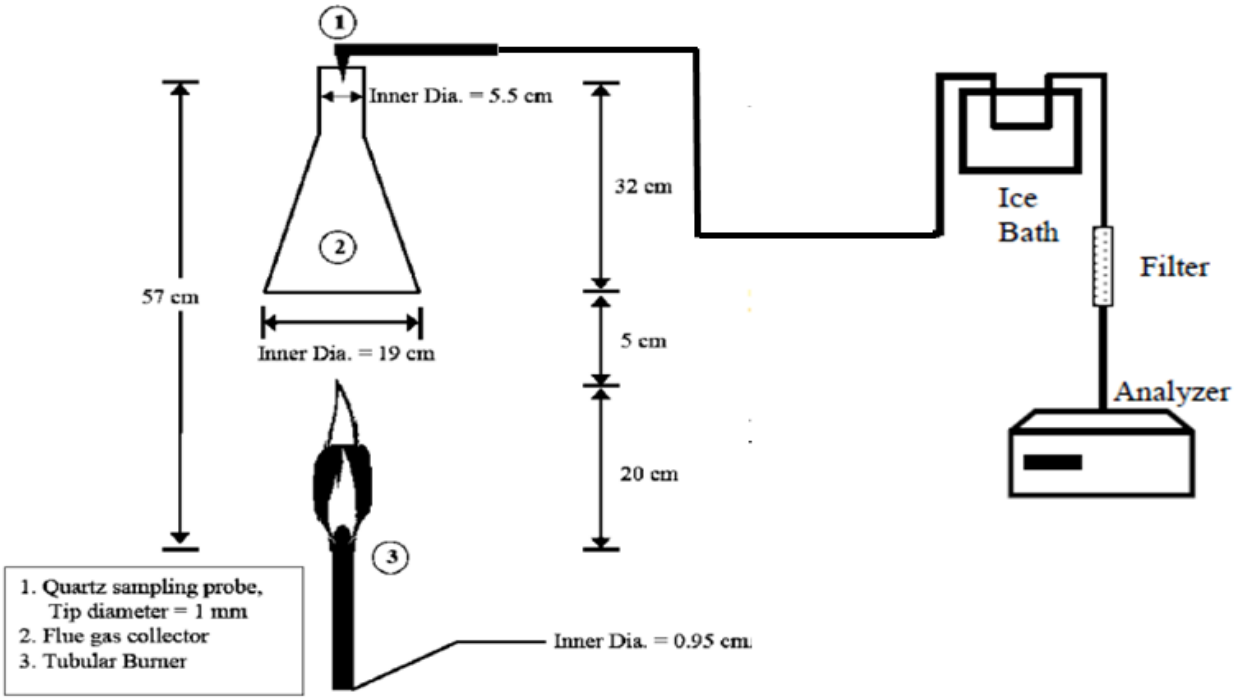

Fig. 10: Schematic diagram of global emissions sampling set-up.

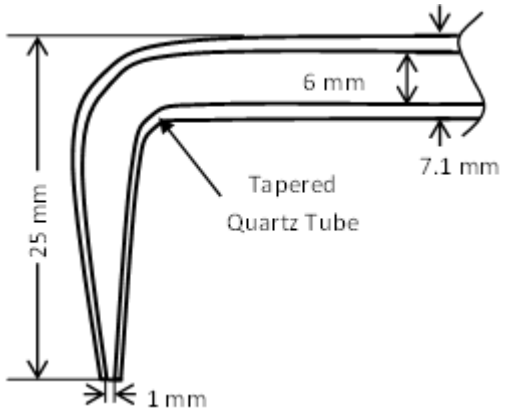

Fig. 11: Probe for global emissions measurement (side-view).

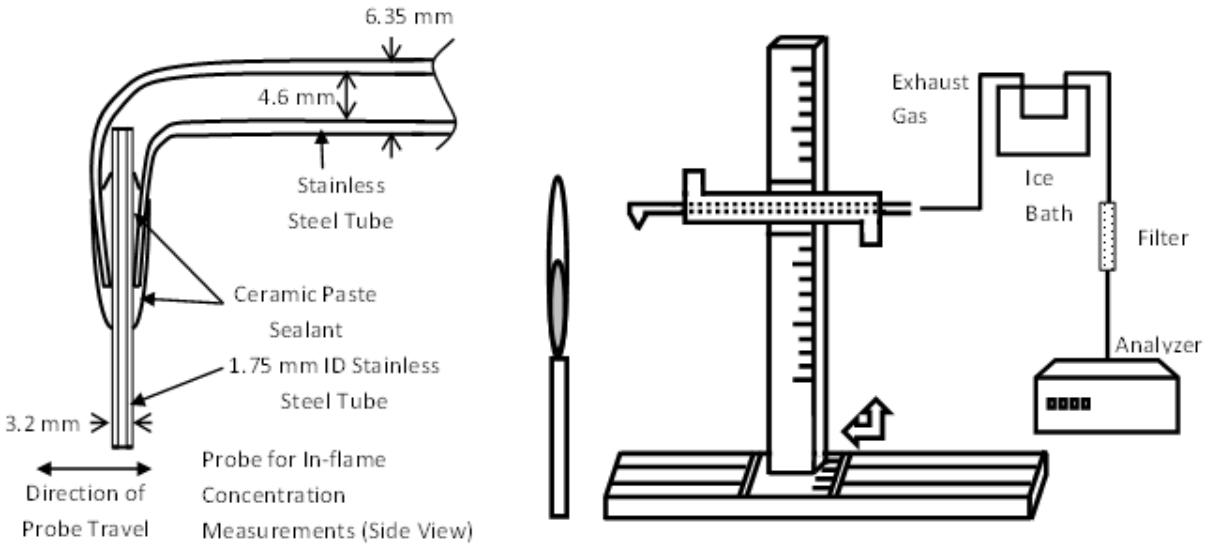

Fig. 12: Schematic diagram of in-flame emissions experimental setup and stainless steel probe

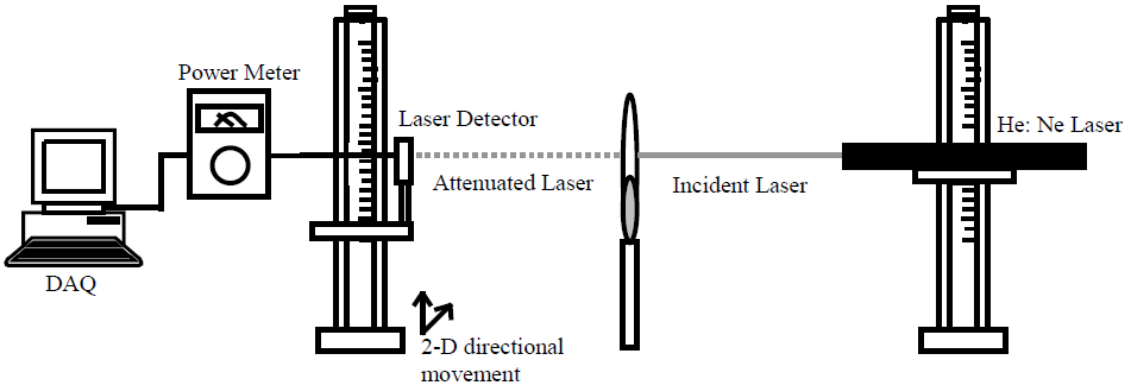

Fig. 13: Schematic drawing of experimental setup used for soot volume fraction measurements

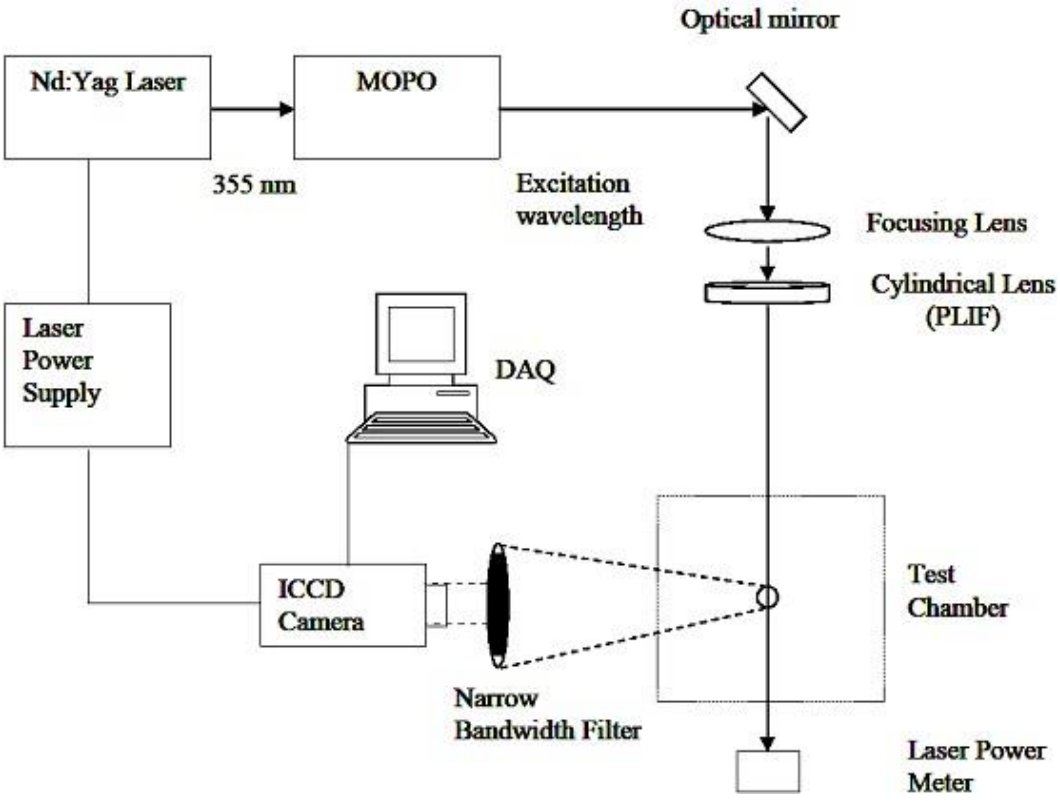

Fig. 14: Experimental setup for PLIF measurements

Table 2: Measured properties of all fuel tested.

Properties	Molecular Formula	Molecular Weight	Density (kg/m^3)	LHV (MJ/kg)	% O_2
Diesel (B0)	$C_{14.4}H_{24.9}$	197.7	843	42.6	0
CME B25	$C_{15.27}H_{27}O_{0.38}$	215.88	846	41.264	2.81
CME B50	$C_{16.28}H_{29.45}O_{0.82}$	237.97	853	39.95	5.51
CME B75	$C_{17.52}H_{32.42}O_{1.35}$	264.32	863	38.665	8.18
CME B100	$C_{19}H_{36}O_2$	296	876	37.4	10.81
SME B25	$C_{15.2}H_{26.71}O_{0.378}$	215.36	848.9	41.154	2.81
SME B50	$C_{16.22}H_{28.91}O_{0.828}$	236.82	857.9	39.74	5.59
SME B75	$C_{17.38}H_{31.48}O_{1.36}$	261.86	867.4	38.35	8.29
SME B100	$C_{18.8}H_{34.6}O_2$	292.2	887	37	11

Table 3(a.): Parts and Instrumentation used for the present study

Instrument	Manufacturer/ Model Number
Syringe Pump	Harvard Apparatus 975
50 cc Interchangeable Syringe	B-D Multifit 512135
High Temperature 11 mm Inlet Septa	Agilent 5183-4757
High Temperature Heavy Insulated Heat Tape	Omega Engineering Inc. STH051-080
Rotameter with Tantalum Ball	Lo-Flo with Tube Type SK ¼''-15-G-5
Omega Temperature Control	Omega Engineering Inc. CN79022
Digital AF SLR 8 MP Camera	EOS Digital Rebel XT/EOS 350D
NO_x, CO, CO_2, O_2 Emission Analyzer	NOVA 376 WP
Type R and Type K Thermocouple	Omega Engineering Inc.
Radiometer	Hy-Cal P-8410-B-10-120-XC-400
Precision Laser Power Meter	Coherent FieldMate 1028297
5 mW He-Ne Laser	Spectra Physics 105-1
Pulsed Nd: YAG Laser	Spectra Physics GCR 250-10
Optical Parametric Oscillator (OPO)	Spectra Physics MOPO-730
Frequency Doubler (FDO)	Spectra Physics FDO 970
Photomultiplier Tube with Cooled Housing	Oriel Instruments 77345/77265
Photomultiplier Power Supply	Oriel Instruments 70705
Spectrometer with Holographic Grating	Oriel Instruments 77700 and 77740
Pulsed Laser Power Meter	Ophir Optronics Ltd. NOVA 30
ICCD Camera	Princeton Instrument PI-MAX3: 1024i
ICCD Camera Image Acquisition Computer	HP Workstation Z210
Data Acquisition Hardware	National Instruments Labview Board SCB-100
Data Acquisition Software	National Instruments Labview 7.1
Data Acquisition Computer	HP Workstation Z210
Image Acquisition Software	Princeton Instrument WinView
Traversing Mechanism	Unislide / Velmex Inc.

Table 3(b.): Experimental Conditions and Measured parameters

Fuel	$(A/F)_{stoic\ by\ mass}$	**Air Flow Rate Range (m^3/s)**	**Volumetric Fuel Flow Rate (m^3/s)**	**Equivalence Ratio**	**Feedline Temperature**	**Measured Parameters**
CME B25	13.72	3.4 – 20.4 x 10^{-5}	2.67 x 10^{-8}	1.2, 2, 3, 7	400 ^{o}C	Flame Length, Emission Index, Radiation, OH/CH concentration, Temperature Profiles, Emission Profiles, Soot Volume Fraction
CME B50	13.24	3.5 – 20.6 x 10^{-5}				
CME B75	12.84	3.6 – 20.8 x 10^{-5}				
SME B25	13.69	3.8 – 22.8 x 10^{-5}				
SME B50	13.19	3.9 – 23 x 10^{-5}				
SME B75	12.77	4.0 – 23.3 x 10^{-5}				

Chapter 4
Results & Discussion (Global Properties)

This chapter covers the results and discussion for global flame properties. Global flame properties which include flame appearance, flame length, radiative fraction and global emissions of the six fuels tested.

Flame Appearance and Length

The flames tested varied in color, structure, and length as Φ was increased. At Φ = 1.2, Fig. 15 for Diesel, SME and CME & Fig. 16 for SME B25, SME B50, SME B75, CME B25, CME B50 and CME B75, all flames visually appeared blue. Two primary regions were observed, a bright blue inner cone surrounded by a second blue less luminous cone. The bright blue inner cone represented the primary gas-phase oxidation reaction zone. Remaining unburned reactants in the surrounding flame zone mixed with ambient air. The second outer cone was used to determine the average visible flame length. As the equivalence ratio was increased to Φ = 2, Fig. 17 & Fig. 18 presenting pure fuels & blends respectively, the flames became partially yellow, nearly doubling in length for all fuels. For increasing Φ less air was supplied, thus more air from the surroundings needed to be entrained, requiring an increase in length to effectively burn remaining fuel or particulates. The lower portion (<6 cm) of the flames remained blue, as gas phase reactions dominated in this zone. The remaining unburned reactants including soot continued to burn downstream with ambient oxygen, emitting continuum radiation at all wavelengths, thus appearing yellow. For Φ = 3, Fig. 19 & Fig. 20, the flame lengths increased for diesel, SME, and CME and did not significantly vary for the

blends. At Φ = 7, Fig. 21 & Fig. 22, the diesel flame appeared completely yellow decreasing in flame length. In contrast, the flame length increased for CME, SME, and the blends. A small blue region was observed near the burner exit (<1 cm) for the biofuels which decreased as the volume percentage of diesel was increased in the blends.

Radiative Fraction

The radiative heat fraction represents the fraction of the energy content in the fuel that is lost as radiation from the flame. The flame radiation is emitted by the burning soot particles and the high-temperature gases present in the flame; it thus depends on the local temperature, gas emissivity and soot emissivity. The measured radiative heat fraction, presented in Fig. 23 & Fig. 24 for CME and SME blends, significantly increased with increasing equivalence ratio (the flames became more yellow, Fig. 15-Fig. 22). As the flame became yellow or luminous, as seen at Φ = 2, 3, and 7, the primary radiative losses came from the presence of solid particles (soot) within the flame. Thus the radiation emitted from the flame, quantified by the F value, was used as a quick way to indicate the amount of soot produced from the different flames. The uncertainties in the measurements are presented as error bars. As the equivalence ratio was increased to 7, significant changes in the flame structure and emitted radiation were observed. All flames were almost completely yellow, thus radiation losses from these flames were primarily due to the presence of soot. At this condition peak soot concentrations were expected. For each equivalence ratio studied, the diesel flame produced the highest F value; a decrease in the measured F value was observed as the volume percentage of CME & SME was increased in the respective blend. The fuel-bound oxygen content in the CME & SME blends played a significant role in the reduction of soot formation in these flames.

Global Emissions:

NO Emission

The measured NOx emission index for the fuels tested at the four equivalence ratios is presented in Fig. 25 & Fig. 26 At Φ = 1.2, SME produced the highest EINO of 5.9 followed by CME (5.7) and the values decreased as the volume percentage of CME and SME was decreased in the respective blend. At this condition it is expected that the Zeldovich (thermal) mechanism was dominant, hence a function of flame residence time (flame length) as seen by NO emission correlation with flame length. As the equivalence ratio was increased to 2, NO production decreased to more than half of that from the condition of Φ = 1.2 with SME again having the highest EINO of 2.9. At this condition the Zeldovich (thermal) mechanism was thought to accompany other formation pathways of NO which became more dominant as the equivalence ratio was increased. Beginning at this condition flame length and radiative heat fraction no longer correlated with the measured NO. Next at Φ = 3 the NO emissions decreased for all fuels, with SME producing the largest amount of NO (1.85). Diesel despite having the longest flame length produced significantly less NO than the pure CME and SME flames. These same trends continued at the next condition of Φ = 7, the most NO was again collected for SME. The results indicate that the NO_x emissions decreased as the equivalence ratio was increased from Φ = 1.2 to Φ = 7 for all the fuels. For each equivalence ratio used, SME produced the highest emission index of NO_x followed by SME B75, SME B50, and SME B25 and the lowest for diesel. Similar trend was observed in the case of CME & its blends with diesel.

CO Emission

Emission Index of CO (EICO) for the six fuels tested at the equivalence ratios of 1.2, 2, 3, and 7 are plotted in Fig. 27 and Fig. 28. The graphs show a decrease in the emission of global CO with increase in biofuel content. This is because of the oxygenated nature of biofuel, which lowers soot formation, and facilitates the oxidation of CO to CO_2. At $\Phi = 1.2$, diesel produced the highest EICO of 1.89. As the equivalence ratio was increased to 2, CO production increased with diesel again having the highest EICO, 2, and did not significantly change other fuels. At $\Phi = 3$ the CO emissions increased for all fuels with diesel producing the largest amount of CO (6.5). At $\Phi = 7$, diesel produced the largest amount of CO (23). In general, the CO emissions increased, as the equivalence ratio was increased from $\Phi = 1.2$ to $\Phi = 7$ for all fuels tested (as seen in Fig. 23 & Fig. 24). The diesel flame produced the highest emission index of CO followed by CME B25, CME B50, CME B75 and CME flames for all equivalence ratios. SME & its blends also followed the same trend. At each equivalence ratio the diesel fuel produced the largest amount of CO compared to all other fuels. At $\Phi = 1.2$, EICO for all fuels were comparable and did not significantly change as the equivalence ratio was increased to 2. As the equivalence ratio was further increased large differences in CO production for the fuels were seen at $\Phi = 3$ and $\Phi = 7$. As the flames became more fuel rich the effect of the molecularly bonded oxygen became increasingly evident. These observations are similar to those documented during *engine testing, as discussed earlier*.

A high level of correlation between radiation, soot, and luminosity can be seen in the results presented above. Flames of CME biofuel and its blends & SME biofuel and its blends produced lower radiation, lower CO emissions, but higher NO_x emissions than the diesel flame. The effect of additional oxygen in the molecular structure of CME and SME and their respective blends contributes to the lower CO emissions and radiative heat emission. The production of low amounts of soot leads to less heat radiated, resulting in higher temperatures, and consequently more thermal NOx formation. However, detailed measurements in the pure biofuel laminar flames indicated the absence of any correlation between peak temperatures and peak NOx concentrations; the NOx formation in these flames was attributed to the Fenimore mechanism than the Zeldovich mechanism (Love 2009). Detailed in-flame measurements of NOx concentrations were necessary to see if a similar trend was followed in the flames of the CME & SME blends which are presented in the next chapter.

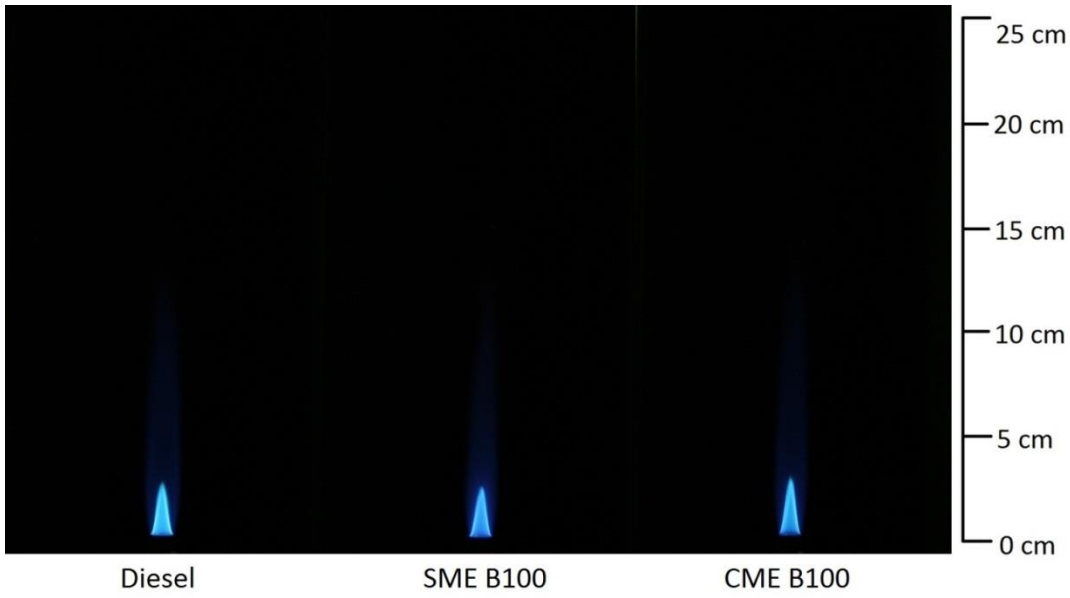

Fig. 15: Visual flame images of diesel, SME and CME at Φ =1.2.

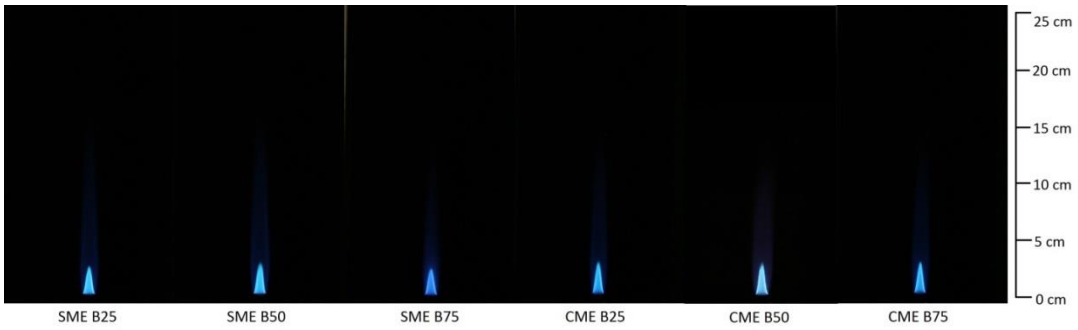

Fig. 16: Visual flame images of SME blends and CME blends at Φ =1.2.

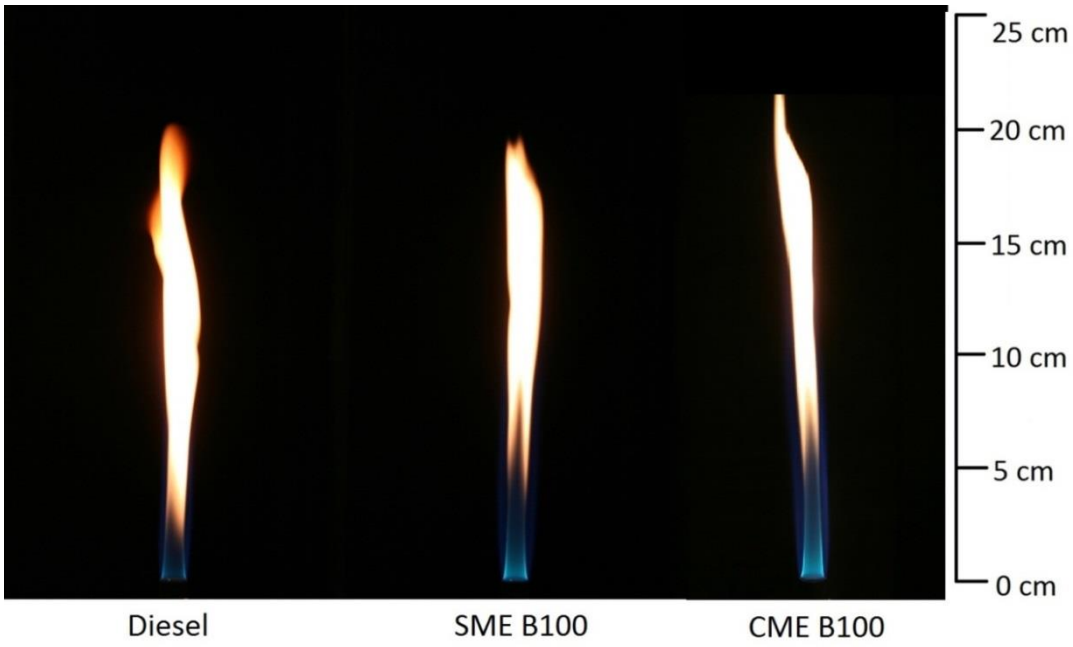

Fig. 17: Visual flame images of diesel, SME and CME at Φ =2.

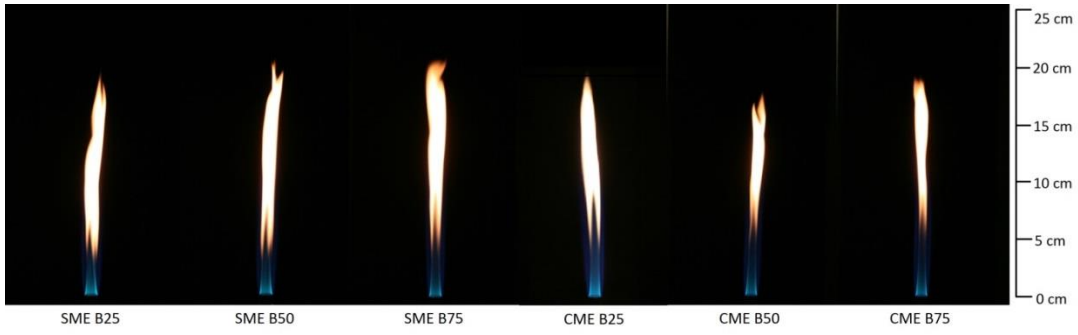

Fig. 18: Visual flame images of SME blends and CME blends at Φ =2.

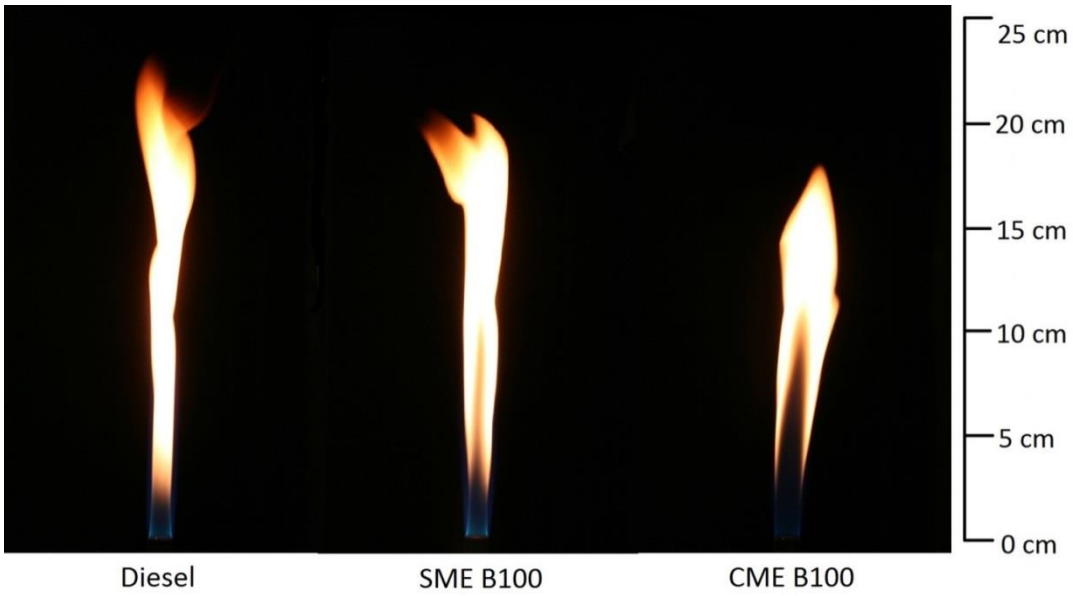

Fig. 19: Visual flame images of diesel, SME and CME at Φ =3.

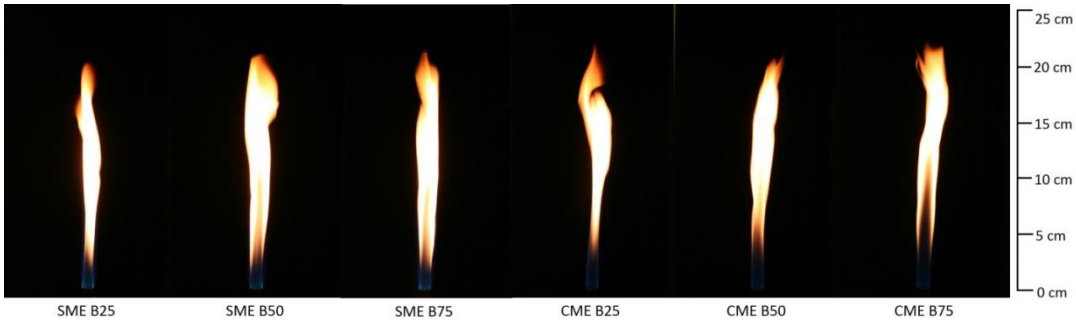

Fig. 20: Visual flame images of SME blends and CME blends at Φ =3.

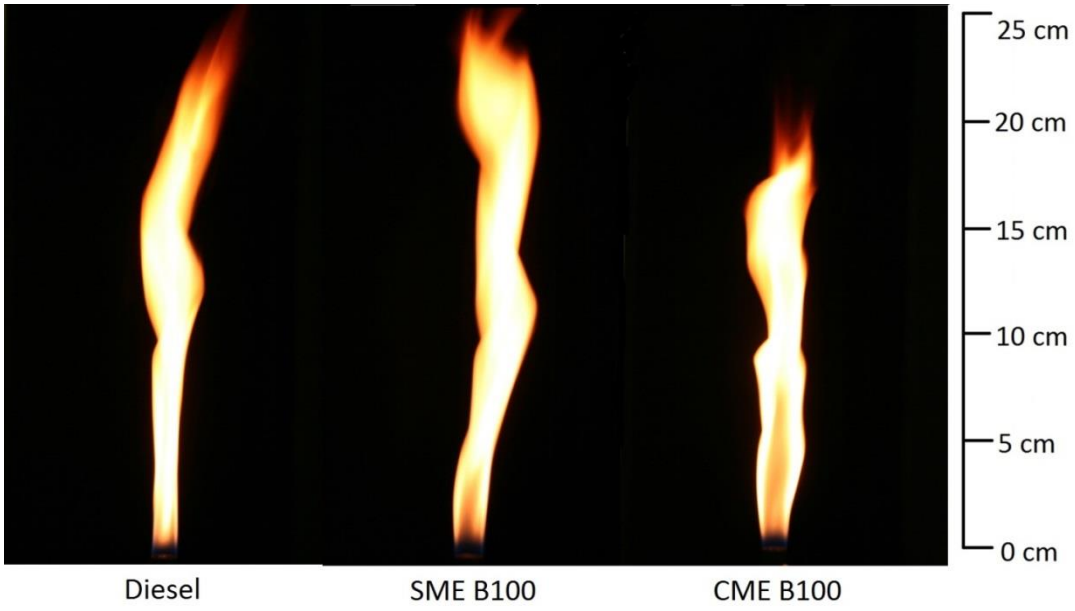

Fig. 21: Visual flame images of diesel, SME and CME at Φ =7.

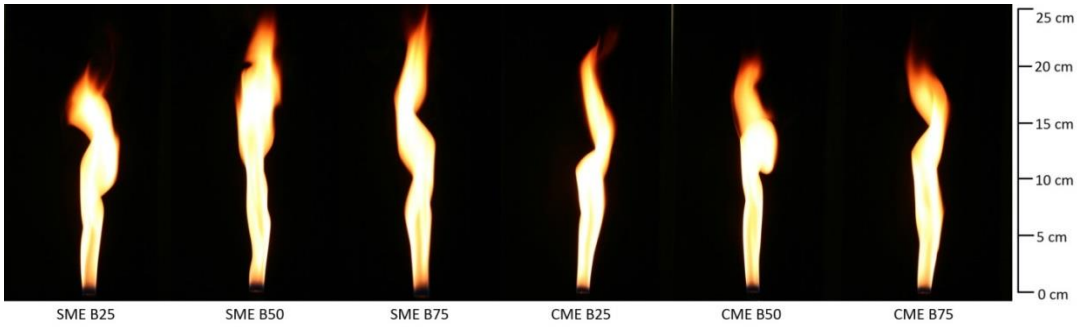

Fig. 22: Visual flame images of SME blends and CME blends at Φ =7.

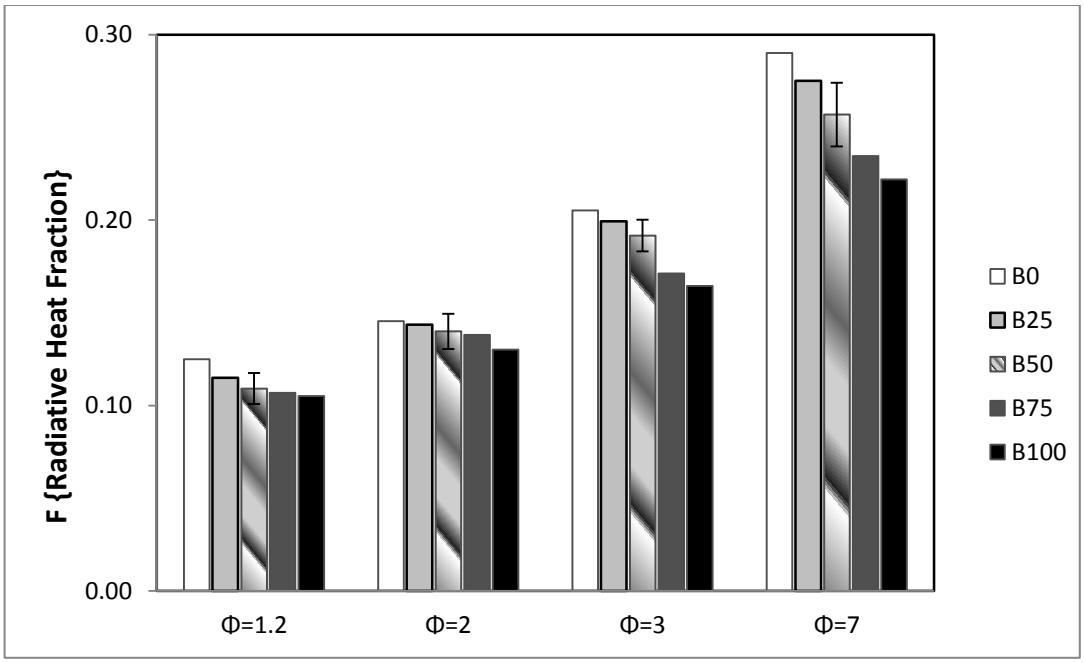

Fig. 23: Radiative fraction of heat released for CME blends tested at different equivalence ratios.

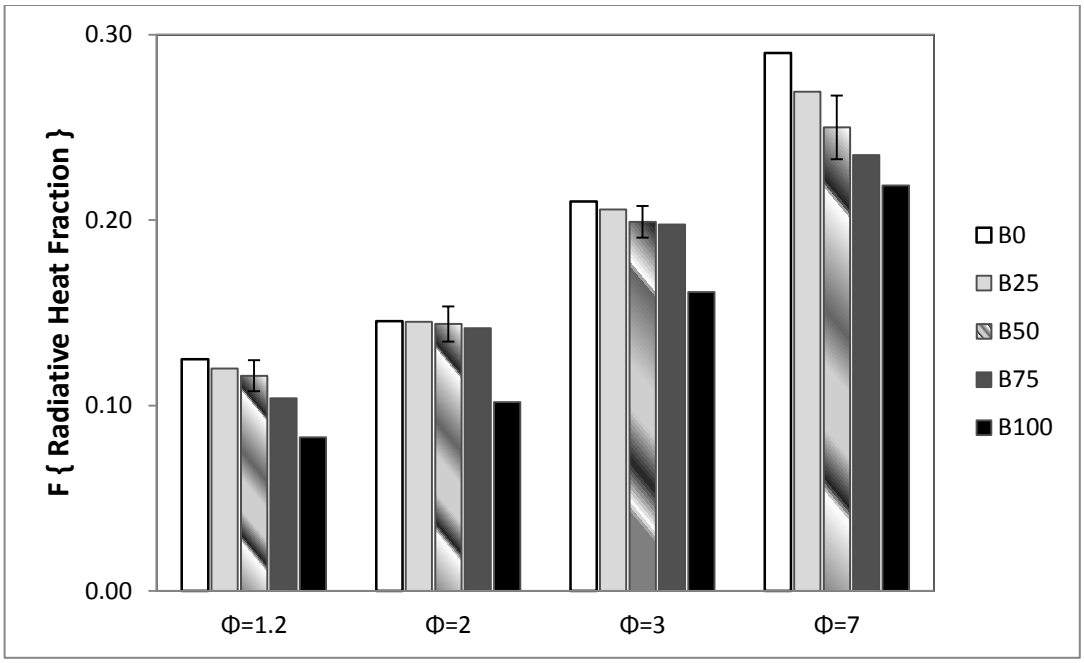

Fig. 24: Radiative fraction of heat released for SME blends tested at different equivalence ratios.

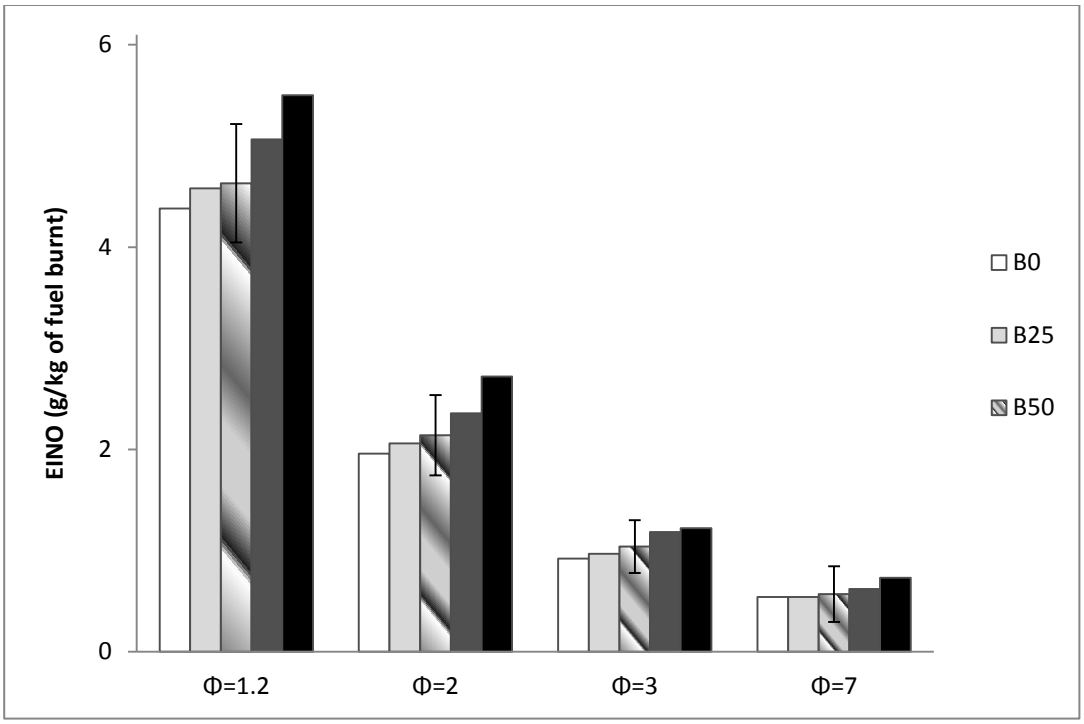

Fig. 25: Emission index of NO_x for CME blends.

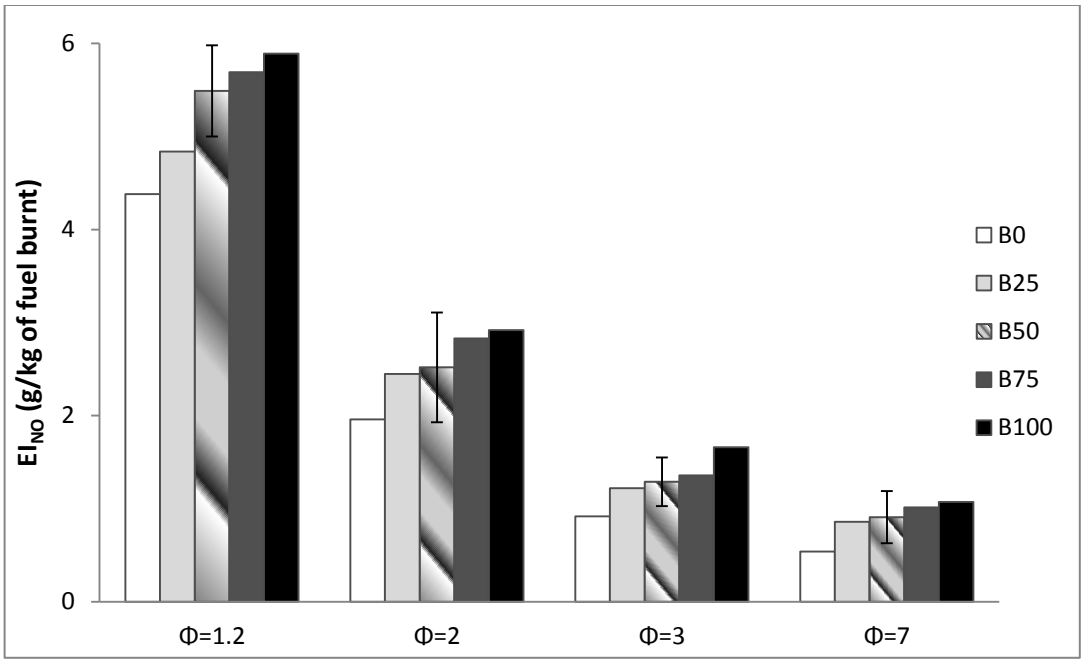

Fig. 26: Emission index of NO_x for SME blends.

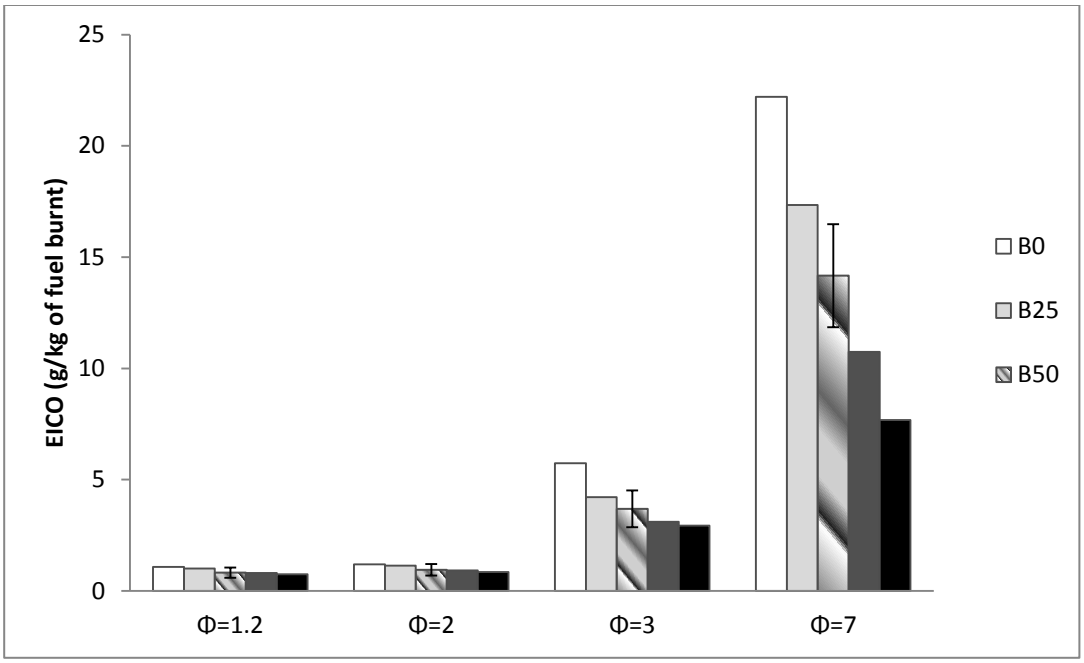

Fig. 27: Emission index of CO for CME blends.

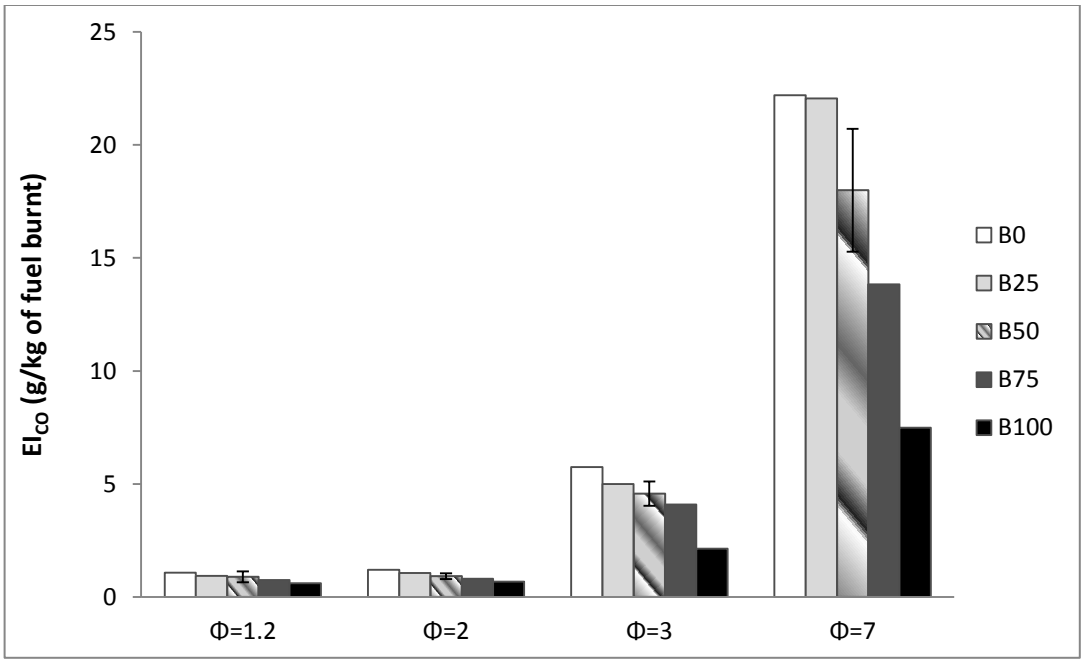

Fig. 28: Emission index of CO for SME blends.

Chapter 5
Results & Discussion (Flame Structure)

This chapter focuses on the inflame characteristics of the six biofuels tested. The inflame experiments were performed at the same conditions at which global experiments were performed, where in the equivalence ratio was varied. The experiments were conducted to determine the effects of equivalence ratio on the inflame temperature, inflame emissions, OH and CH radical concentrations, and the soot volume fraction in the flames of the fuels tested. All the experiments, except the PLIF experiment, were conducted at three flame heights; near burner (0.25 flame height), mid burner (0.50 flame height) and far burner (0.75 flame height). The flame height for different conditions (Φ = 1.2, Φ = 2, Φ = 3 and Φ = 7) for all the six fuels were determined by an imaging software as discussed in the previous chapter. For the PLIF experiment the readings were gathered at the near burner location, which will be discussed later in the chapter.

Temperature Profiles:

The temperature distribution in the laminar flames of the six fuels is shown at equivalence ratios of 1.2, 2, 3, and 7 for the near burner, mid burner and far burner locations in Figs. 29 - 52. The temperature distribution profiles were corrected for radiation and conduction losses (Jha et al., 2008, Hariharan, 2004, Chinthamony, 2005). The maximum temperature was documented at an equivalence ratio of 1.2 for CME B75 fuel. This flame was predominantly blue at this condition, as seen in the previous chapter. As the equivalence ratio was increased, the presence of less premixed air resulted in the fuel to depend on entrained air for burning; hence, the maximum

temperatures decreased progressively. This result was expected as maximum temperatures occur at or near stoichiometry. As the equivalence ratio was increased, the flames became fuel rich, and less premixed air resulted in the fuel dependence on mixing with the surrounding air. The consequent dilution lowered the reaction rate of the flame, hence lowering the maximum temperature.

At Φ = 1.2, the flame was closer to a fully premixed stoichiometric flame; therefore, the temperatures peaked at the centerline. As the equivalence ratio was increased to 2 and 3, double humps in the temperature profiles, typical of diffusion flames were observed. The flame temperatures were lowest at the flame centerline at these conditions. The double humps disappeared and peak temperatures were measured at the centerline at 75% flame height for the Φ = 3 flame, indicating that the surrounding air was well mixed with the reacting mixture in the flame at this location. The double humps were not observed in the flame at Φ = 7, as the thermocouple was traversed radially. Flame oscillations due to ambient disturbances were observed at this condition, which resulted in the flattening of the temperature profiles. Data points recorded were averaged over the 60 second acquisition time at each radial location which included this movement of the flame and resulted in a temperature distribution that did not significantly vary in the radial direction. The temperatures recorded in the far-burner region of the flames were lower than those recorded in the mid and near-burner portion of the flame due to radiation from burning soot (as discussed later in the chapter). The highest temperature was recorded for CME B75 (2254.7 K) at the near-burner location for Φ = 1.2. The lowest flame temperature was recorded for SME B25 (480 K) at the far-burner location for Φ = 7. The peak temperatures were comparable in

flames of all fuels; the computed adiabatic flame temperature was comparable for diesel and the biofuels. Adiabatic flame temperatures and the corresponding enthalpies of reactants are presented in Table 4. Adiabatic flame temperatures were calculated at atmospheric pressure and initial temperature of 700K using the computer code developed by Olikara and Borman (1975) which solved for 12 species, 7 equilibrium reactions, and atom conservation relations for C, H, N, and O. According to Table 3 for pure fuels, diesel was expected to have the highest adiabatic flame temperature (2282 K) followed by CME (2268 K), and SME (2266 K). In the case of blends, CME B25 and SME B25 were expected to have the highest adiabatic flame temperature of (2275.3 K) and (2274.6 K) respectively, which decreased as the volume percentage of diesel was decreased in the blends.

At Φ = 1.2, however, the highest temperature was recorded for CME B75 (2254.7 K) which decreased as the volume percentage of diesel was increased in the blend. SME blends showed a similar trend with SME B75 recording the highest temperature (2238 K). These temperature profiles are presented in Figs. 29, 33, 37, 41, 45 and 49. All measured peak temperatures occurred in the near burner region and were within experimental uncertainties, not significantly varying between each fuel blend.

At Φ = 2, the structure of the temperature profiles changed from the previous condition, as the flames became more ‘yellow’. Figure 38 shows the temperature profile for the CME B75 flame which produced the highest peak temperature of all other fuel blends at this condition, 1876 K. Temperatures recorded in the far-burner region of the flames were lower than those recorded in the mid and near-burner portion of the flame. The other five fuel blends were similar in flame structure to CME B75 demonstrated by

their temperature distributions which peaked in the near-burner or mid-flame regions along the edge of the flame.

At $\Phi = 3$, the structure of the temperature profiles was similar to those at $\Phi = 2$. Flame temperatures were observed to peak in either the near-burner or mid-flame regions decreasing in the far-burner portion of the flame. At $\Phi = 3$, the CME B75 flame produced the highest peak temperature of 1519 K in the near burner region. The effect of radiative heat transfer due to the presence of soot in flame was again observed at this condition. CME B25 and SME B25 produced an F-value (radiative fraction of heat release) significantly higher than other fuel blends, hence resulting in the lowest measured flame temperatures.

At $\Phi = 7$, temperature profiles were different in shape and structure than all other previous conditions in that they did not vary significantly as the thermocouple was traversed radially. Peak temperatures occurred in the near-burner region for all fuel blends, decreasing for the other two downstream flame regions. CME B75 produced the highest peak flame temperature, 1126 K, in the near burner region.

In-flame species concentration profiles

In-flame concentration profiles of CO, CO_2, NO and O_2 were made using a NOVA 376WP gas analyzer. For combustion applications it is very important to know where and how much are the combustion products being formed. The concentration profiles provide an insight on that. All the radial concentration profiles are plotted with origin at the axis of the flame. Experiments were performed at the same axial locations where inflame temperature measurements were performed and are presented in Figs. 53-148.

Nitric Oxide (NO)

Nitric oxide is an important air pollutant because of its contribution to smog and acid rain. There are many factors that have an impact of NO formation, typically, oxidizer and fuel composition, burner design, flame temperature, preheating air temperature, flame geometry etc. NO concentration profiles are presented in Figs. 53-76 for all six fuels tested at equivalence ratios of 1.2, 2, 3, and 7. In general, it was observed that emissions of NO increased as the volume percentage of biofuel was increased in the blend.

At Φ = 1.2, the flames of all fuels demonstrated similar distributions of NO, with peaks occurring along the flame boundary where the primary region of gas-phase oxidations reactions took place. NO concentration peaked in the far-burner region and was highest in the SME B25 flame (578 ppm). An increase in NO was observed at farther locations downstream of the injector exit, which can be attributed to the effects of an increase in cumulative residence time. The NO concentration profiles at this condition showed resemblance with temperature profiles. The oxygen content in the biofuel blends resulted in an increase in the temperature of the flames, thus assisting the increase in the NOx emissions at this condition. Based on these results the dominant formation of NO at this condition can be attributed to the thermal (Zeldovich) mechanism.

At Φ = 2, as the flames became more ‘yellow’, the NO production did not follow temperature. Figure 58 shows the NO concentration profile for the CME B50

flame which produced the highest peak concentration (550 ppm) of all other fuel blends at this condition. The flames of the other five fuel blends were similar in structure to the CME B50 flame, as demonstrated by their concentration distributions which peaked in the near-burner. Since primary NO formation was observed in the near-burner region of these flames, the relatively longer residence time responsible for the thermal mechanism did not contribute much to NO production. These findings indicate that a transition was occurring and the thermal mechanism was no longer dominant.

At $\Phi = 3$, NO concentrations peaked in the near-burner region and significantly dropped to much lower values at the mid and far burner locations in the flame. In this region, the CMEB75 flame produced the highest peak NO (875 ppm). Again, the measured values of NO did not correlate with the peak measured temperatures. At $\Phi = 7$, NO concentration significantly increased in the near burner region of the flame reaching peak values of 967 ppm for the SME B75 flame. High NO concentration near the injector exit, where low (<1800 K) flame temperatures existed implied the dominance of NO formation through the prompt mechanism.

Carbon Monoxide (CO)

CO is a flammable gas which is nonirritating, colorless, odorless, tasteless and normally noncorrosive. It is a significant species in the combustion of rich mixtures such as those in the present study and typically represents the incomplete combustion product of pyrolyzed fuel components. Concentration profiles of CO are presented in Figs. 77-100 for all flames at equivalence ratios of 1.2, 2, 3, and 7. In general, the CO concentration remained higher at the near burner region where the O_2 concentration was low. The CO molecules were then further oxidized to CO_2 as they travelled along the flame to a region with higher O_2 concentration. The flames of all fuels demonstrated similar distributions of CO in the radial and axial profiles of the flames. Peak values were achieved in the near-burner region of the flames decreasing at the mid-flame and far burner locations as CO was oxidized to CO_2. Low values were recorded until reaching the flame boundary increasing along the flame centerline.

At $\Phi = 1.2$, all flames demonstrated similar distributions of CO concentration, with peaks occurring along the fuel-rich flame centerline. The CME B75 flame produced the highest value of 7.1% in the near burner region. Similar results were obtained at $\Phi = 2$ and 3. Flames increased in thickness, thus the CO concentrations began to increase at locations farther from the flame centerline. Peak CO concentrations again occurred in the near burner regions decreasing at downstream locations. At $\Phi = 2$ and 3, the SME B25 flame produced the largest amount of CO; (7.01%) and (6.93%) respectively. In-flame concentration values of CO for the other flames were comparable at the two conditions. At $\Phi = 7$, the CME B50 flame (6.40 %) showed the largest

amount of CO. Profiles were similar to those at the lower equivalence ratios, decreasing as the probe was moved further downstream of the injector exit.

Carbon Dioxide (CO_2)

Carbon dioxide (CO_2) is a colorless, odorless, inert gas. CO_2, a product of complete combustion, indicates the oxidation of fuel fragments and CO within the flame. Recently, emphasis has been placed on reducing CO_2 emissions and on 'carbon-neutral' technologies. Concentration profiles of CO_2 from this study are presented in Figs. 101-124 for the flames of six fuels tested at equivalence ratios of 1.2, 2, 3, and 7. For the tested fuels, CO_2 production was directly affected by fuel equivalence ratio and flame temperatures, remaining higher for the lowest equivalence ratio of 1.2 and decreasing for the subsequent conditions. At $\Phi = 1.2$, peak values were obtained along the flame reaction zone boundary and decreased toward the flame centerline. The peak was where most oxidation took place, where O_2 from the air diffused into the flame and oxidized with the soot particles and other species, like CO and CO_2. Profiles above this region became flatter in the mid and far-burner regions, mostly peaking at the center line. The centerline peak at the mid and far-burner regions was because of the oxidation of the soot particles, which were concentrated at the center of the flame. No significant differences were observed in the peak CO_2 concentrations for all flames at this condition with the CME B50 flame showing the highest value (14%).

As the equivalence ratio was increased to 2 and less oxygen was supplied, peak concentrations of CO_2 dropped. The flames maintained similar structure to that at $\Phi = 1.2$ with peaks along the flame boundary, decreasing as the probe traversed near the centerline. SME B50 produced the highest peak value of CO_2 (12.9 %). At $\Phi = 3$, peak concentrations dropped further with the SME B75 flame producing 10.6%. At the next

condition of $\Phi = 7$, peak concentrations dropped again with the SME B75 flame producing 10.5%.

Oxygen (O_2)

Oxygen in the exhaust gases represents the oxidizer which did not react during the combustion process, and therefore, decreasing values of O_2 concentration, in general, indicates a more complete combustion. O_2 concentrations at the same locations as the other emissions are presented in Figs. 125-148. The O_2 concentration shows a general trend of decreasing oxygen content towards the center of the axis of the flame. O_2 concentration profiles were inverted as compared to the combustion product profiles. The slopes were steeper in the near-burner and mid-burner regions and in the far-burner region the concentration was higher.

At the lowest equivalence ratio of 1.2, as the probe approached the flame boundary, the O_2 concentration values began to decrease to zero as the probe entered the reaction region. It was observed that as the probe moved further downstream to the mid-flame and far burner regions more oxygen was present. At $\Phi = 2$, up to 6% oxygen was measured in the far burner region along the centerline indicating the entrainment of more air was entrained than that required to oxidize fuel fragments, soot, and CO. The CME B50 flame showed the highest amount of O_2 in the far-burner region up to 6% along the centerline. Next at $\Phi = 3$, oxygen concentrations remained about zero in the near burner region for all fuels and increased in the mid flame regions to 4.4% for the CME B50 flame. As the probe traversed across the far-burner region near the centerline, the O_2 concentration values rose to 9.4%, and 9%, for CME B25, and CME B50 flames respectively. For $\Phi = 7$, more oxygen was detected in all regions of the flames for all

fuels, except that oxygen concentrations dropped to about zero in the near burner region. This was due to the low flow rate of air supplied.

Soot Volume Fraction

Figures 149 to 172 show the radial profiles of soot volume concentration for all the flames. In general, soot volume fraction showed an increase in concentration at the far burner regions as compared to near-burner and mid-burner regions. Soot volume fraction profiles were measured at the same axial and radial positions as the temperature measurements. At $\Phi = 1.2$, the soot volume fraction was small. A similar pattern was observed at an equivalence ratio of 2, with the peak soot volume fraction values significantly higher than those corresponding to $\Phi = 1.2$. In these figures soot volume fraction is presented as a fraction of the maximum value (normalized), $f_v/f_{v,max}$, where the maximum value occurred for the SME B25 flame at $\Phi = 7$ with a value of 2 ppmv. This was done since the extinction coefficient (k_λ), which depended on the refractive index of soot, was unavailable for the soot of biofuels. In general, it was observed that as the equivalence ratio was increased the peak soot volume fraction measurements also increased. This was expected in an environment where less air has been supplied, such as those in this study.

Uncertainties in the measurements are presented as error-bars. At $\Phi = 1.2$, the soot volume fraction values were small and similar in structure for all fuels. The largest amount of air was supplied at this condition, which resulted in the oxidation of hydrocarbon pyrolysis species that lead to the production of soot. CME B25 flame had the peak soot volume concentration at this condition. The profiles in the near-burner region showed that higher values occurred along the edges of the flame boundary and decreased along the flame centerline. In the mid-burner region the profiles resembled parabolic shape. As indicated earlier, the flames at high equivalence ratios needed

entrained air for burning; therefore, larger amounts of soot were measured at these conditions. The width of the flame containing significant amount of soot also became larger at these conditions. At $\Phi = 3$, the CME B25 flame again had a peak soot concentration of 65% of the maximum value. Peak soot volume fraction values occurred for the CME B25 flame in the mid-flame region and in the far-burner region for all other fuels. Although the measured peak soot volume fraction values were comparable for the flames at equivalence ratios of 3 and 7, the overall soot content in the flame was significantly larger at the equivalence ratio of 7. At $\Phi = 7$, the SME B25 flame produced the peak soot concentration for which all other values were normalized. The soot volume fraction profiles are not as symmetric as the temperature profiles because the soot volume was computed from path-integrated measurements, whereas the temperature was measured at each point. Also, flame oscillations due to ambient disturbances affected the soot volume measurements more than the temperature measurements.

PLIF measurements

OH Concentration:

The results presented below will discuss importance of the OH in oxidizing the soot particle. Neoh et al. (1984) study showed that OH radical is important in the soot oxidation process in an atmospheric pressure flame at temperature range of 1580 to 1860K. Figures 173 to 179 show a qualitative representation of OH concentration presented as normalized signal intensities for all the flames. In these figures, OH concentration is presented as a fraction of the maximum value (normalized), where the maximum intensity detected by the ICCD camera, occurring for the No. 2 diesel flames at $\Phi = 1.2$, was used to normalize all other detected values. In general, it was observed that as the equivalence ratio was increased signal intensities in OH measurements decreased

At $\Phi = 1.2$, the highest OH concentration was recorded for the diesel flame, followed by the CME B25 flame which decreased as the volume percentage of CME was increased in the blend. The flames of SME blends showed a similar trend with the SME B25 flame recording the highest OH Concentration, not significantly varying between each fuel blend. At $\Phi = 1.2$, the signal intensities were high and similar in distribution for all flames. The largest amount of air was supplied at this condition.

At $\Phi = 2$, peak OH concentration of all the flames were observed to be significantly lower than at $\Phi = 1.2$. Also, at $\Phi = 2$, a shift was observed in the production of OH with the CME B75 flame having the highest concentration of OH,

followed by the CME B50 flame and so on, with all flames producing the major concentration of OH $\leq$ 2 cm above the burner. Above this location, low amounts of OH were documented. Since the major differences were seen near the injector exit, this difference is attributed to the presence of molecularly-bonded oxygen within the CME fuel. For Φ = 3 and 7, OH concentrations in the diesel and CME flames were low, between 20 and 30% of the full scale value. Therefore, no significant differences were observed between the two OH concentration fields of the flames at Φ = 3 and 7. Also, the population of OH radials dropped significantly due to OH depleting oxidation reactions. In other words, OH radical dominates the soot oxidation in the chemical-dominated flame.

CH Concentration:

Figures 180 to 186 show a qualitative representation of CH concentration presented as normalized signal intensities for all the fuels tested. Since CH radicals are intermediately linked with the formation of NO through the Fenimore (prompt) mechanism, CH PLIF was qualitatively used to determine relative concentrations of CH. The maximum intensity detected by the ICCD camera, occurring for the SME B75 flame at $\Phi = 7$, was used to normalize all other detected values.

At $\Phi = 1.2$, distributions of CH radicals for all flames were greatest within the flame reaction zone. CH concentration regions were similar in size and distribution to OH concentration regions, with diesel producing peak signal intensity.

At $\Phi = 2$, the signal intensities decreased. The levels of CH were found to be less than 40% of the peak concentration value for all fuels. The formation of CH seemed to be a transition point at this equivalence ratio since sufficient oxygen was supplied to suppress their formation demonstrated by the low soot volume fraction values.

As the equivalence ratio was increased to 3, increased signal intensities for CH radicals were detected at about 3-5 cm above the injector exit. Near the injector exit where oxidation reactions were expected low concentrations of CH were detected, similar to results from $\Phi = 2$. B25 produced the highest peak CH concentrations with the largest detected region followed by SME B25. As the volume percentage of Diesel was increased in the fuel blends, although similar behavior was demonstrated, signal intensities decreased.

As the equivalence ratio was increased to 7, high values of CH concentrations were again detected at 4-5 cm above the injector exit. Highest peak values of CH were recorded for CME B25, followed by SME B25. All the fuel blends produced a similar distribution to that at $\Phi = 3$ with CH detected in the near burner region extending to the 4-5 cm region where peak intensities were detected. As the volume percentage of biofuel was increased, peak intensities decreased, with CME B75 and SME B75 producing the lowest intensities of CH radicals and were the only fuels that did not produce a high concentration of CH or distribution comparable to the other fuels.

One of the important investigations in the current study was carried through the measurement of the concentration of OH and CH radicals, to determine the dominant route of soot and NOx formation in flames of the six biofuel blends. Planar Laser-Induced Fluorescence (PLIF) images of hydroxyl radicals OH and CH radicals were captured with a diagnostic system consisting of a pulsed Nd:YAG laser and an Optical Parametric Oscillator (OPO) with frequency doubler option (FDO) using proper wavelengths. At $\Phi = 1.2$, flames from all fuels produced peak OH concentration fields and peak temperatures, with diesel fuel recording the highest concentration. Although the OH concentration decreased as the volume percentage of CME and SME was increased in the blend, the concentration did not significantly between each fuel blend. Also, it was observed that residence time increased with NO_x concentration. These results indicated the dominance of the thermal (Zeldovich) mechanism for all fuels at this condition.

As the equivalence ratio was increased, it was found that the population of OH radicals decreased and was low in the flames of all fuels, but significant CH radical concentrations were detected in all the flames, with the maximum population occurring in the CME B25 fuel flame at $\Phi = 7$. The peak intensities decreased as the volume percentage of biofuel was increased. The presence of high concentrations of CH measured in the regions of peak NOx indicate that NOx formation is primarily through the Fenimore mechanism, rather than the thermal mechanism, at fuel-rich conditions. From the results of the OH concentration and the soot concentration measurements t, for all flames at $\Phi = 1.2$, it can be concluded that the OH radical dominated the soot oxidation process.

Table 4: Adiabatic flame temperature of all fuels at stoichiometry for Initial temperature of 700K (Olikara and Borman (1975))

Fuel	Diesel	CME	SME	CME B25	CME B50	CME B75	SME B25	SME B50	SME B75
Adiabatic Flame Temperature at Stoichiometry (K)	2282	2268	2266	2275.35	2270.3	2267.71	2274.66	2269.04	2265.53
Enthalpy of Reactants (kJ/kmol – fuel)	-256037	-760220	-771217	-382083	-508129	-634174	-384832	-513627	-642422

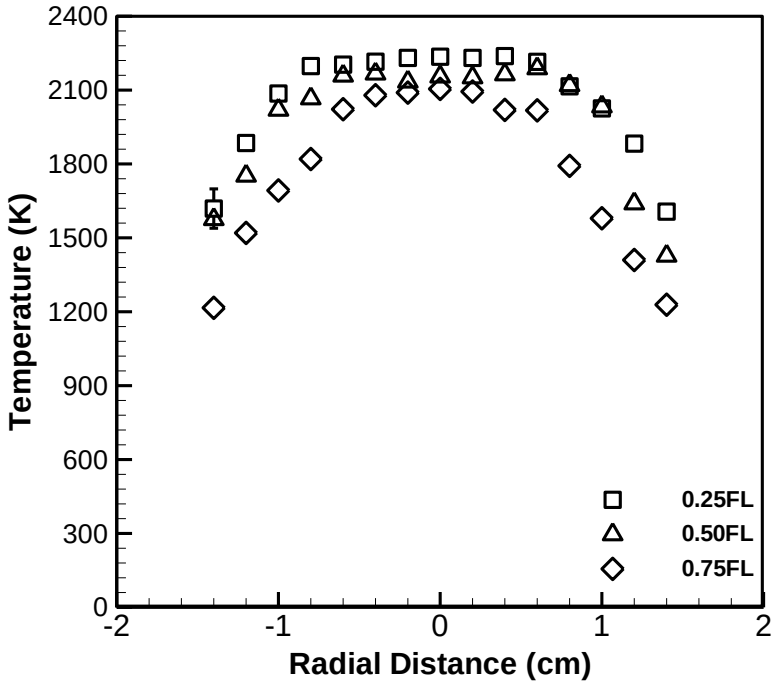

Fig. 29: Temperature profiles of CME B25 flame at Φ = 1.2

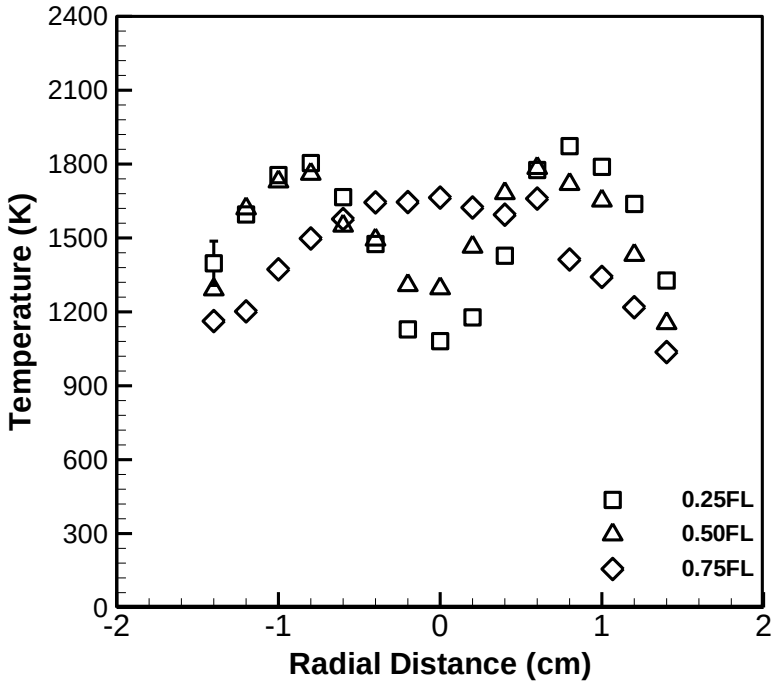

Fig. 30: Temperature profiles of CME B25 flame at Φ = 2

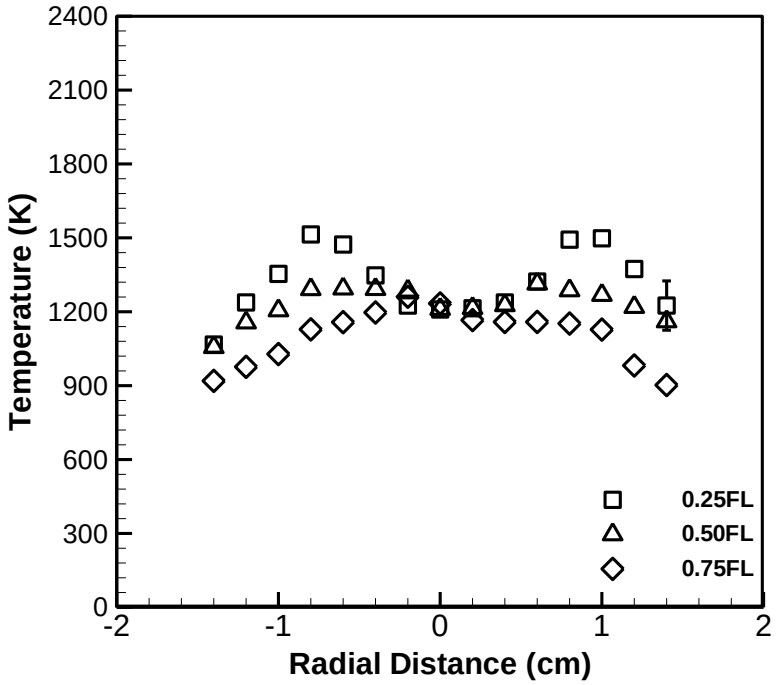

Fig. 31: Temperature profiles of CME B25 flame at Φ = 3

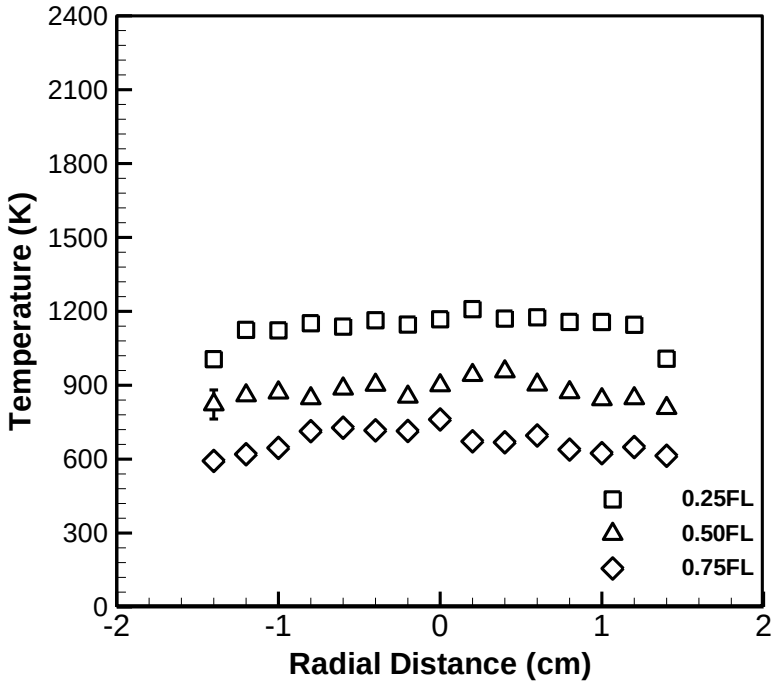

Fig. 32: Temperature profiles of CME B25 flame at Φ = 7

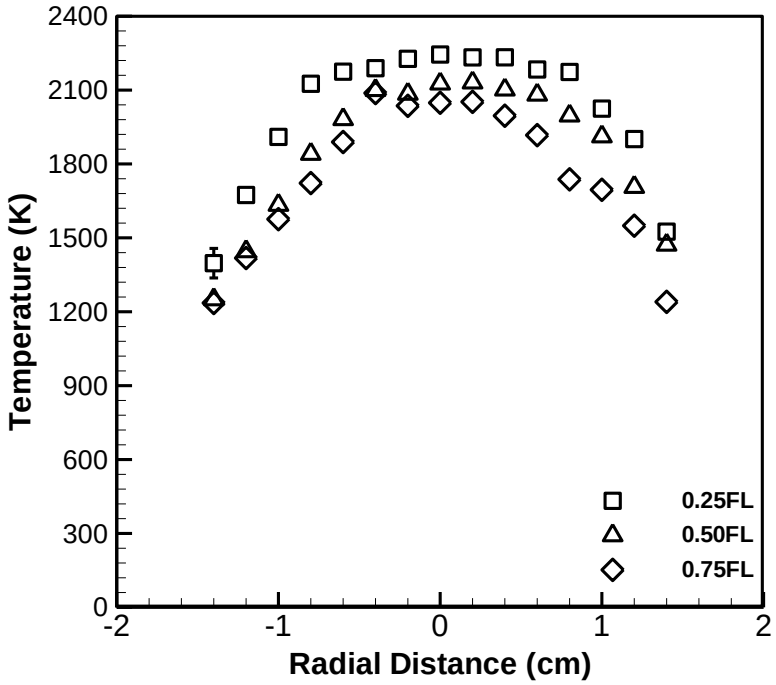

Fig. 33: Temperature profiles of CME B50 flame at Φ = 1.2

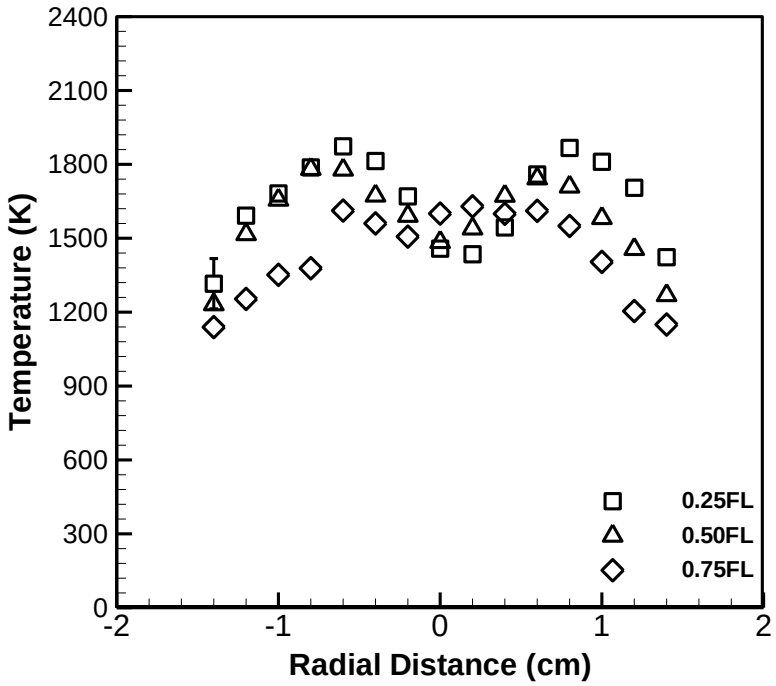

Fig. 34: Temperature profiles of CME B50 flame at Φ = 2

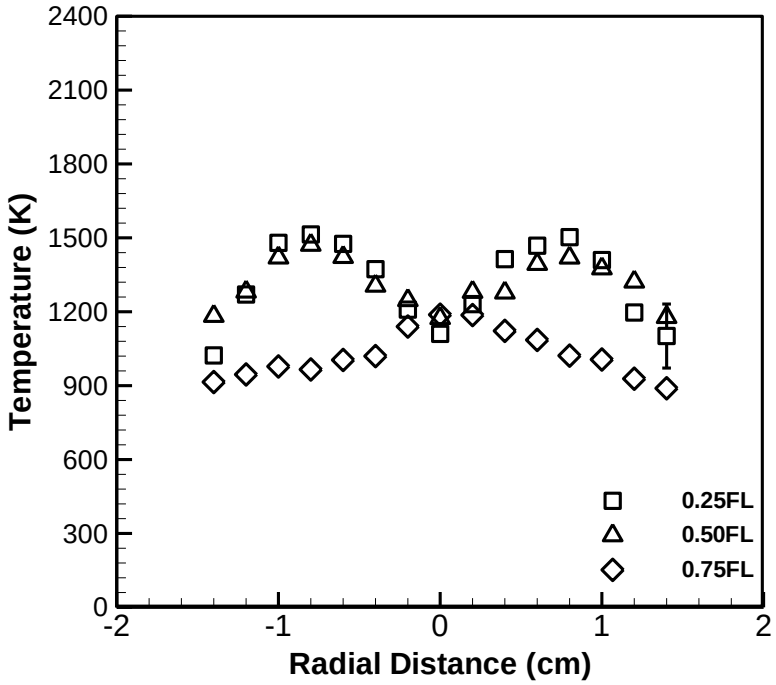

Fig. 35: Temperature profiles of CME B50 flame at Φ = 3

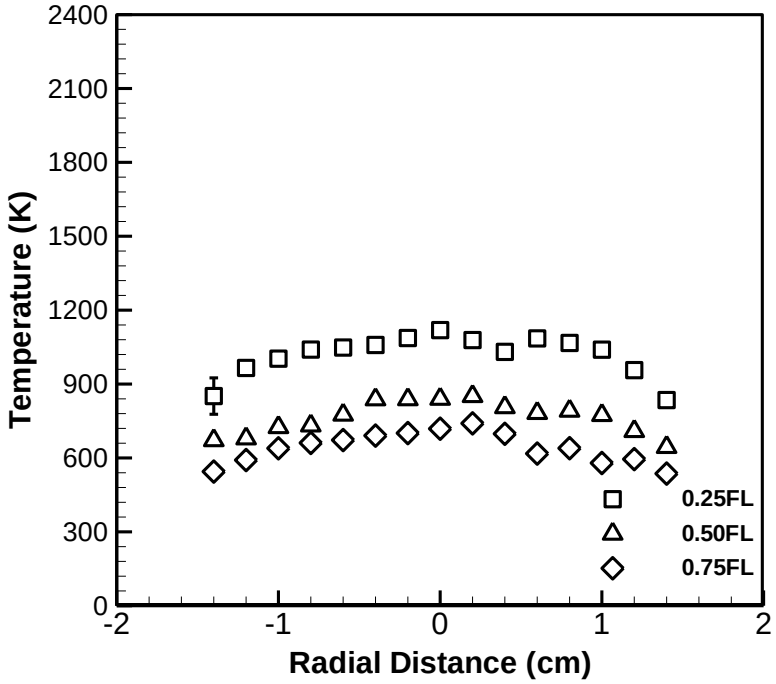

Fig. 36: Temperature profiles of CME B50 flame at Φ = 7

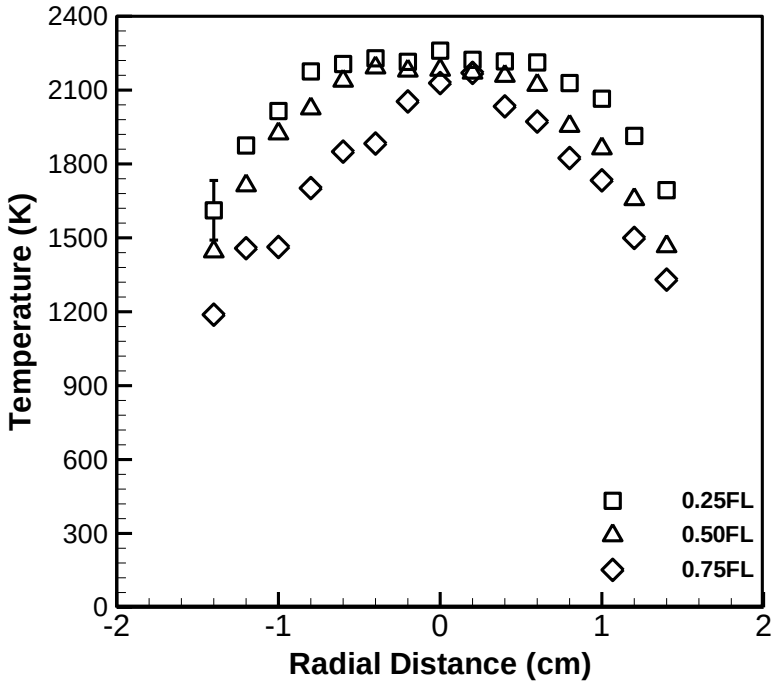

Fig. 37: Temperature profiles of CME B75 flame at Φ = 1.2

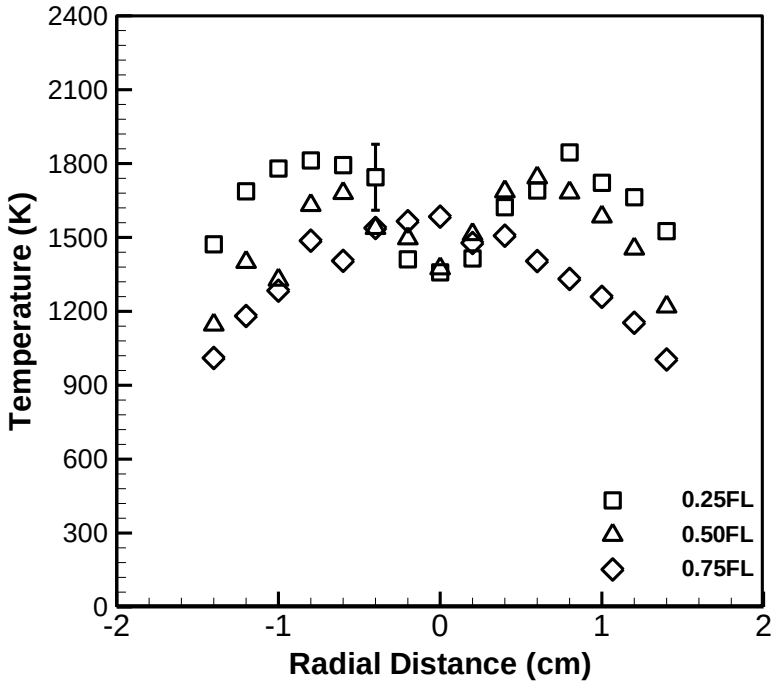

Fig. 38: Temperature profiles of CME B75 flame at Φ = 2

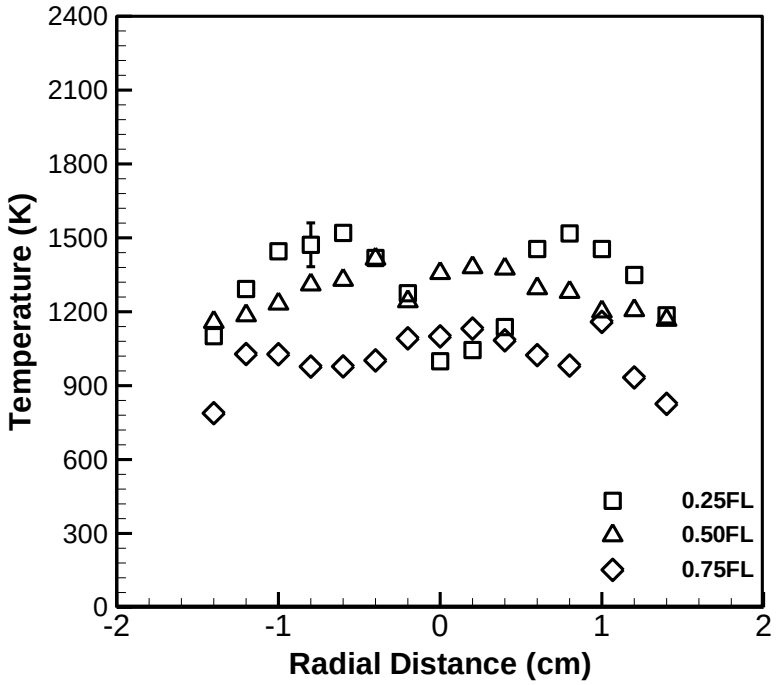

Fig. 39: Temperature profiles of CME B75 flame at Φ = 3

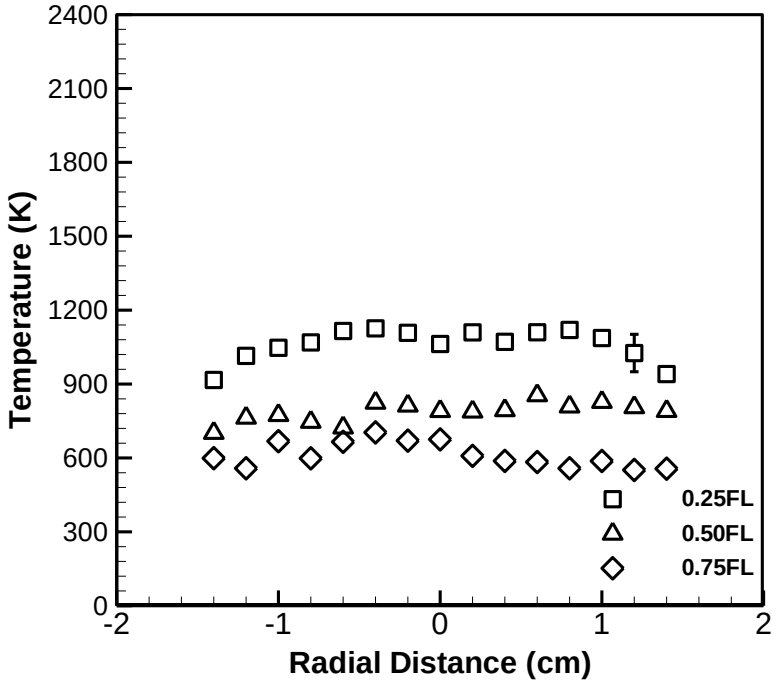

Fig. 40: Temperature profiles of CME B75 flame at Φ = 7

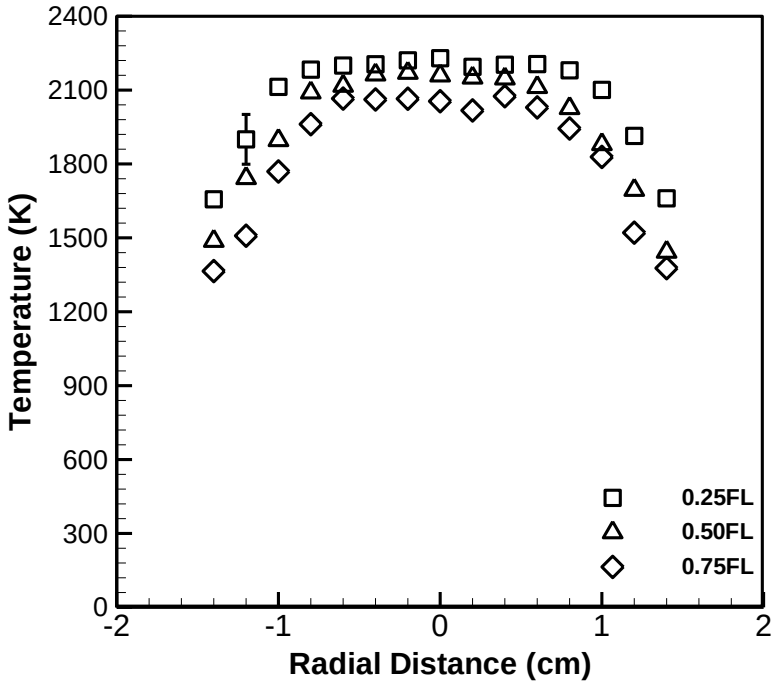

Fig. 41: Temperature profiles of SME B25 flame at Φ = 1.2

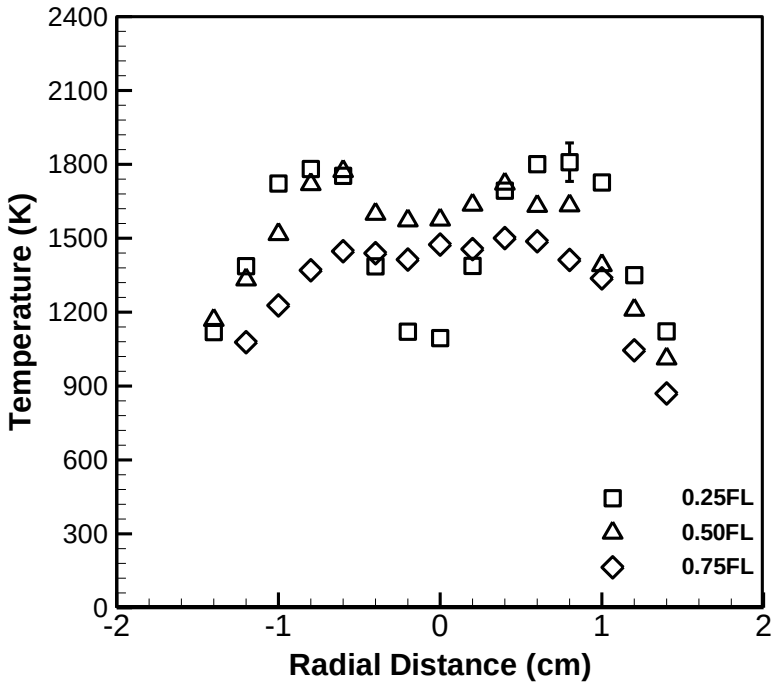

Fig. 42: Temperature profiles of SME B25 flame at Φ = 2

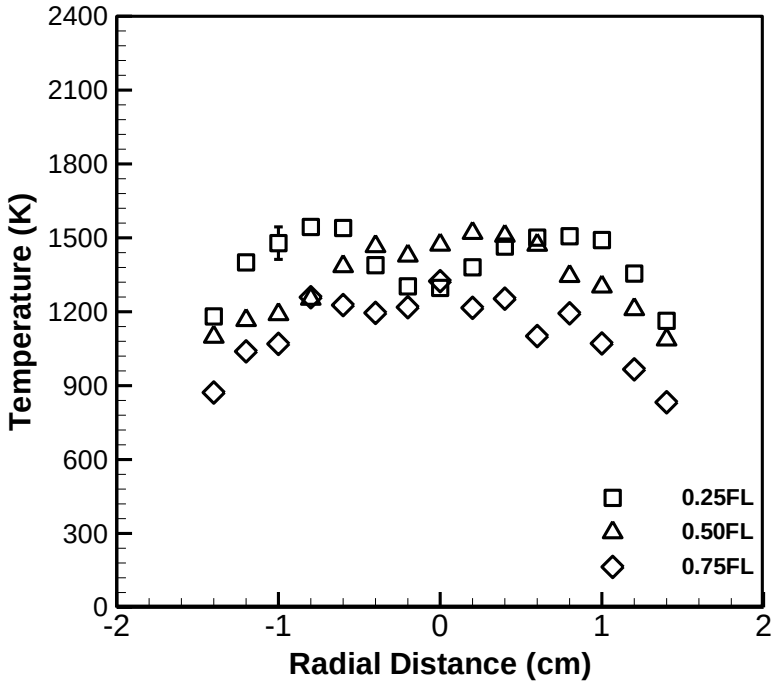

Fig. 43: Temperature profiles of SME B25 flame at Φ = 3

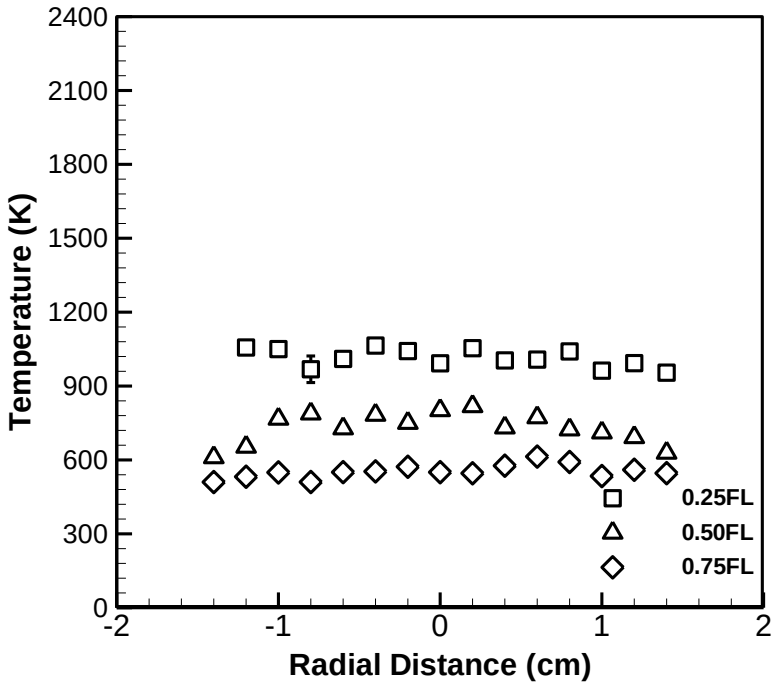

Fig. 44: Temperature profiles of SME B25 flame at Φ = 7

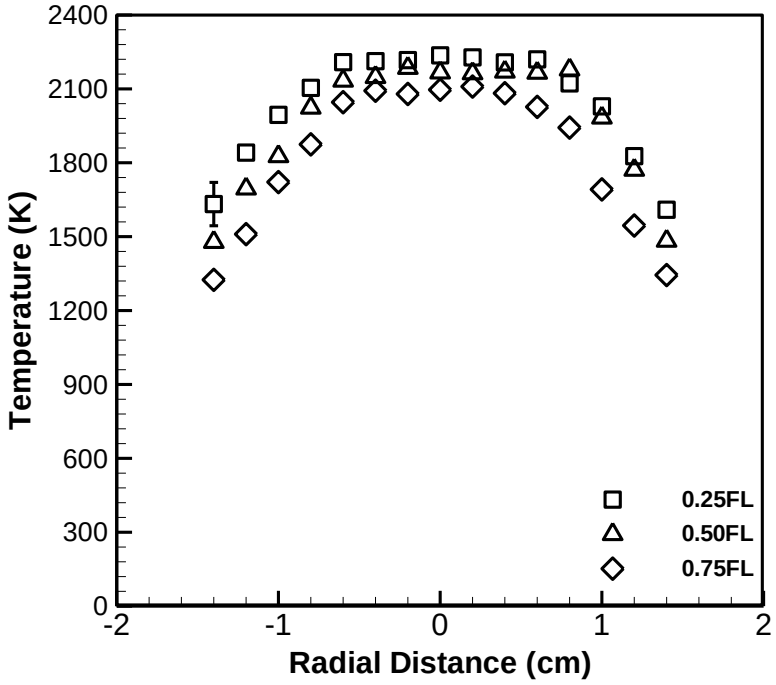

Fig. 45: Temperature profiles of SME B50 flame at Φ = 1.2

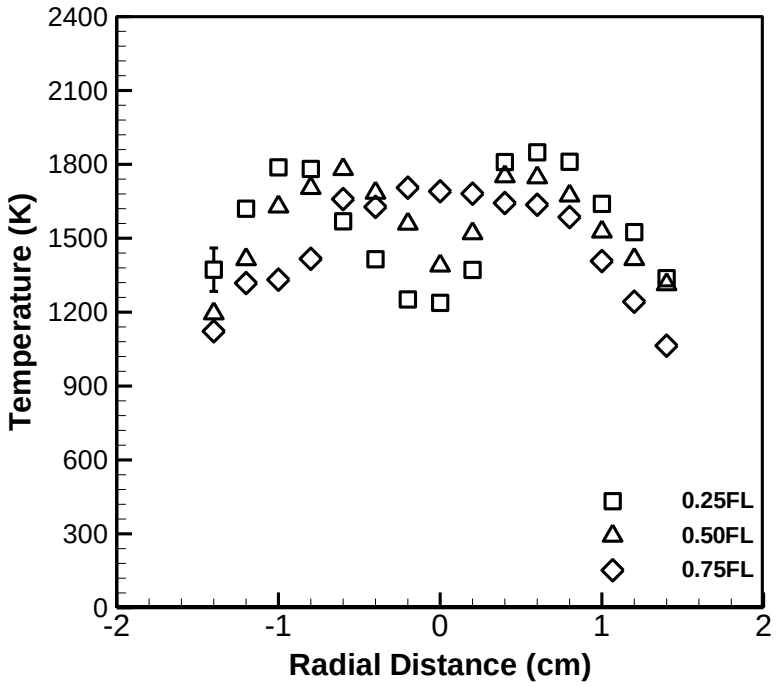

Fig. 46: Temperature profiles of SME B50 flame at Φ = 2

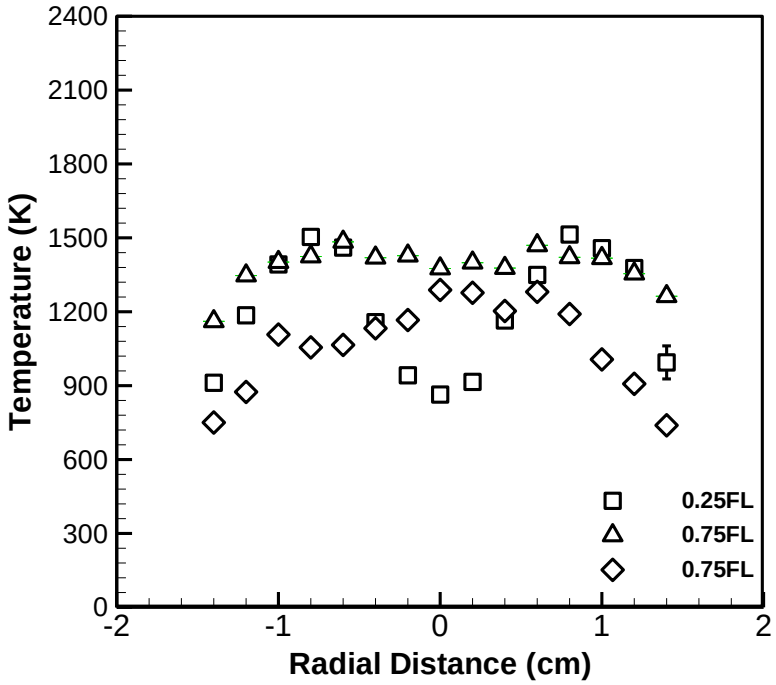

Fig. 47: Temperature profiles of SME B50 flame at Φ = 3

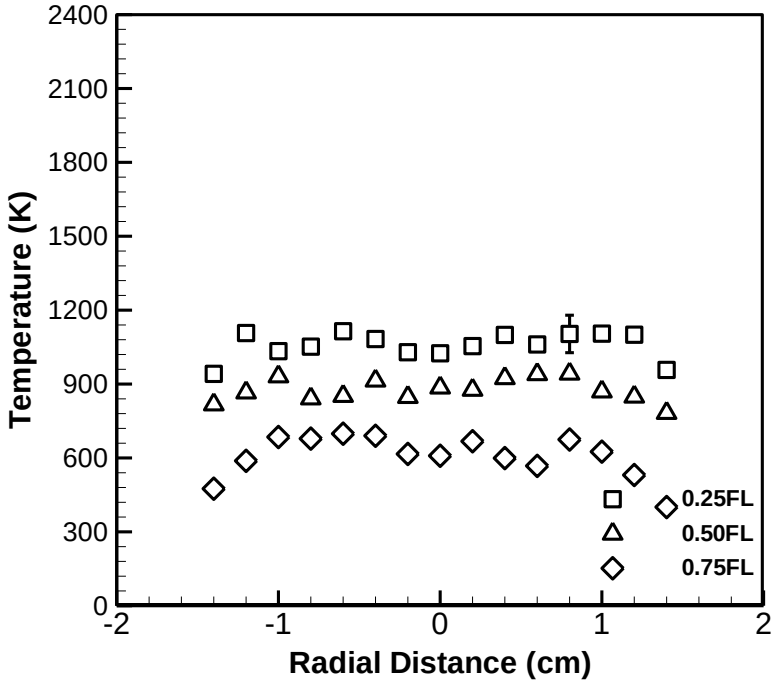

Fig. 48: Temperature profiles of SME B50 flame at Φ = 7

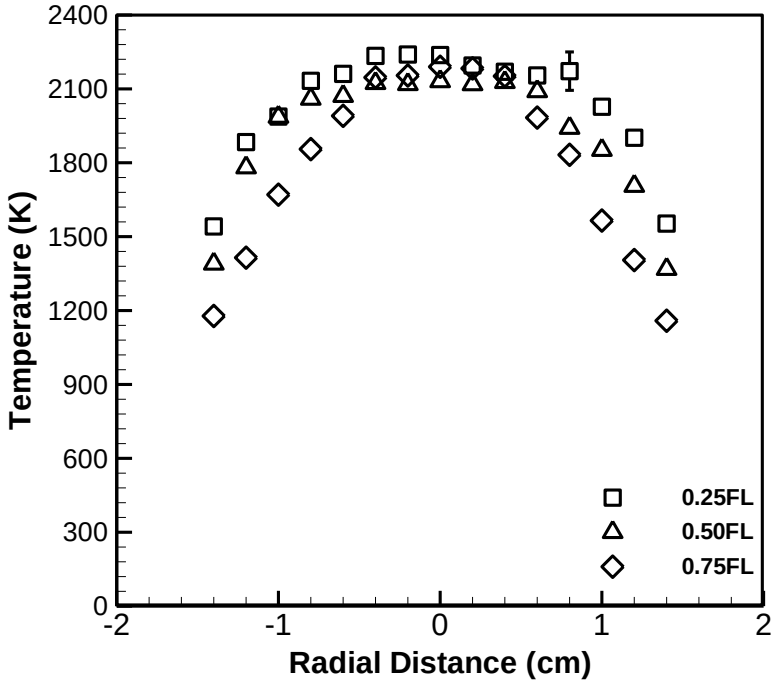

Fig. 49: Temperature profiles of SME B75 flame at Φ = 1.2

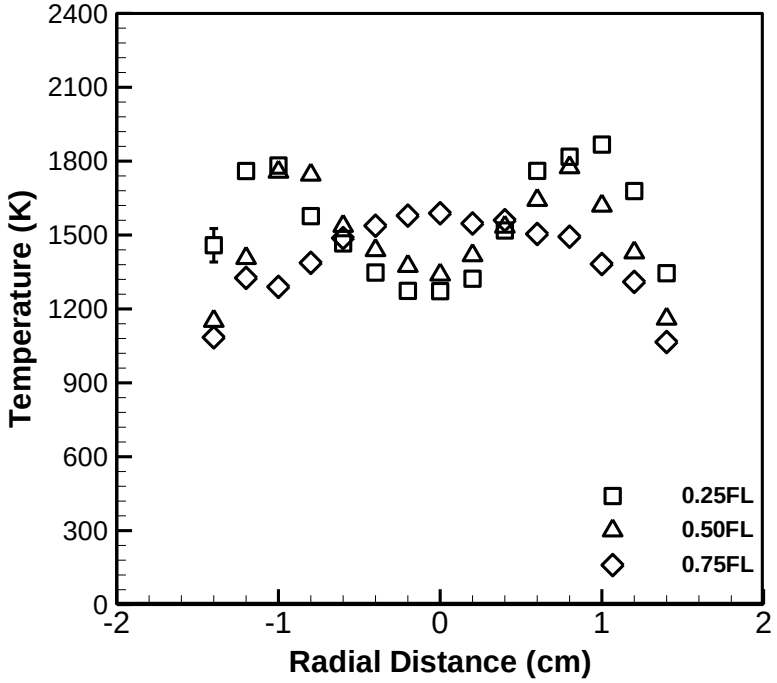

Fig. 50: Temperature profiles of SME B75 flame at Φ = 2

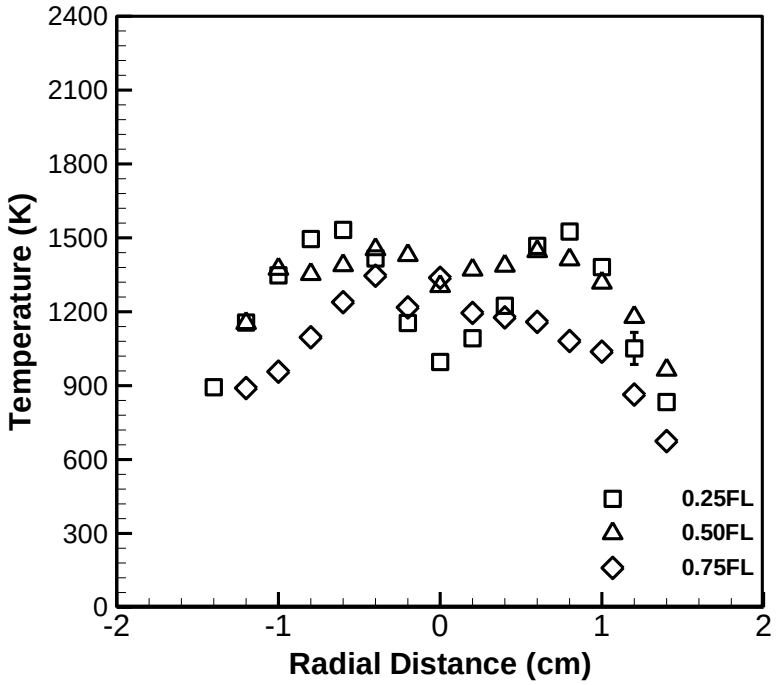

Fig. 51: Temperature profiles of SME B75 flame at Φ = 3

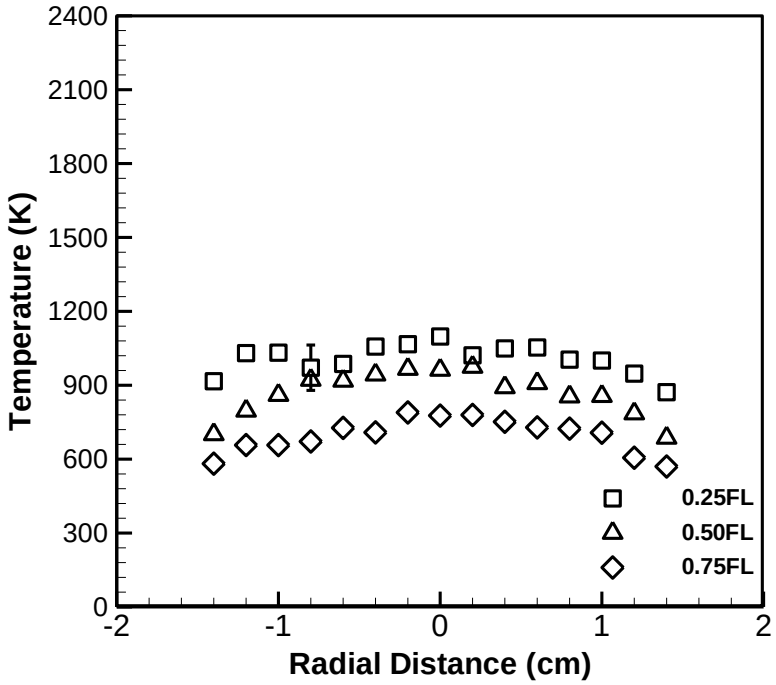

Fig. 52: Temperature profiles of SME B75 flame at Φ = 7

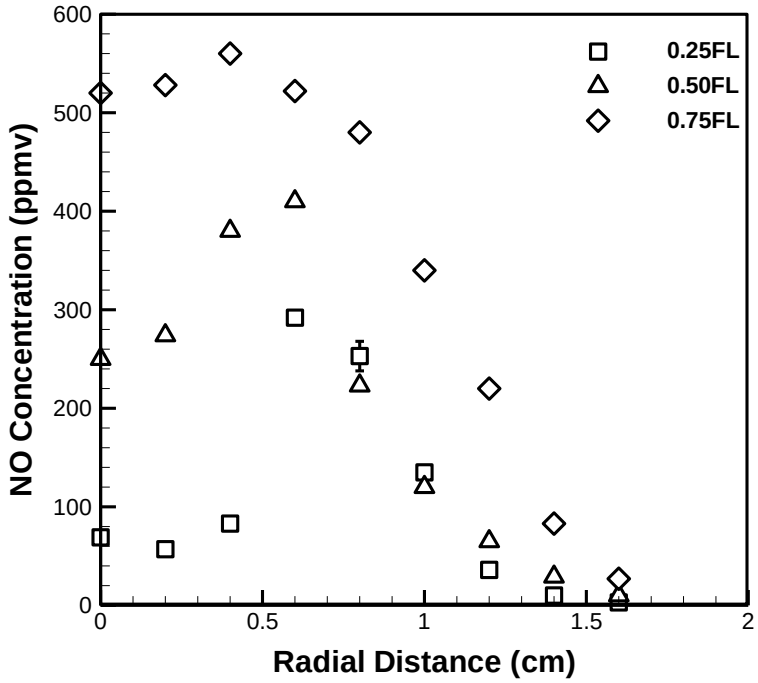

Fig. 53: NO concentration profiles of CME B25 flame at Φ =1.2

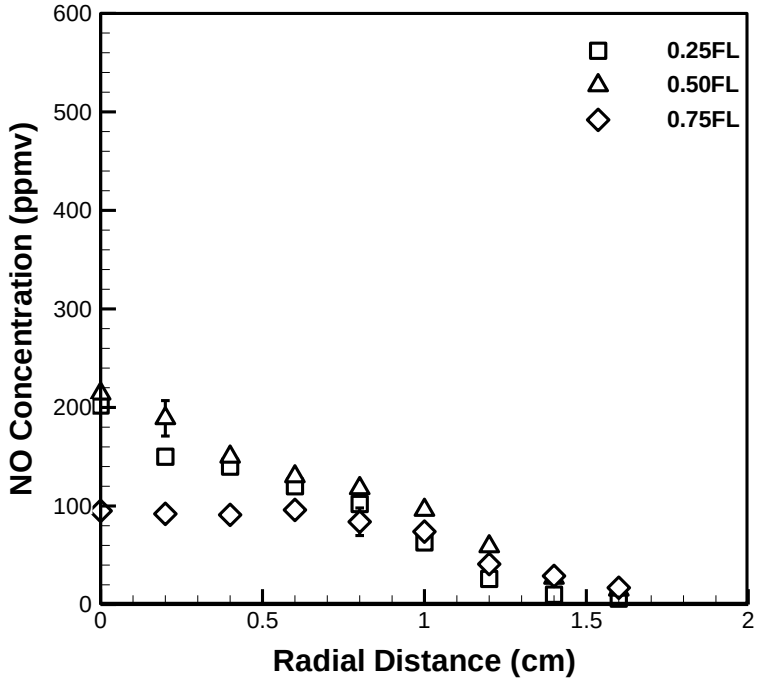

Fig. 54: NO concentration profiles of CME B25 flame at Φ =2

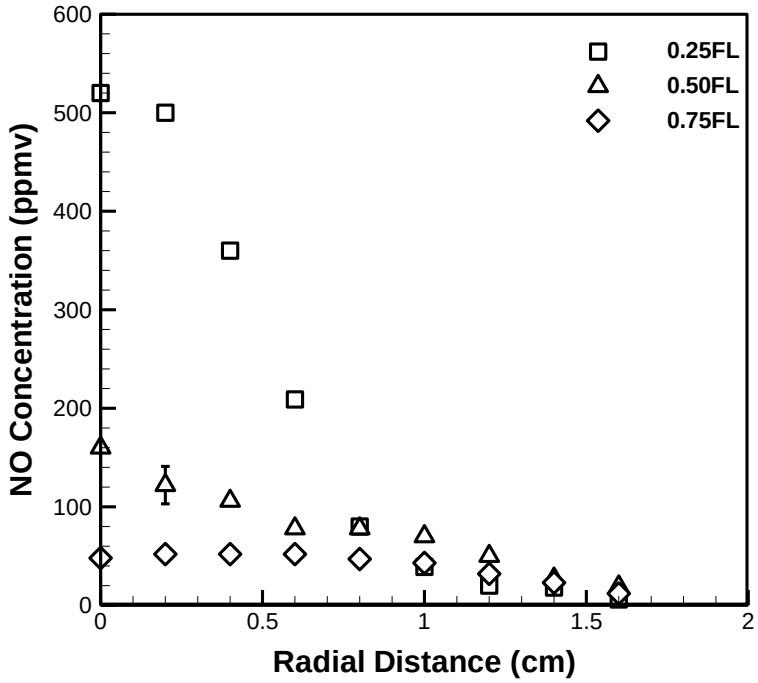

Fig. 55: NO concentration profiles of CME B25 flame at Φ =3

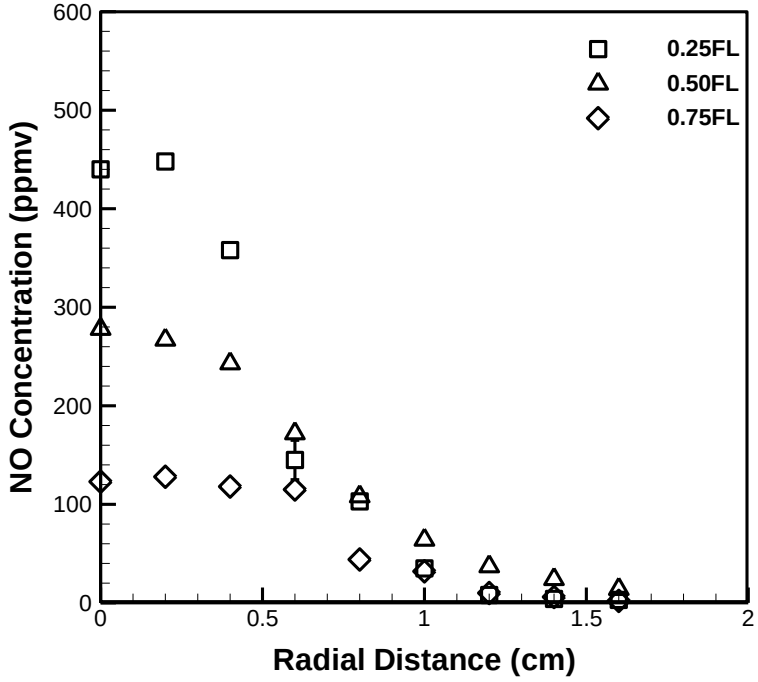

Fig. 56: NO concentration profiles of CME B25 flame at Φ =7

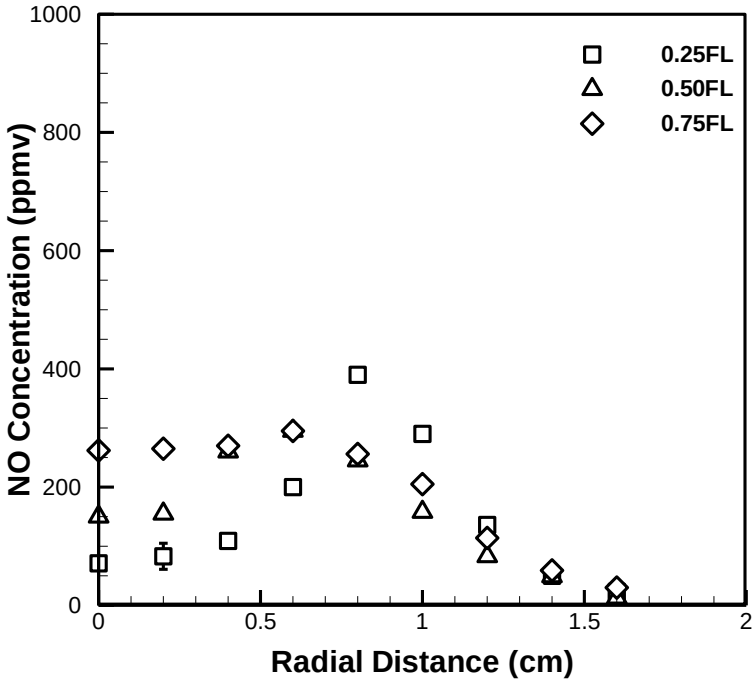

Fig. 57: NO concentration profiles of CME B50 flame at Φ =1.2

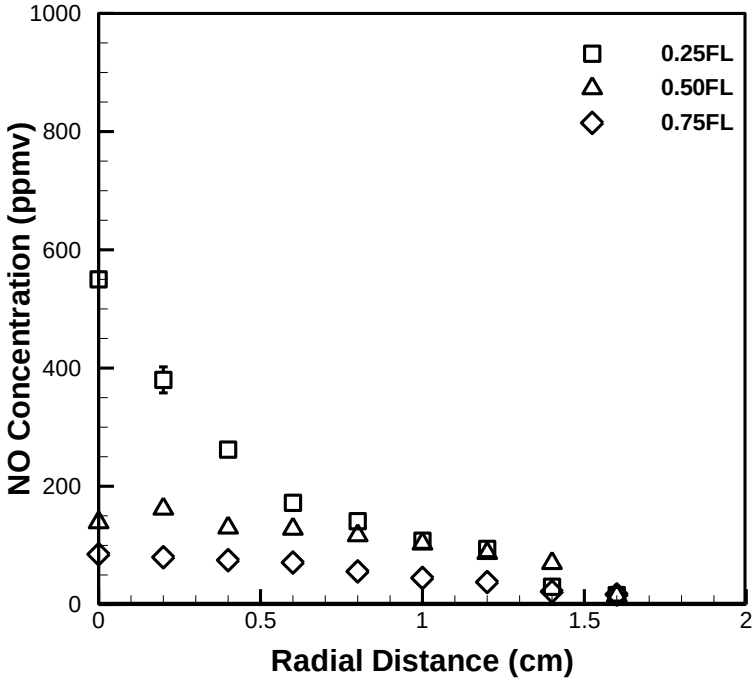

Fig. 58: NO concentration profiles of CME B50 flame at Φ =2

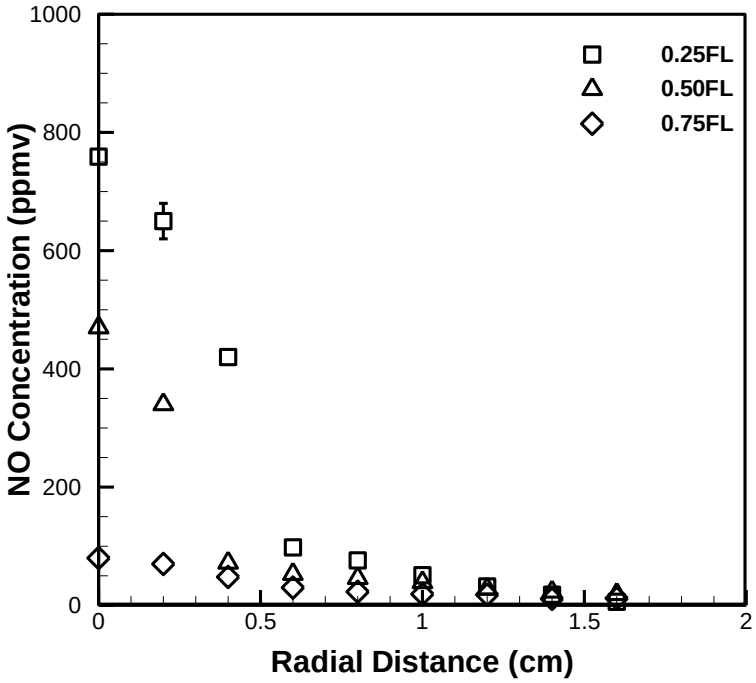

Fig. 59: NO concentration profiles of CME B50 flame at Φ =3

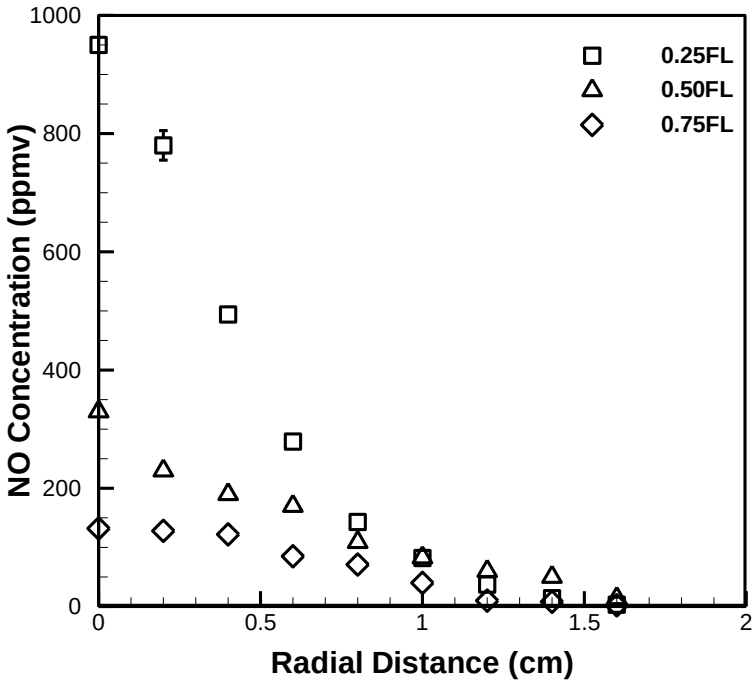

Fig. 60: NO concentration profiles of CME B50 flame at Φ =7

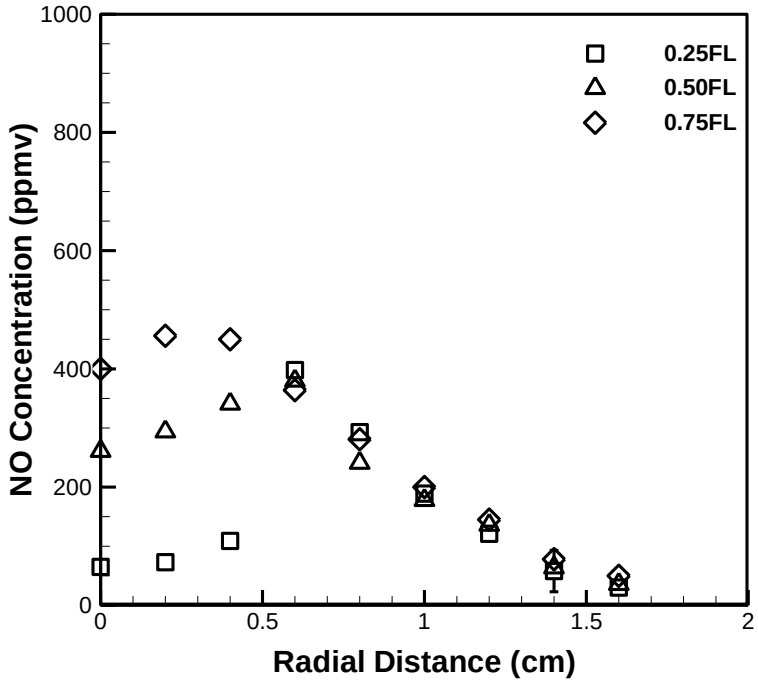

Fig. 61: NO concentration profiles of CME B75 flame at Φ =1.2

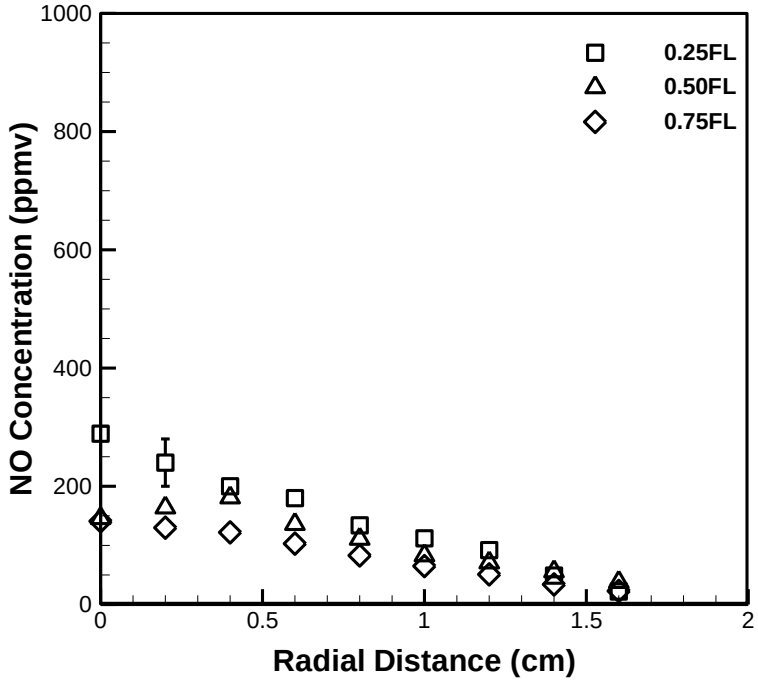

Fig. 62: NO concentration profiles of CME B75 flame at Φ =2

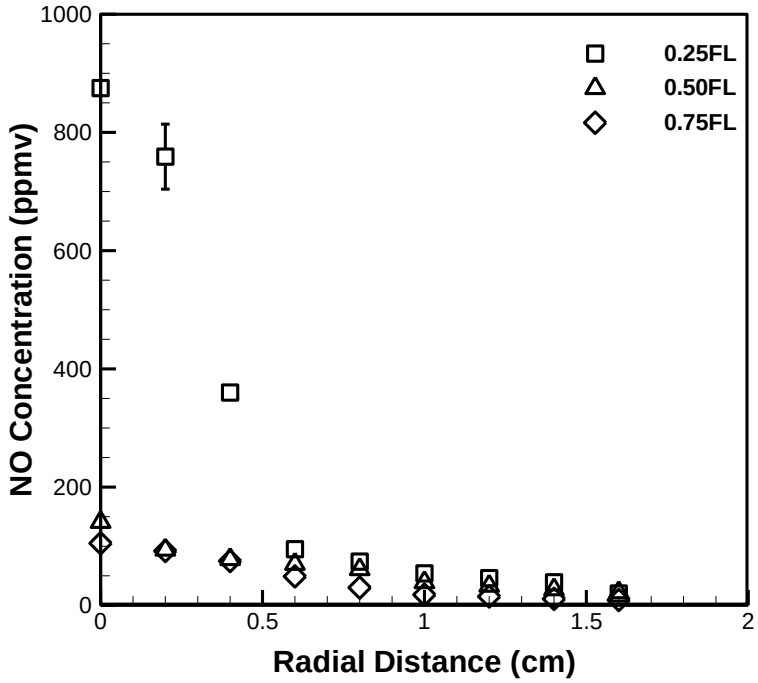

Fig. 63: NO concentration profiles of CME B75 flame at Φ =3

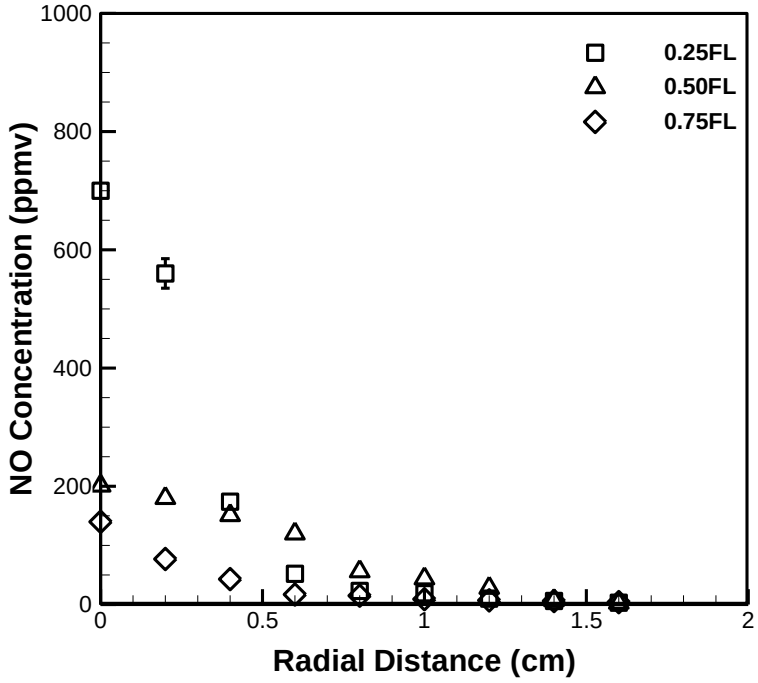

Fig. 64: NO concentration profiles of CME B75 flame at Φ =7

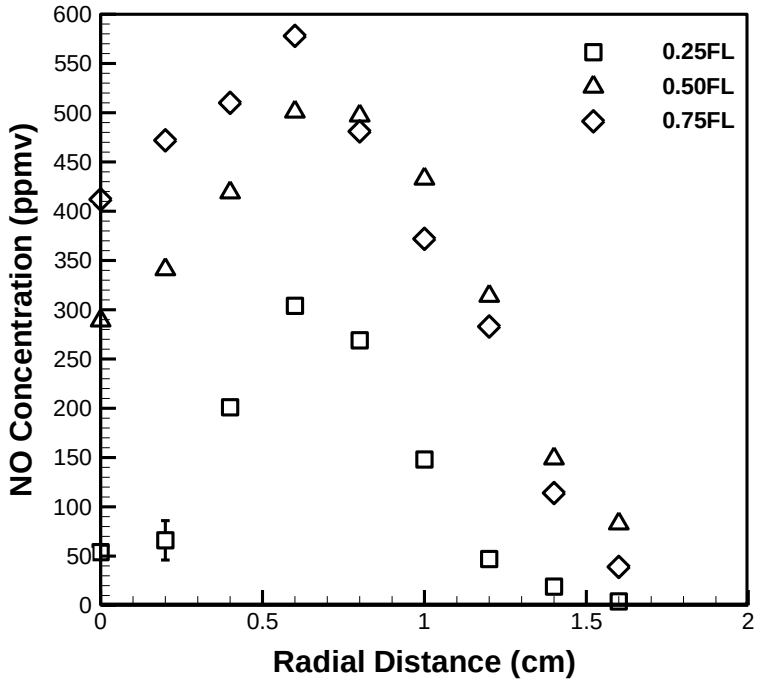

Fig. 65: NO concentration profiles of SME B25 flame at Φ =1.2

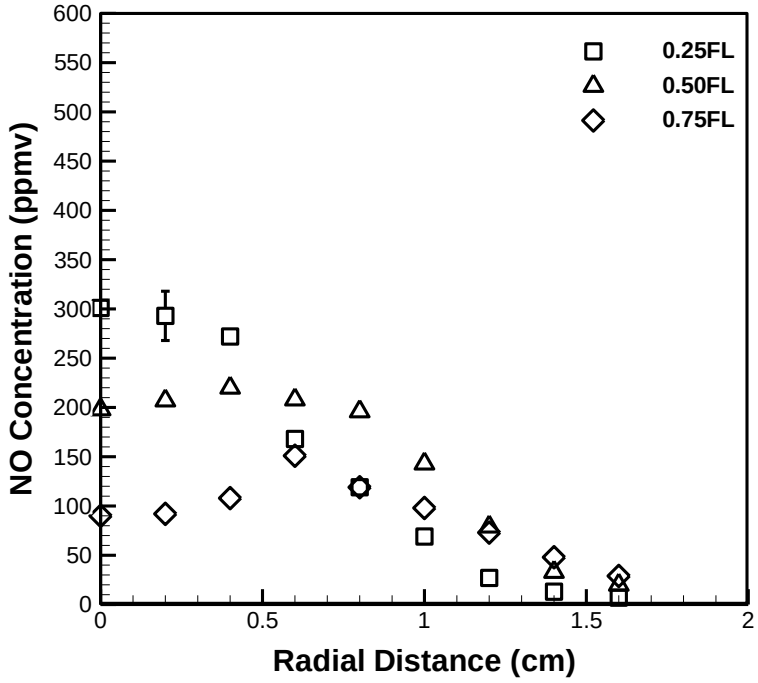

Fig. 66: NO concentration profiles of SME B25 flame at Φ =2

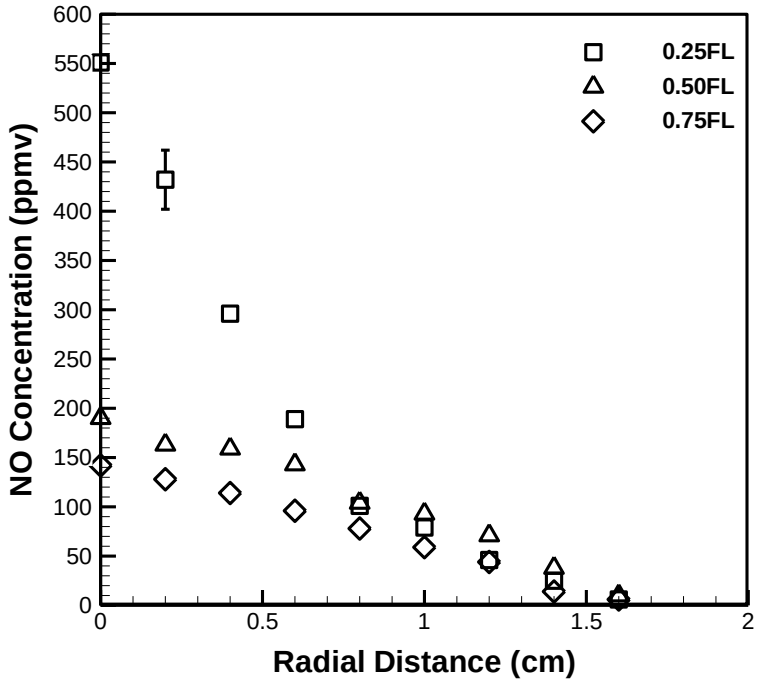

Fig. 67: NO concentration profiles of SME B25 flame at Φ =3

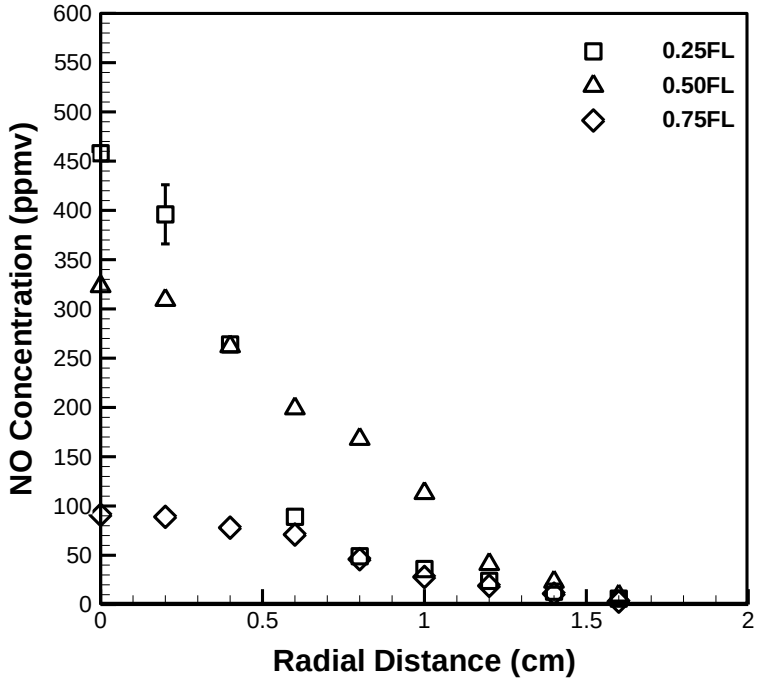

Fig. 68: NO concentration profiles of SME B25 flame at Φ =7

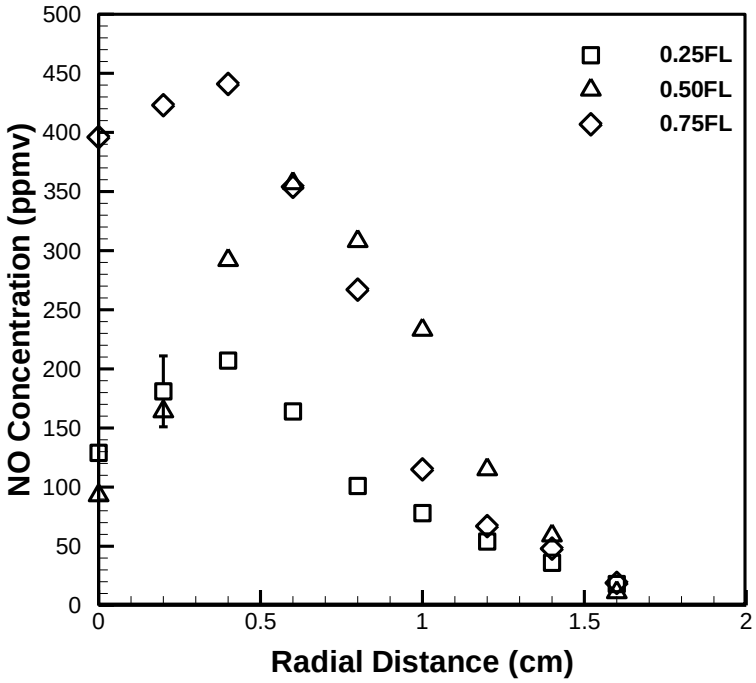

Fig. 69: NO concentration profiles of SME B50 flame at Φ =1.2

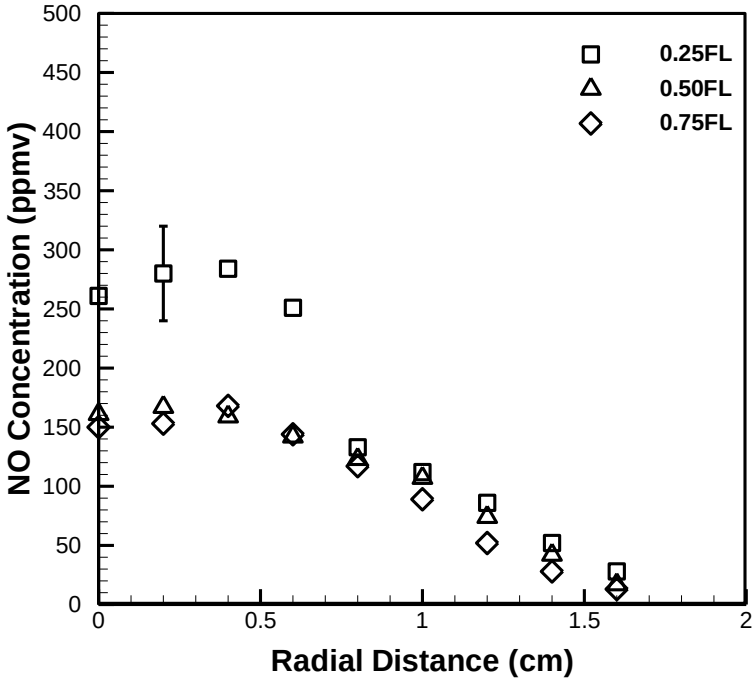

Fig. 70: NO concentration profiles of SME B50 flame at Φ =2

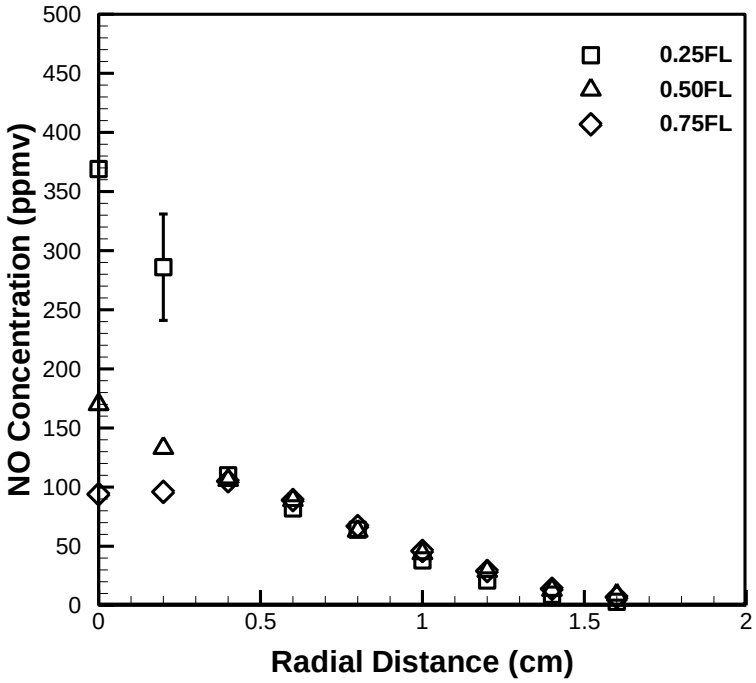

Fig. 71: NO concentration profiles of SME B50 flame at Φ =3

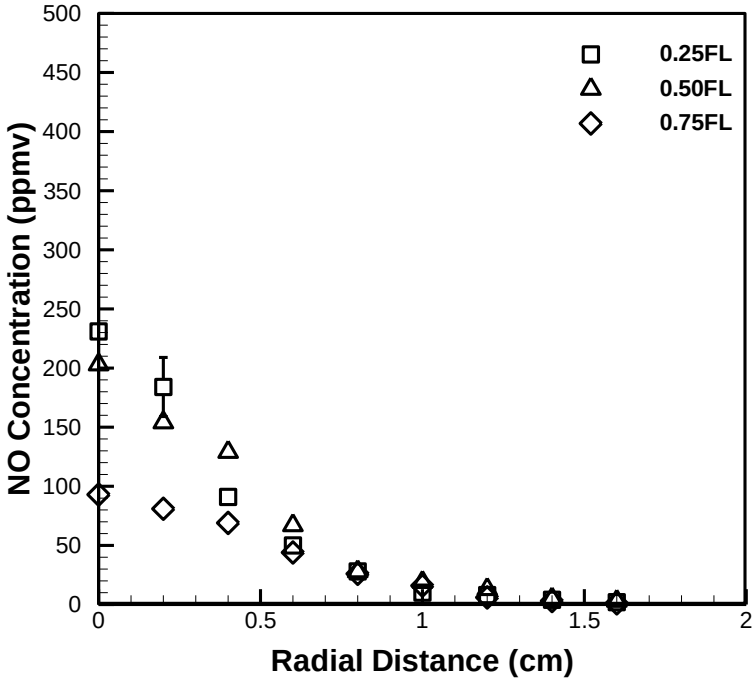

Fig. 72: NO concentration profiles of SME B50 flame at Φ =7

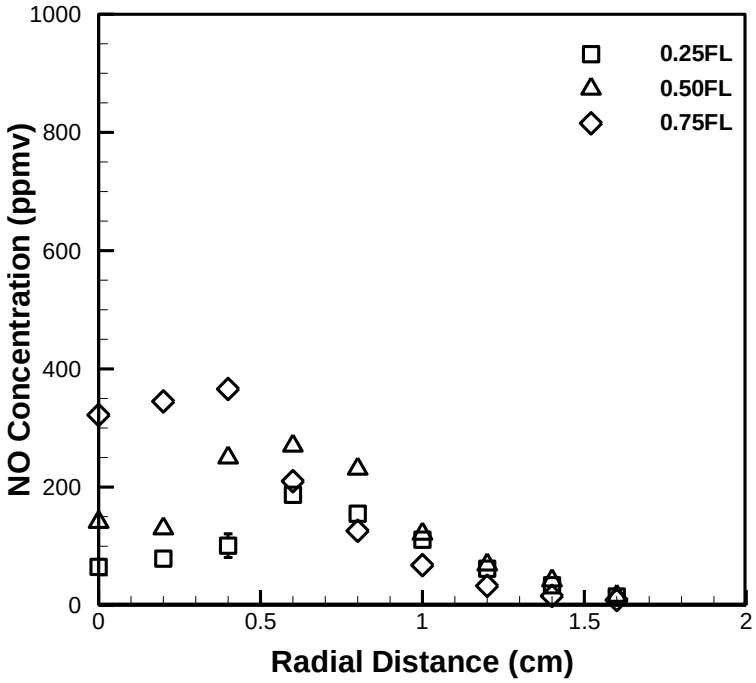

Fig. 73: NO concentration profiles of SME B75 flame at Φ =1.2

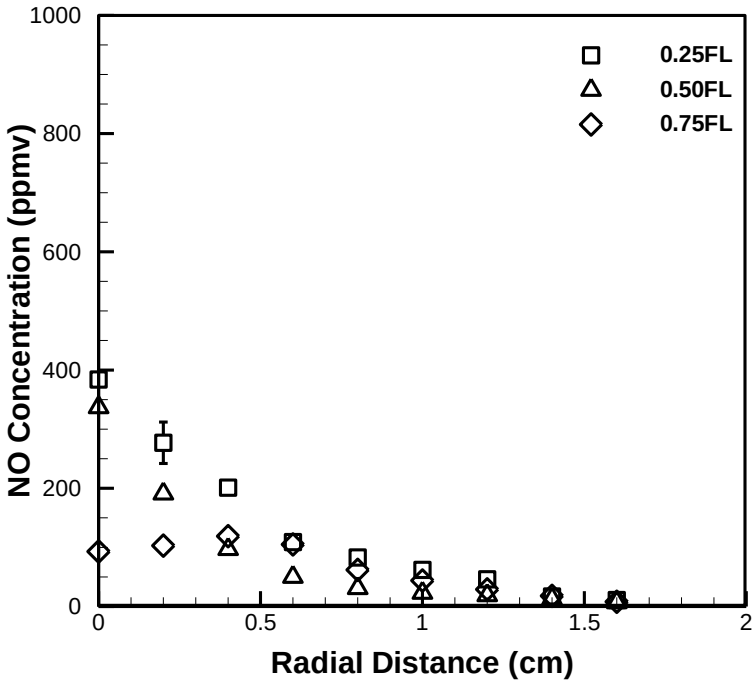

Fig. 74: NO concentration profiles of SME B75 flame at Φ =2

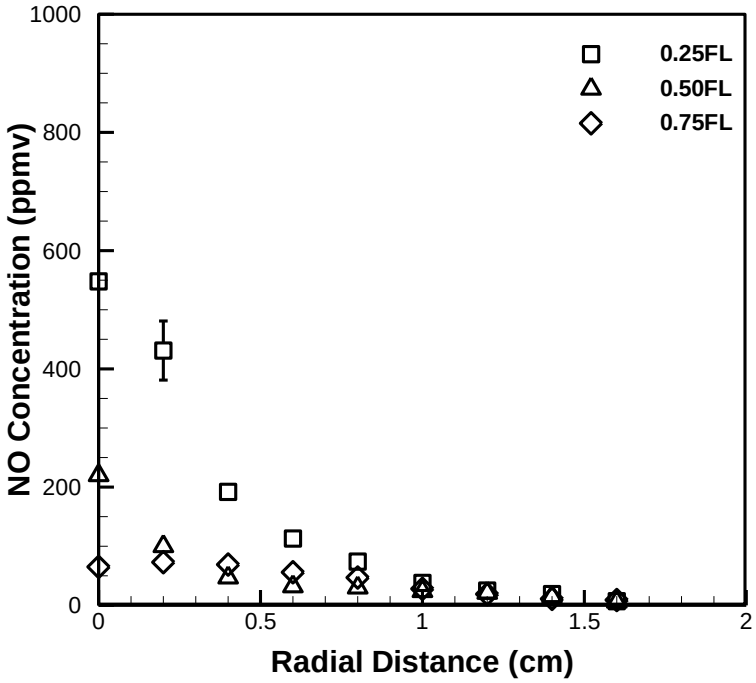

Fig. 75: NO concentration profiles of SME B75 flame at Φ =3

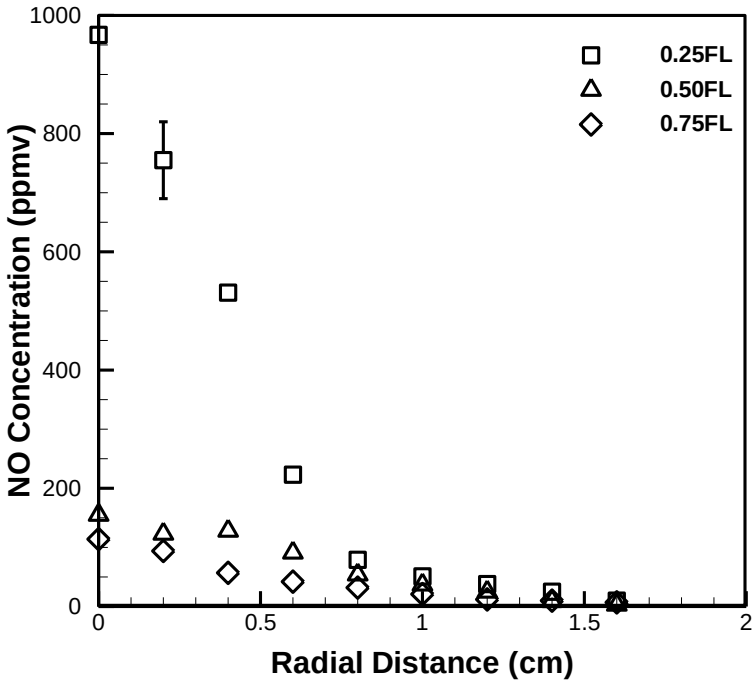

Fig. 76: NO concentration profiles of SME B75 flame at Φ =7

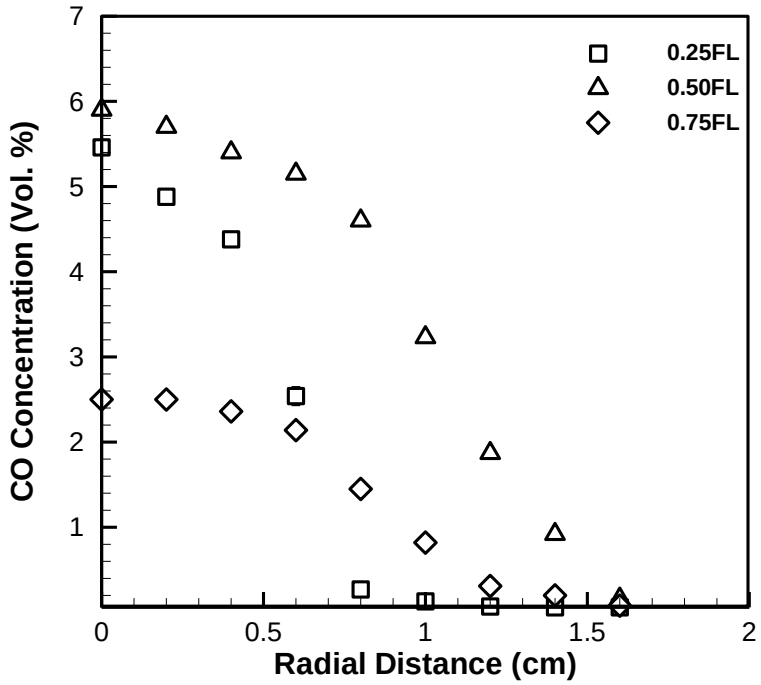

Fig. 77: CO concentration profiles of CME B25 flame at Φ =1.2

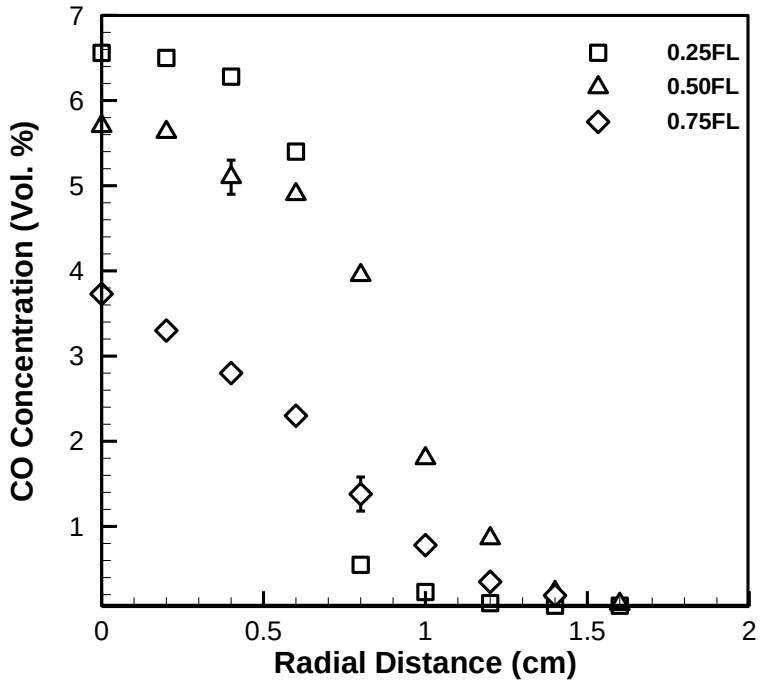

Fig. 78: CO concentration profiles of CME B25 flame at Φ =2

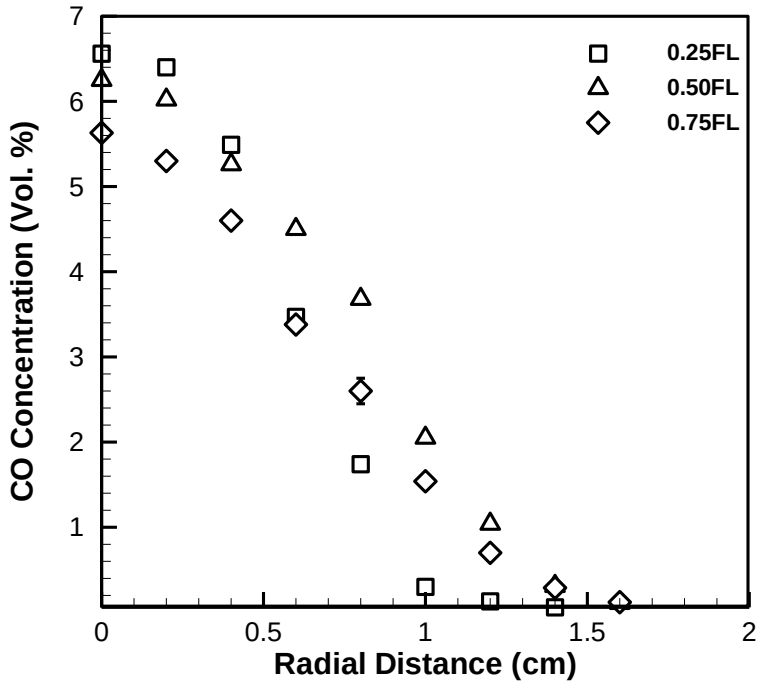

Fig. 79: CO concentration profiles of CME B25 flame at Φ =3

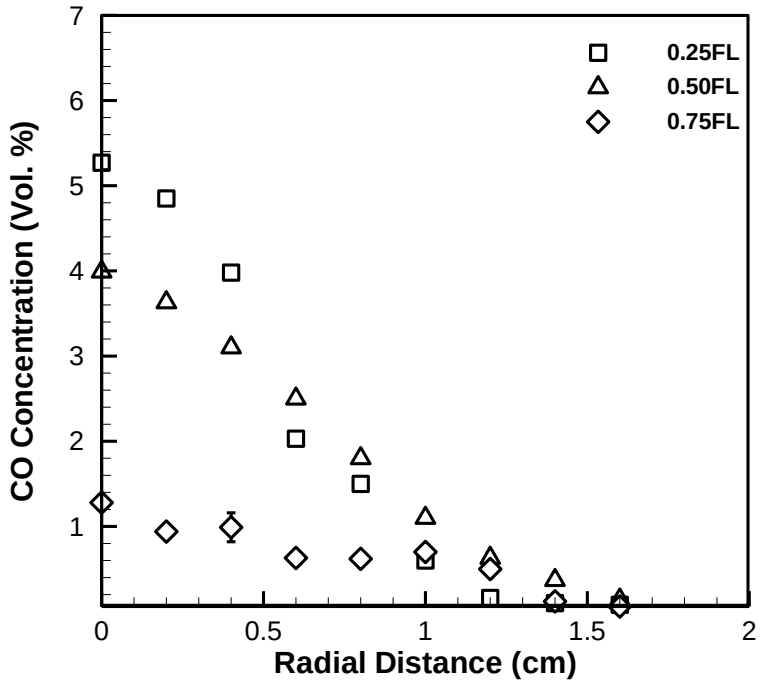

Fig. 80: CO concentration profiles of CME B25 flame at Φ =7

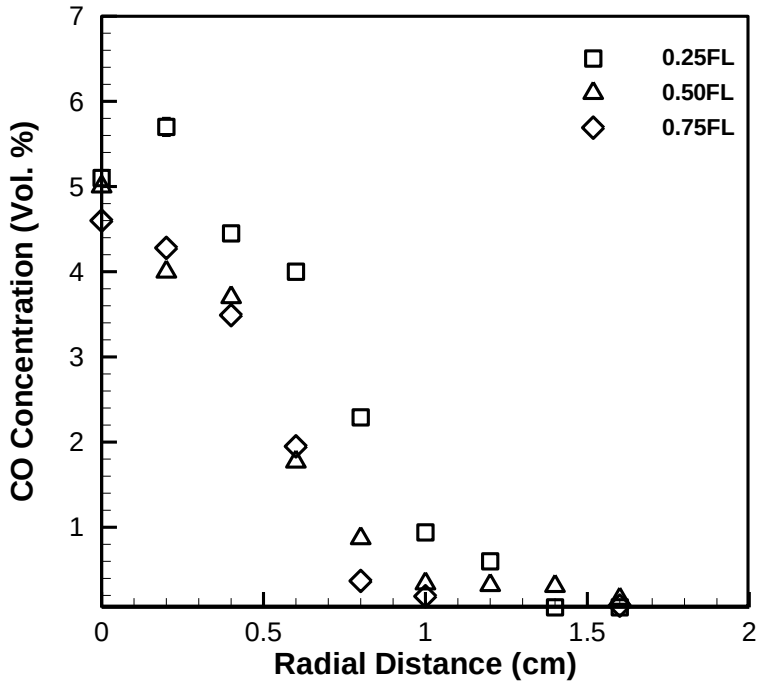

Fig. 81: CO concentration profiles of CME B50 flame at Φ =1.2

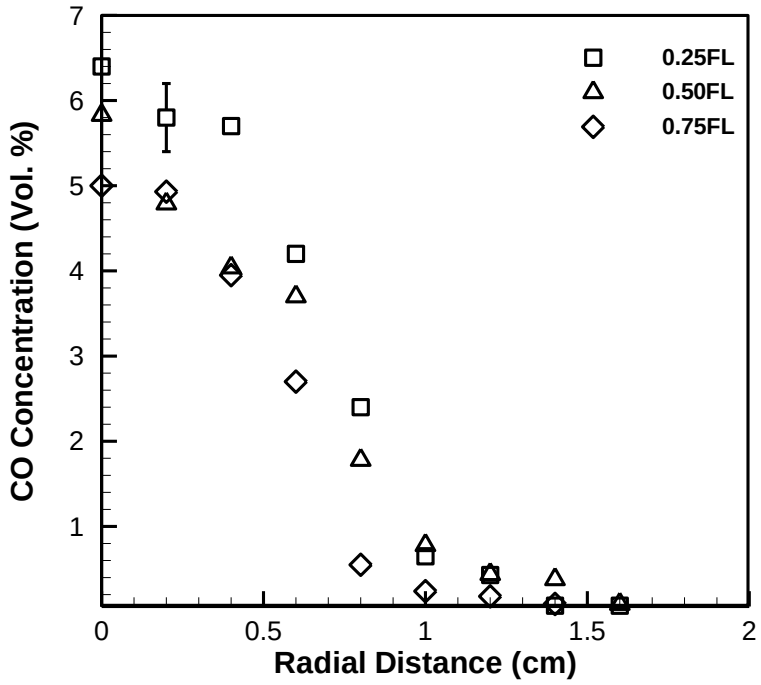

Fig. 82: CO concentration profiles of CME B50 flame at Φ =2

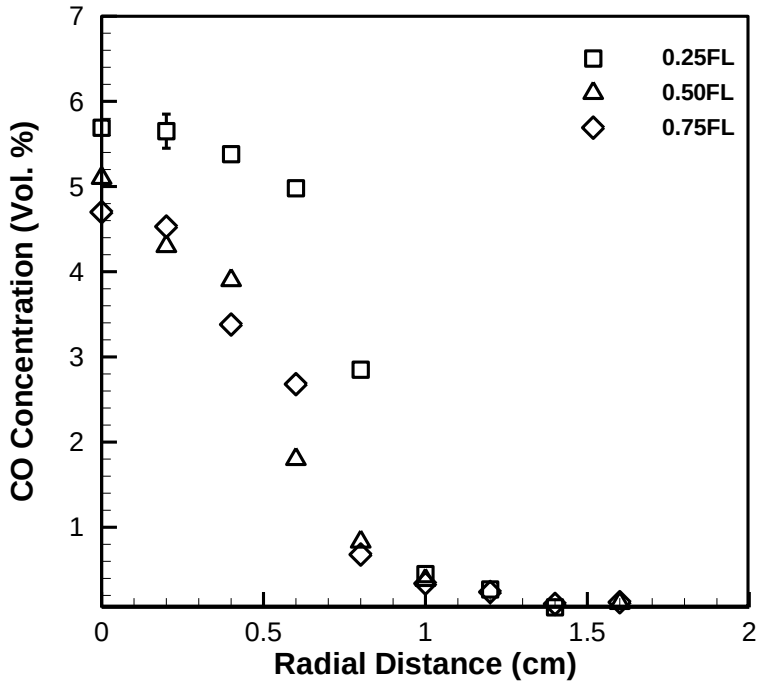

Fig. 83: CO concentration profiles of CME B50 flame at Φ =3

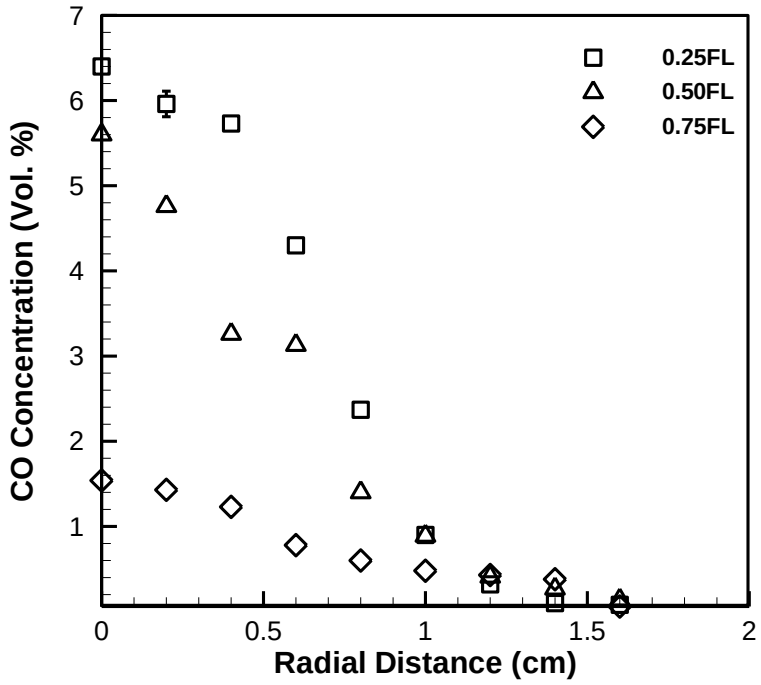

Fig. 84: CO concentration profiles of CME B50 flame at Φ =7

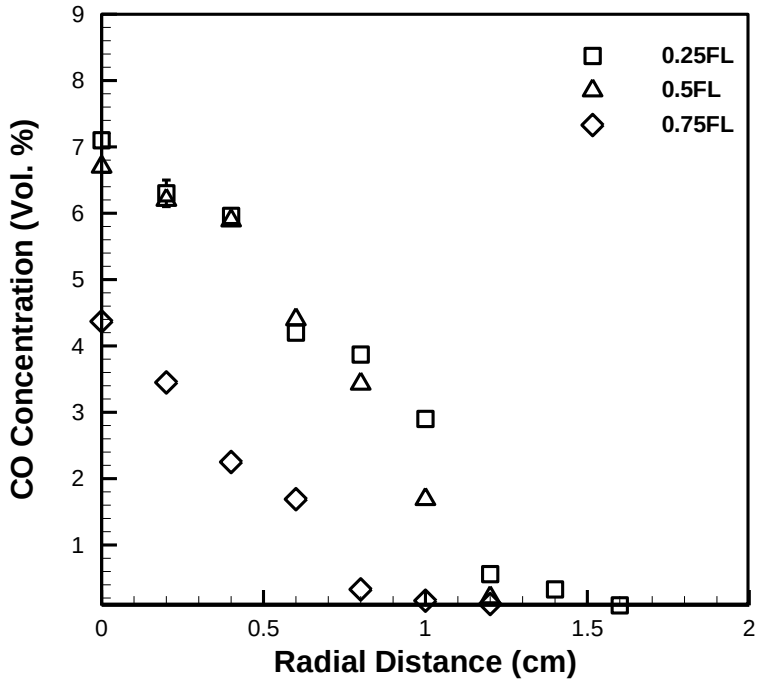

Fig. 85: CO concentration profiles of CME B75 flame at Φ =1.2

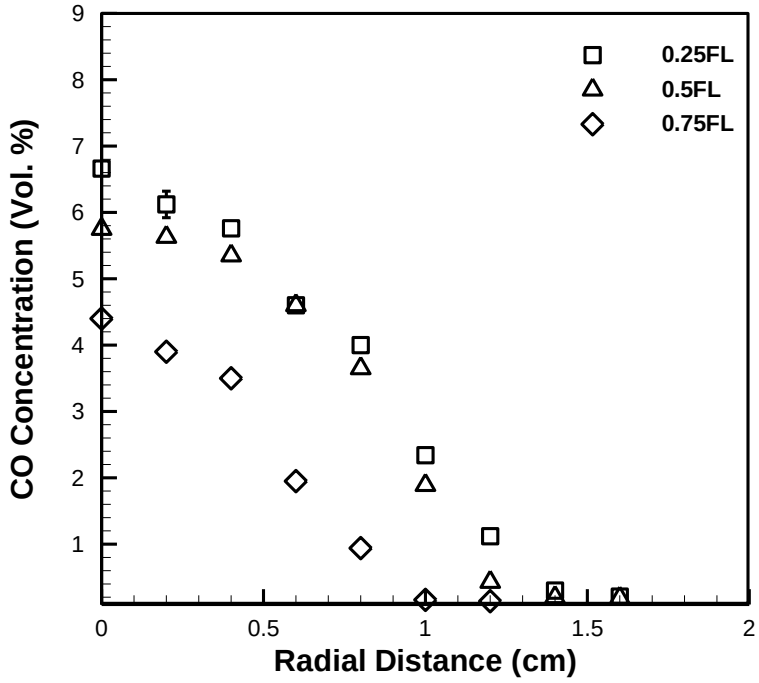

Fig. 86: CO concentration profiles of CME B75 flame at Φ =2

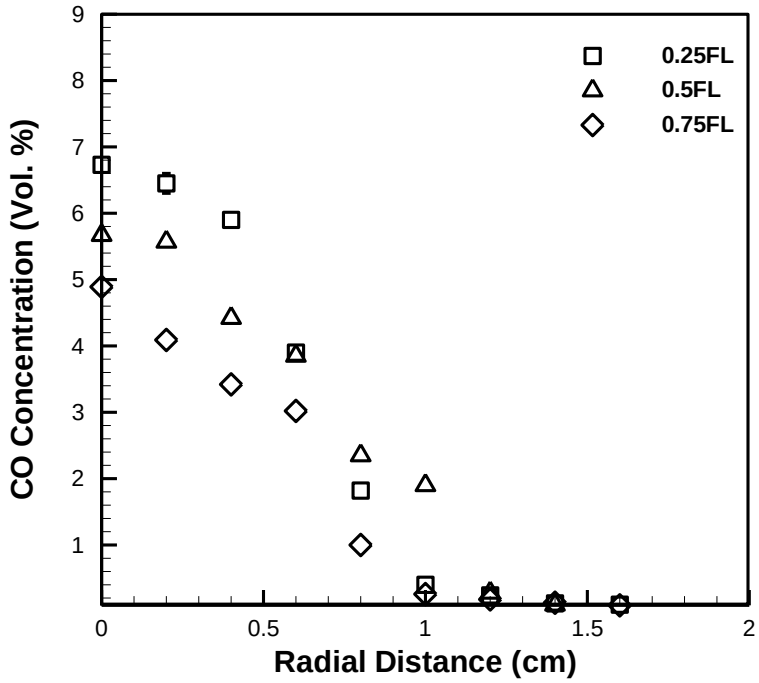

Fig. 87: CO concentration profiles of CME B75 flame at Φ =3

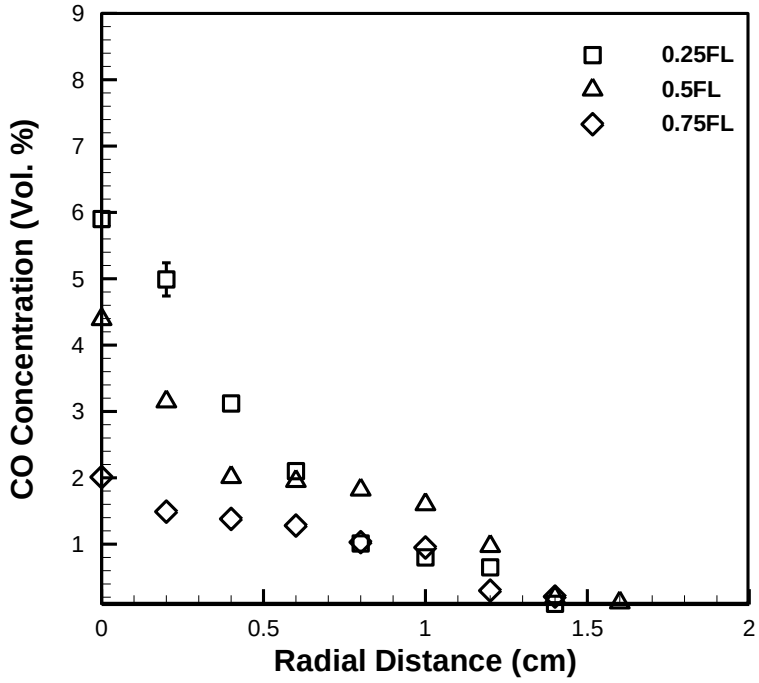

Fig. 88: CO concentration profiles of CME B75 flame at Φ =7

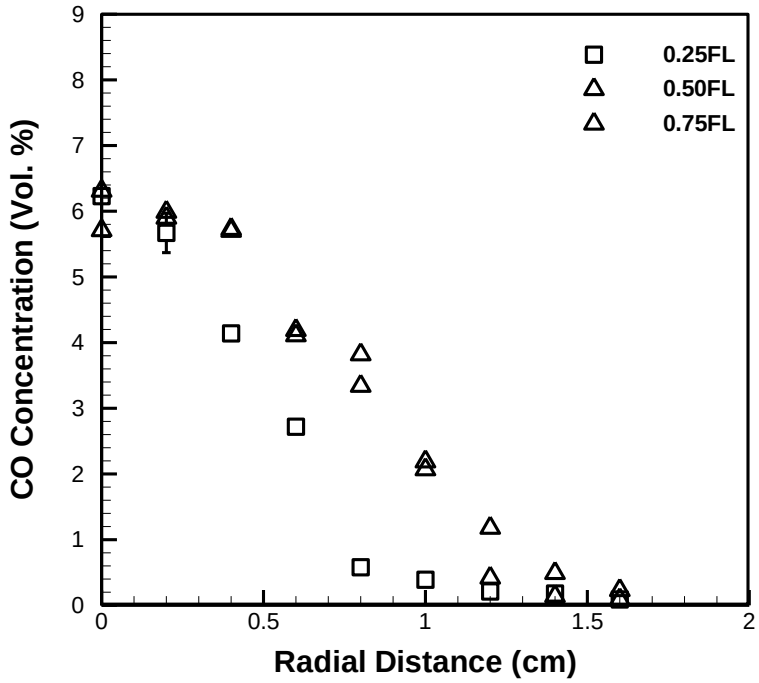

Fig. 89: CO concentration profiles of SME B25 flame at Φ =1.2

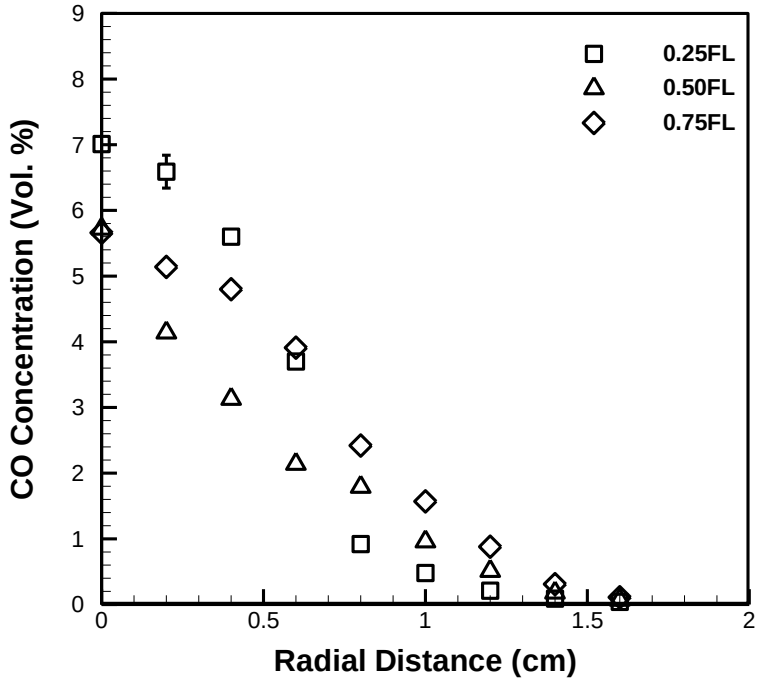

Fig. 90: CO concentration profiles of SME B25 flame at Φ =2

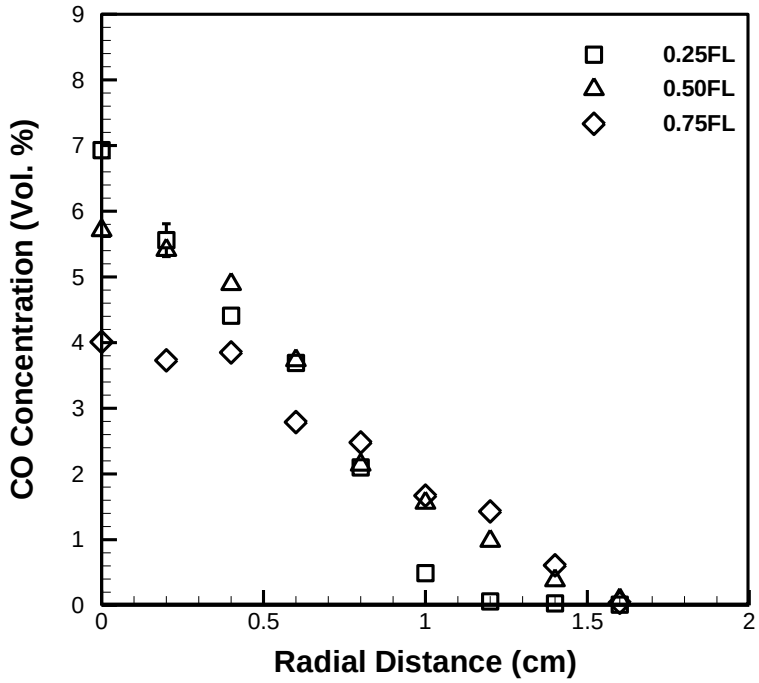

Fig. 91: CO concentration profiles of SME B25 flame at Φ =3

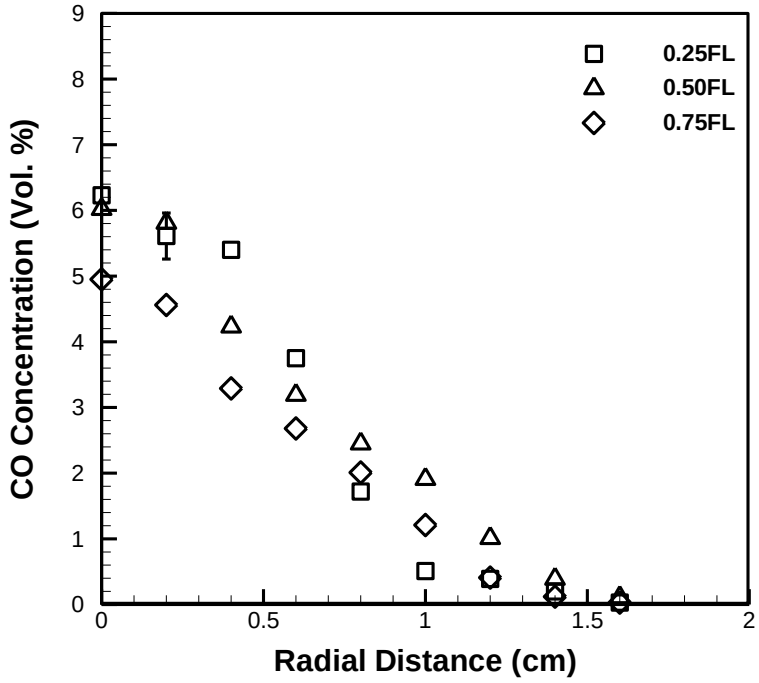

Fig. 92: CO concentration profiles of SME B25 flame at Φ =7

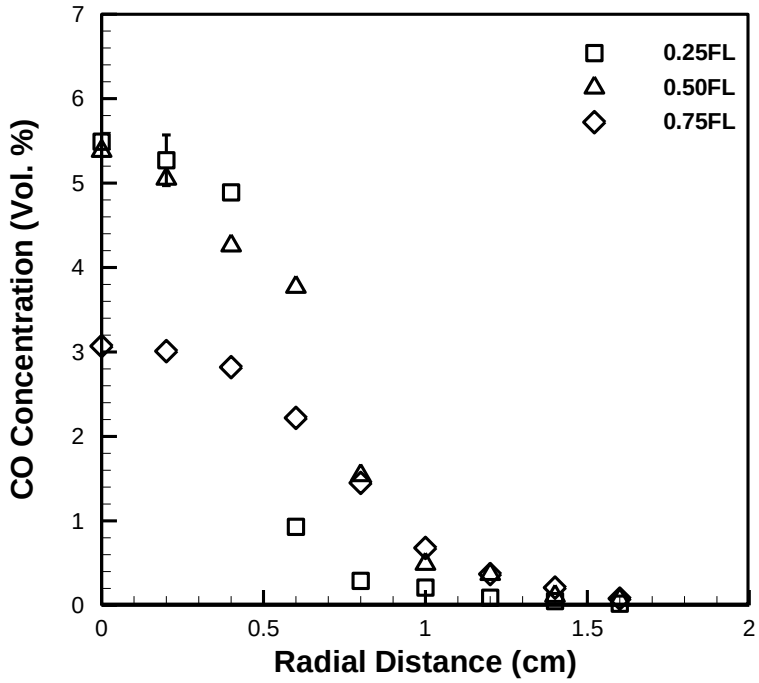

Fig. 93: CO concentration profiles of SME B50 flame at Φ =1.2

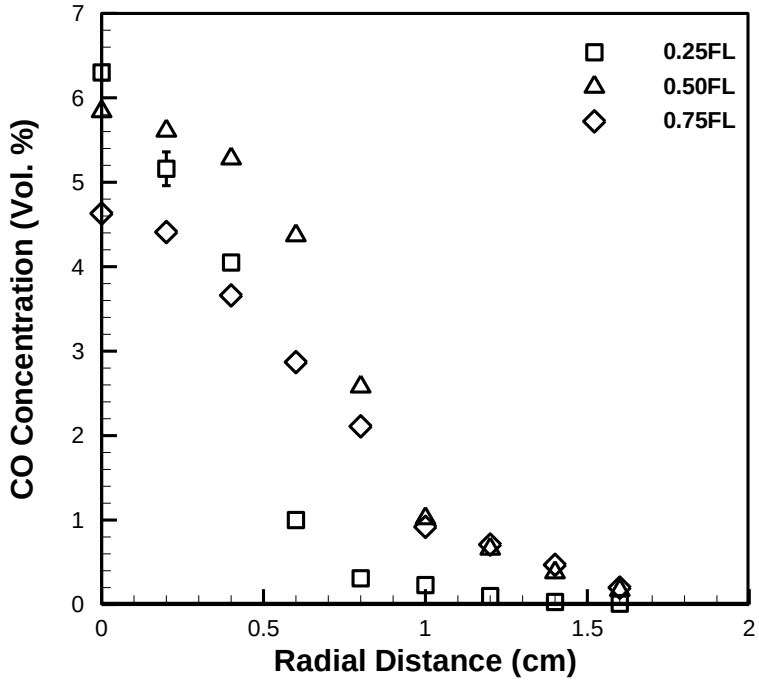

Fig. 94: CO concentration profiles of SME B50 flame at Φ =2

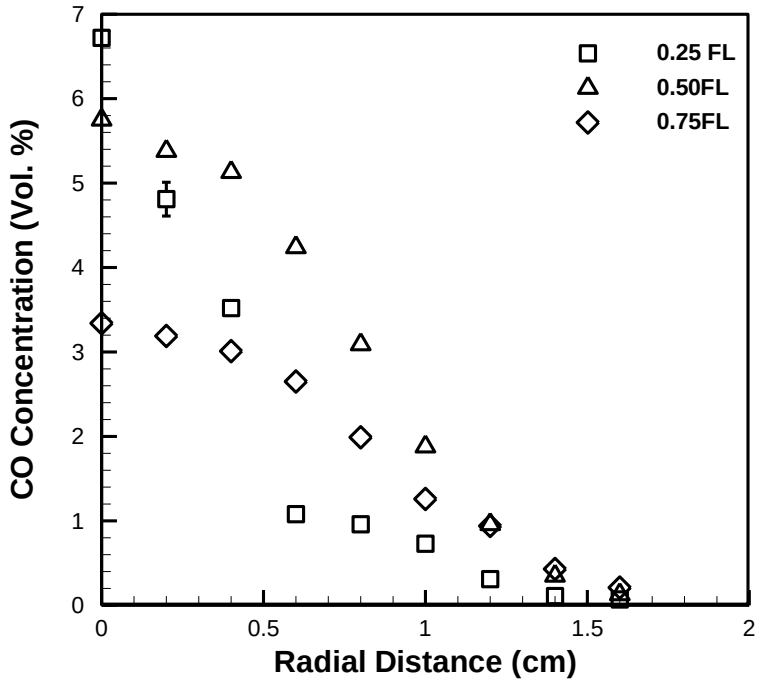

Fig. 95: CO concentration profiles of SME B50 flame at Φ =3

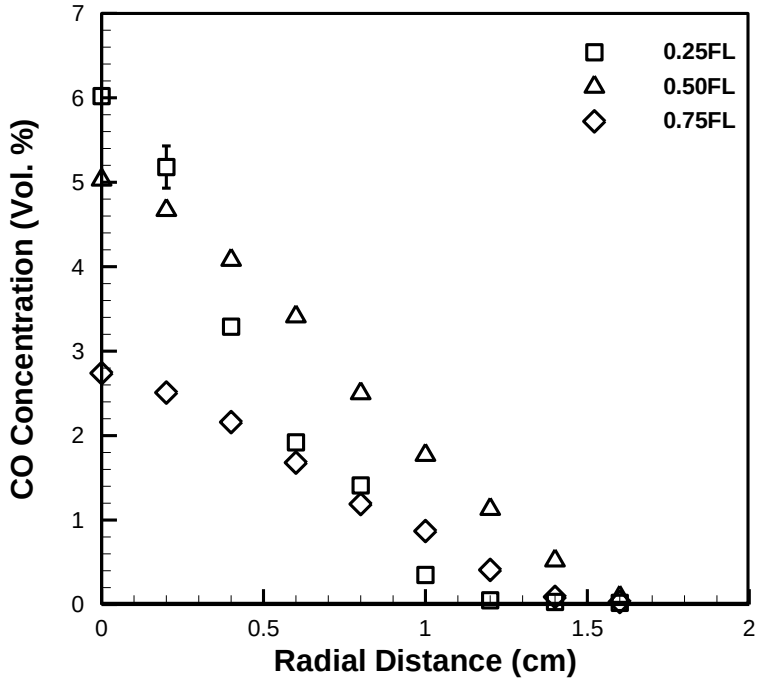

Fig. 96: CO concentration profiles of SME B50 flame at Φ =7

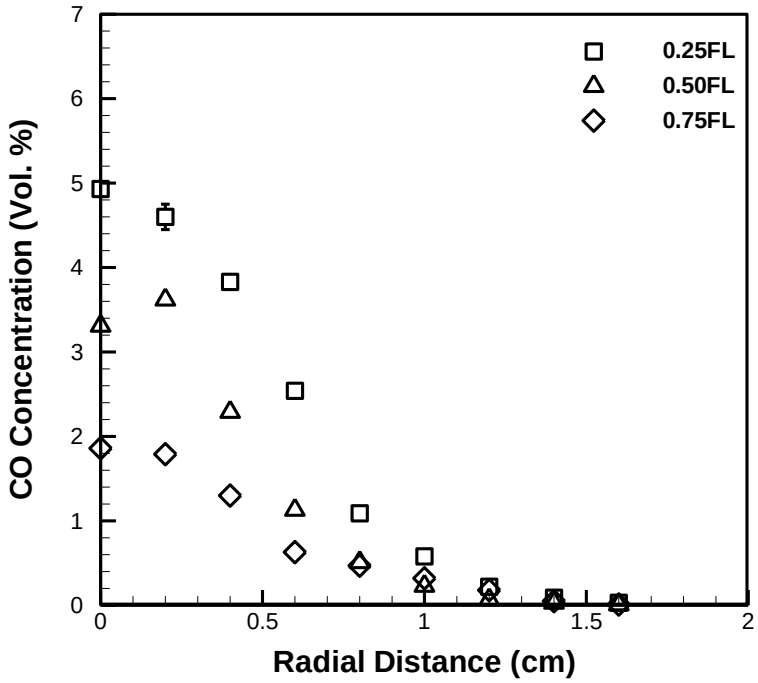

Fig. 97: CO concentration profiles of SME B75 flame at Φ =1.2

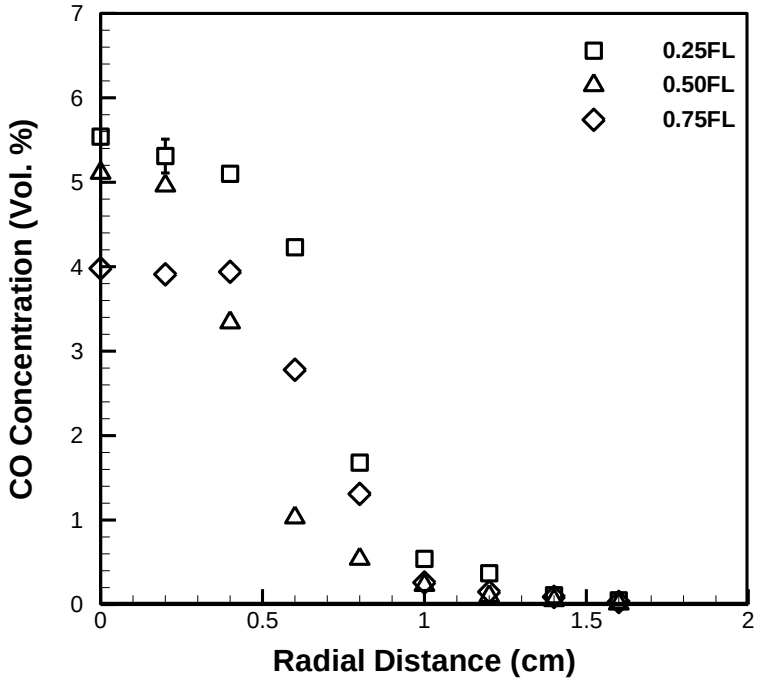

Fig. 98: CO concentration profiles of SME B75 flame at Φ =2

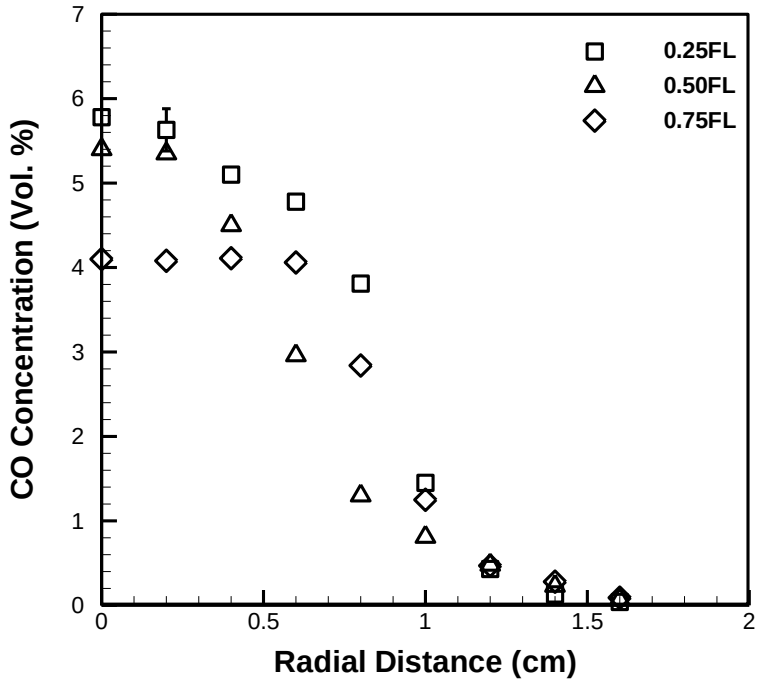

Fig. 99: CO concentration profiles of SME B75 flame at Φ =3

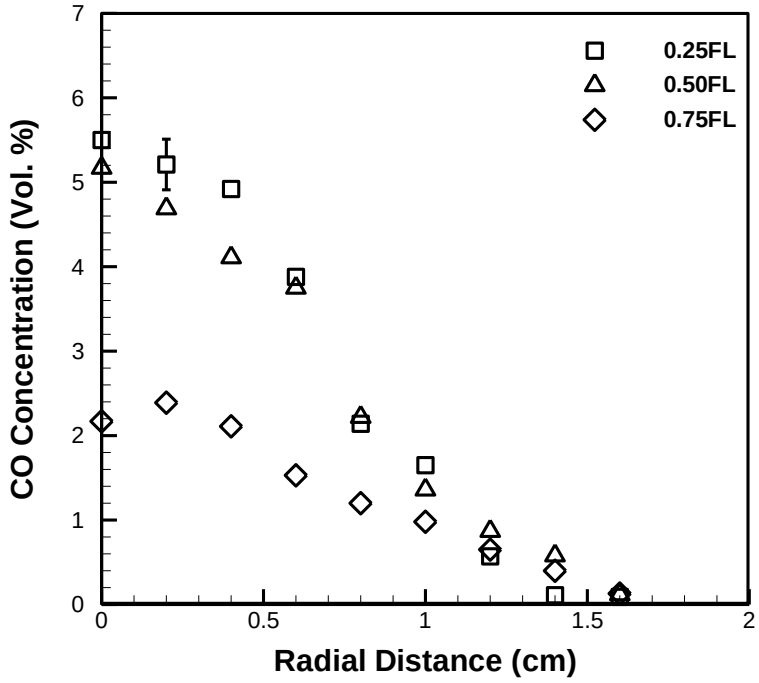

Fig. 100: CO concentration profiles of SME B75 flame at Φ =7

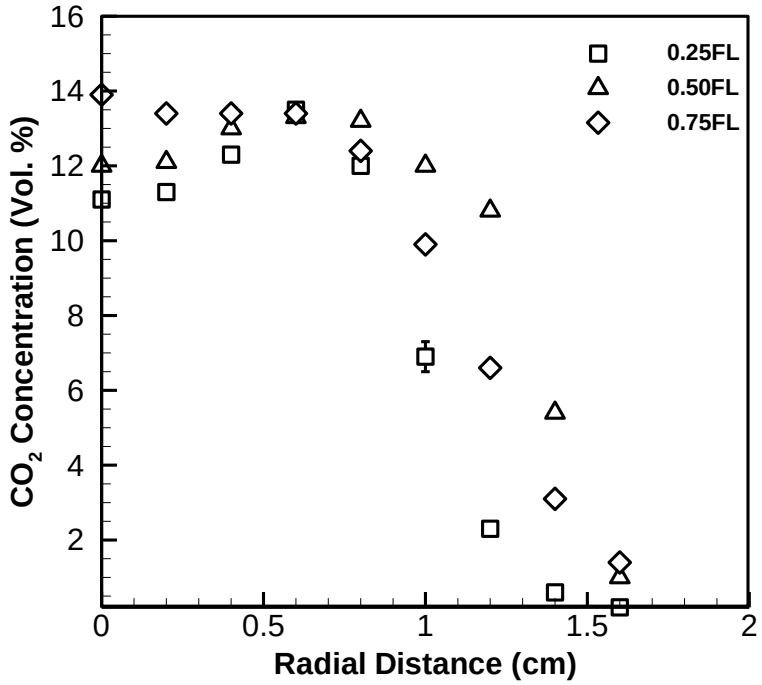

Fig. 101: CO_2 concentration profiles of CME B25 flame at Φ =1.2

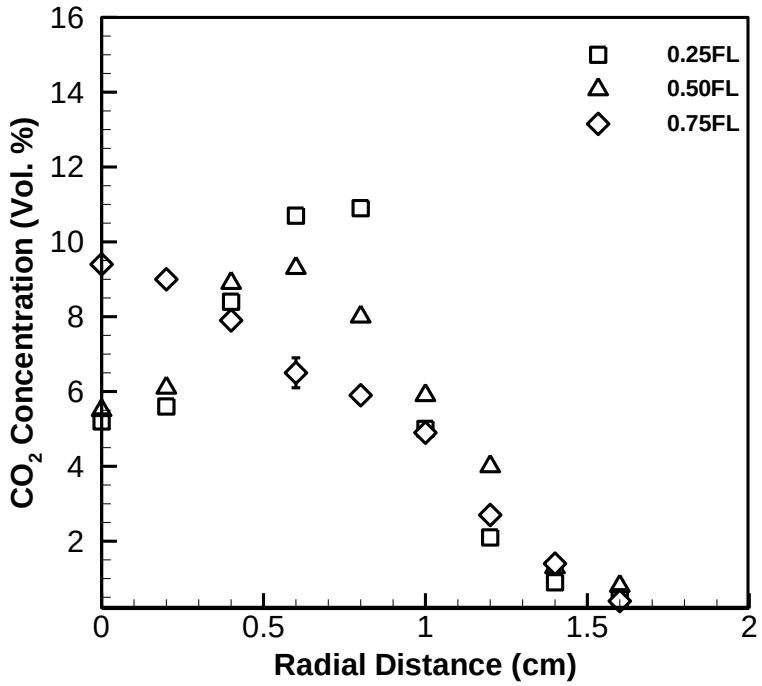

Fig. 102: CO_2 concentration profiles of CME B25 flame at Φ =2

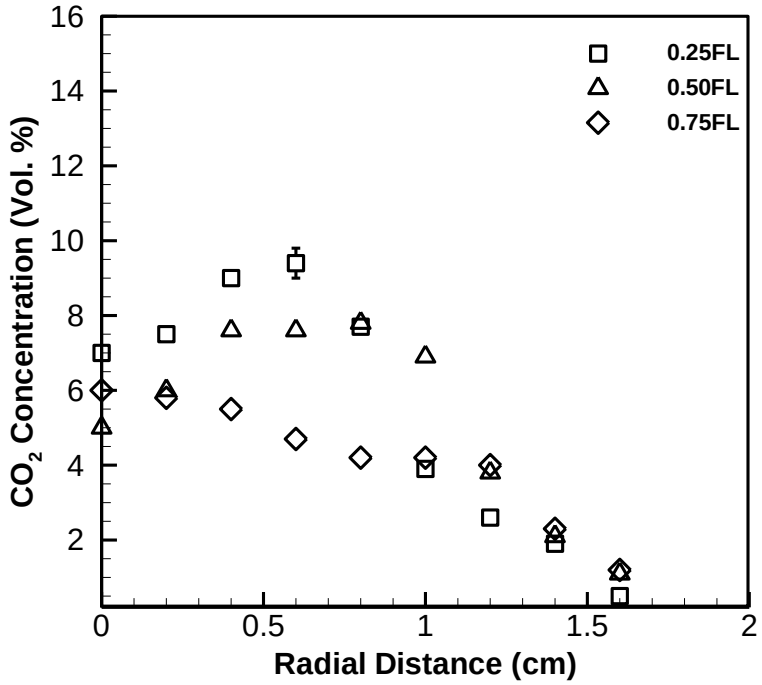

Fig. 103: CO_2 concentration profiles of CME B25 flame at Φ =3

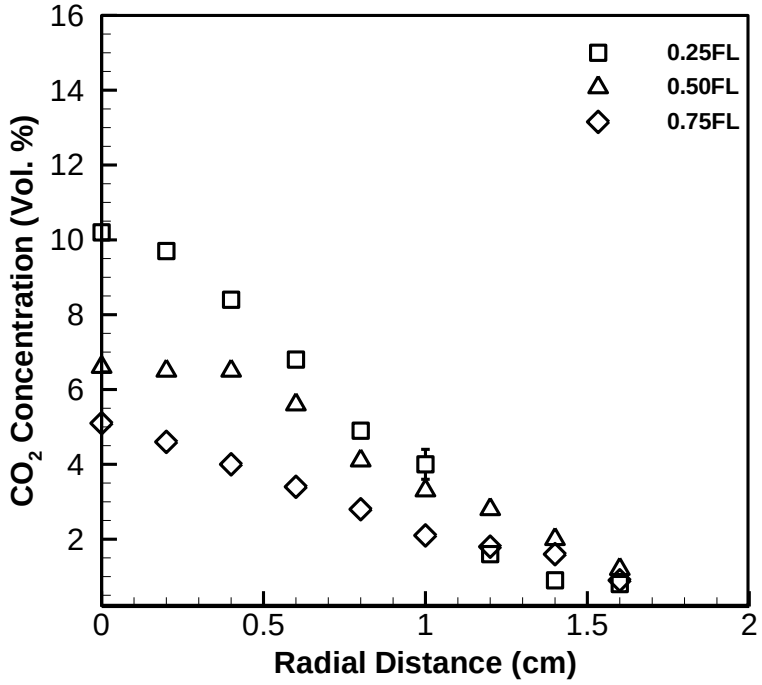

Fig. 104: CO_2 concentration profiles of CME B25 flame at Φ =7

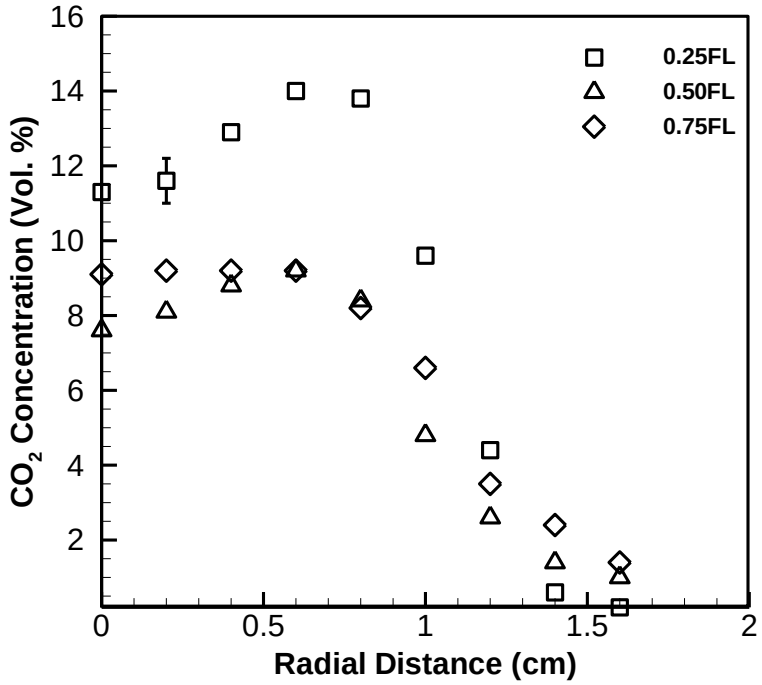

Fig. 105: CO_2 concentration profiles of CME B50 flame at Φ =1.2

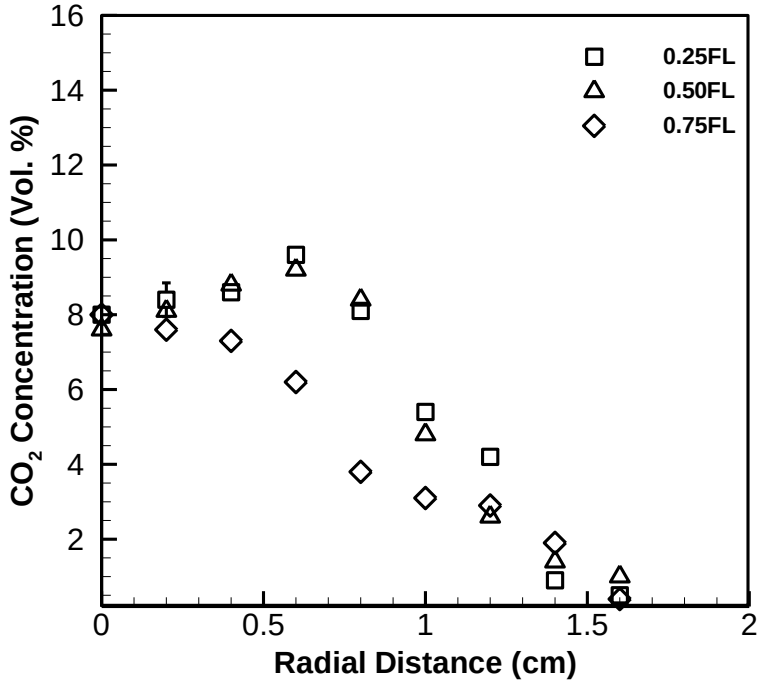

Fig. 106: CO_2 concentration profiles of CME B50 flame at Φ =2

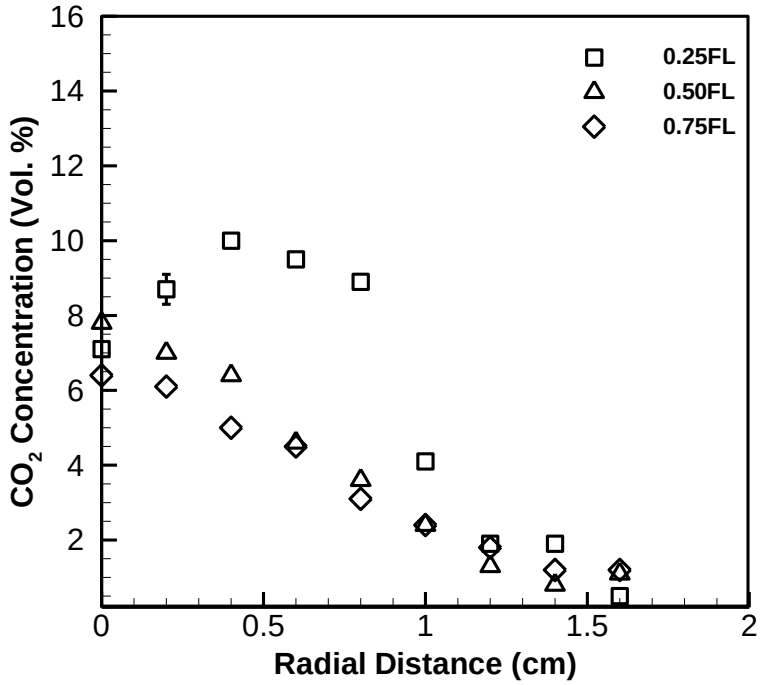

Fig. 107: CO_2 concentration profiles of CME B50 flame at Φ =3

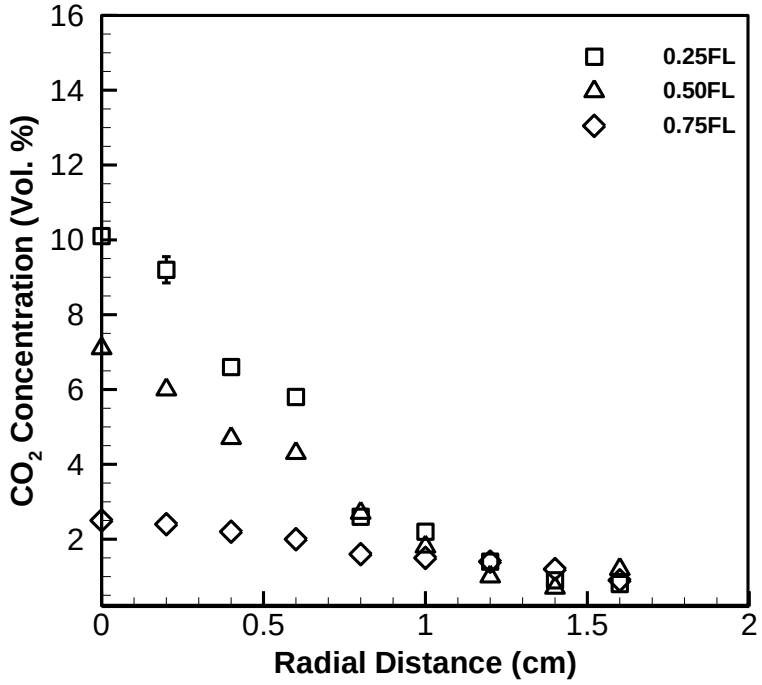

Fig. 108: CO_2 concentration profiles of CME B50 flame at Φ =7

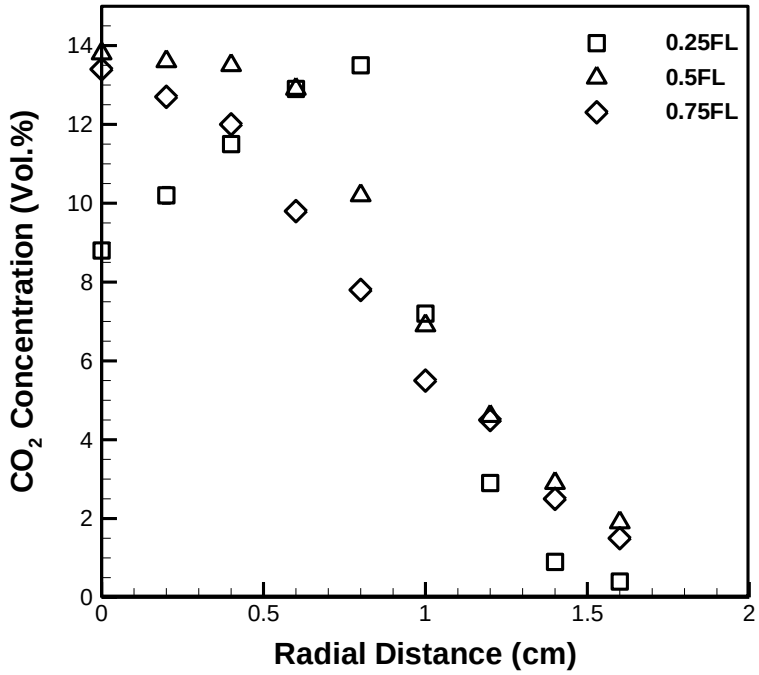

Fig. 109: CO_2 concentration profiles of CME B75 flame at Φ =1.2

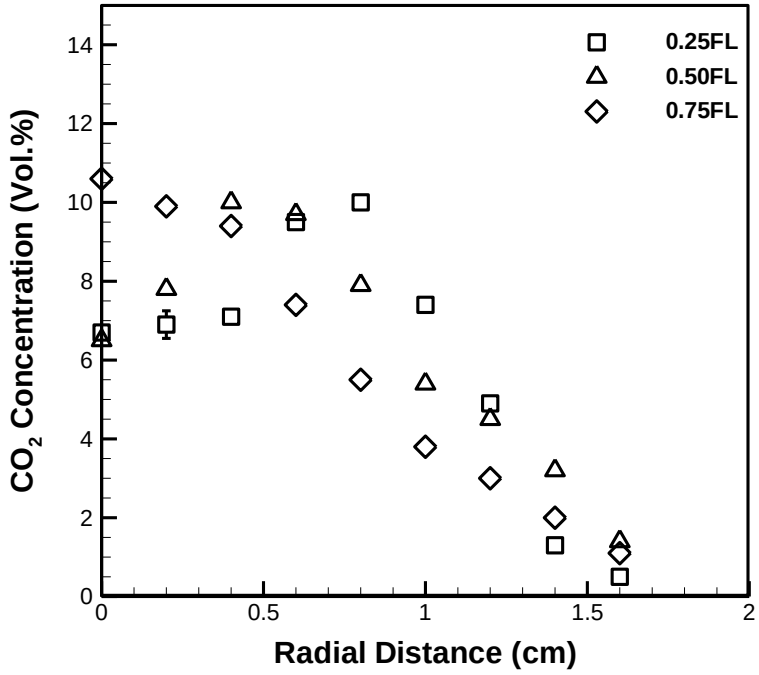

Fig. 110: CO_2 concentration profiles of CME B75 flame at Φ =2

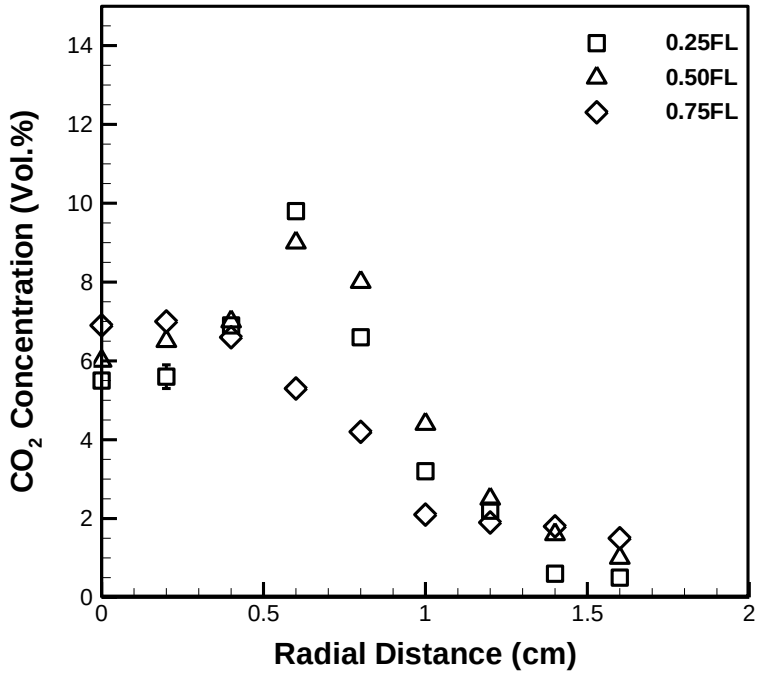

Fig. 111: CO_2 concentration profiles of CME B75 flame at Φ =3

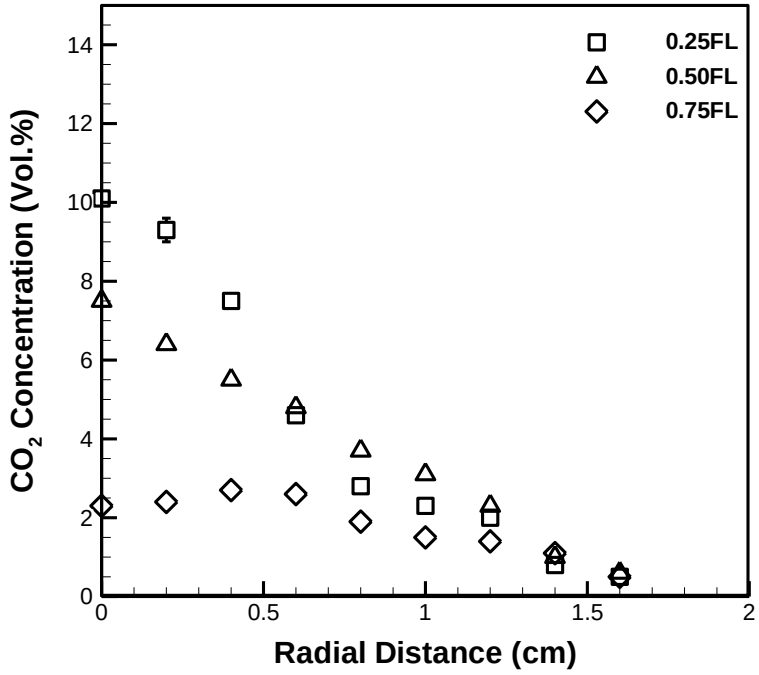

Fig. 112: CO_2 concentration profiles of CME B75 flame at Φ =7

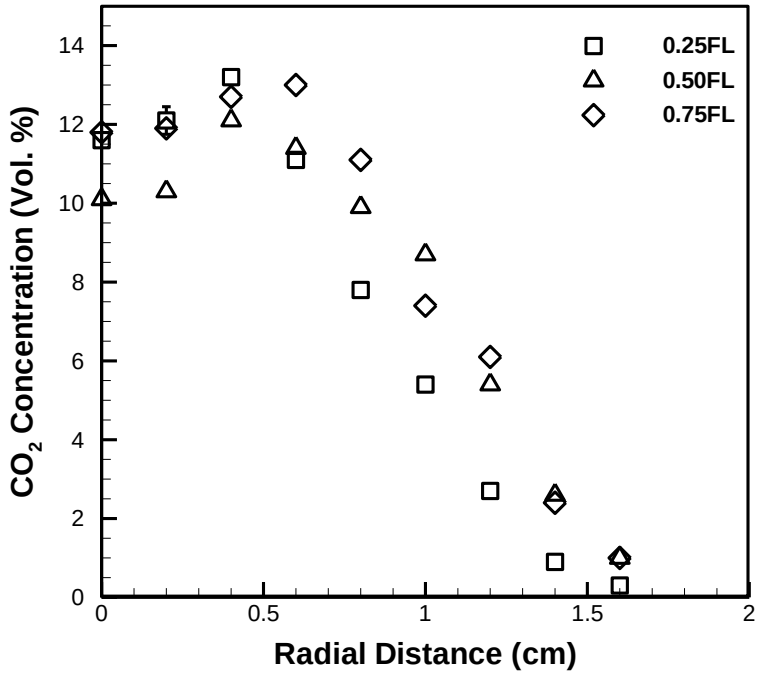

Fig. 113: CO_2 concentration profiles of SME B25 flame at Φ =1.2

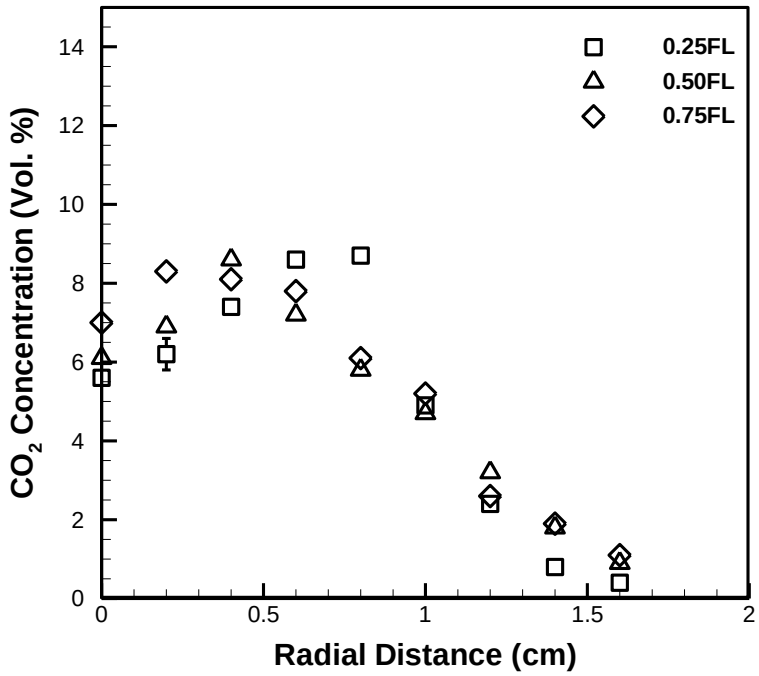

Fig. 114: CO_2 concentration profiles of SME B25 flame at Φ =2

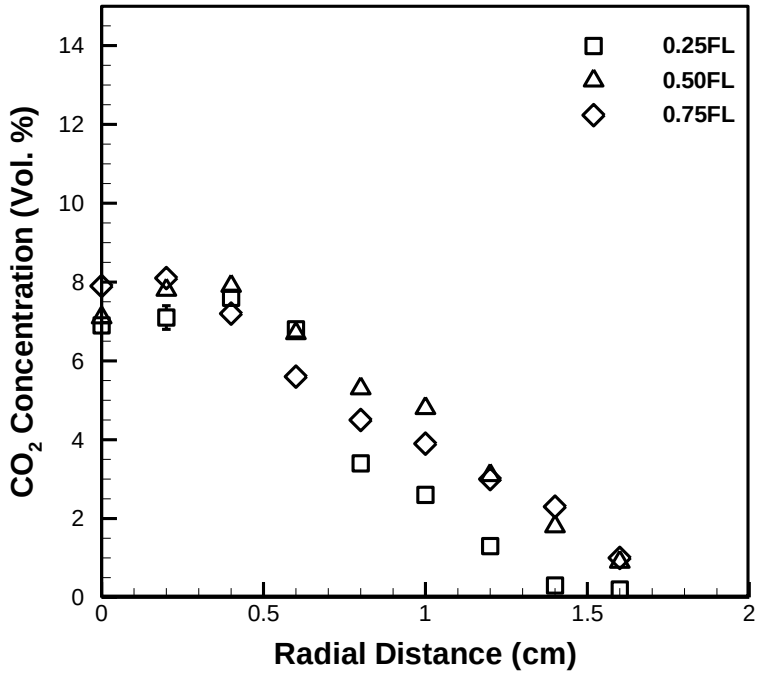

Fig. 115: CO_2 concentration profiles of SME B25 flame at Φ =3

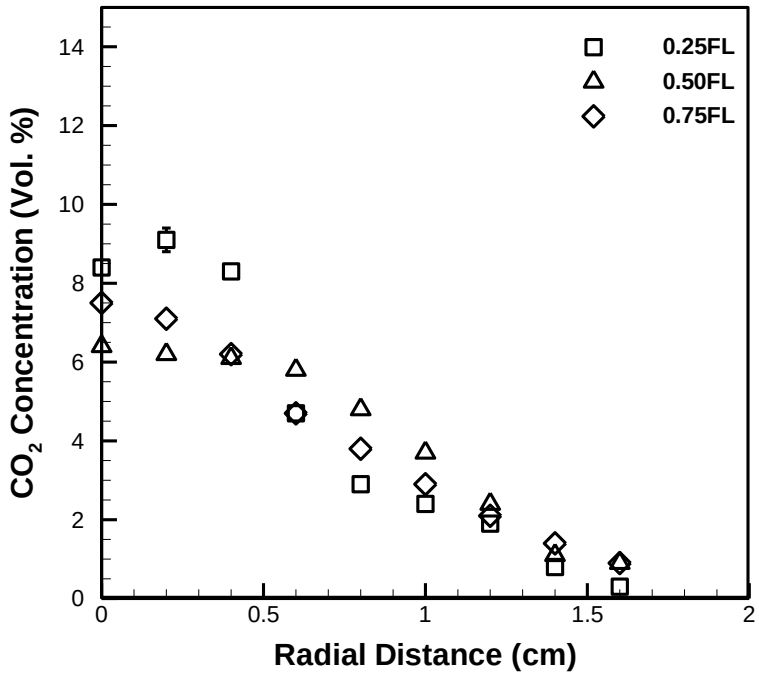

Fig. 116: CO_2 concentration profiles of SME B25 flame at Φ =7

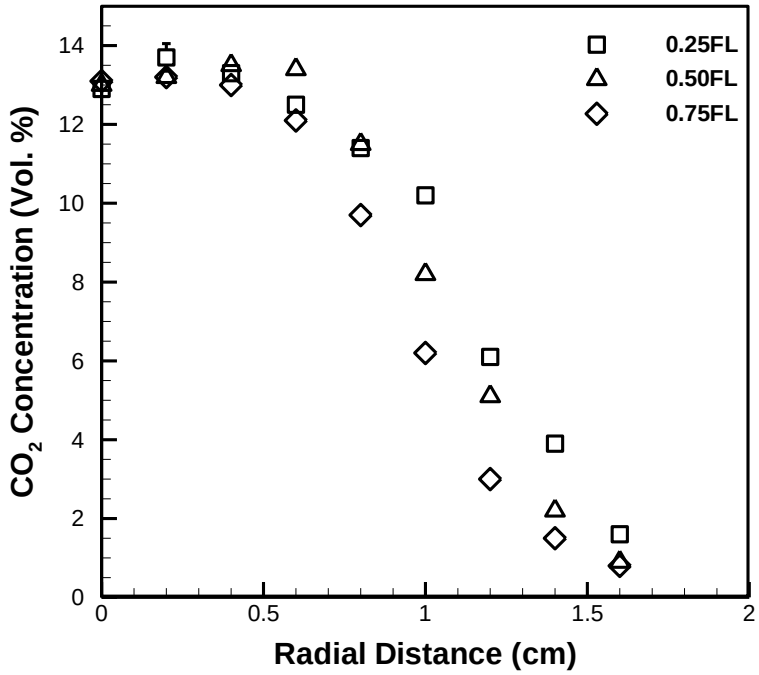

Fig. 117: CO_2 concentration profiles of SME B50 flame at Φ =1.2

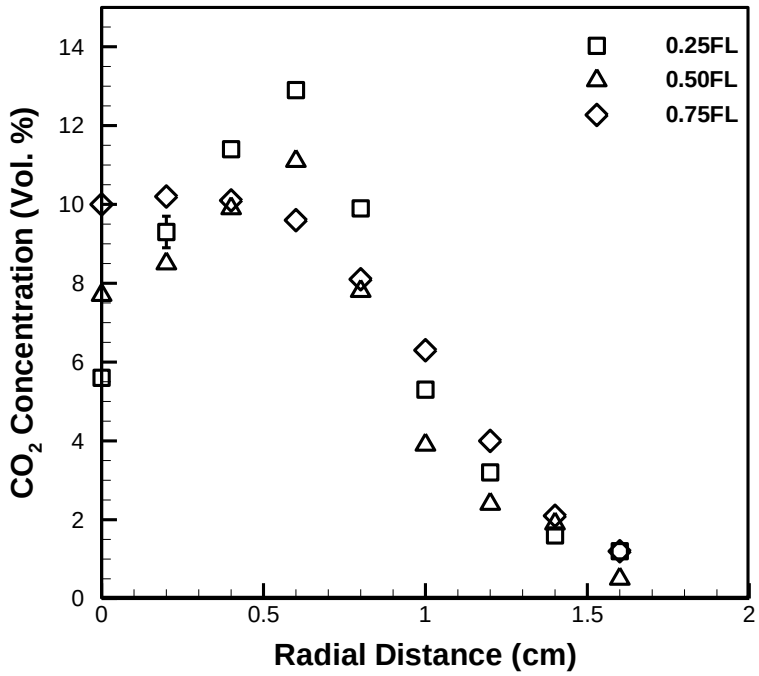

Fig. 118: CO_2 concentration profiles of SME B50 flame at Φ =2

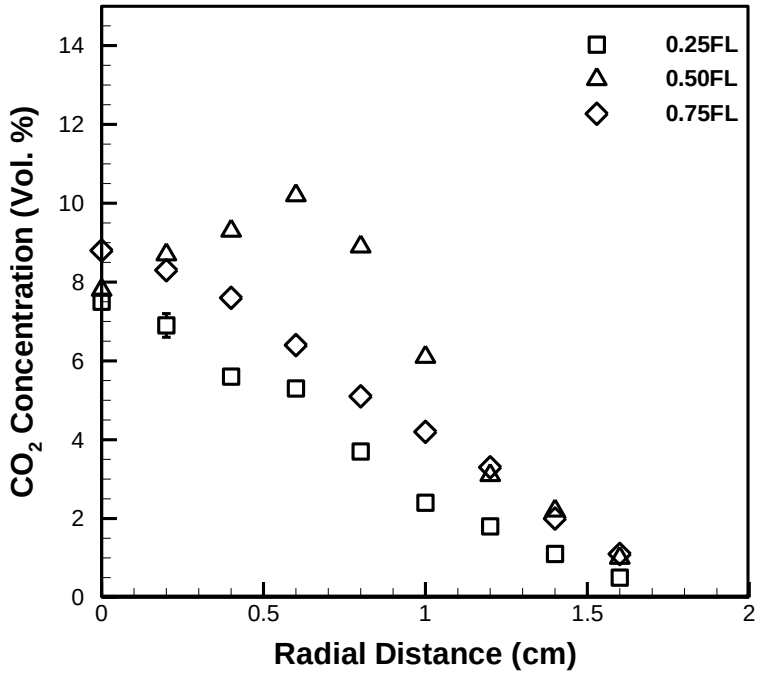

Fig. 119: CO_2 concentration profiles of SME B50 flame at Φ =3

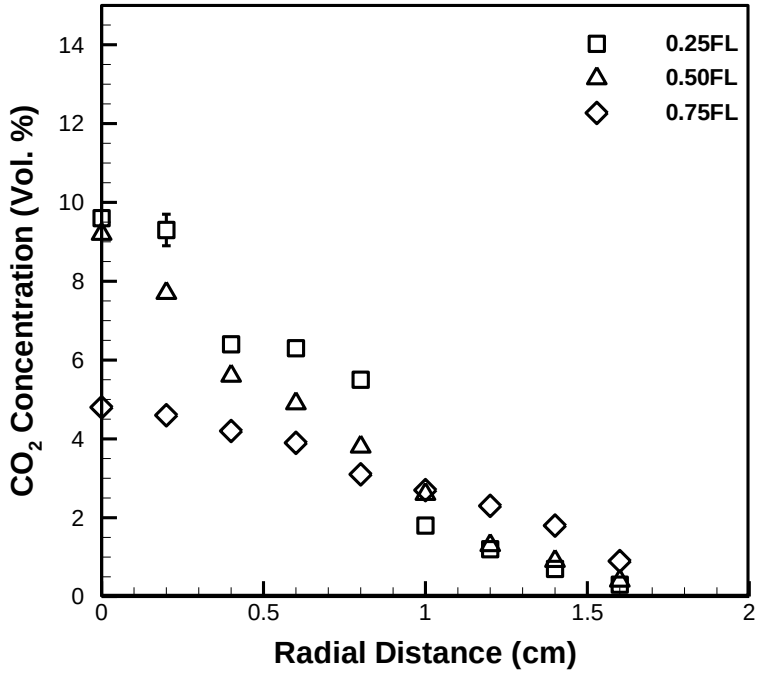

Fig. 120: CO_2 concentration profiles of SME B50 flame at Φ =7

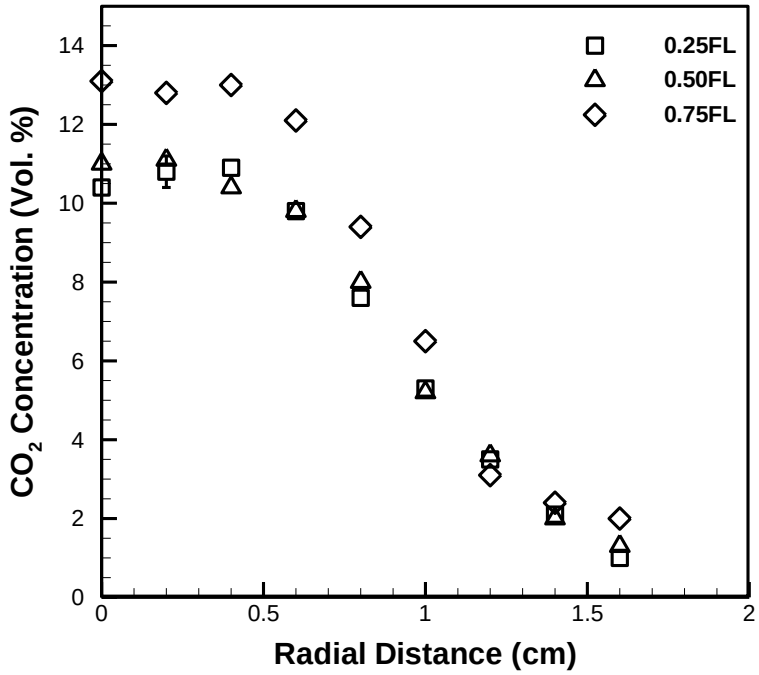

Fig. 121: CO_2 concentration profiles of SME B75 flame at Φ =1.2

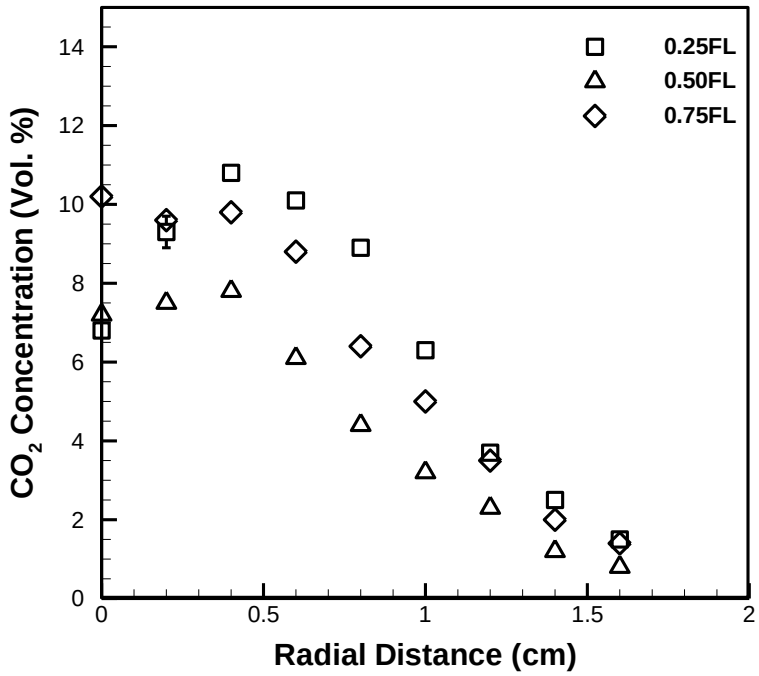

Fig. 122: CO_2 concentration profiles of SME B75 flame at Φ =2

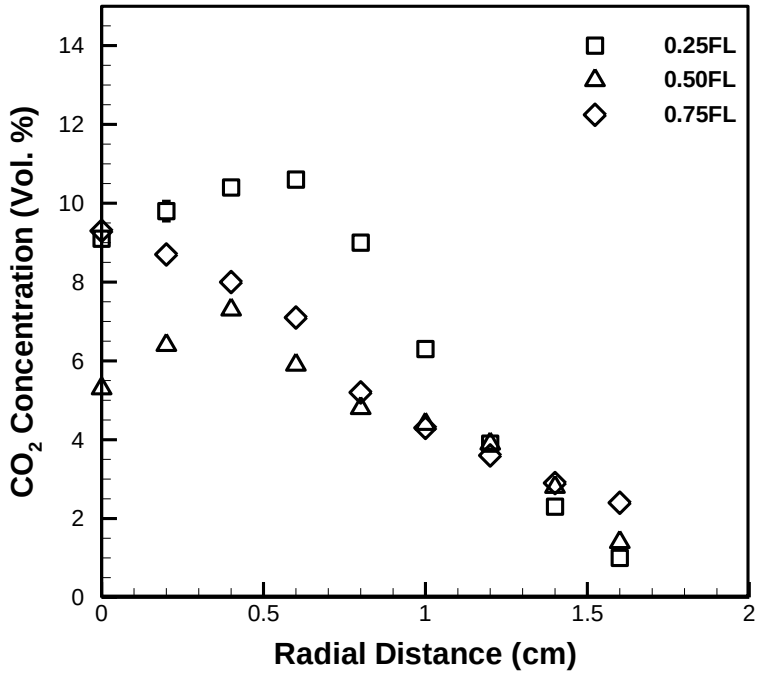

Fig. 123: CO_2 concentration profiles of SME B75 flame at Φ =3

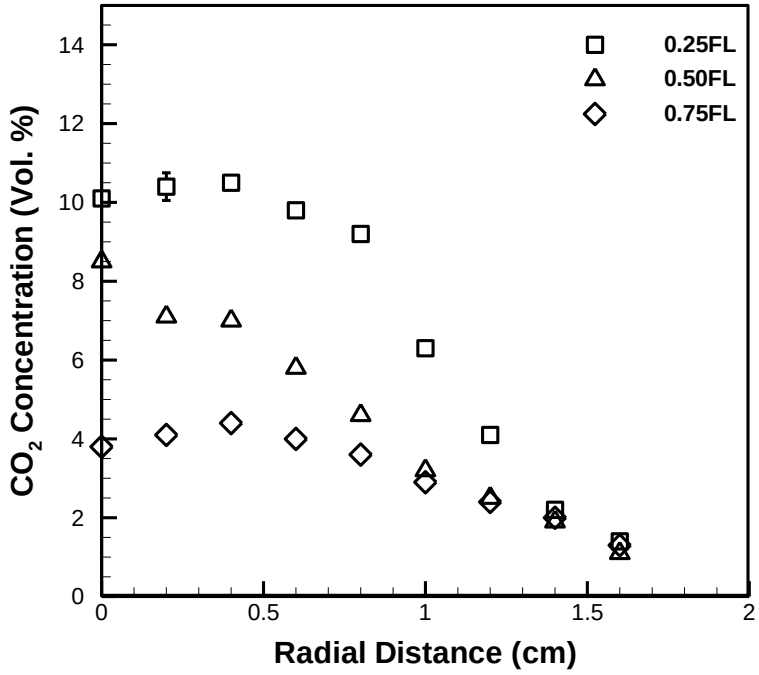

Fig. 124: CO_2 concentration profiles of SME B75 flame at Φ =7

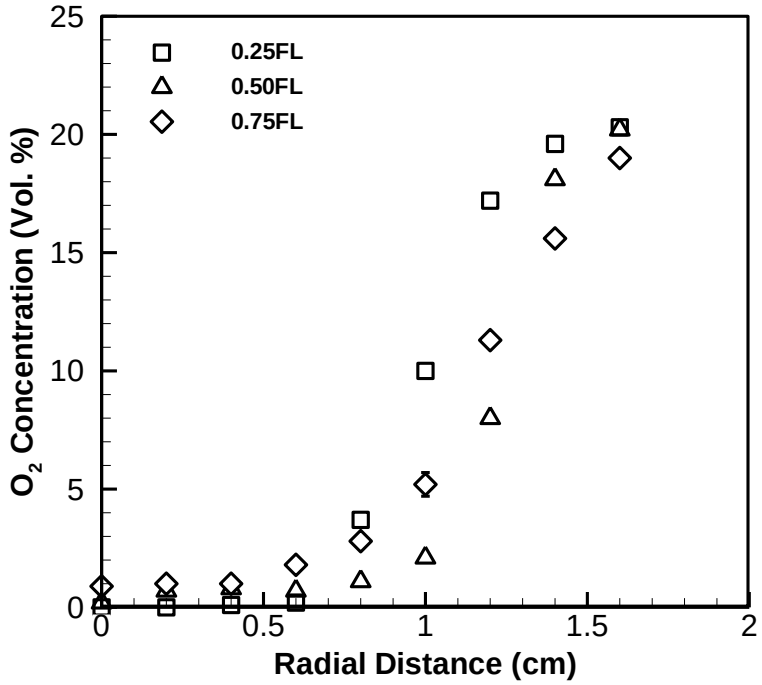

Fig. 125: O_2 concentration profiles of CME B25 flame at Φ =1.2

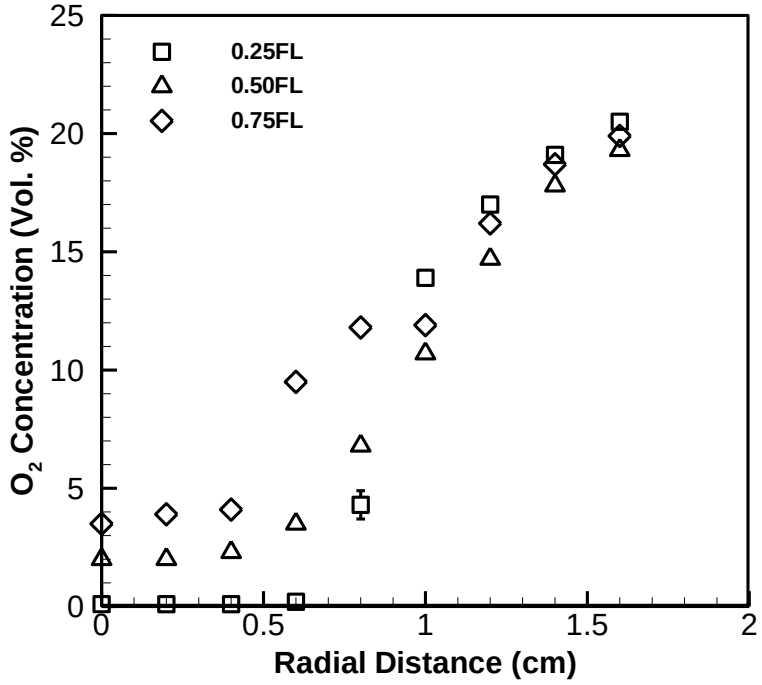

Fig. 126: O_2 concentration profiles of CME B25 flame at Φ =2

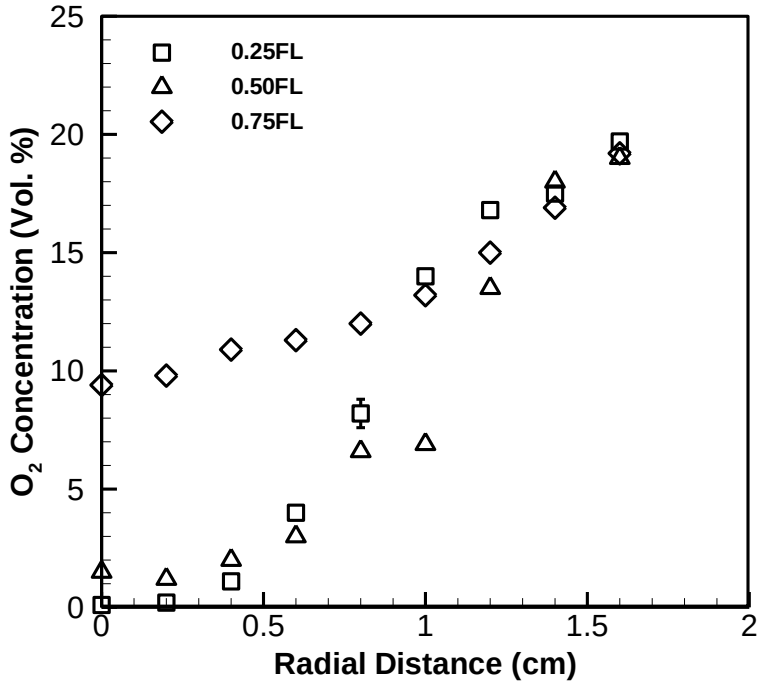

Fig. 127: O_2 concentration profiles of CME B25 flame at Φ =3

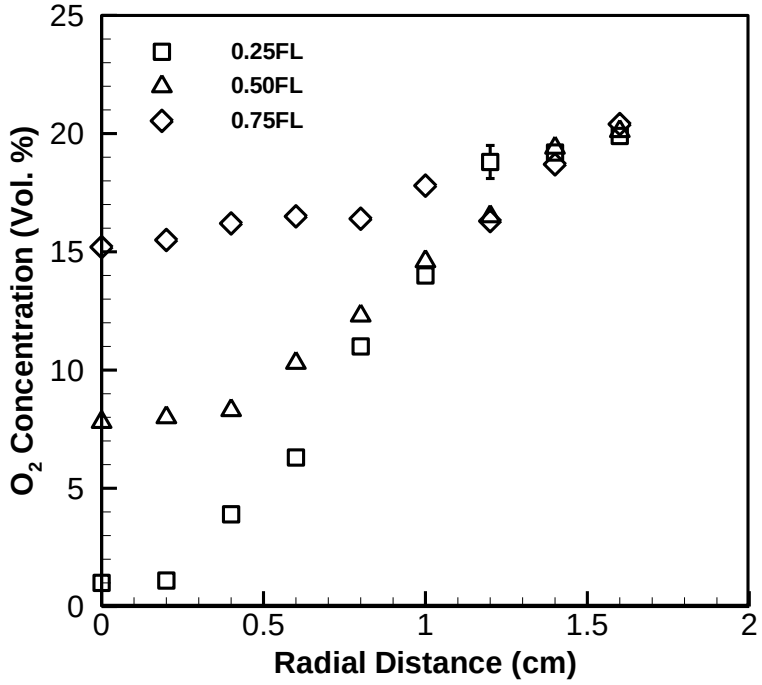

Fig. 128: O_2 concentration profiles of CME B25 flame at Φ =7

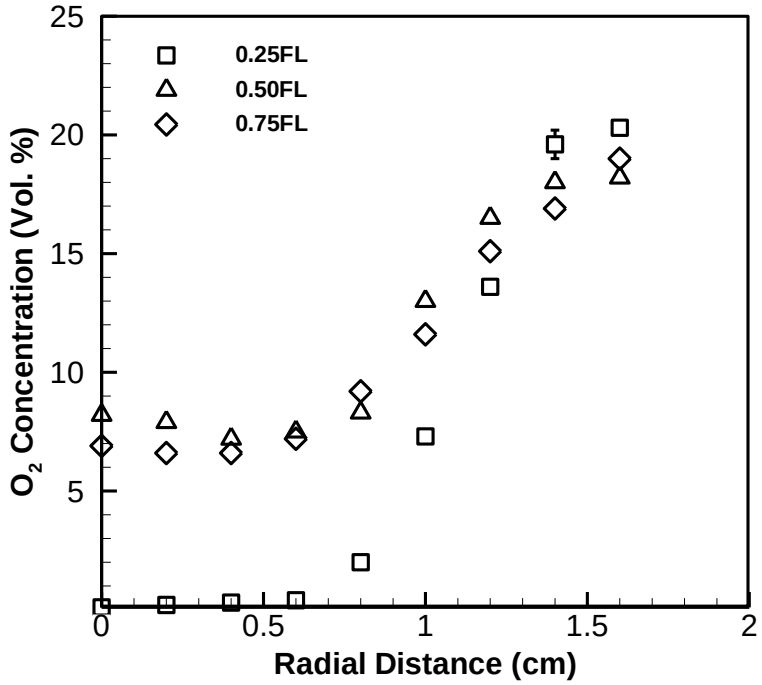

Fig. 129: O_2 concentration profiles of CME B50 flame at Φ =1.2

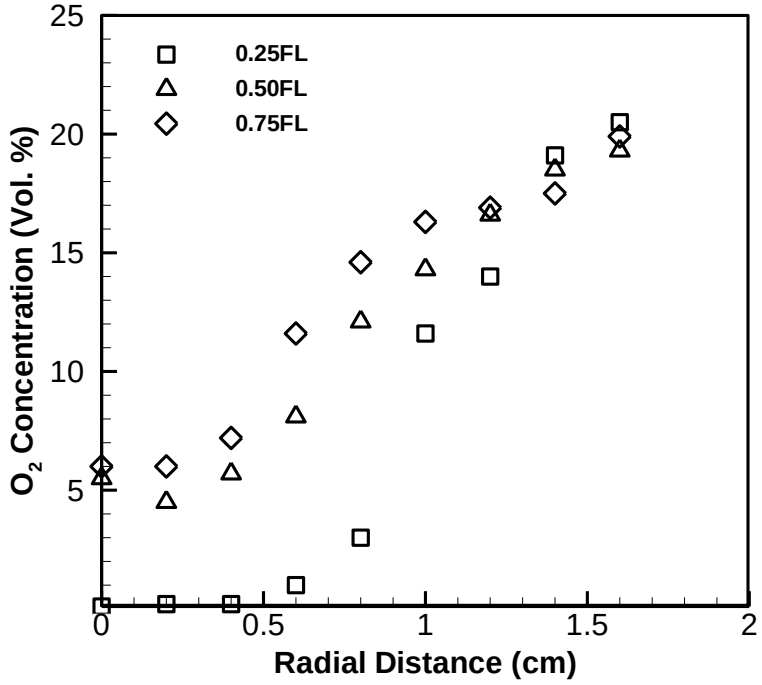

Fig. 130: O_2 concentration profiles of CME B50 flame at Φ =2

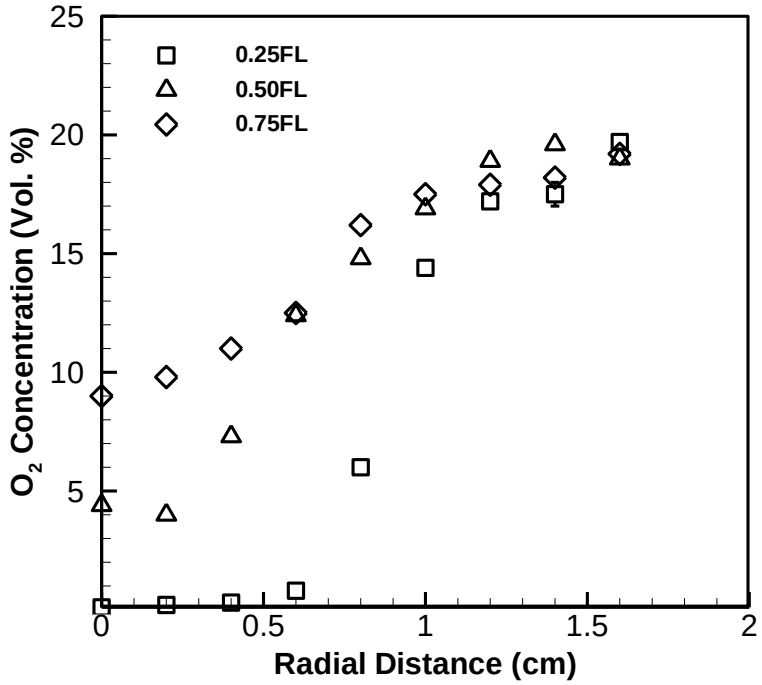

Fig. 131: O_2 concentration profiles of CME B50 flame at Φ =3

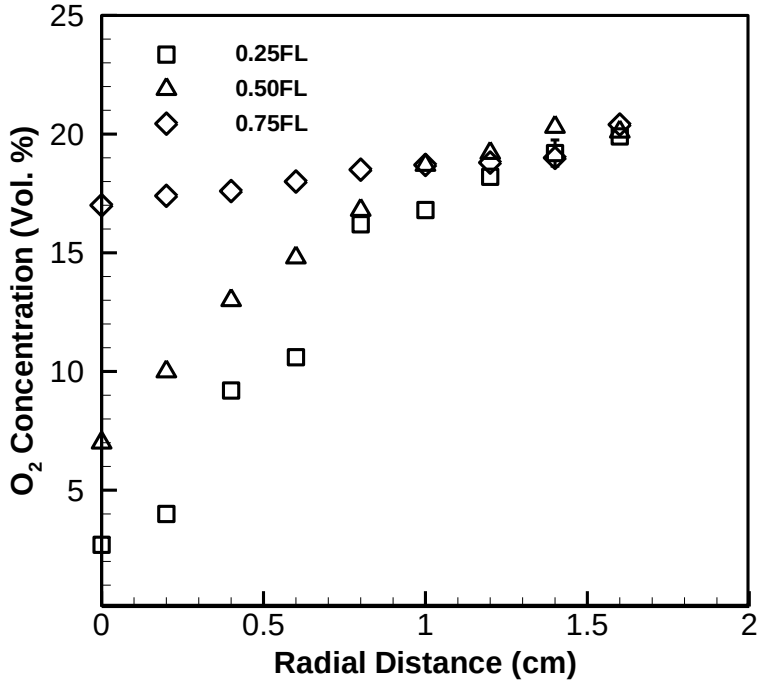

Fig. 132: O_2 concentration profiles of CME B50 flame at Φ =7

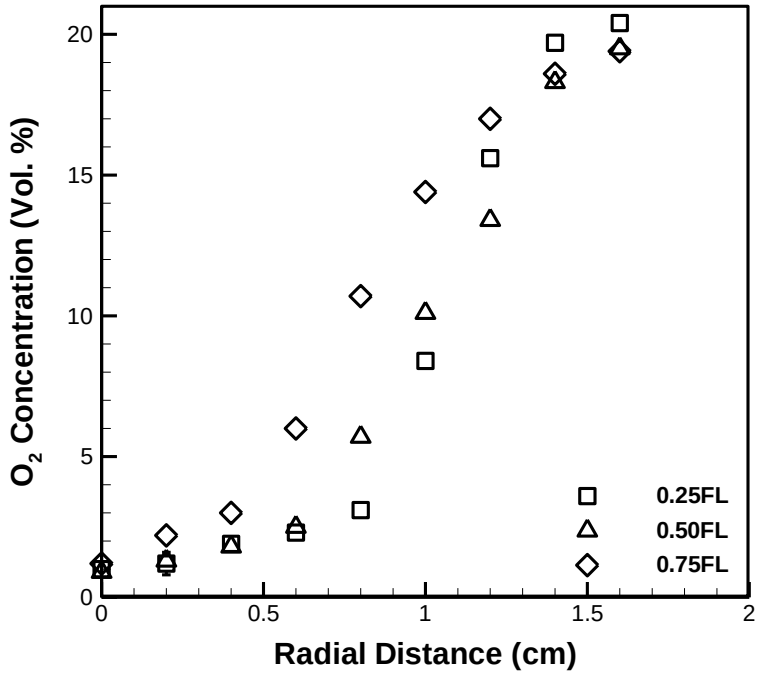

Fig. 133: O_2 concentration profiles of CME B75 flame at Φ =1.2

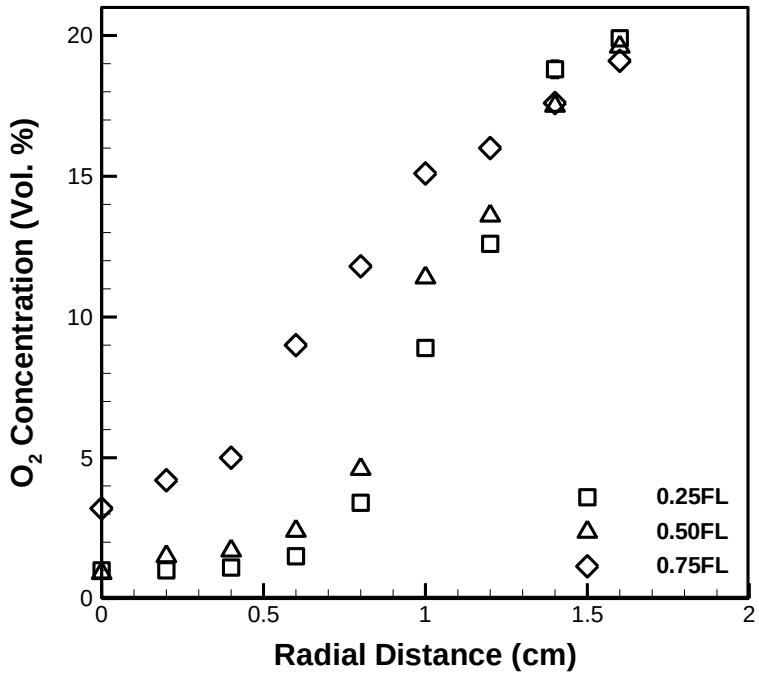

Fig. 134: O_2 concentration profiles of CME B75 flame at Φ =2

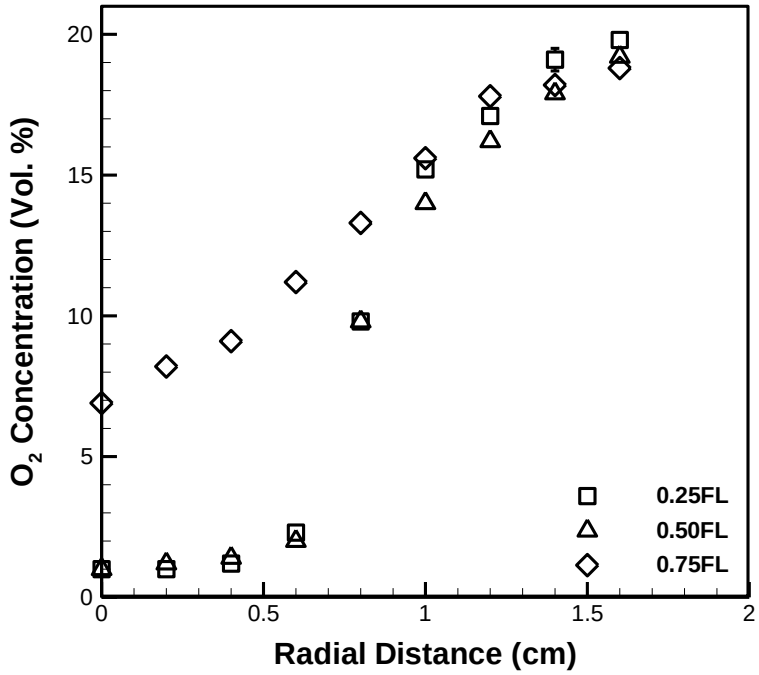

Fig. 135: O_2 concentration profiles of CME B75 flame at Φ =3

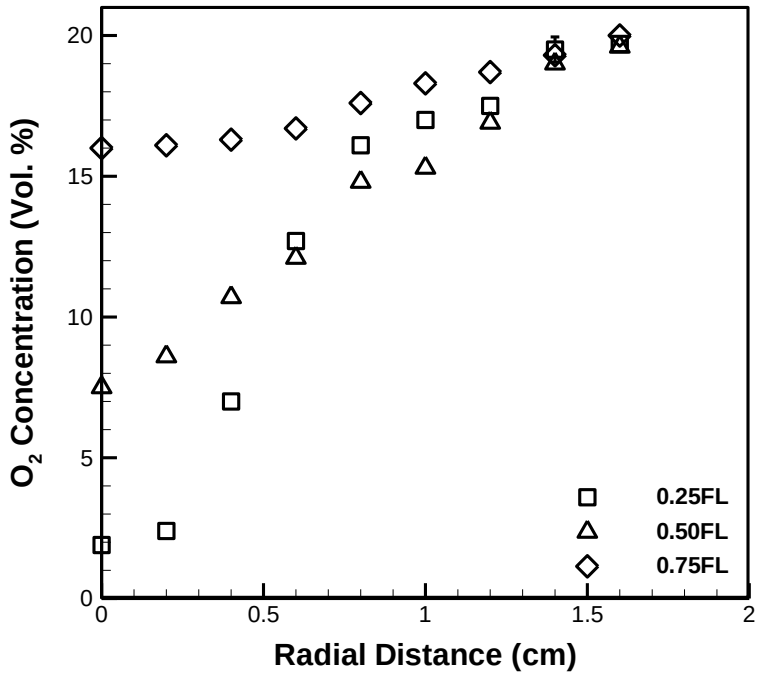

Fig. 136: O_2 concentration profiles of CME B75 flame at Φ =7

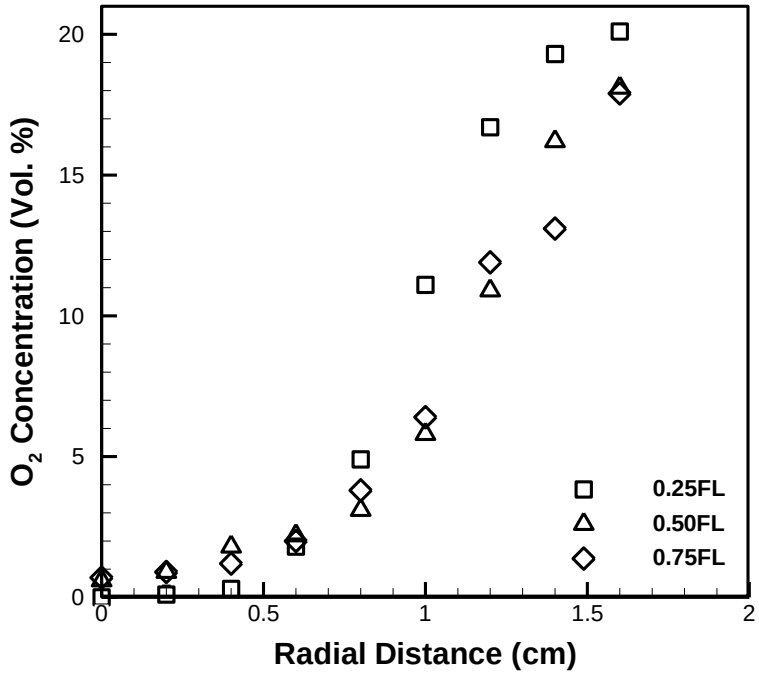

Fig. 137: O_2 concentration profiles of SME B25 flame at Φ =1.2

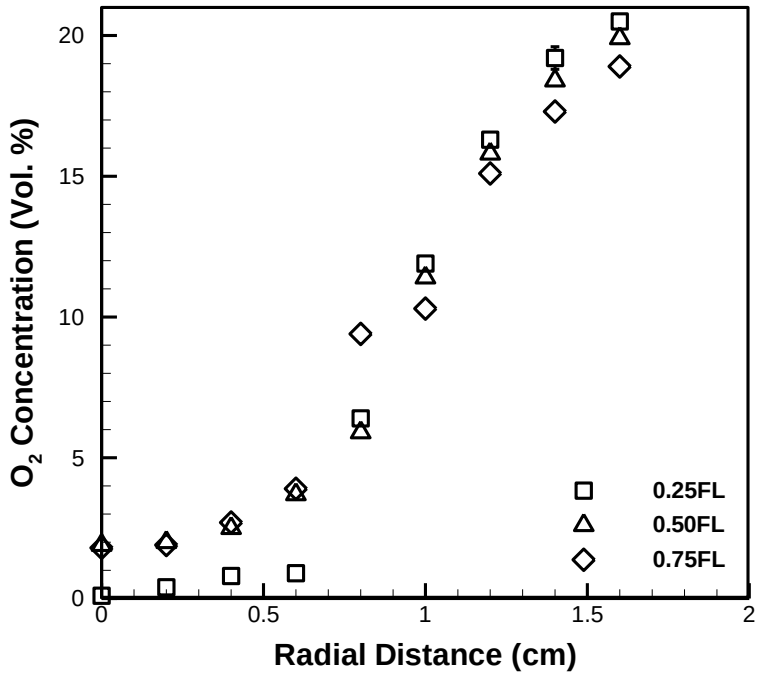

Fig. 138: O_2 concentration profiles of SME B25 flame at Φ =2

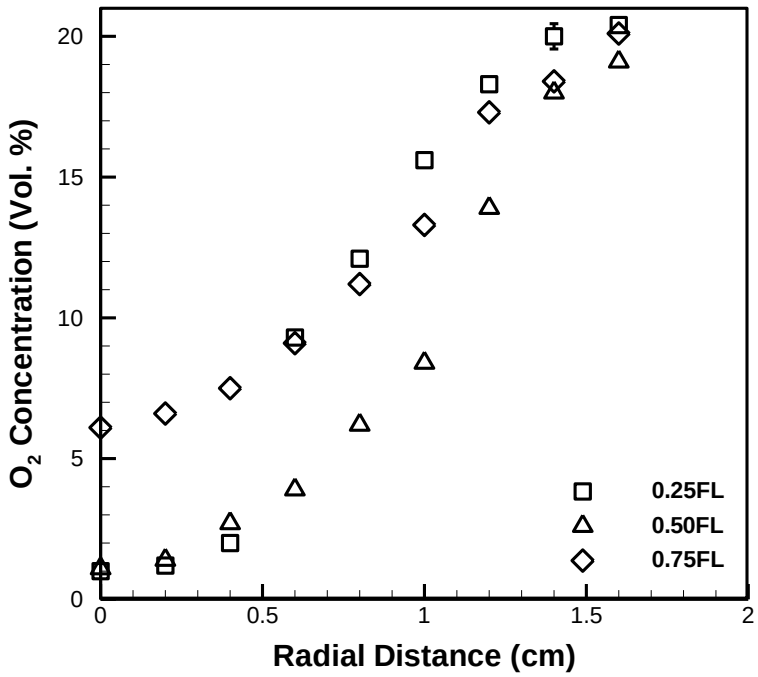

Fig. 139: O_2 concentration profiles of SME B25 flame at Φ =3

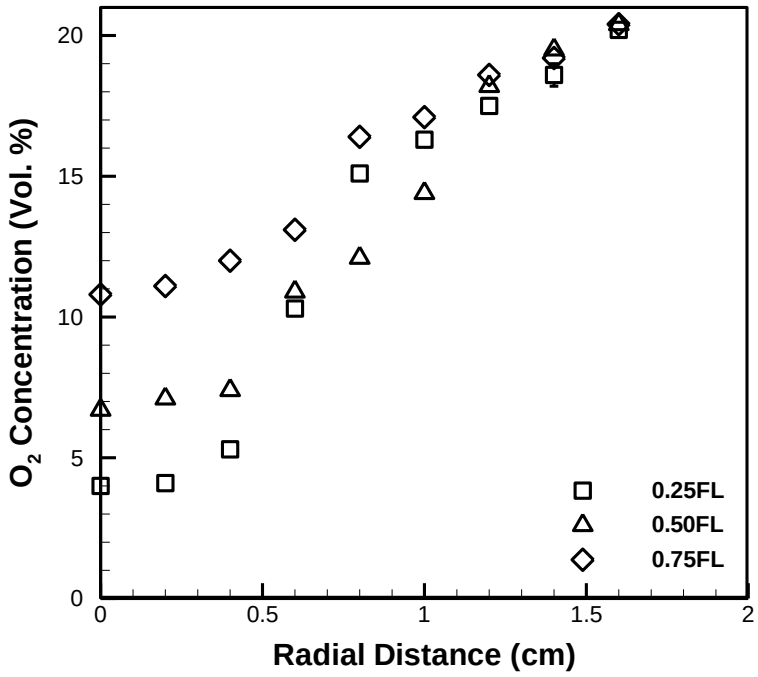

Fig. 140: O_2 concentration profiles of SME B25 flame at Φ =7

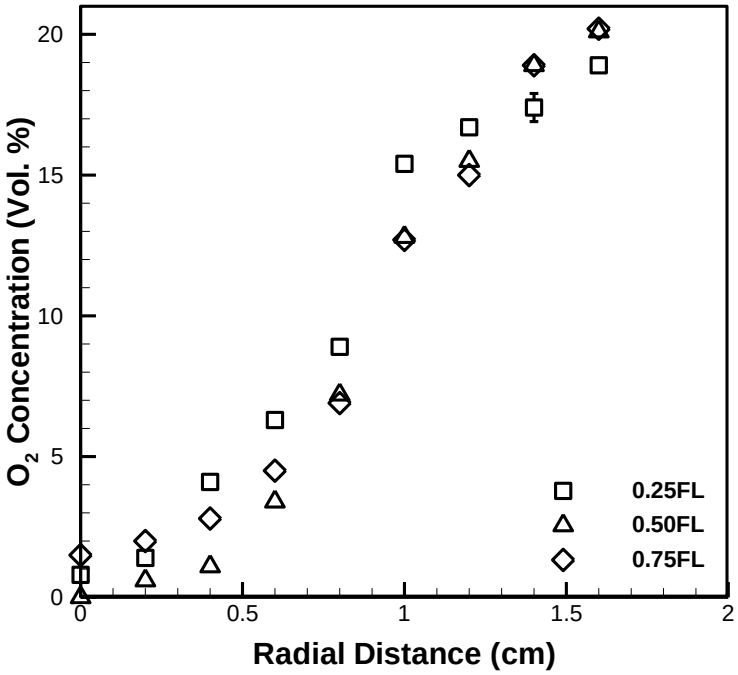

Fig. 141: O_2 concentration profiles of SME B50 flame at Φ =1.2

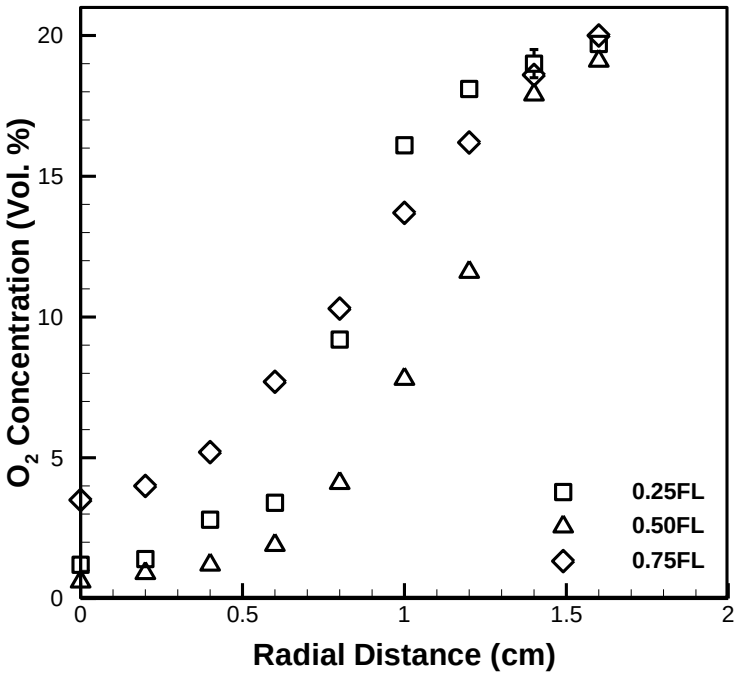

Fig. 142: O_2 concentration profiles of SME B50 flame at Φ =2

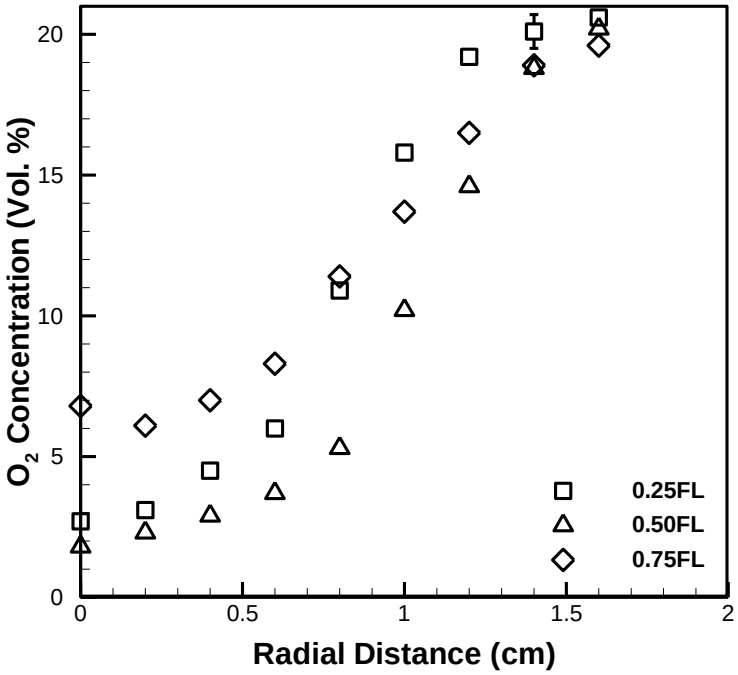

Fig. 143: O_2 concentration profiles of SME B50 flame at Φ =3

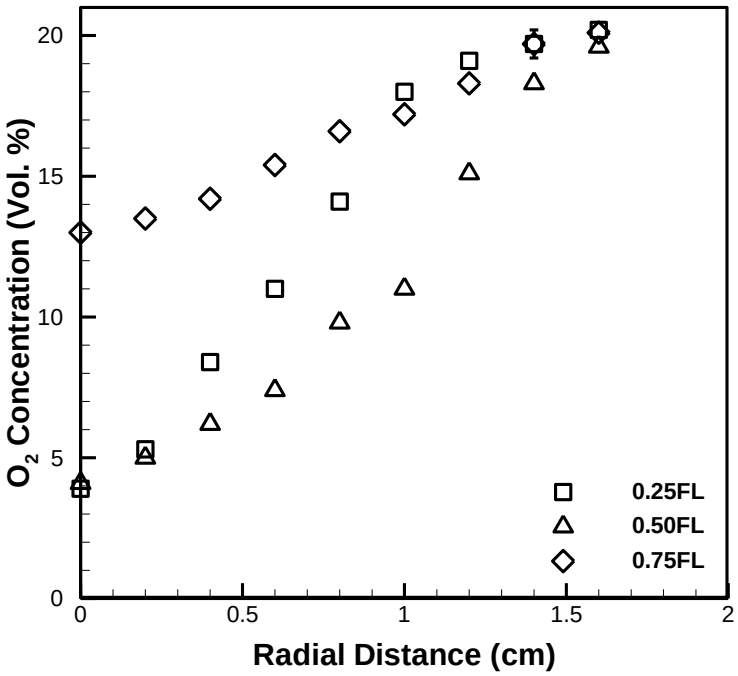

Fig. 144: O_2 concentration profiles of SME B50 flame at Φ =7

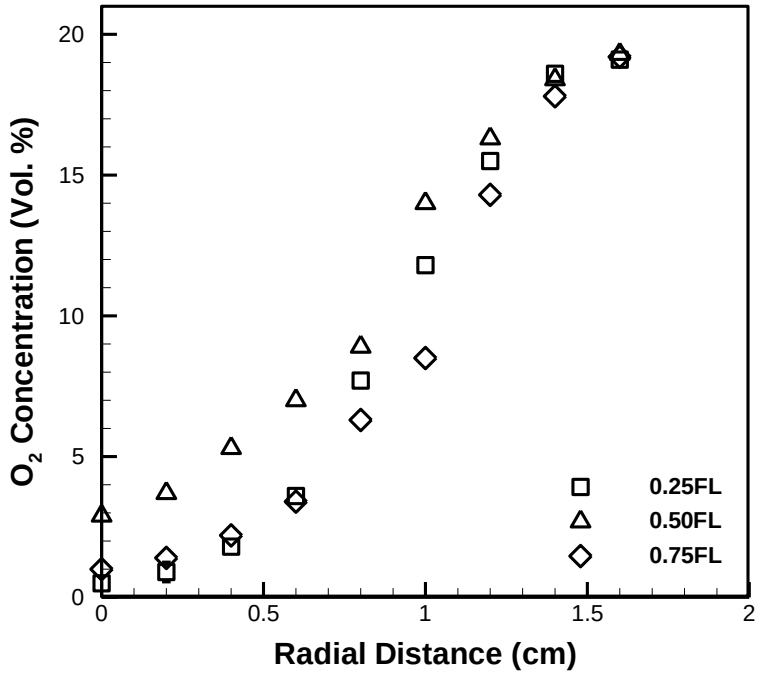

Fig. 145: O_2 concentration profiles of SME B75 flame at Φ =1.2

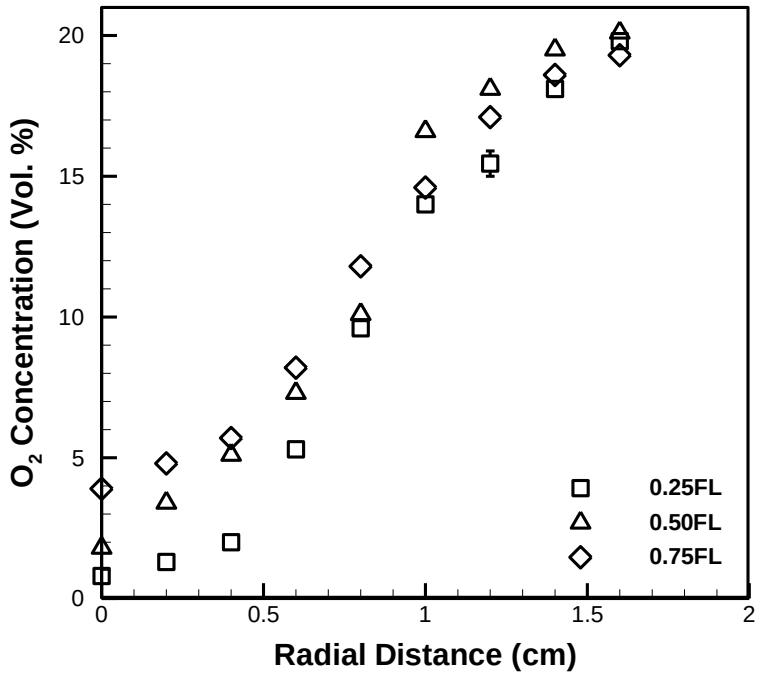

Fig. 146: O_2 concentration profiles of SME B75 flame at Φ =2

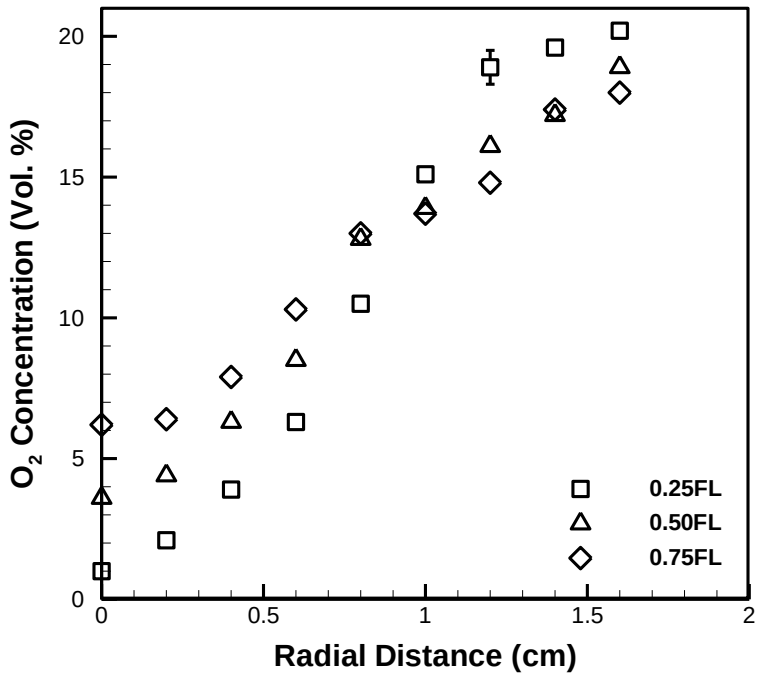

Fig. 147: O_2 concentration profiles of SME B75 flame at Φ =3

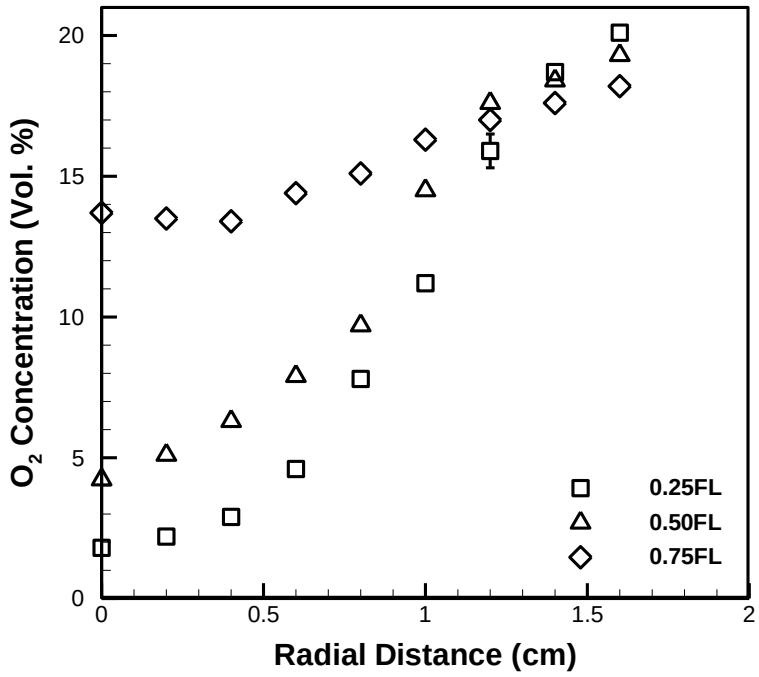

Fig. 148: O_2 concentration profiles of SME B75 flame at Φ =7

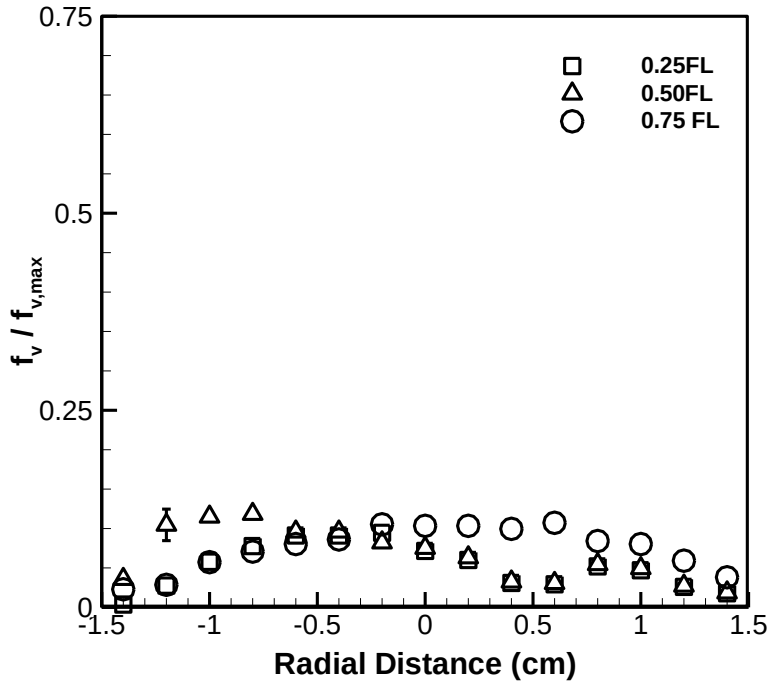

Fig. 149: CME B25 soot volume fraction profiles at Φ =1.2

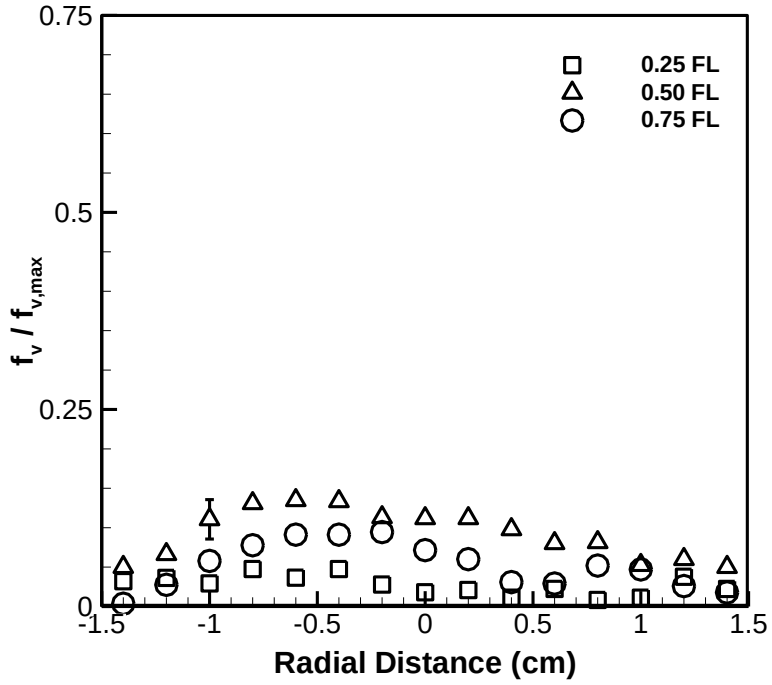

Fig. 150: CME B25 soot volume fraction profiles at Φ =2

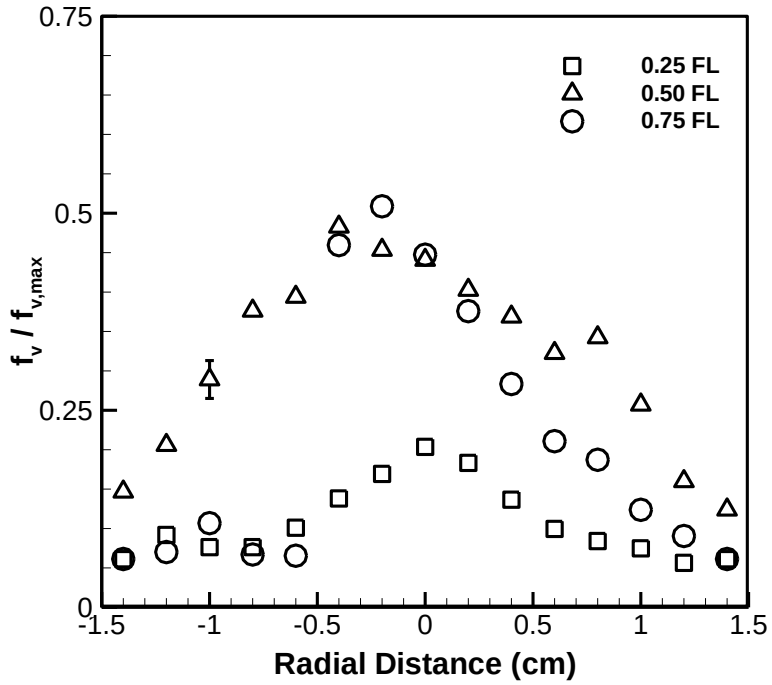

Fig. 151: CME B25 soot volume fraction profiles at Φ =3

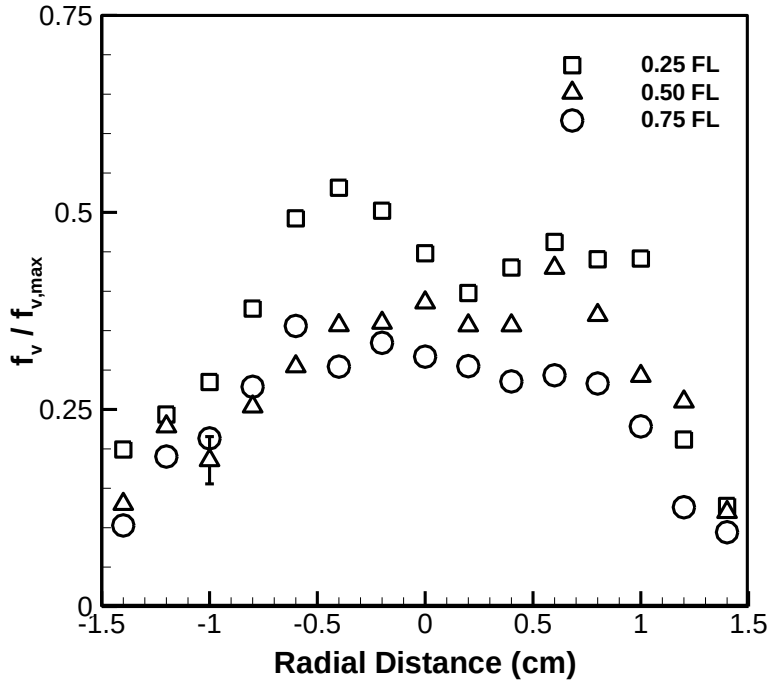

Fig. 152: CME B25 soot volume fraction profiles at Φ =7

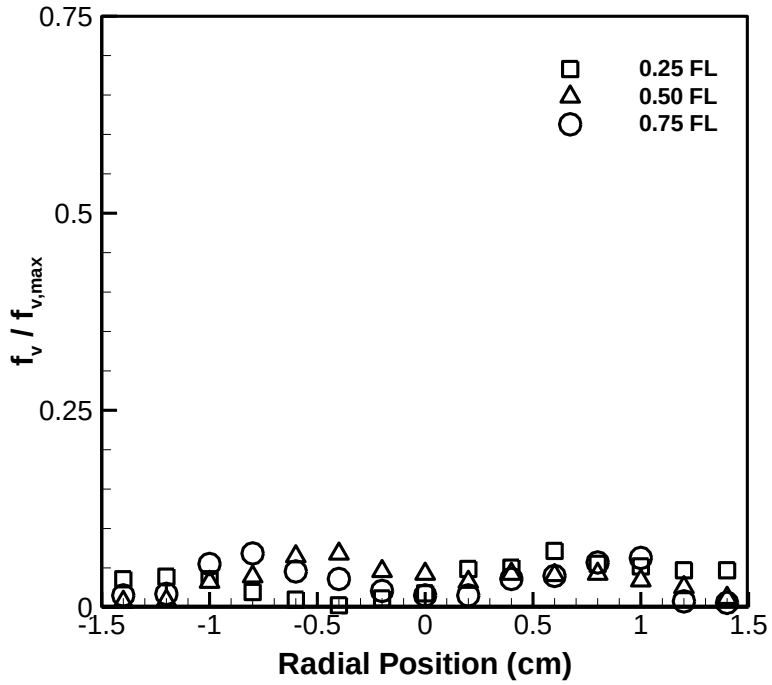

Fig. 153: CME B50 soot volume fraction profiles at Φ =1.2

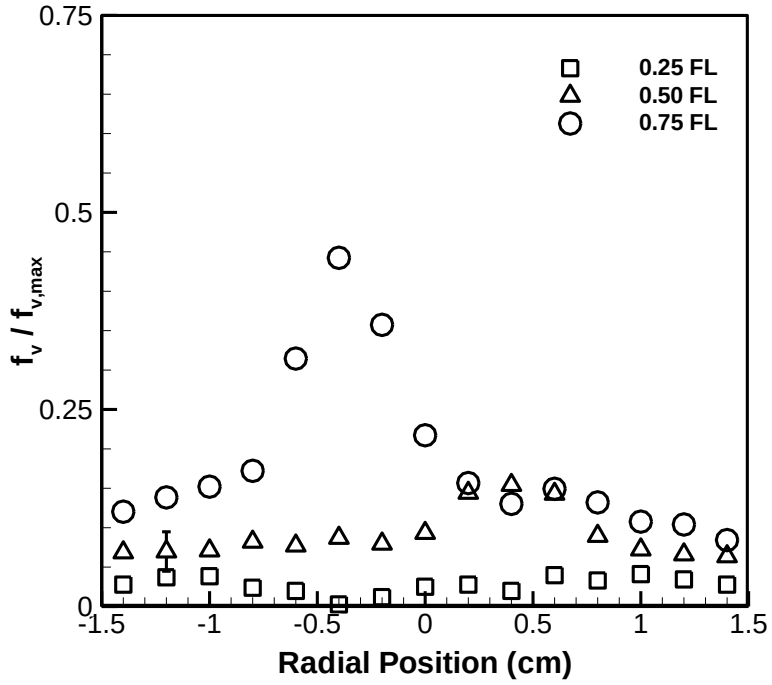

Fig. 154: CME B50 soot volume fraction profiles at Φ =2

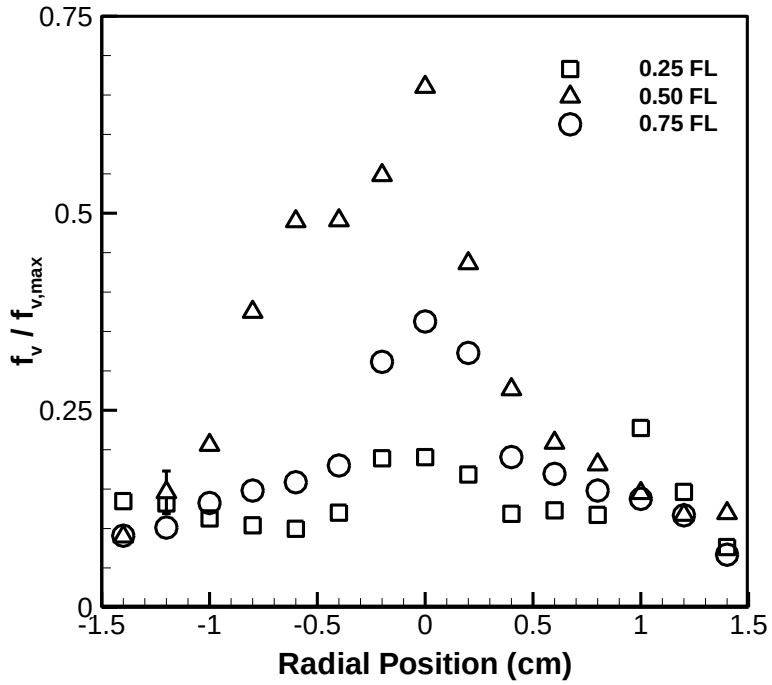

Fig. 155: CME B50 soot volume fraction profiles at Φ =3

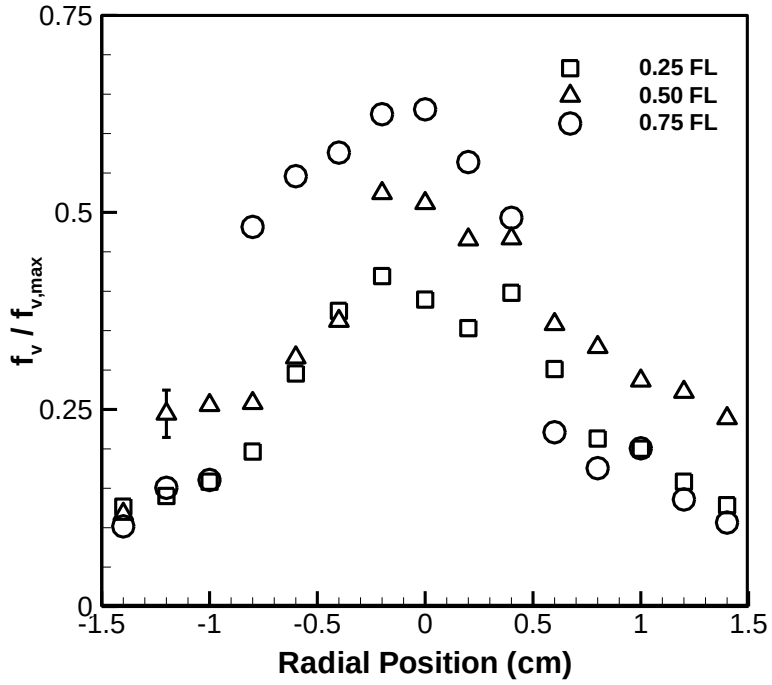

Fig. 156: CME B50 soot volume fraction profiles at Φ =7

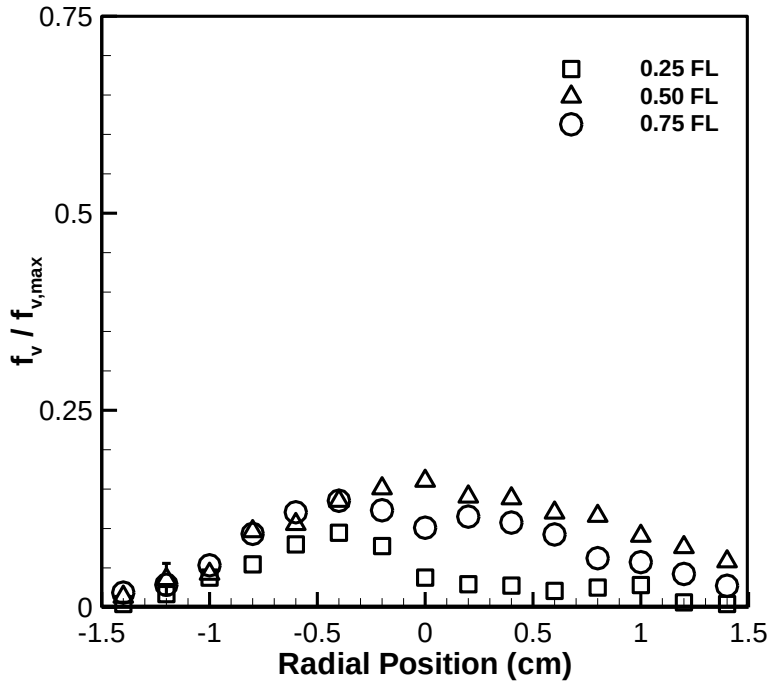

Fig. 157: CME B75 soot volume fraction profiles at Φ =1.2

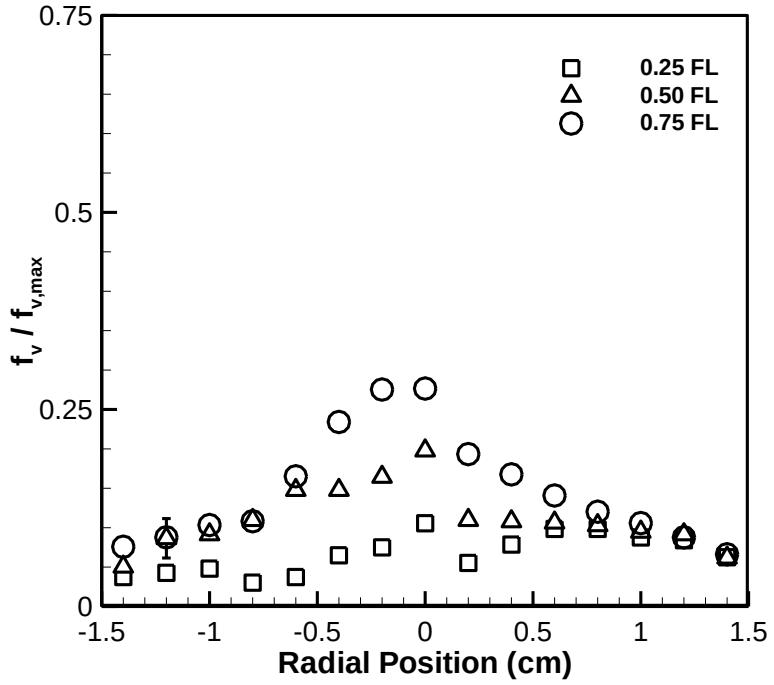

Fig. 158: CME B75 soot volume fraction profiles at Φ =2

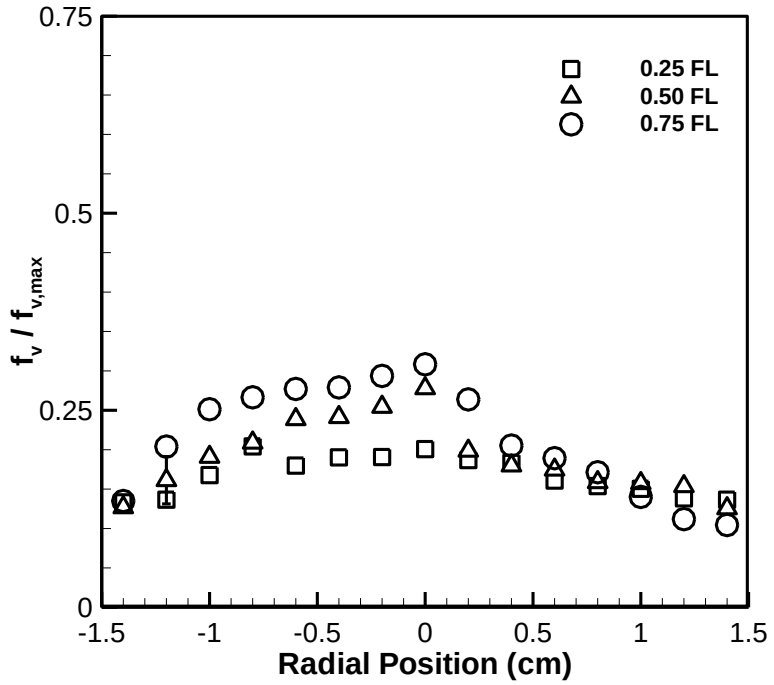

Fig. 159: CME B75 soot volume fraction profiles at Φ =3

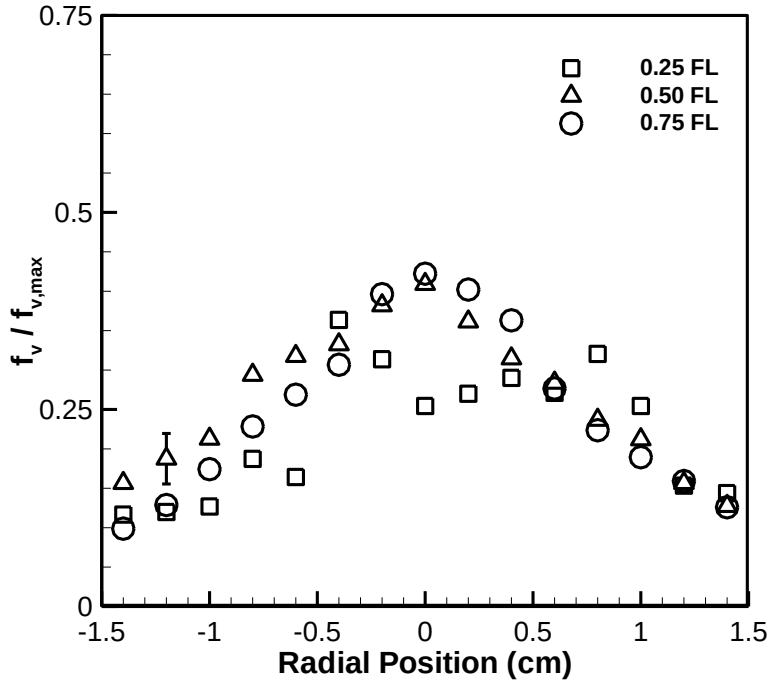

Fig. 160: CME B75 soot volume fraction profiles at Φ =7

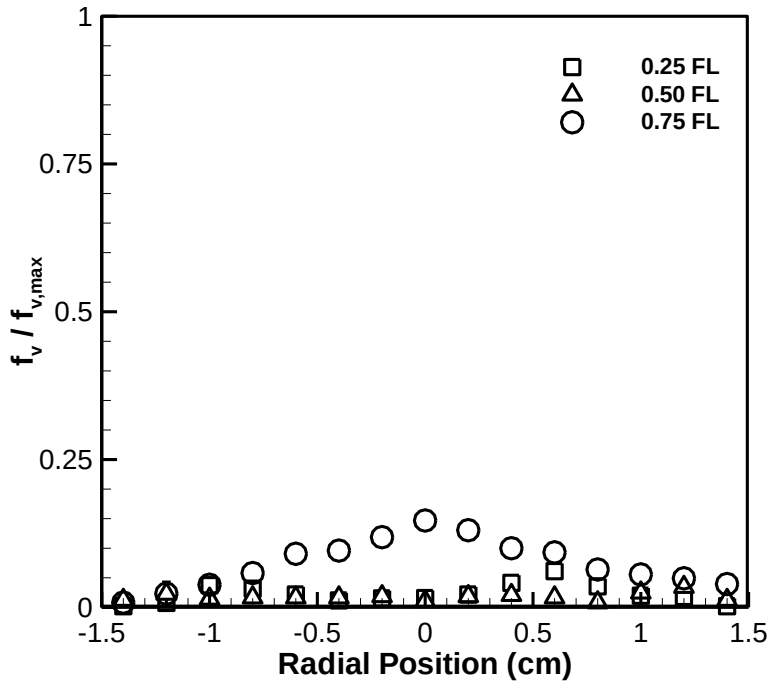

Fig. 161: SME B25 soot volume fraction profiles at Φ =1.2

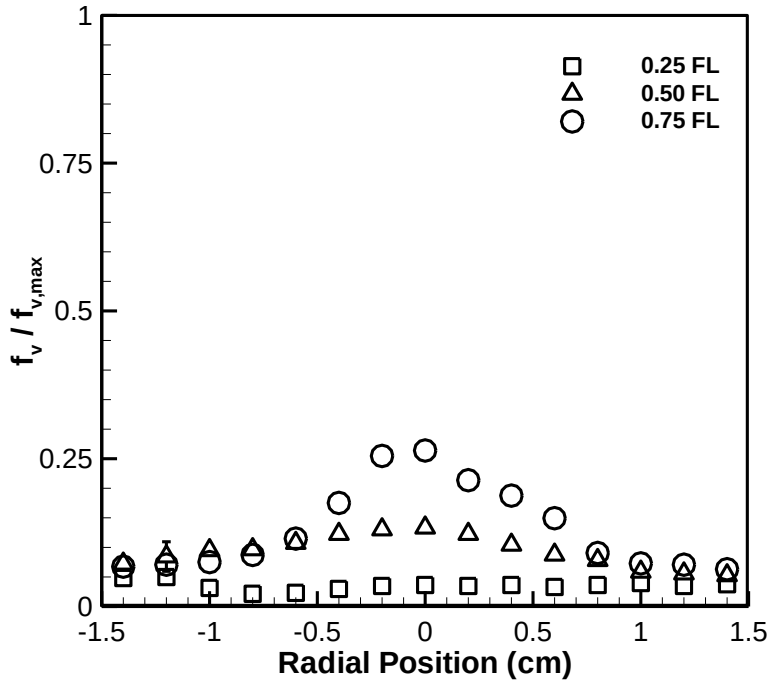

Fig. 162: SME B25 soot volume fraction profiles at Φ =2

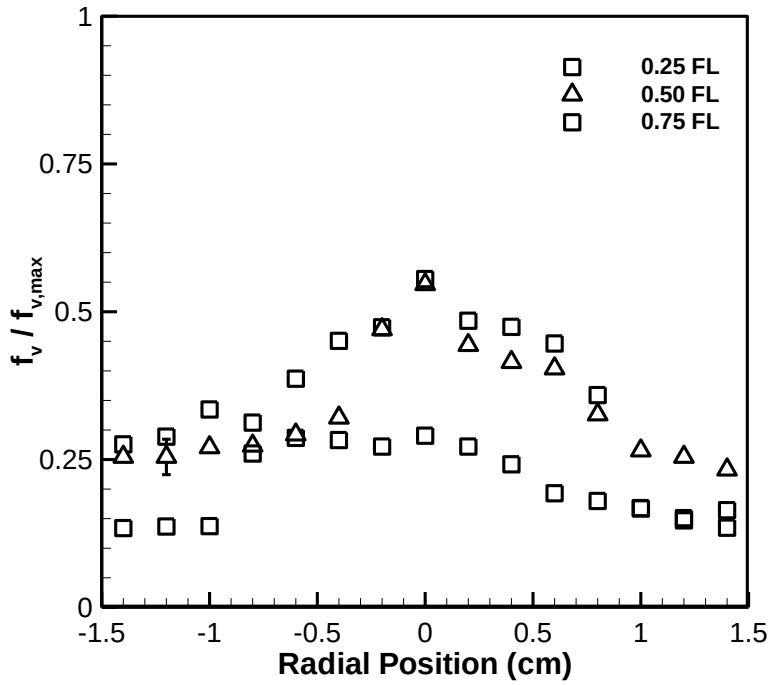

Fig. 163: SME B25 soot volume fraction profiles at Φ =3

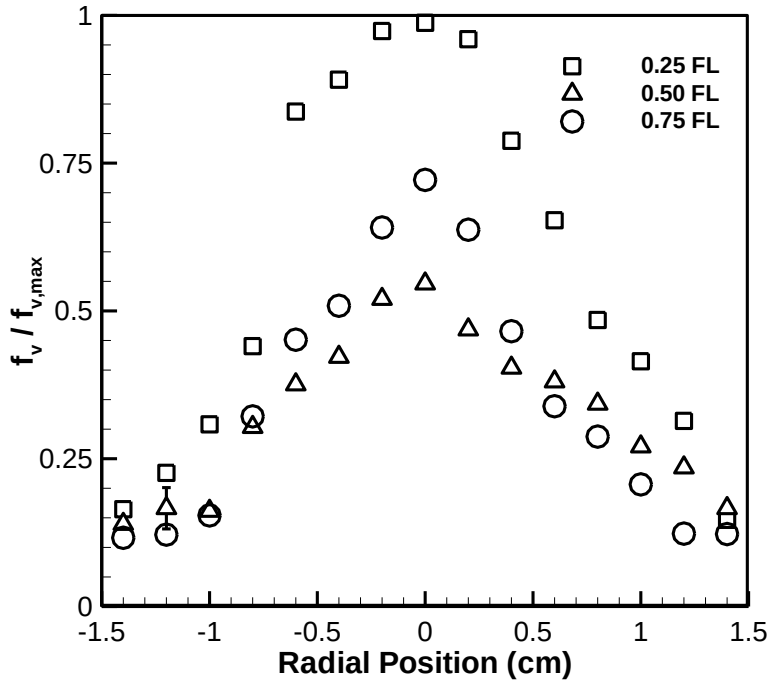

Fig. 164: SME B25 soot volume fraction profiles at Φ =7

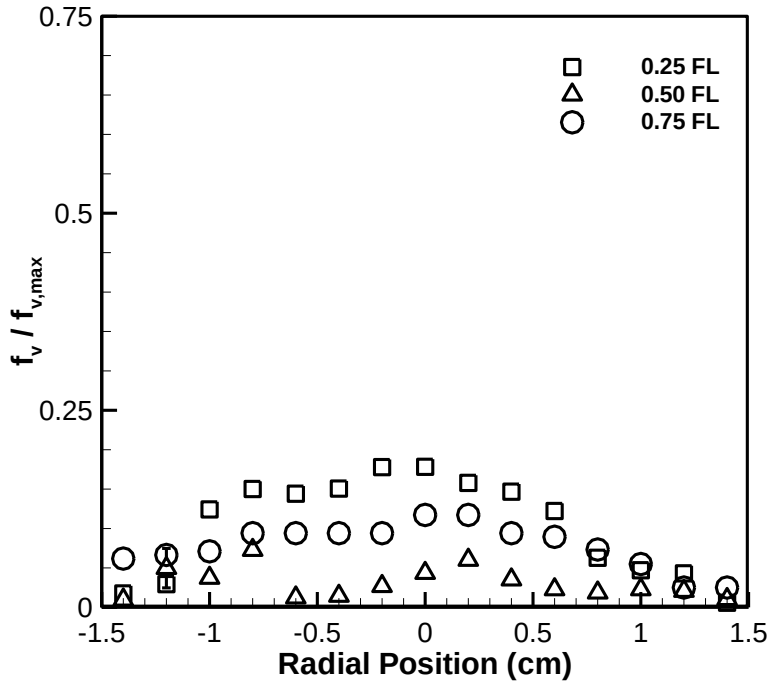

Fig. 165: SME B50 soot volume fraction profiles at Φ =1.2

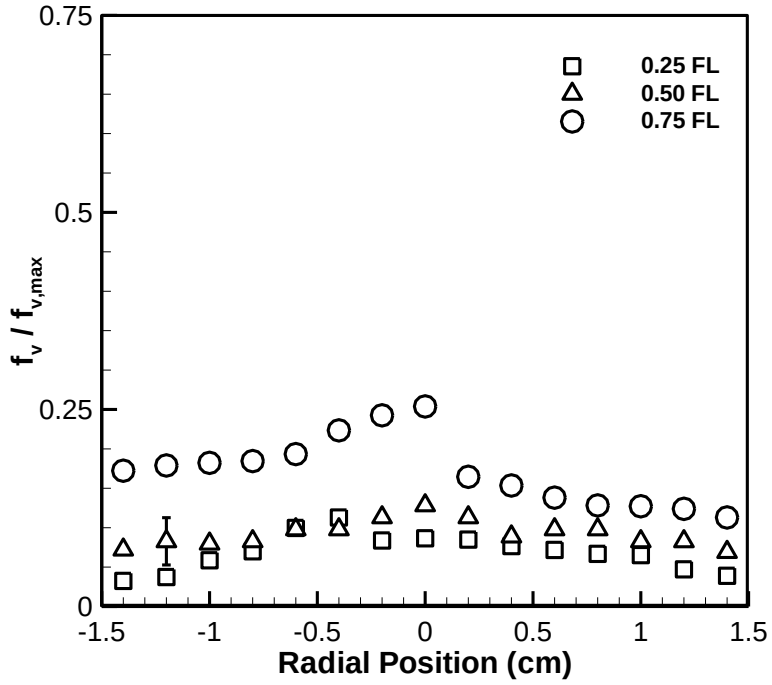

Fig. 166: SME B50 soot volume fraction profiles at Φ =2

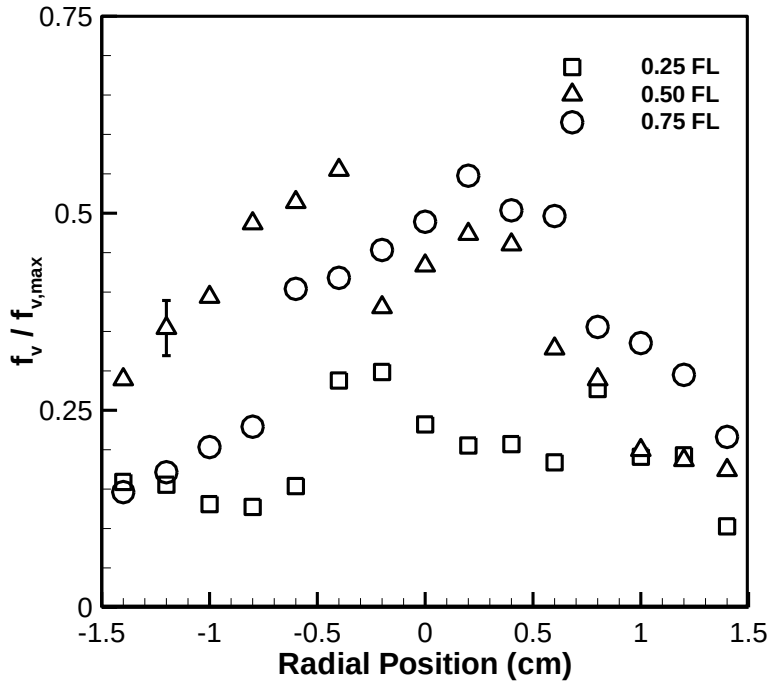

Fig. 167: SME B50 soot volume fraction profiles at Φ =3

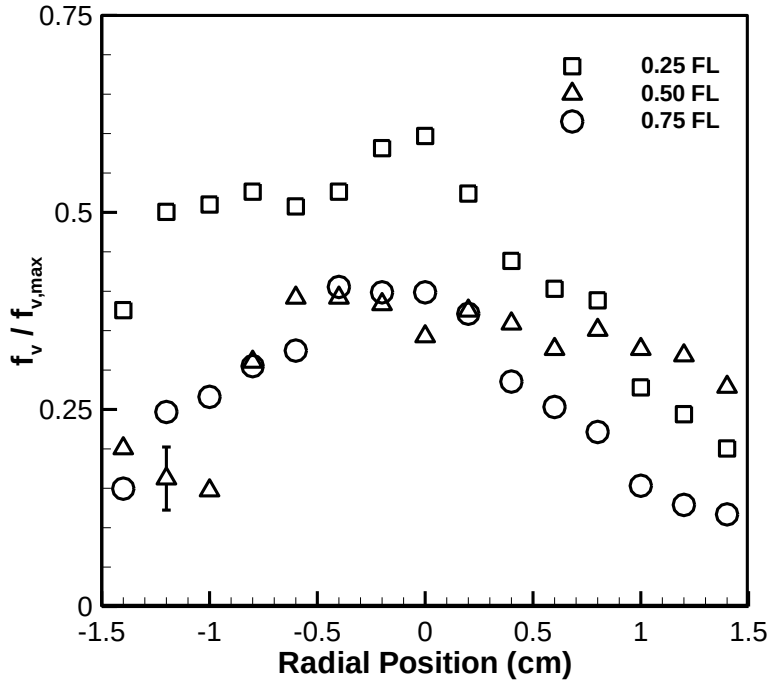

Fig. 168: SME B50 soot volume fraction profiles at Φ =7

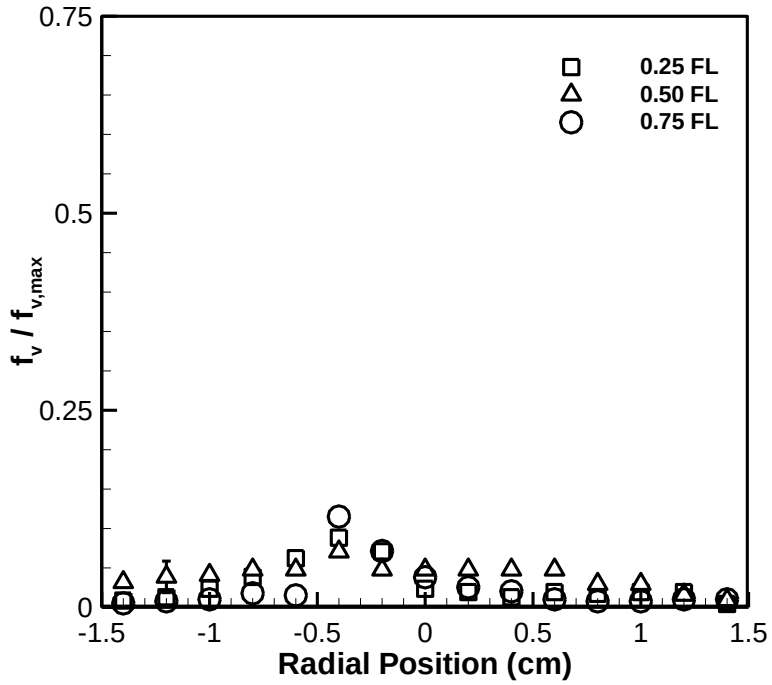

Fig. 169: SME B75 soot volume fraction profiles at Φ =1.2

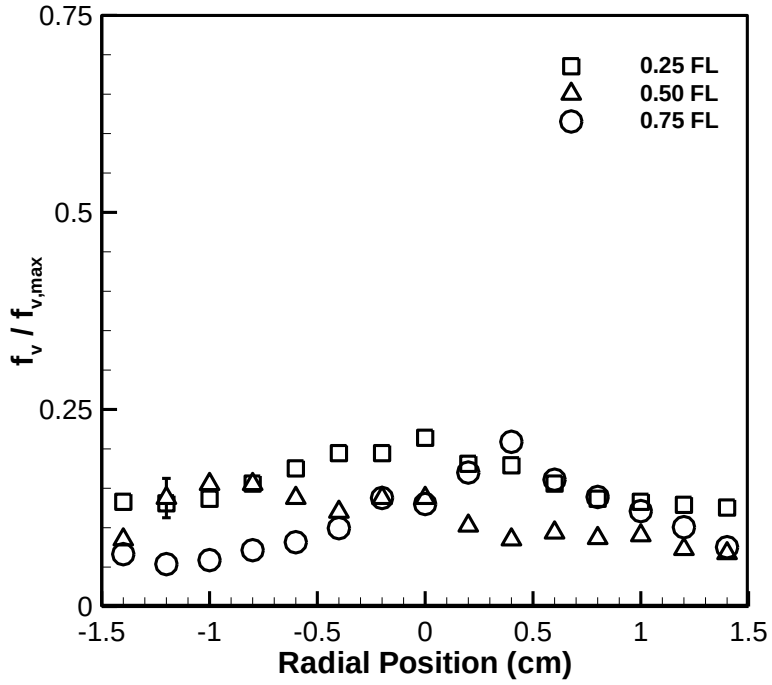

Fig. 170: SME B75 soot volume fraction profiles at Φ =2

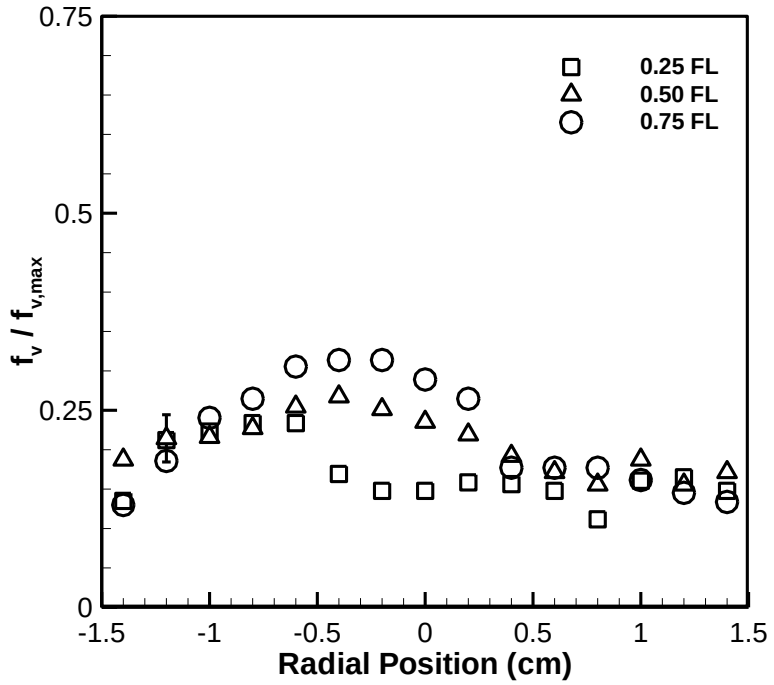

Fig. 171: SME B75 soot volume fraction profiles at Φ =3

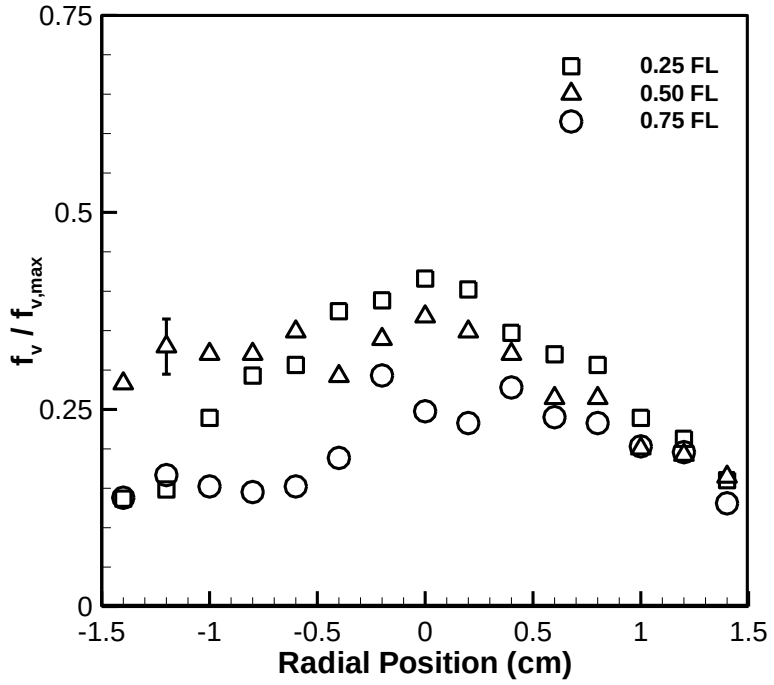

Fig. 172: SME B75 soot volume fraction profiles at Φ =7

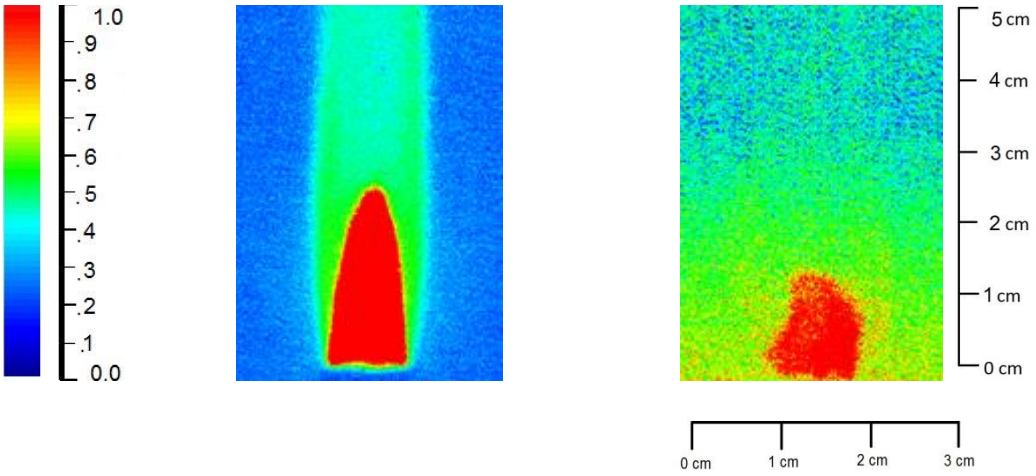

Φ=1.2 Φ=2

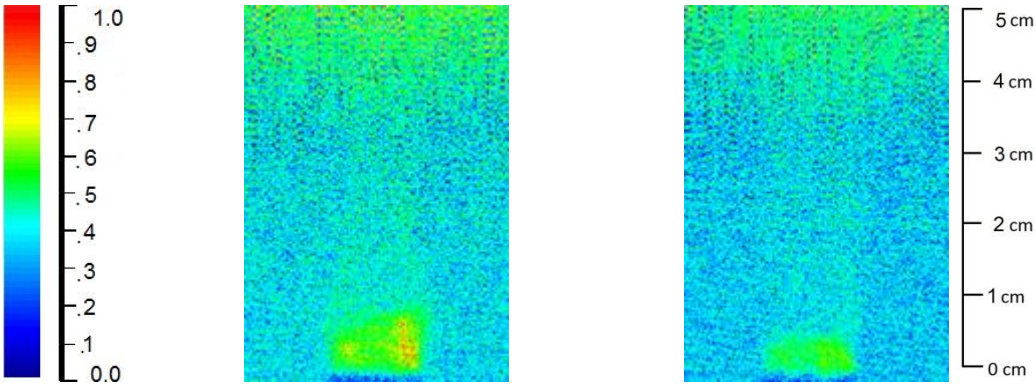

Φ=3 Φ=7

Fig. 173: Diesel OH PLIF images at varying equivalence ratios

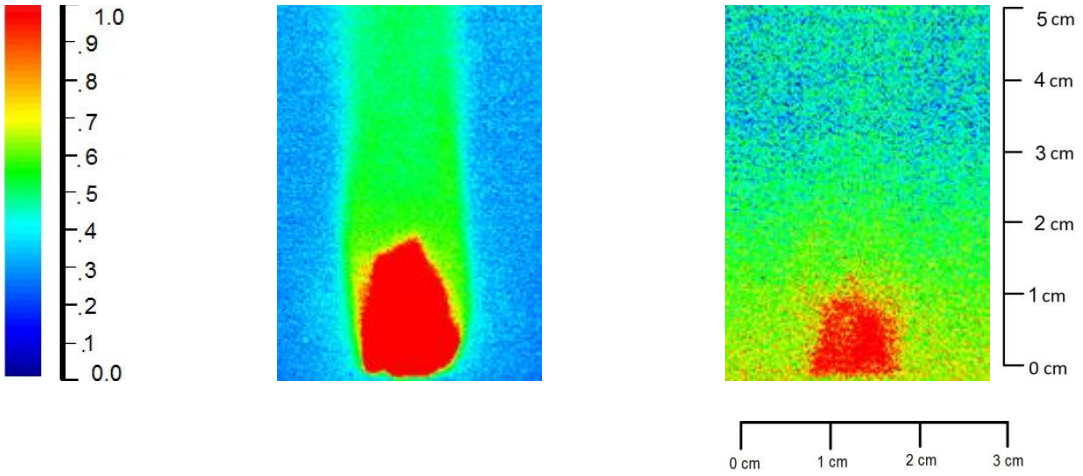

Φ=1.2 Φ=2

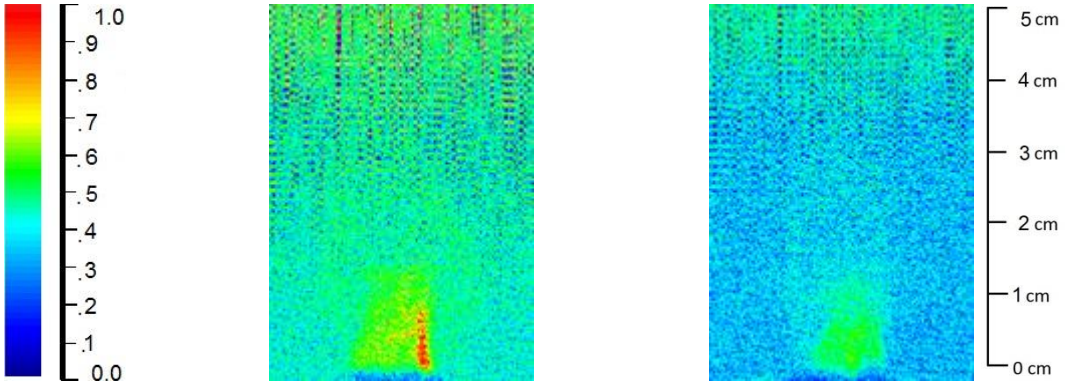

Φ=3 Φ=7

Fig. 174: CME B25 OH PLIF Images at varying equivalence ratios

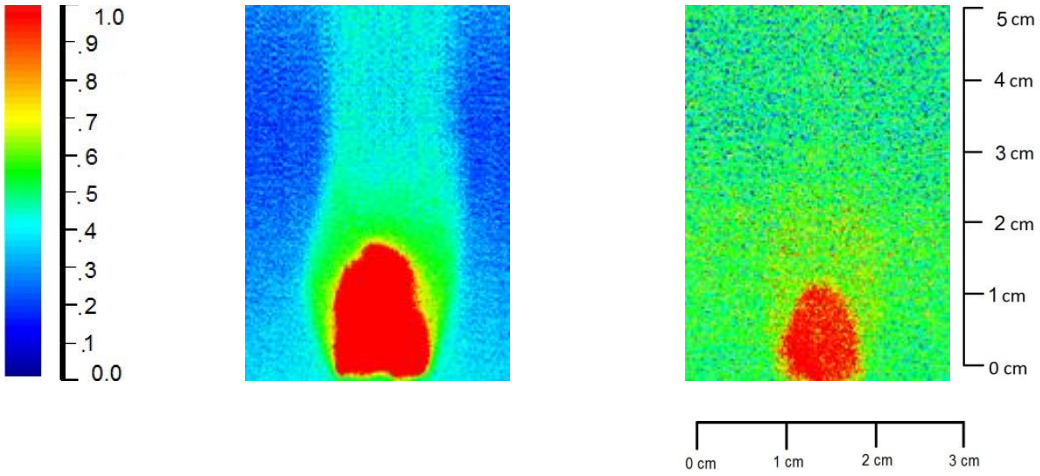

Φ=1.2 Φ=2

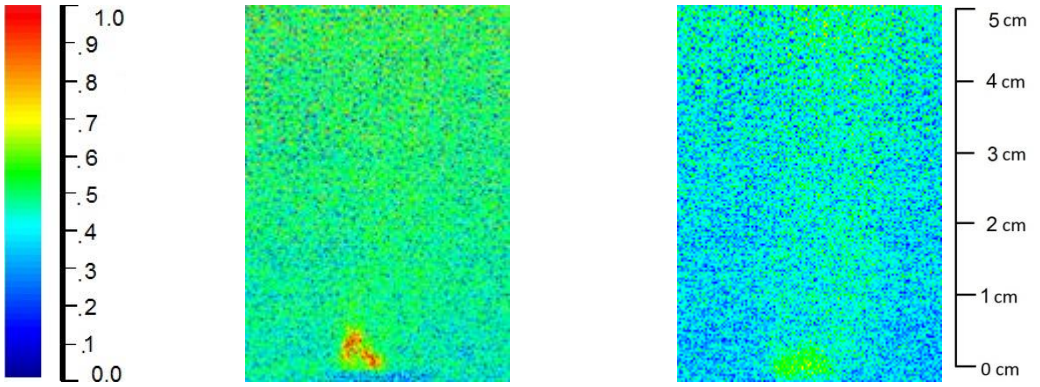

Φ=3 Φ=7

Fig. 175: CME B50 OH PLIF Images at varying equivalence ratios

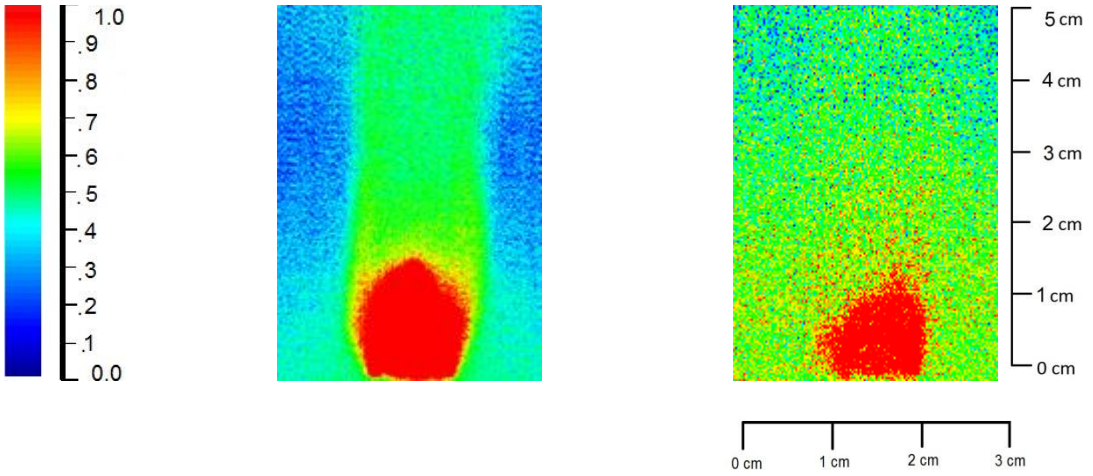

Φ=1.2 Φ=2

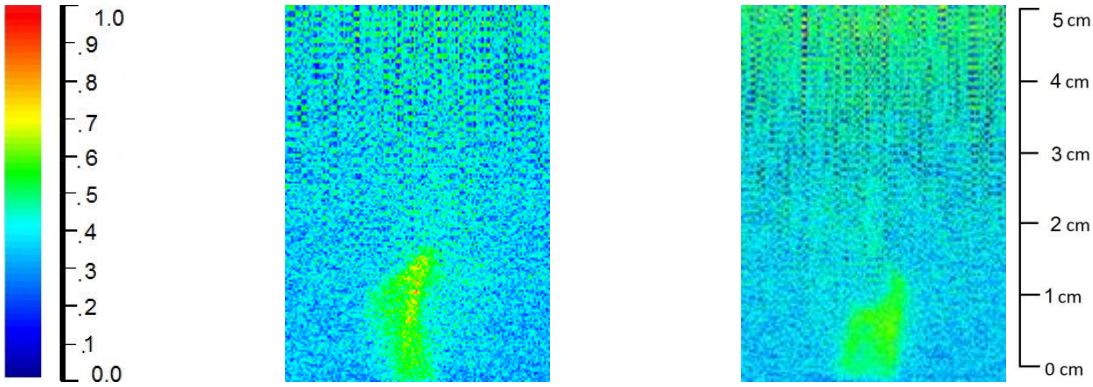

Φ=3 Φ=7

Fig. 176: CME B75 OH PLIF Images at varying equivalence ratios

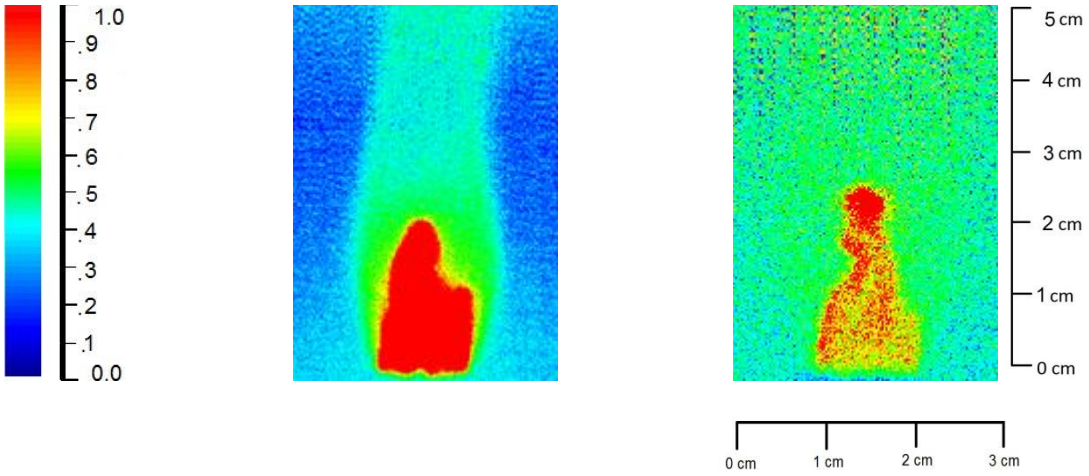

Φ=1.2 Φ=2

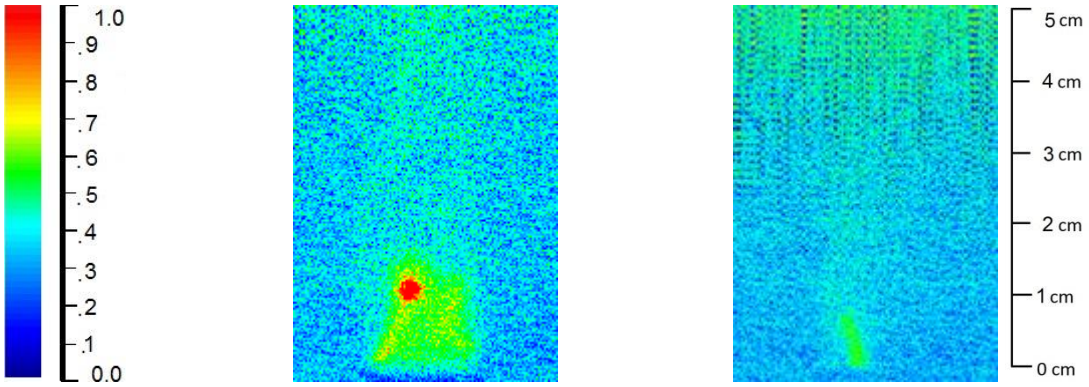

Φ=3 Φ=7

Fig. 177: SME B25 OH PLIF Images at varying equivalence ratios

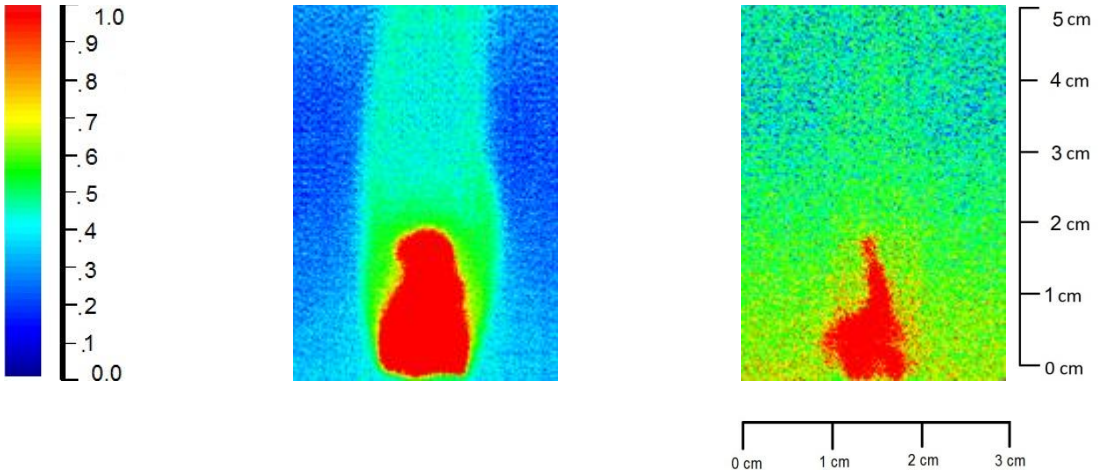

Φ=1.2 Φ=2

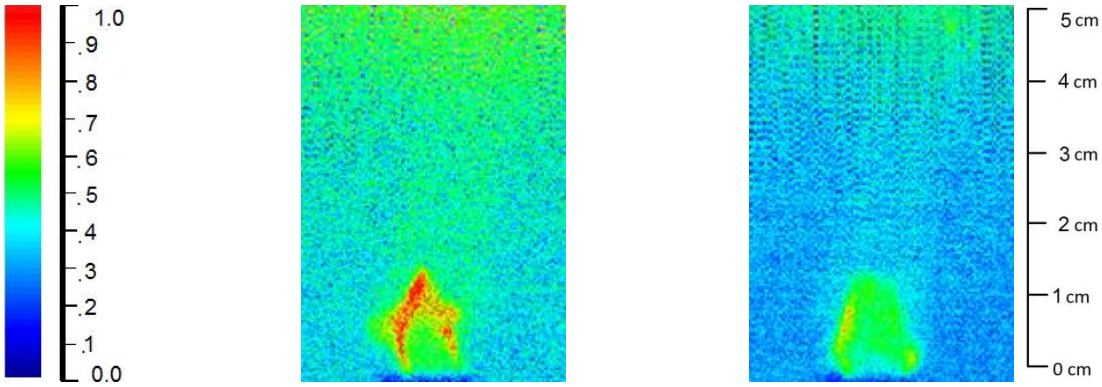

Φ=3 Φ=7

Fig: 178: SME B50 OH PLIF Images at varying equivalence ratios

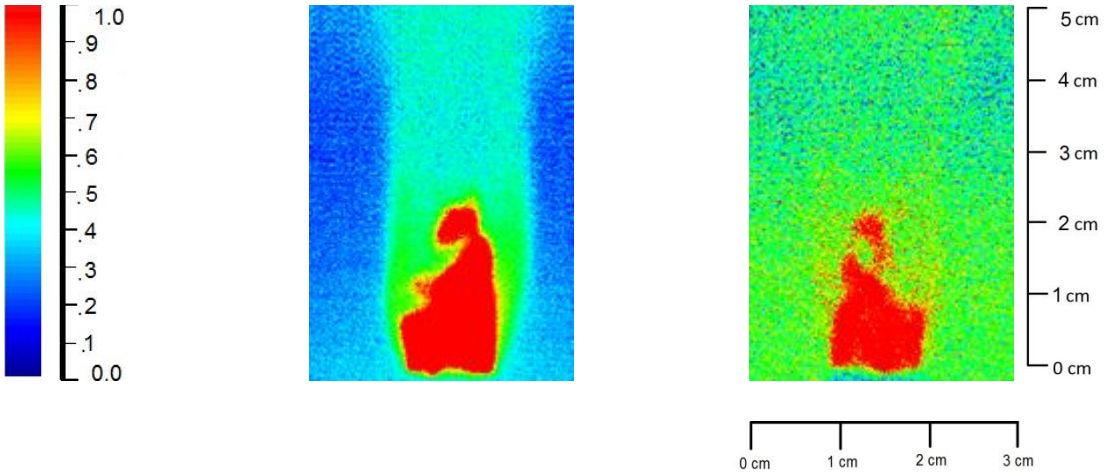

Φ=1.2 Φ=2

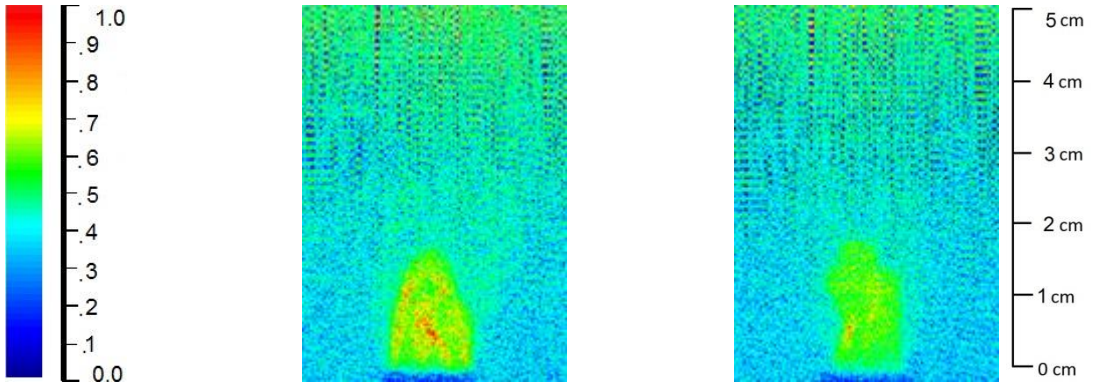

Φ=3 Φ=7

Fig. 179: SME B75 OH PLIF Images at varying equivalence ratios

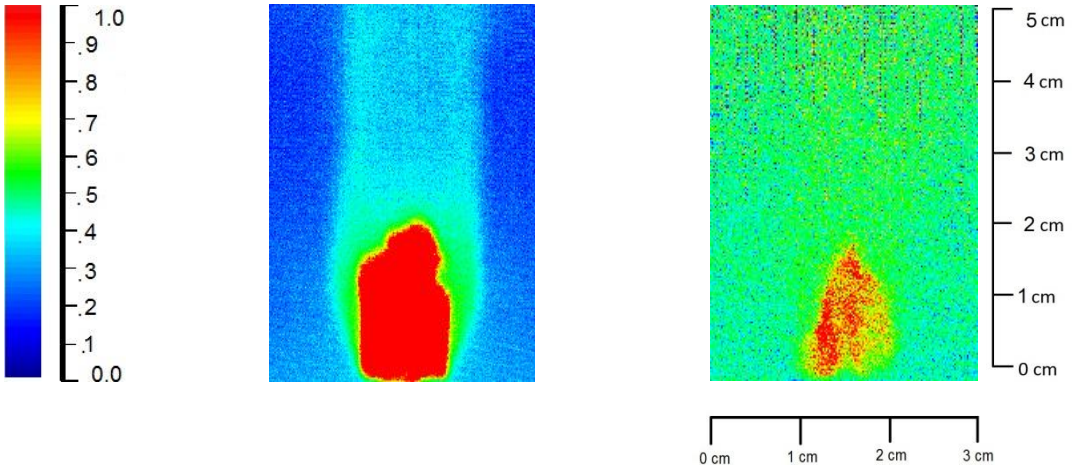

Φ=1.2 Φ=2

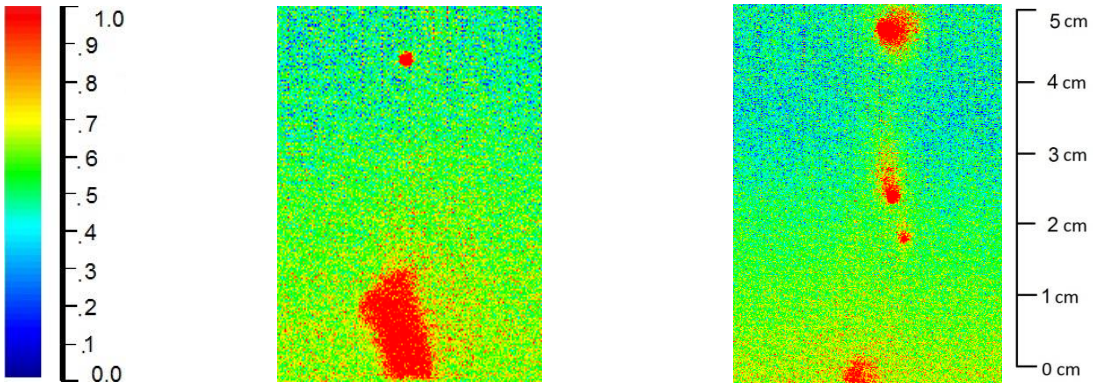

Φ=3 Φ=7

Fig. 180: Diesel CH PLIF Images at varying equivalence ratios

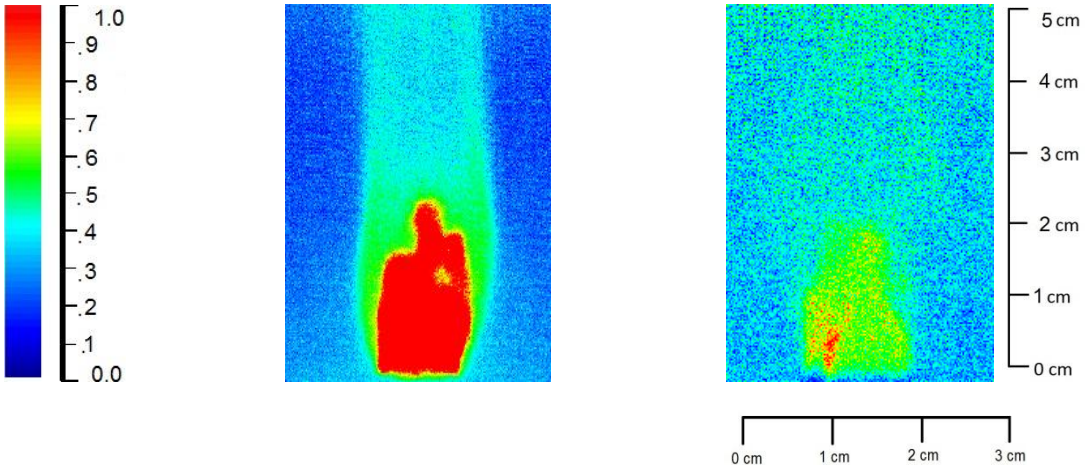

Φ=1.2 Φ=2

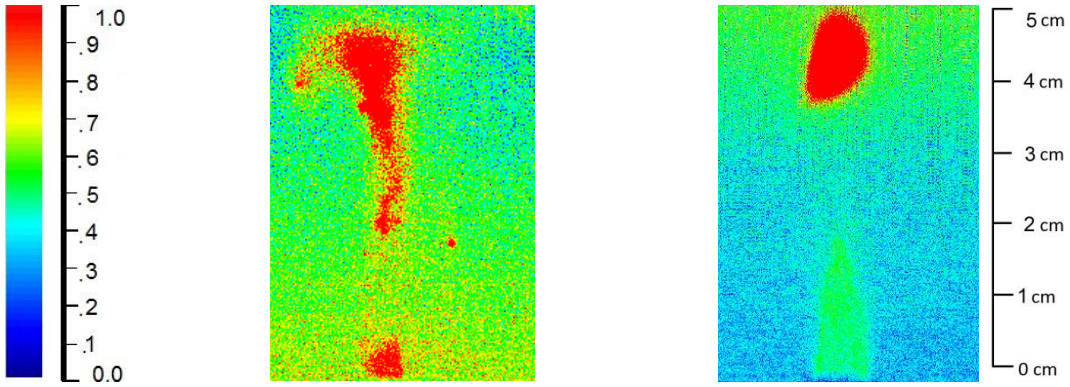

Φ=3 Φ=7

Fig. 181: CME B25 CH PLIF Images at varying equivalence ratios

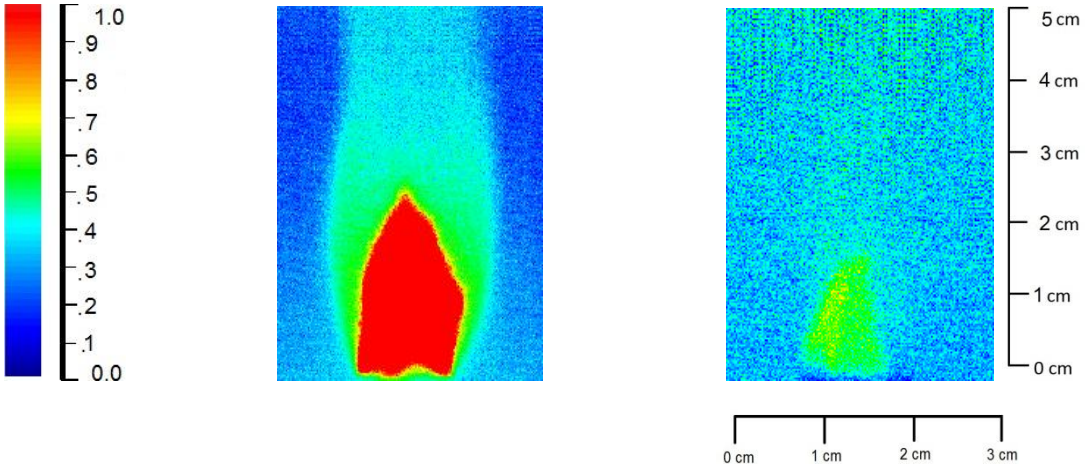

Φ=1.2 Φ=2

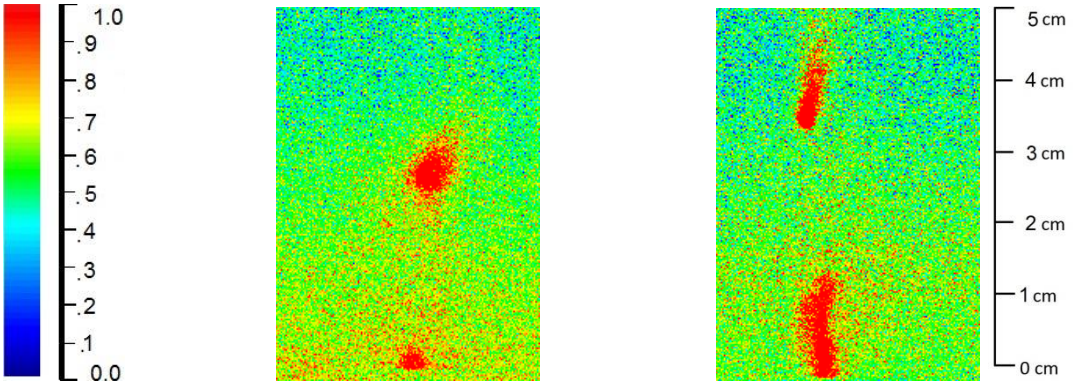

Φ=3 Φ=7

Fig. 182: CME B50 CH PLIF Images at varying equivalence ratios

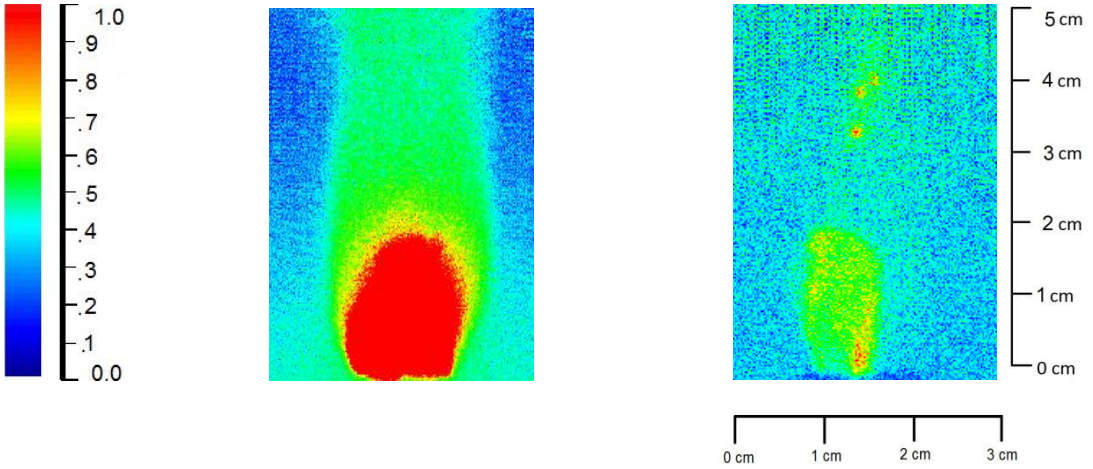

Φ=1.2 Φ=2

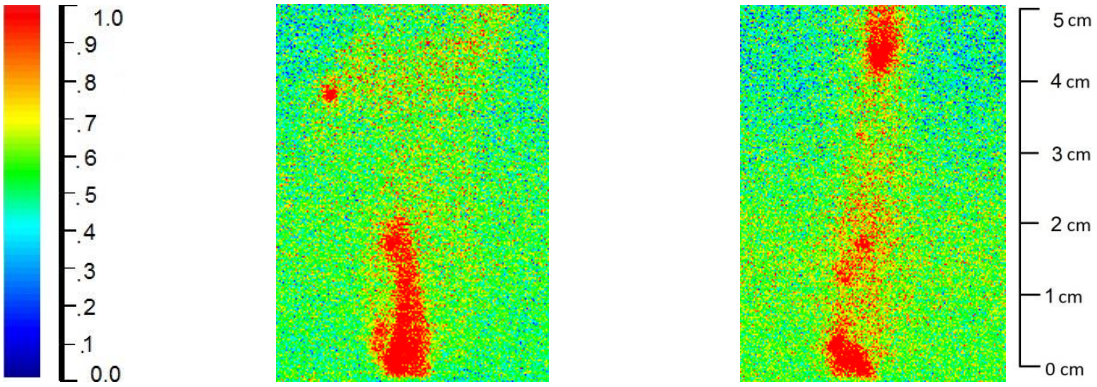

Φ=3 Φ=7

Fig. 183: CME B75 CH PLIF Images at varying equivalence ratios

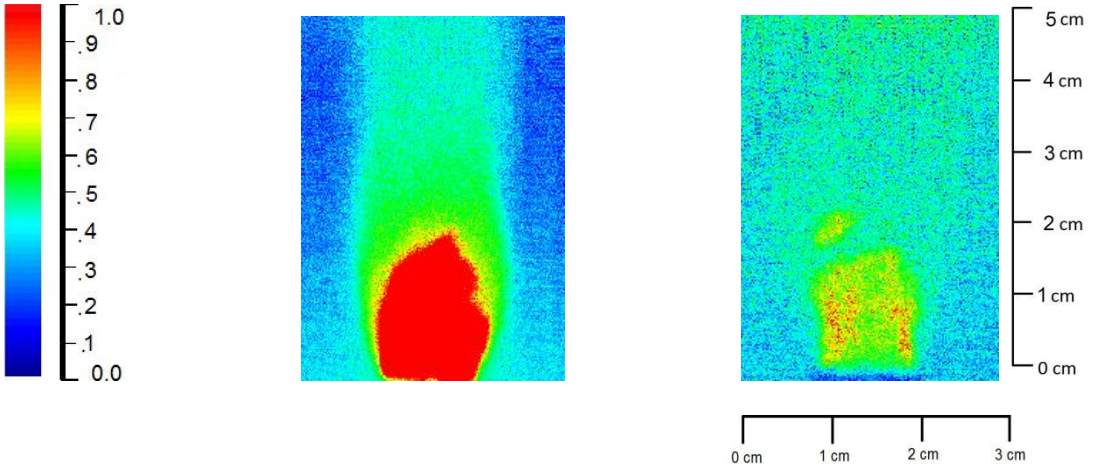

Φ=1.2 Φ=2

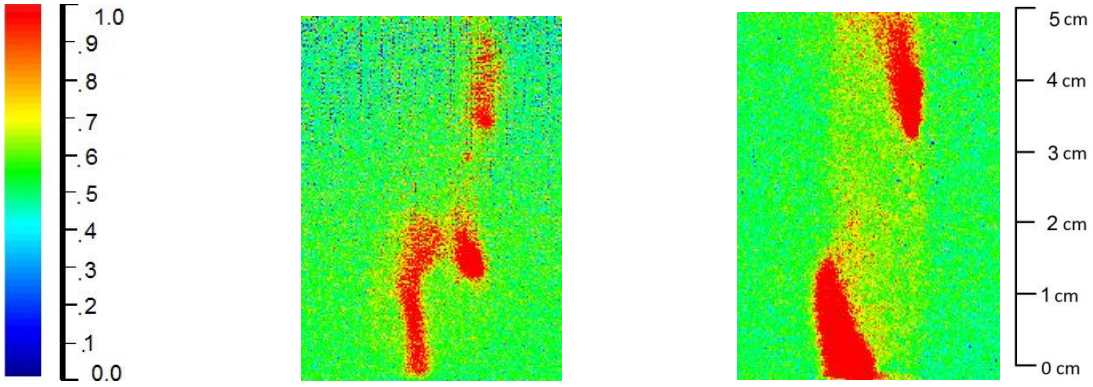

Φ=3 Φ=7

Fig. 184: SME B25 CH PLIF Images at varying equivalence ratios

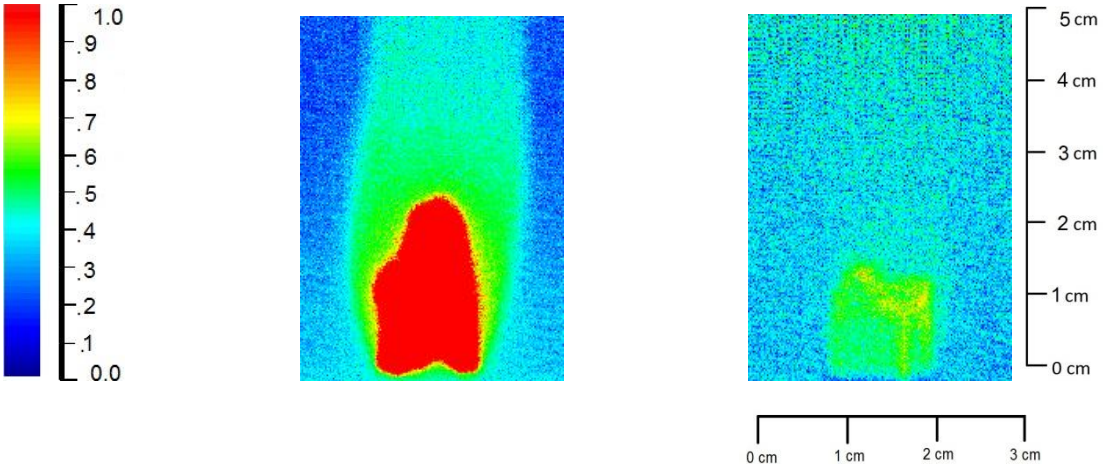

Φ=1.2 Φ=2

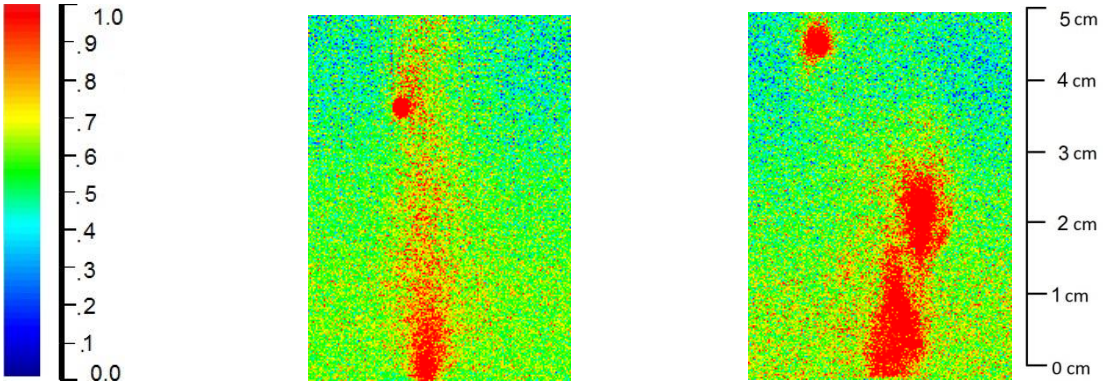

Φ=3 Φ=7

Fig. 185: SME B50 CH PLIF Images at varying equivalence ratios

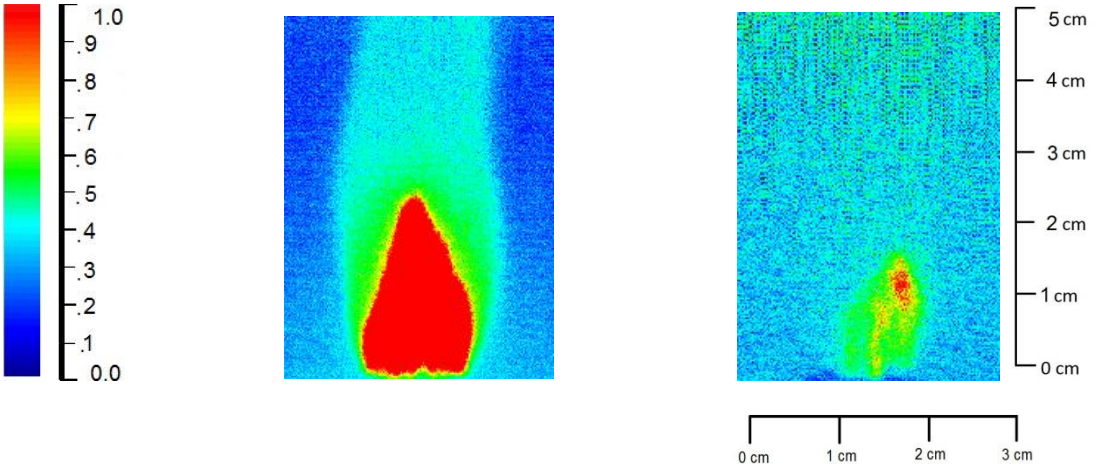

Φ=1.2 Φ=2

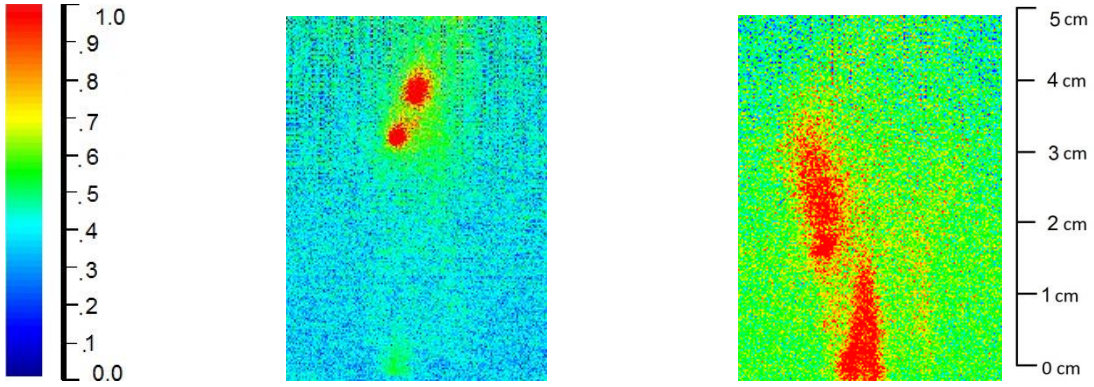

Φ=3 Φ=7

Fig. 186: SME B75 CH PLIF Images at varying equivalence ratios

Chapter 6
Computational Analysis

The purpose of the computational study was to establish a predictive method by which the combustion properties of diesel (n-heptane) and biodiesel (methyl decanoate) their blend (methyl decanoate + n-heptane) burning in a laminar flame could be documented at a fuel rich equivalence ratio and to further investigate the reasons for the observable increase in NO for biodiesel blends compared to diesel as documented in the experimental portion.

A 2-D model was used for computation of the laminar partially premixed flame because the flame was axisymmetric. The numerical analysis was conducted in a two-step approach, where-in the local fuel/air mixtures were calculated from the non-reacting jet in the first step and in the second step the local mixtures were used to determine the temperature and concentrations of CO, CO_2, O_2, and NO at each point using the CHEMKIN software package with the non-equilibrium combustion model.

The temperature, CO, CO_2, O_2, and NO concentrations were computed for laminar premixed flames of n-heptane, methyl decanoate and a blend of n-heptane and methyl decanoate. Computational fluid dynamics software FLUENT version 6.3.26, and GAMBIT version 2.3.16 and chemical kinetics software CHEMKIN version 4.1 were used and the results are presented in this chapter.

Reaction Models

There have been many studies on the detailed chemical kinetics of methyl esters. Most of these studies have been on methyl butanoate ($C_5H_{10}O_2$). The first detailed kinetic model for the oxidation of methyl butanoate was developed by Fischer et al. (2000). The model was validated against limited available experimental pressure data in closed vessels. Dooley et al. (2008) studied methyl butanoate reactions in shock tube and rapid compression machine. The authors made further modifications to the methyl butanoate reaction mechanism to reproduce their experimental data and also literature data from a stirred reactor, flow reactor, and opposed flow diffusion flame. These studies allowed clarifying the specific kinetic features due to the presence of the ester group.

The study of ignition delay times of methyl esters and biodiesel fuels droplets in microgravity showed that methyl butanoate was not a good surrogate for large methyl esters in biodiesel fuels. Methyl butanoate is much less reactive than soybean biodiesel whereas larger species such as methyl decanoate and methyl dodecanoate have about the same reactivity as biodiesel. In their Homogeneous charge compression ignition (HCCI) engine simulations of blends of soy-based biodiesel and ultra-low sulfur diesel, Szybist et al. (2008) speculated that the cetane number of methyl butanoate was too low to account for experimentally observed changes in burn duration and phasing when the biodiesel concentration was changed.

Hence, methyl decanoate was selected as the biodiesel surrogate in the current study. The methyl decanoate mechanism provides a realistic kinetic tool for simulation of biodiesel fuels (Herbinet et al., 2008). A blend surrogate model of methyl decanoate and n-heptane was one of the only few detailed reaction mechanisms for blended fuels

that were available during the study; therefore, this blend was selected as biodiesel blend surrogate. The methyl decanoate model was combined together with a model for the oxidation of n-heptane to obtain this blend surrogate model which was a better representation of biodiesel blends (methyl decanoate + n-heptane mechanism available here: https://www-pls.llnl.gov/?url=science_and_technology-chemistry-combustion-biodiesel). As a result, the n-heptane mechanism was selected to simulate diesel fuel, although other fuel mechanisms were available which would closely match the properties of diesel fuel. Experimental measurements were hence performed for n-heptane fuel to provide a reference to the computational values predicted by the n-heptane model. The experimental values for n-heptane fuel are presented in Figures 189 to 203.

Model Assumptions

To simplify the complexities involved in obtaining the solution of the modeling equations, the following assumptions were made:

1. Single component fuels, methyl decanoate ($C_{11}H_{22}O_2$) for biodiesel and n-heptane (C_7H_{16}) for diesel, were assumed to avoid multi-component effects.
2. The computational domain was assumed to be symmetric about the injector axis.
3. Heat transfer from the heated fuel-air jet and burner tip was neglected. The radiative losses from the flame in the combustion model were also neglected.
4. The fuel was above the boiling point of both fuels and assumed to be completely in vapor form.

Continuity and Momentum Equations

In this study, the Computational fluid dynamics software FLUENT was used to solve conservation equations for mass and momentum. For flows involving heat transfer or compressibility, an additional equation for energy conservation was solved. For flows involving species mixing or reactions, a species conservation equation was solved. The combustion model solved conservation equations for the mixture fraction.

The continuity equation was expressed as

$$\nabla \cdot \left(\rho \vec{v}\right) = 0 \qquad [6.1]$$

and the momentum equation was

$$\nabla \cdot \left(\rho \vec{v} \vec{v}\right) = -\nabla P + \nabla \cdot \left(\bar{\tau}\right) + \rho \vec{g} \qquad [6.2]$$

where P was the static pressure and $\bar{\tau}$ is the stress tensor term. $\rho \vec{g}$ was the gravitational body force. In this study, the gravity was only in the z direction.

Energy Equation

Flows in this study also involved heat transfer thus required additional equations for energy conservation. Equation (6.3) shows the energy equation used for this purpose where the dissipation due to viscosity was assumed small.

$$\frac{\partial}{\partial x_i}\left[u_i\left(\rho E + P\right)\right] = \frac{\partial}{\partial x_j}\left(k\frac{\partial T}{\partial x_j}\right) \qquad [6.3]$$

Here k is the thermal conductivity, T is the temperature, and E is defined in Eq. (6.3) as:

$$E = h - \frac{P}{\rho} + \frac{\upsilon^2}{2} \qquad [6.4]$$

Species Transport Equation

Further, since flows in this study involved species mixing the species conservation equation was also solved, Eq. (6.6) and Eq. (6.7).

$$\nabla \cdot \left(\rho \vec{\upsilon} Y_i\right) = -\nabla \cdot \vec{J}_i \qquad [6.6]$$

$$\vec{J}_i = -\sum_{j=1}^{N_o - 1} \rho D_{ij} \nabla Y_j \qquad [6.7]$$

where D_{ij} is the binary mass diffusion coefficient in the mixture, N_o is the number of chemical species, and Y_i is the mass fraction of species i.

Grid Development

A schematic diagram of the computational domain with boundary conditions can be seen in Fig. 187(a). The grid was generated using the Computational fluid dynamics software GAMBIT version 2.3.16. The grid extended to 1.5 m in the axial direction and 0.05 m in the radial direction. This included the burner section (0.00475 m radial and 0.475 m axial distance) which had an initial section prior to the outlet that was sufficiently long for fully developed flow to occur (50 diameters). The axisymmetric computational domain was aligned along the center of the burner. The grid had 52500 quadrilateral cells, 54051 nodes and 106550 faces. To reduce the computational time, a very coarse mesh was initially created (4 cells/cm in the axial and radial direction). After the solution was obtained, the grid was refined (20 cells/cm in the axial and radial direction) and tested again. As the results from the refined grid and the coarse grid were within 5%, it was determined that the solution was independent of the grid resolution. Temperature profiles for different grid variations for n-heptane/air are shown at near-burner location in Fig. 187(b).

Model Definition:

The CHEMKIN file (.inp) and thermodynamics data file (.db) for the three fuels were imported into FLUENT. The reaction rates were determined by Arrhenius expressions.

The strong temperature and composition dependence of the specific heat had a significant impact on the predicted flame temperature. Hence, the specific heat, thermal conductivity, viscosity and mass diffusivity were computed using the local mass-fraction weighted average of all the species.

The default under-relaxation parameters in FLUENT were set to high values. For a combustion model, it was necessary to reduce the under-relaxation to stabilize the solution. Some experimentation is typically necessary to establish the optimal under-relaxation. For this study, it was sufficient to reduce the species under-relaxation to 0.95 (FLUENT 6.3, 2006). Calculations for NO were performed assuming thermal mechanism in the model, for all the equivalence ratios. For equivalence ratios of 1.2, NO was calculated by both, the thermal and prompt mechanisms and has been presented in the results section.

Results and Discussion

The results for the n-heptane/air, methyl decanoate/air and methyl decanoate+n-heptane/air jets are presented in Figures 189 to 323 for three flame lengths respectively. The numerical values for methyl decanoate and methyl decanoate+n-heptane model were compared with experimental values for CME B100 and CME B50 fuel respectively. The model described above performed relatively well for the premixed laminar flames. Results include in-flame concentration profiles for O_2, CO_2, NO and CO and temperature profiles for the three fuel/air jets. Temperature, CO, CO_2, NO and O_2 concentrations showed trends that were in agreement with experimental data for all three fuels.

Profiles of the species concentration were modeled, calculated and are presented at three locations downstream of the injector exit, corresponding to 0.25FL, 0.5FL and 0.75FL where FL is the visible flame length acquired from the experimental measurements.

(a.) N-heptane model results:

At Φ = 1.2, for all three locations the modeled values were similar to the measured quantities for temperature, oxygen and carbon dioxide profiles except for carbon monoxide and nitric oxide profiles where the measured values were consistently higher, although within experimental uncertainties. Experimental data for heptane was used for comparison. The numerical results for carbon dioxide and nitric oxide profiles showed that the flames were narrower than the experimental results. This observation was mainly caused by the assumption of rapid reaction in the equilibrium model. In the

Sivathanu and Faeth (1990) study, the numerical data based on the equilibrium model departed from the experimental results when the stoichiometric ratio was not close or equal to unity. At the region of 0.75 FL, the numerical temperature results were lower than experimental results.

Furthermore, the model assumed an adiabatic flame condition. As a result, the radiative heat loss by the soot particles in the experimental flame was not accounted for in the computation, which resulted in higher computed flame temperature in high soot regions. The overestimation of the temperature caused the overestimation of CO_2 at 0.25 FL and 0.50 FL of the flame length.

O_2 results matched well with the experimental results, at all three locations. The concentration of O_2 in the numerical calculation was more diffusion dependent, rather than temperature dependent likes the CO and CO_2. Hence, the O_2 concentration results were well matched with the experimental results.

The numerical results of CO concentration showed an overestimation of CO. Although the predicted values of CO were larger the measured quantities, trends of the numerical values and measured quantities were similar. Since, the model did account for soot in the flame, there was an excess of carbon in carbon-contained species.

At 0.25FL and 0.50FL, the numerical results for NO (modeled for thermal NO condition) were slightly higher for n-heptane compared to the experimental results, although both values showed the same trend. The numerical results for NO also showed similar region of peak and trend when compared with numerical temperature values with the exception in the far burner region where temperature values were lower;

although the data were within experimental uncertainties. Hence thermal mechanism can be attributed for NO production at this condition. Peak values were observed from NO concentration and temperature profiles near the flame boundaries where local equivalence ratios were near unity.

At this condition, NO values were also modeled using the prompt NO condition, which predicted values very close to experimental values at the far-burner location, but did not correspond with the experimental results at the near-burner and mid-burner locations.

As the equivalence ratio was increased to 2 and 3, numerical profiles were again in trend with the experimental values for all the three locations.

Oxygen numerical values were consistently higher than experimental values for all three locations at these conditions. On the other hand, carbon dioxide numerical values were consistently lower than the experimental values.

(b.) Methyl decanoate model results:

For the results of the methyl decanoate model, the experimental data for CME B100 was used for comparison. At $\Phi = 1.2$ the numerical temperature values in the methyl decanoate model were lower than the measured values for all three locations. This was due to the effects of radiative losses particularly due to soot combustion from the flame which were not accounted for in the numerical model. While performing experiments the heat released from the flame radiation resulted in higher temperatures being measured as compared to numerical values.

Numerical values for CO_2 followed the same trend as the experimental results, but were lower than the experimental data consistently at all locations. The lower values for CO_2 numerical data can be attributed to the model assumption, where residence time and soot history were not considered in the model.

Numerical values for NO, though slightly higher than the experimental data, followed similar trend with experimental data. At all three locations NO numerical values peaked in same region as numerical values for temperature. Similar behavior was observed in experimental results for CME B100. Hence Zeldovich thermal mechanism can be held responsible for NO production for this condition.

The predicted values of NO, when modeled under the prompt NO condition, did not correlate well with the experimentally measured data as seen in Figs. 213-215. In the far-burner location, the predicted values agreed well with experimental data.

CO numerical values matched very closely to the experimental values and followed the same trend as the experimental values.

As the equivalence ratio was increased to 2 and 3, numerical profiles were again in trend with the experimental values for all the three locations. The predicted temperature values were lower than the predicted temperature values at $\Phi = 1.2$. On the other hand, the predicted values of CO were higher than the CO values at $\Phi = 1.2$. This is consistent with the experimental findings.

(c.) Methyl decanoate+n-heptane results:

Methyl decanoate+n-heptane model predicted lower temperature and carbon dioxide values for all three locations when compared with experimental values for CME

B50 fuel. Again, the model followed similar trends as compared to experimental data for temperature as well as species profiles. On other hand the model predicted higher values for NO and CO when compared with experimental data. NO values peaked in line with the numerical temperature values, confirming thermal mechanism as the cause for NO production at this condition.

In conclusion, the numerical model for the combustion of laminar flames of n-heptane, methyl decanoate and their blend was successfully developed. From the comparison, the experimental and numerical temperature and O_2 concentration profiles showed good agreement in most cases. Model predictions for the CO concentration compared to the experimental results for all fuel mechanisms were within experimental uncertainties. All the results showed that the flame predicted by the computational model was shorter and narrower than the experimental flame. This was mainly due to the rapid reaction assumption and the presence of soot in the experimental flame. Based on the numerical results, NO production can be attributed to the thermal mechanism at this condition.

Boundary Conditions/Input Parameters

Table 5 (a): Boundary Conditions (Heptane Mechanism, C_7H_{16})

Outflow Boundaries	
Pressure Outlet	
Gauge Pressure (Pa)	0
Backflow Total Temperature (K)	300
Backflow Direction Specification Method	Normal to Boundary
Species Mass Fractions	C_7H_{16} = 0 O_2 = 0.23 N_2= 0.77
Inlet	
Velocity Inlet	
Velocity Specification Method	Magnitude, Normal to Boundary
Reference Frame	Absolute
Velocity Magnitude (m/s)	7
Temperature (K)	700
Species Mass Fractions	C_7H_{16} = 0.06 O_2 = 0.22 N_2= 0.71
Burner Top and Side	
Wall	
Wall Motion	Stationary
Shear Condition	No Slip
Heat Flux (W/m^2)	0
Heat Generation (W/m^3)	0
Species	Zero Diffusive Flux
Symmetry	
Axis	

Table 5(b): Boundary Conditions (Methyl Decanoate Mechanism, $C_{11}H_{22}O_2$)

Outflow Boundaries	
Pressure Outlet	
Gauge Pressure (Pa)	0
Backflow Total Temperature (K)	300
Backflow Direction Specification Method	Normal to Boundary
Species Mass Fractions	$C_{11}H_{22}O_2 = 0$ $O_2 = 0.23$ $N_2 = 0.77$
Inlet	
Velocity Inlet	
Velocity Specification Method	Magnitude, Normal to Boundary
Reference Frame	Absolute
Velocity Magnitude (m/s)	7
Temperature (K)	700
Species Mass Fractions	$C_{11}H_{22}O_2 = 0.08$ $O_2 = 0.21$ $N_2 = 0.71$
Burner Top and Side	
Wall	
Wall Motion	Stationary
Shear Condition	No Slip
Heat Flux (W/m^2)	0
Heat Generation (W/m^3)	0
Species	Zero Diffusive Flux
Symmetry	
Axis	

Table 5(c): Boundary Conditions (Methyl Decanoate+n-Heptane Mechanism)

Outflow Boundaries	
Pressure Outlet	
Gauge Pressure (Pa)	0
Backflow Total Temperature (K)	300
Backflow Direction Specification Method	Normal to Boundary
Species Mass Fractions	$C_9H_{19}O = 0$ $O_2 = 0.23$ $N_2 = 0.77$
Inlet	
Velocity Inlet	
Velocity Specification Method	Magnitude, Normal to Boundary
Reference Frame	Absolute
Velocity Magnitude (m/s)	7
Temperature (K)	700
Species Mass Fractions	$C_9H_{19}O = 0.07$ $O_2 = 0.21$ $N_2 = 0.72$
Burner Top and Side	
Wall	
Wall Motion	Stationary
Shear Condition	No Slip
Heat Flux (W/m^2)	0
Heat Generation (W/m^3)	0
Species	Zero Diffusive Flux
Symmetry	
Axis	

As the computational grid replicated the experimental burner, the jet velocity at the inlet was determined by considering the mass flow rate and the density of the fuel and air mixture from the experimental calculations. A sample calculation for the burner jet velocity has been shown in Appendix A.

Table 6(a): Material properties for fuel air mixture for n-heptane @ Temperature = 700K

Inlet A/F Ratio by Mass (Φ = 1.2)	12.59
Thermal Conductivity (W/m-K)	0.126
Viscosity (kg/m-s)	3.76e-04
Mass Diffusivity (m^2/s)	6.54e-06
Density (kg/m^3)	Ideal Gas
Cp (J/kg-K)	Mixing-Law

Table 6(b): Material properties for fuel air mixture for methyl decanoate @ Temperature = 700K

Inlet A/F Ratio by Mass (Φ = 1.2)	9.54
Thermal Conductivity (W/m-K)	0.126
Viscosity (kg/m-s)	4.00e-04
Mass Diffusivity (m^2/s)	6.54e-06
Density (kg/m^3)	Ideal Gas
Cp (J/kg-K)	Mixing-Law

Table 6(c): Material properties for fuel air mixture for methyl decanoate+n-heptane @ Temperature = 700K

Inlet A/F Ratio by Mass ($\Phi = 1.2$)	11
Thermal Conductivity (W/m-K)	0.126
Viscosity (kg/m-s)	3.88e-04
Mass Diffusivity (m^2/s)	6.54e-06
Density (kg/m^3)	Ideal Gas
Cp (J/kg-K)	Mixing-Law

Table 7: Under - Relaxation Parameters

Pressure	0.3
Density	1
Body Forces	1
Momentum	0.7
C_7H_{16}	0.95
O_2	0.95
Energy	1

Table 8: Discretization Methods

Pressure	Standard
Momentum	First Order Upwind
C_7H_{16}	First Order Upwind
O_2	First Order Upwind
Energy	First Order Upwind

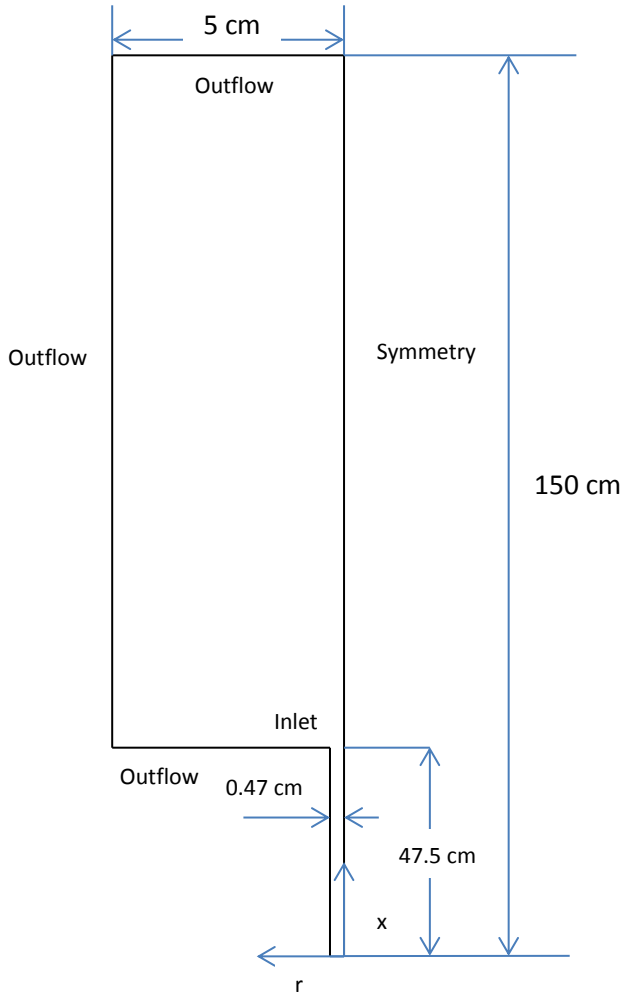

Fig. 187(a): Schematic drawing of the computational domain

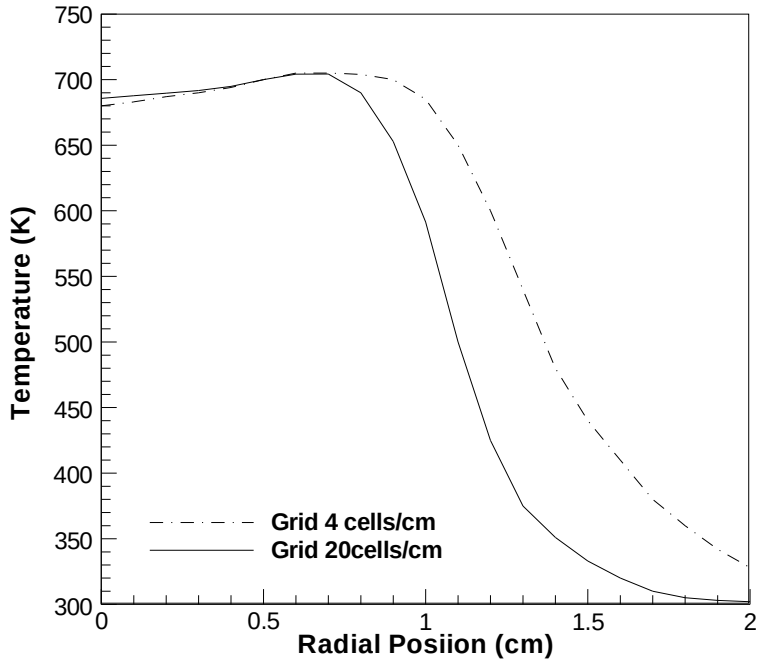

Fig. 187 (b): Temperature variation with grid size at near-burner location (x = 0.024 m) for n-heptane/air

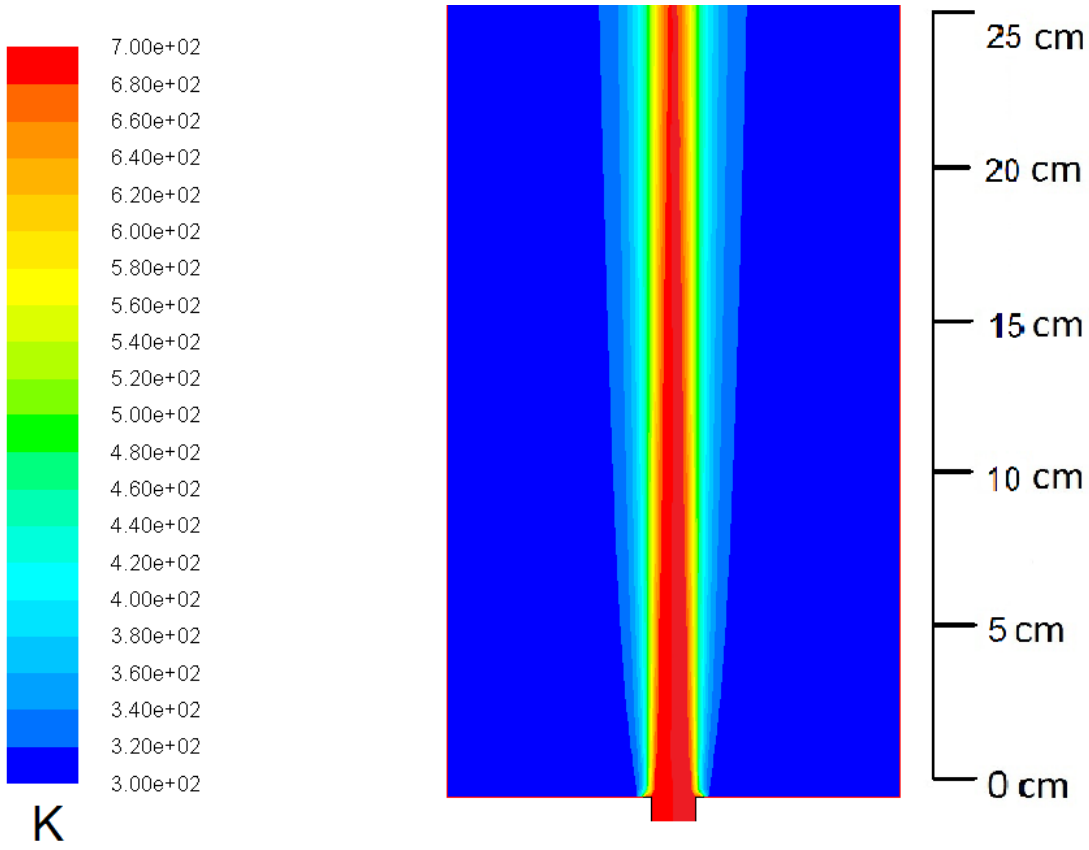

Fig.188 (a): Temperature distributions for n-heptane heated fuel/air jets in region of interest up to 25 cm above injector exit

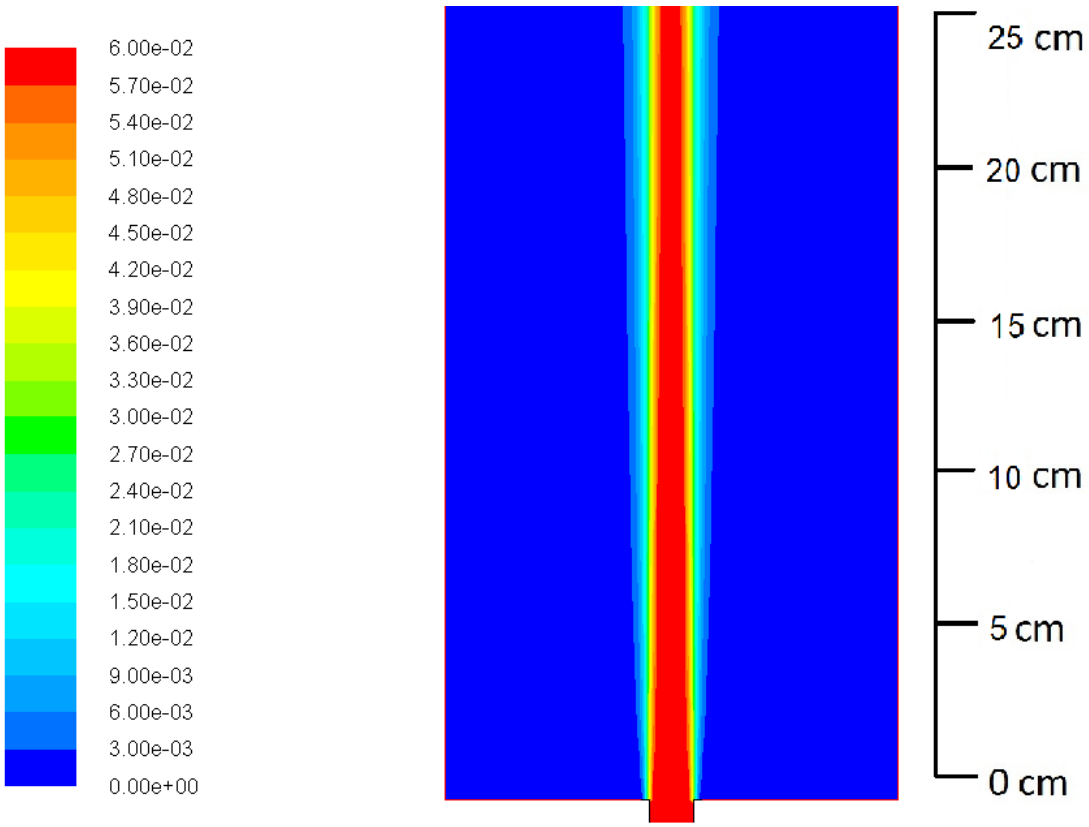

Fig. 188 (b) Mass fraction of n-heptane in heated fuel/air jets in region of interest up to 25 cm above injector exit

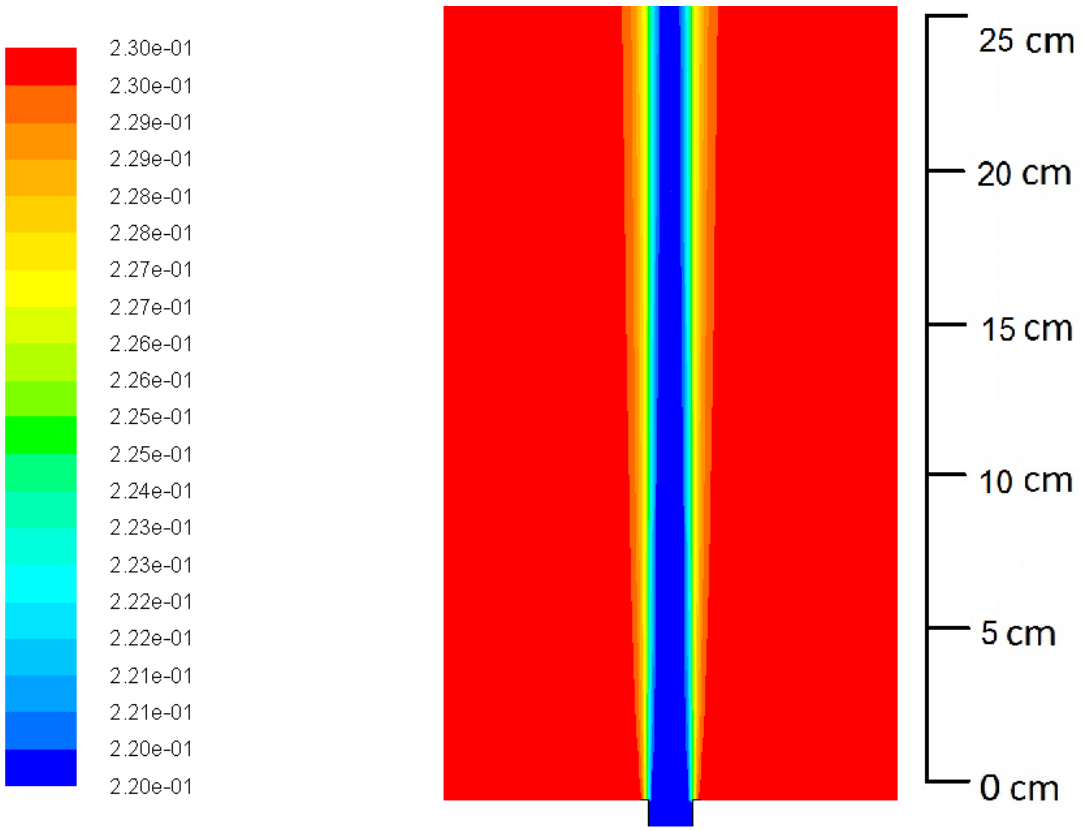

Fig. 188 (c) Mass fraction of O_2 in heated fuel/air jets in region of interest up to 25 cm above injector exit

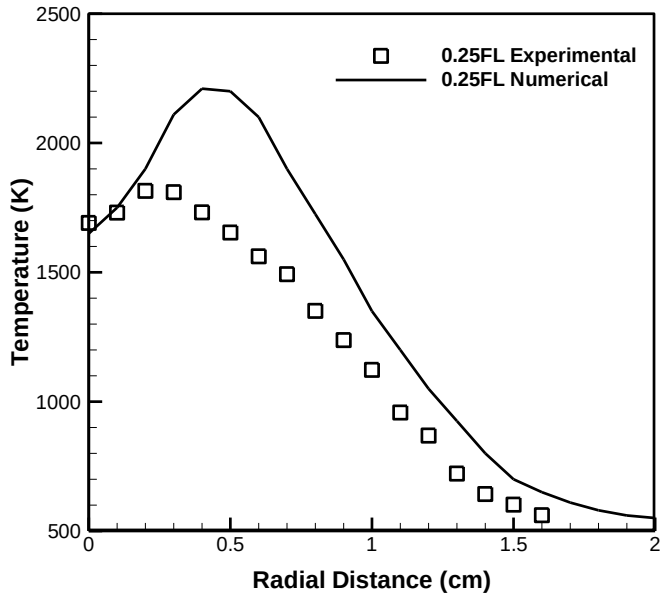

Fig. 189: Temperature profiles for n – heptane flame at 0.25 FL at Φ=1.2

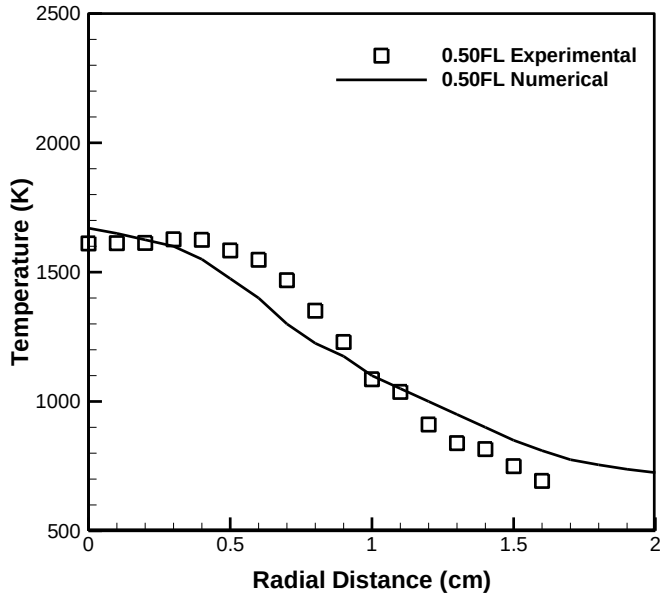

Fig. 190: Temperature profiles for n – heptane flame at 0.50 FL at Φ=1.2

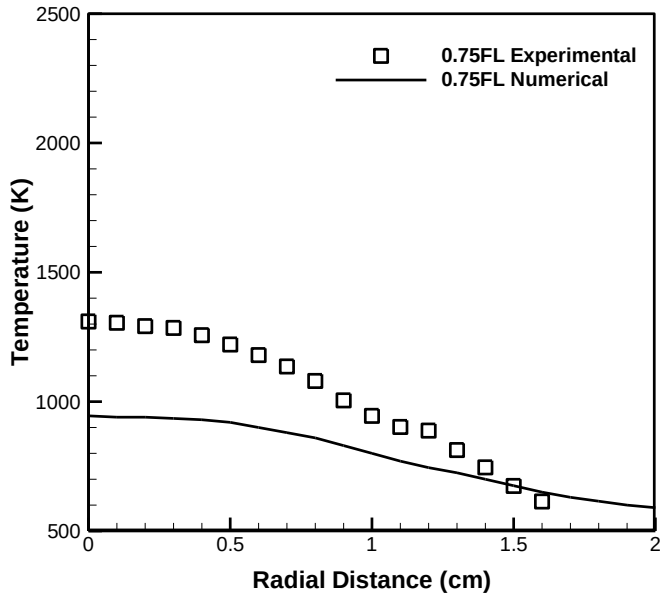

Fig. 191: Temperature profiles for n – heptane flame at 0.75 FL at Φ=1.2

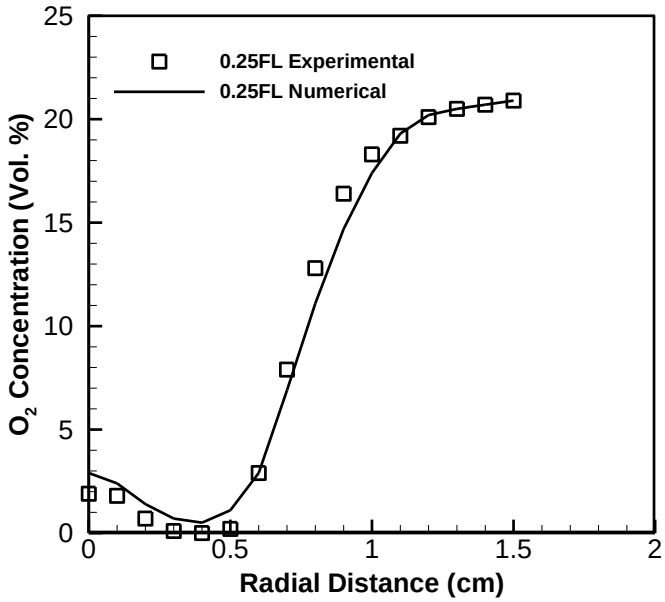

Fig. 192: O_2 concentration profiles for n – heptane flame at 0.25 FL at Φ=1.2

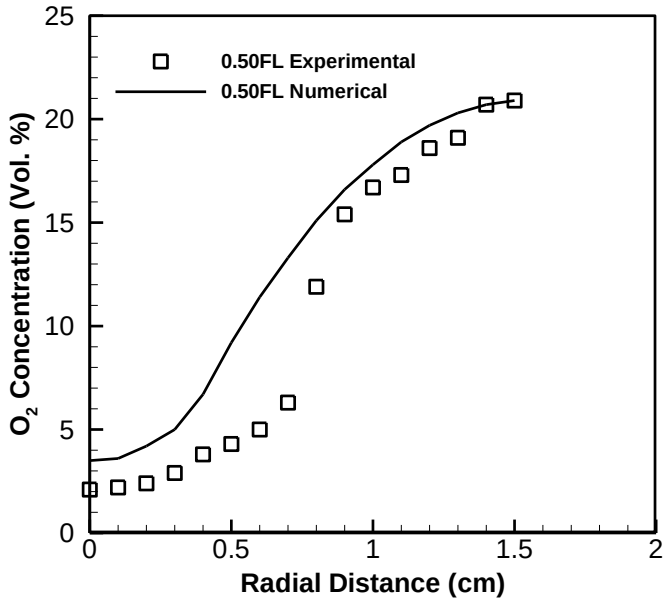

Fig. 193: O_2 concentration profiles for n – heptane flame at 0.50 FL at Φ=1.2

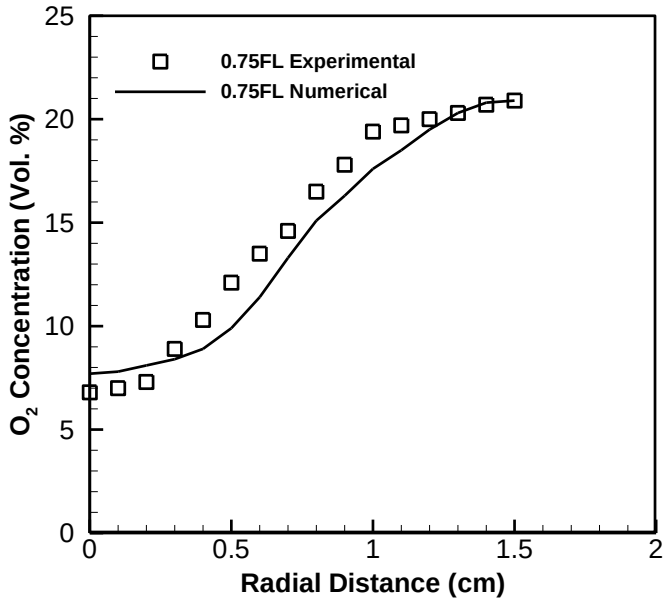

Fig. 194: O_2 concentration profiles for n – heptane flame at 0.75 FL at Φ=1.2

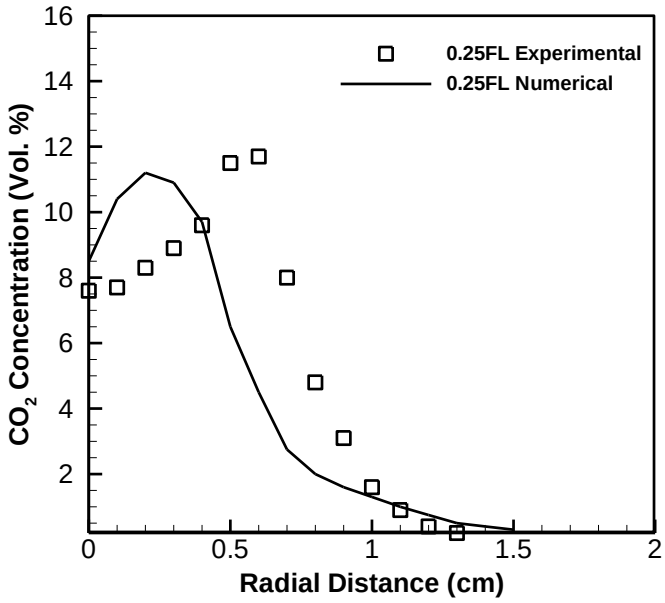

Fig. 195: CO_2 concentration profiles for n – heptane flame at 0.25 FL at Φ=1.2

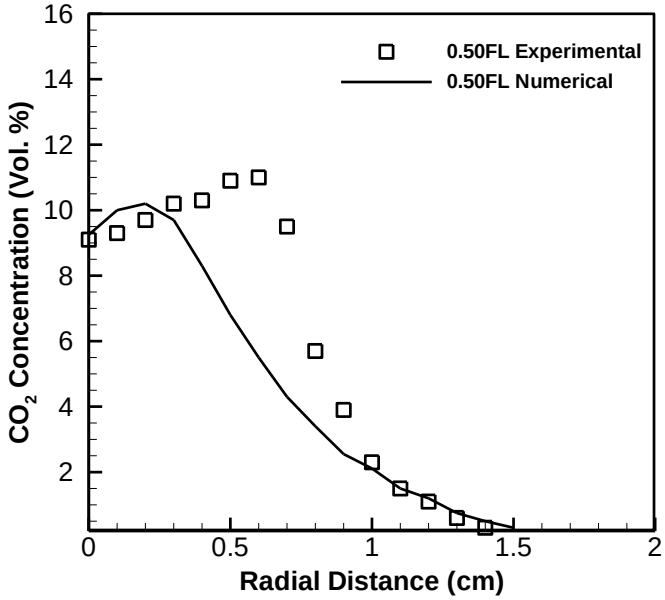

Fig. 196: CO_2 concentration profiles for n – heptane flame at 0.50 FL at Φ=1.2

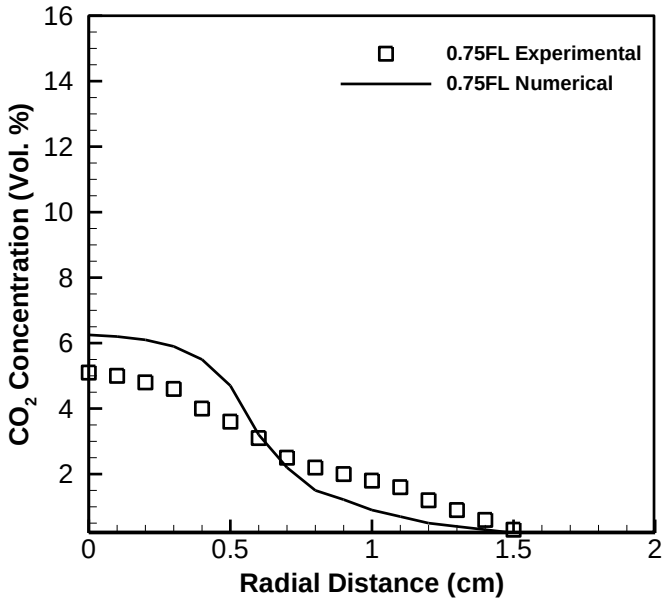

Fig. 197: CO_2 concentration profiles for n – heptane flame at 0.75 FL at Φ=1.2

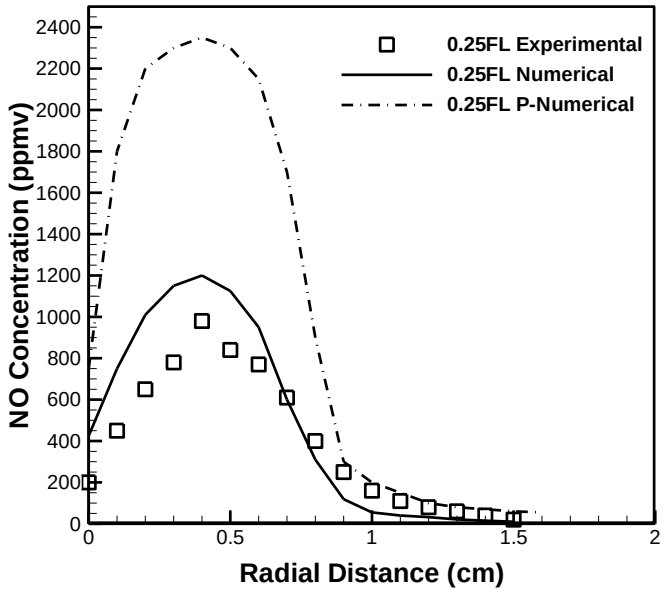

Fig. 198: NO concentration profiles for n – heptane flame at 0.25 FL at Φ=1.2

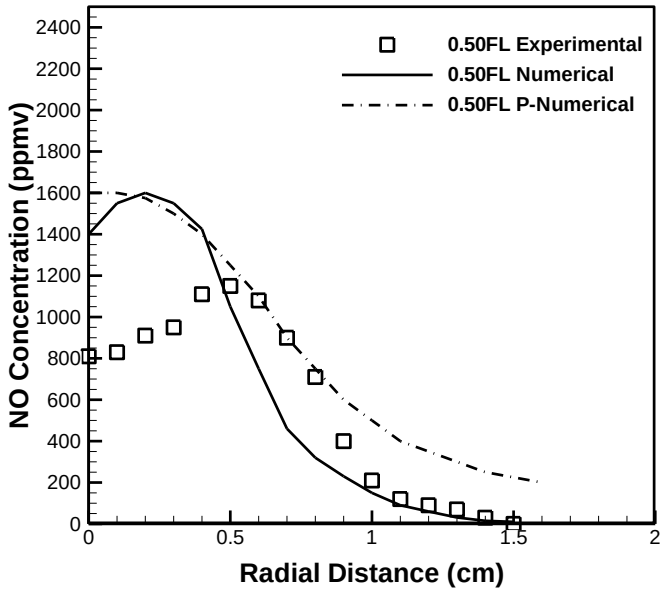

Fig. 199: NO concentration profiles for n – heptane flame at 0.50 FL at Φ=1.2

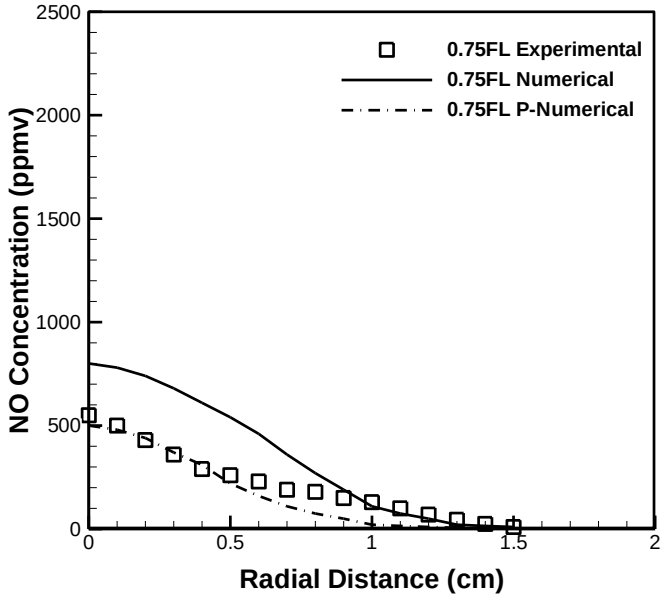

Fig. 200: NO concentration profiles for n – heptane flame at 0.75 FL at Φ=1.2

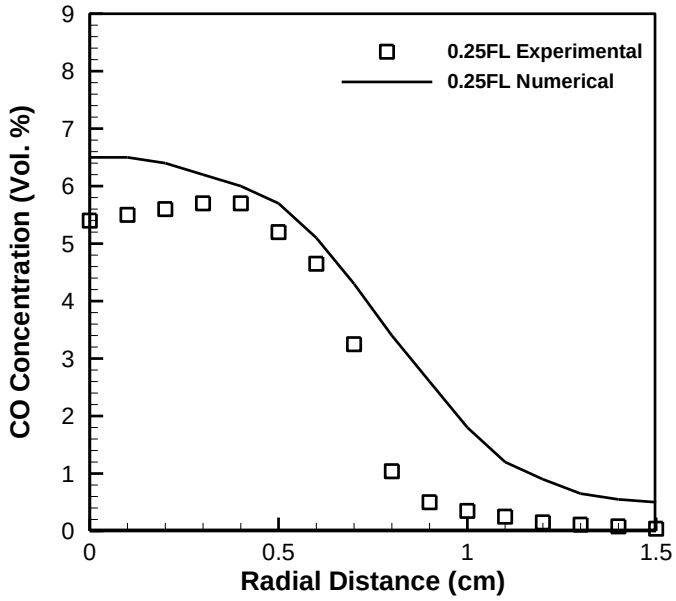

Fig. 201: CO concentration profiles for n – heptane flame at 0.25 FL at Φ=1.2

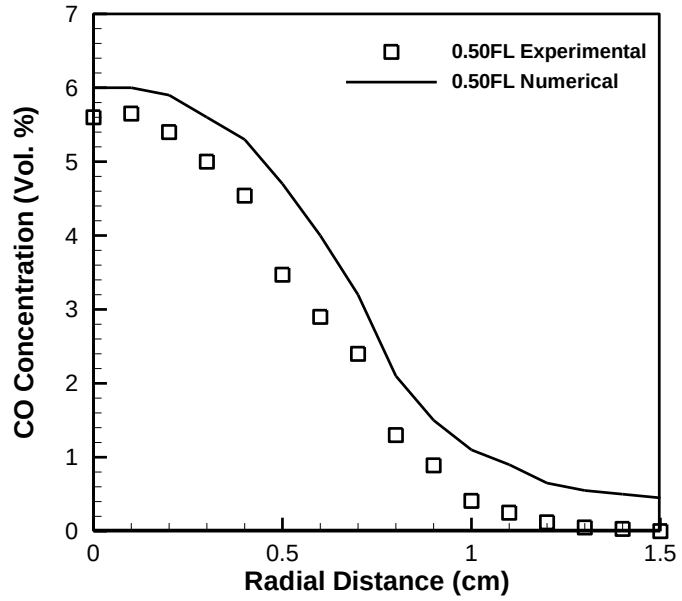

Fig. 202: CO concentration profiles for n – heptane flame at 0.50 FL at Φ=1.2

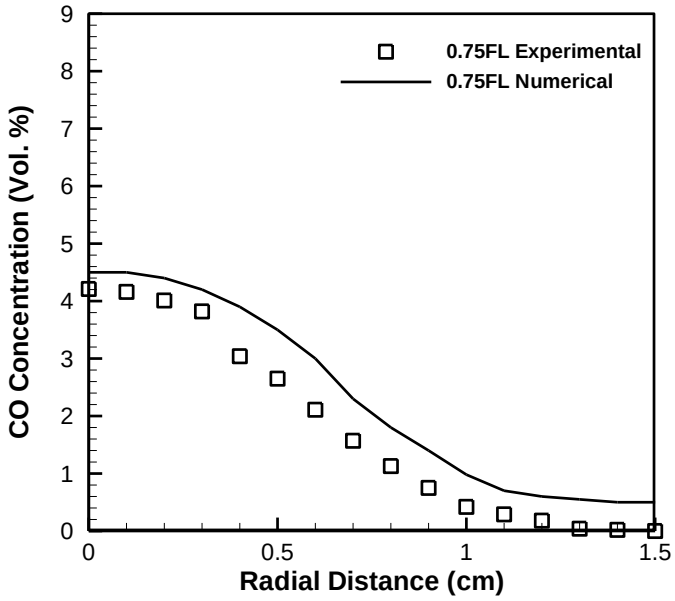

Fig. 203: CO concentration profiles for n – heptane flame at 0.75 FL at Φ=1.2

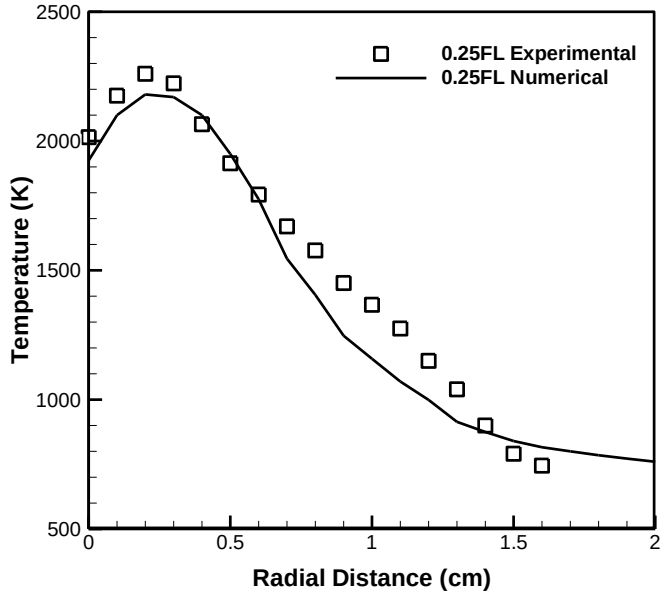

Fig. 204: Temperature profiles for methyl decanoate flame at 0.25 FL at Φ=1.2

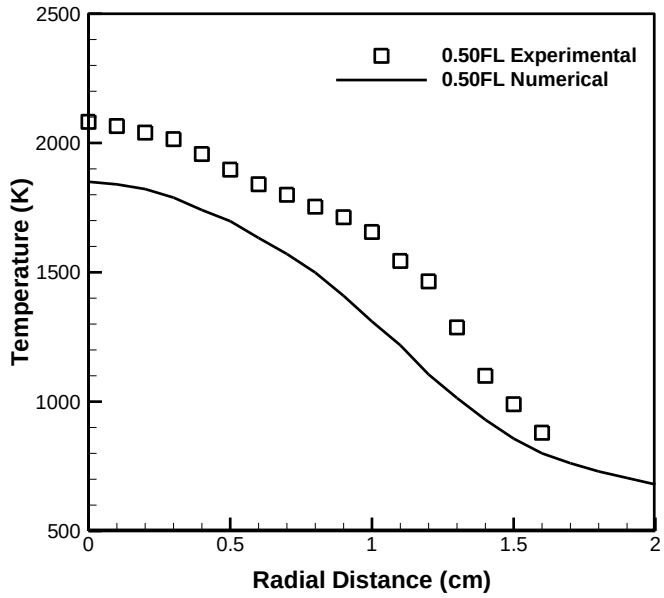

Fig. 205: Temperature profiles for methyl decanoate flame at 0.50 FL at Φ=1.2

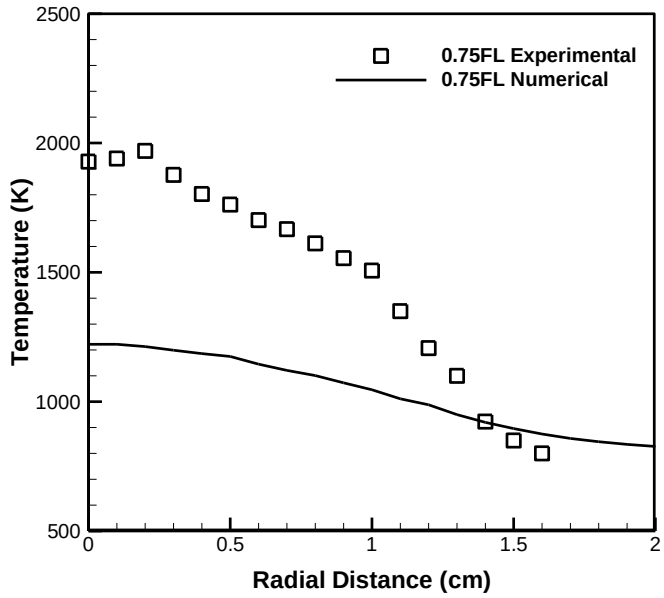

Fig. 206: Temperature profiles for methyl decanoate flame at 0.75 FL at Φ=1.2

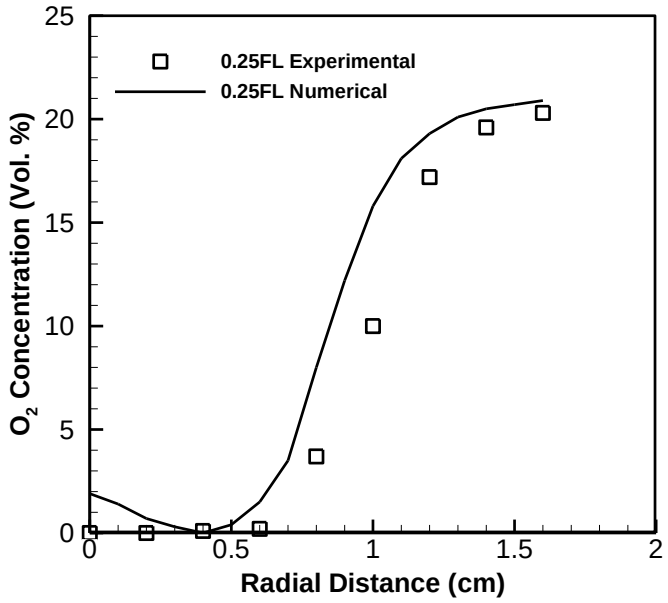

Fig. 207: O_2 concentration profiles for methyl decanoate flame at 0.25 FL at Φ=1.2

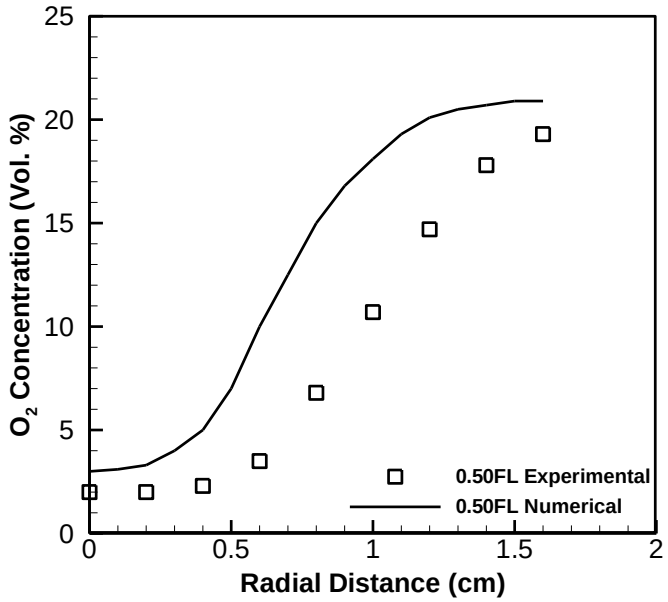

Fig. 208: O_2 concentration profiles for methyl decanoate flame at 0.50 FL at Φ=1.2

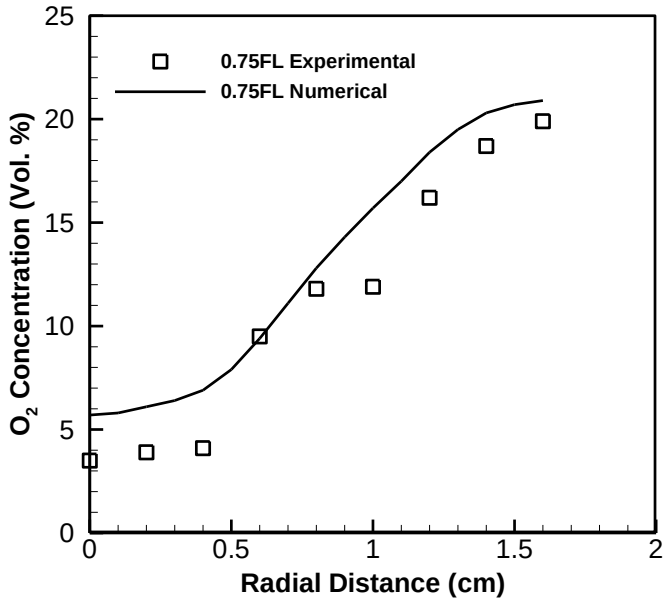

Fig. 209: O_2 concentration profiles for methyl decanoate flame at 0.75 FL at Φ=1.2

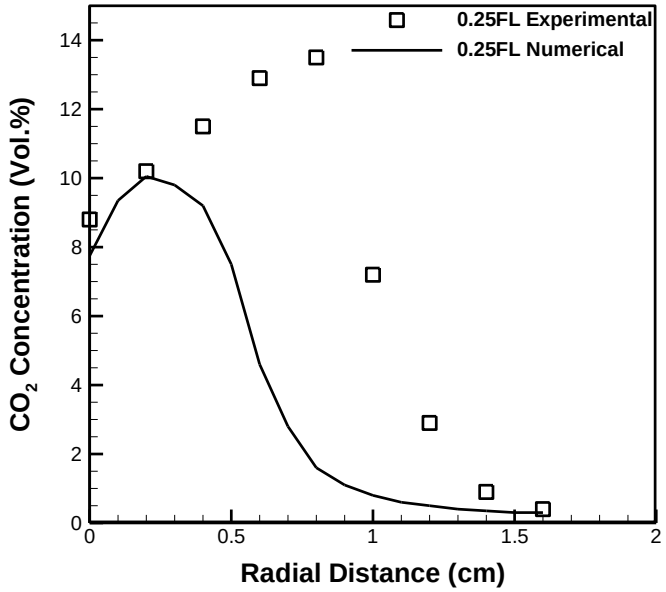

Fig. 210: CO_2 concentration profiles for methyl decanoate flame at 0.25 FL at Φ=1.2

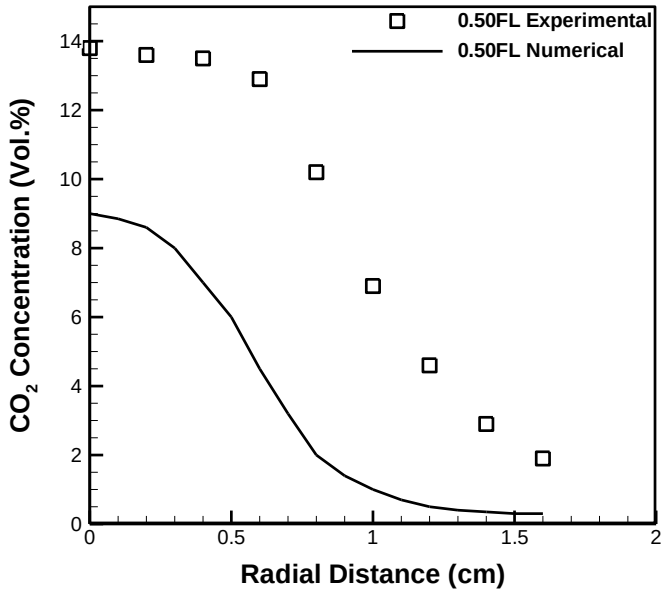

Fig. 211: CO_2 concentration profiles for methyl decanoate flame at 0.50 FL at Φ=1.2

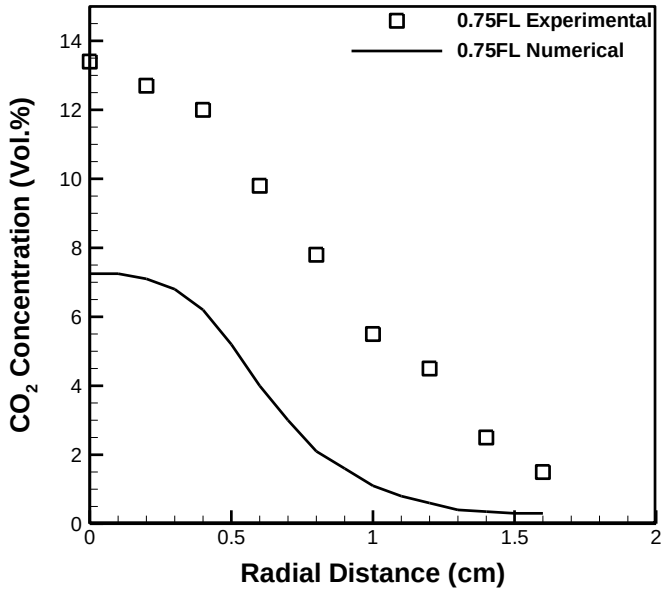

Fig. 212: CO_2 concentration profiles for methyl decanoate flame at 0.75 FL at Φ=1.2

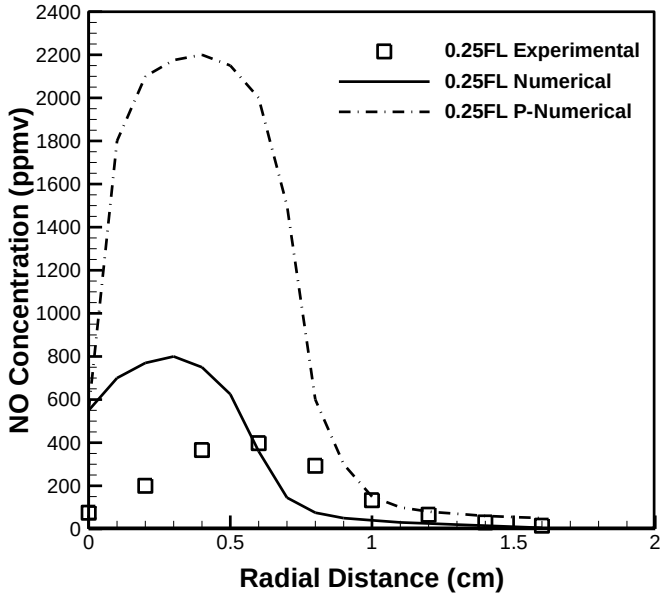

Fig. 213: NO concentration profiles for methyl decanoate flame at 0.25 FL at Φ=1.2

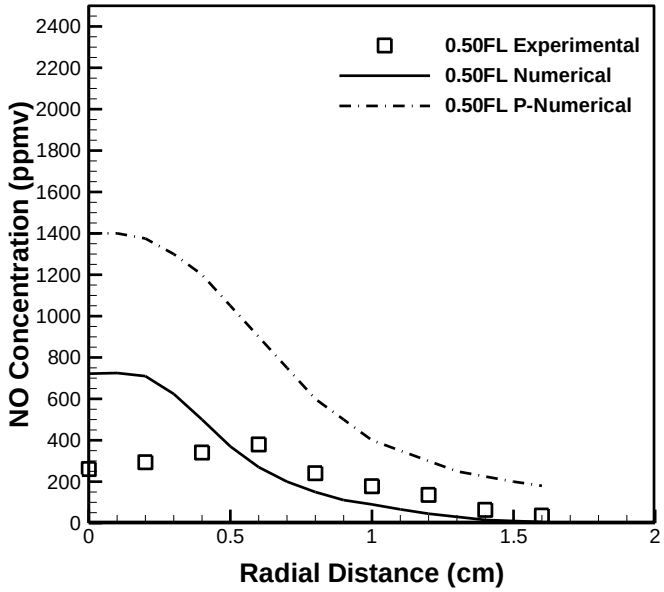

Fig. 214: NO concentration profiles for methyl decanoate flame at 0.50 FL at Φ=1.2

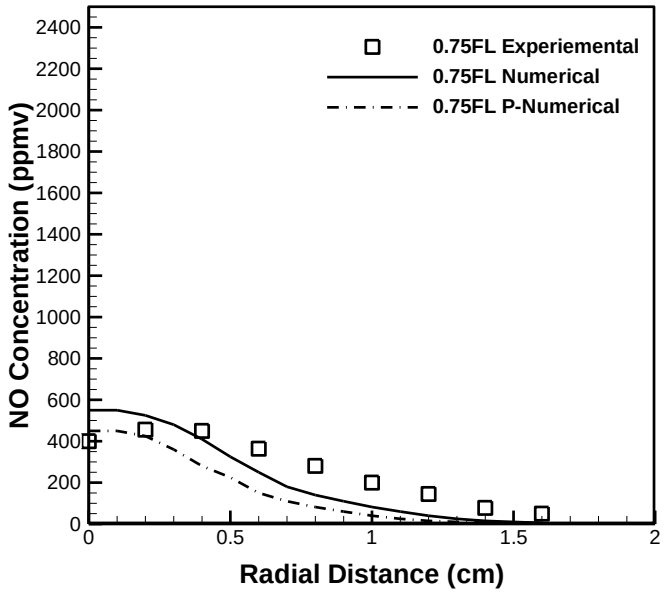

Fig. 215: NO concentration profiles for methyl decanoate flame at 0.75 FL at Φ=1.2

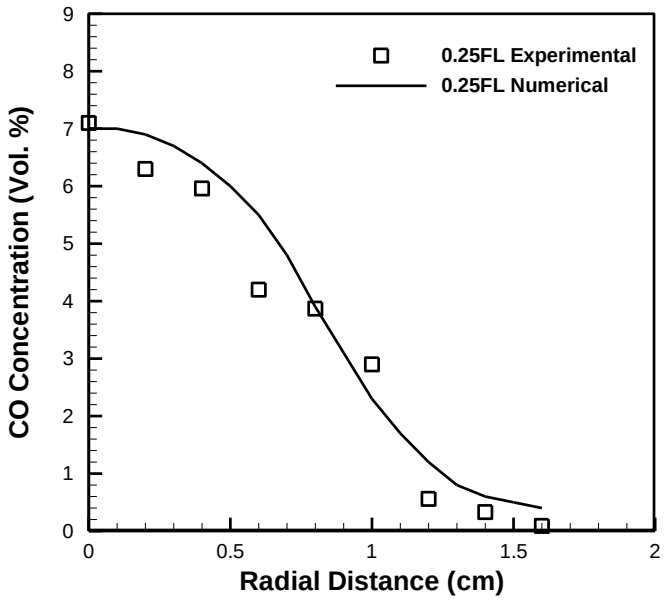

Fig. 216: CO concentration profiles for methyl decanoate flame at 0.25 FL at Φ=1.2

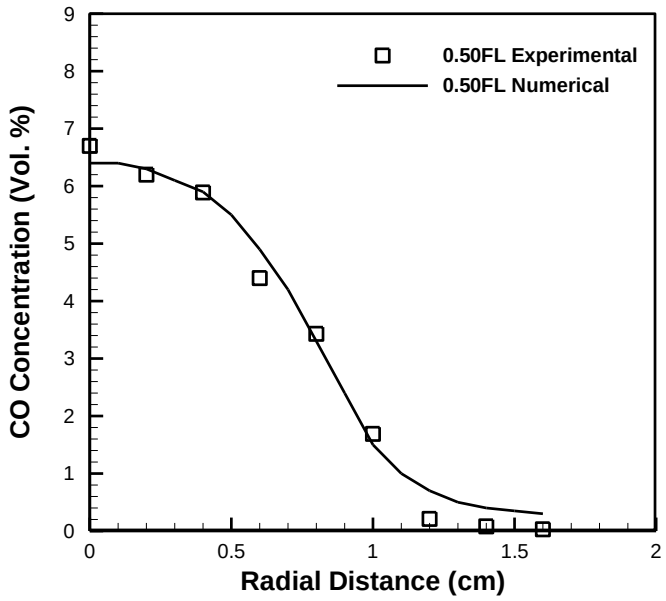

Fig. 217: CO concentration profiles for methyl decanoate flame at 0.50 FL at Φ=1.2

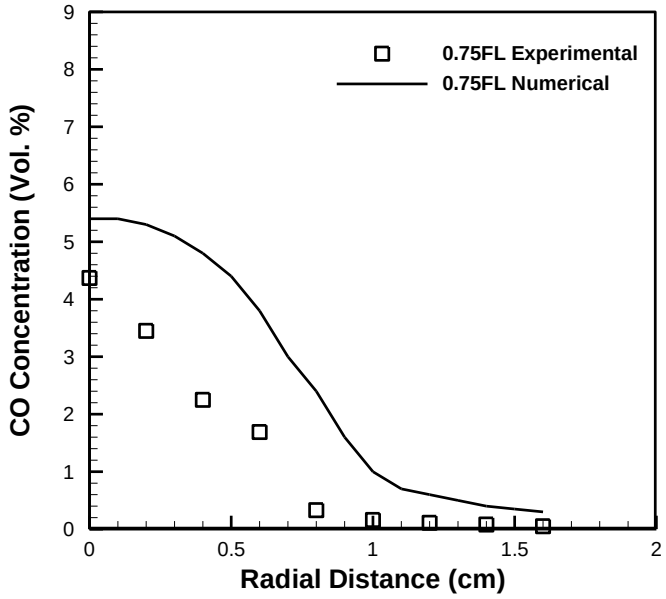

Fig. 218: CO concentration profiles for methyl decanoate flame at 0.75 FL at Φ=1.2

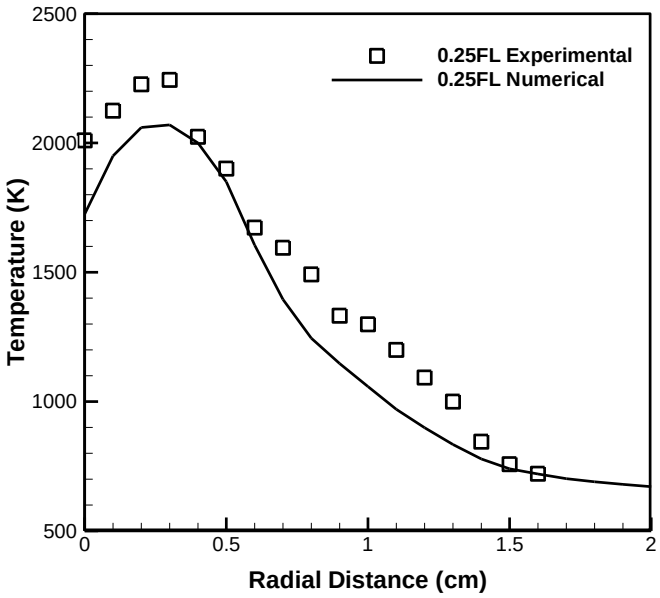

Fig. 219: Temperature profiles for methyl decanoate + n–heptane flame at 0.25 FL at Φ=1.2

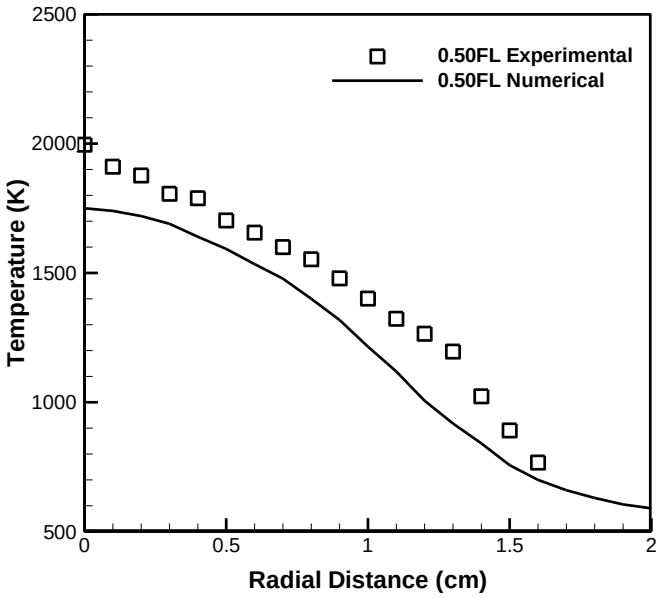

Fig. 220: Temperature profiles for methyl decanoate + n–heptane flame at 0.50 FL at Φ=1.2

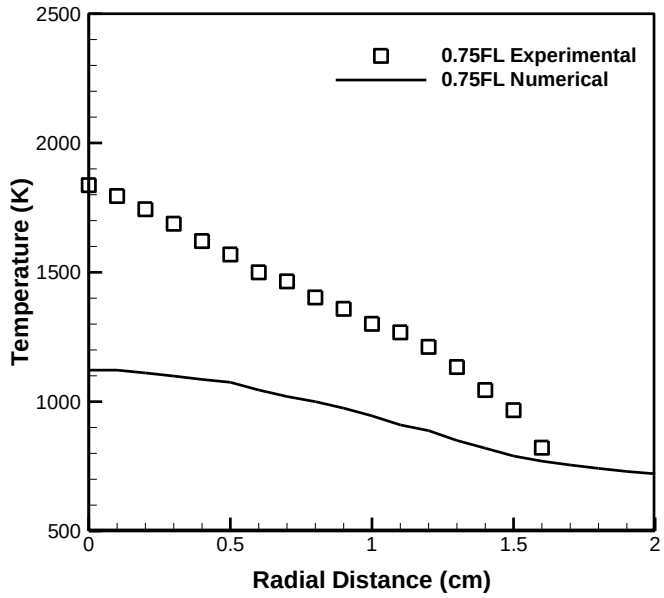

Fig. 221: Temperature profiles for methyl decanoate + n–heptane flame at 0.75 FL at Φ=1.2

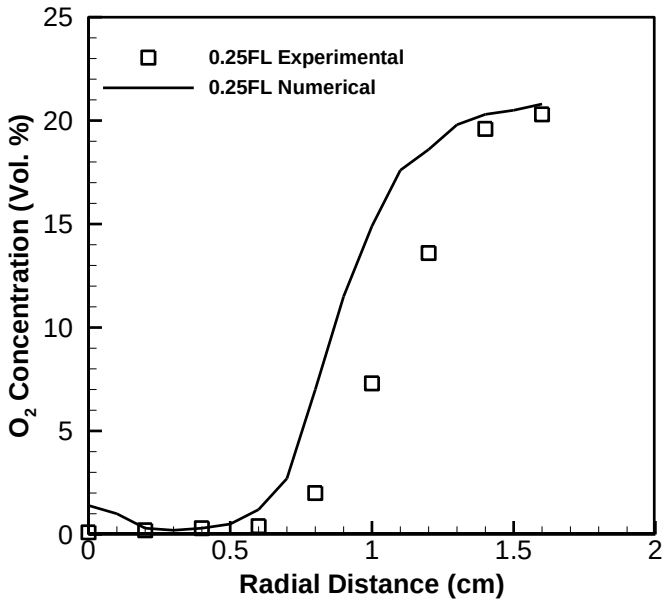

Fig. 222: O_2 concentration profiles for methyl decanoate + n–heptane flame at 0.25 FL at Φ=1.2

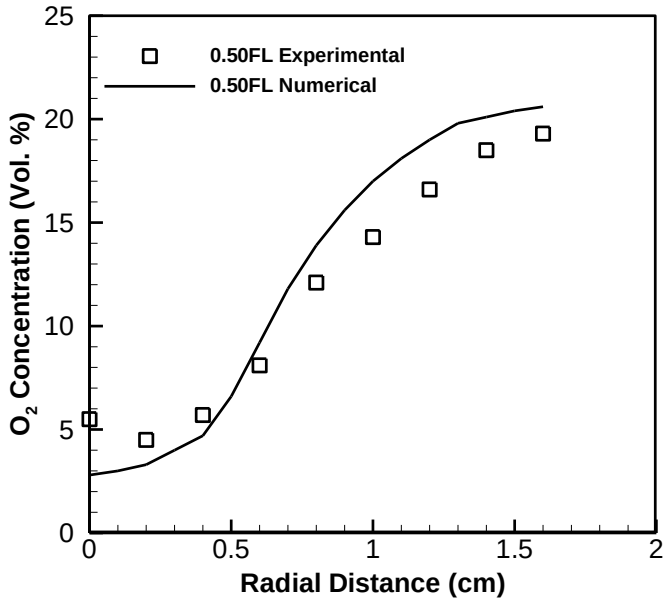

Fig. 223: O_2 concentration profiles for methyl decanoate + n–heptane flame at 0.50 FL at Φ=1.2

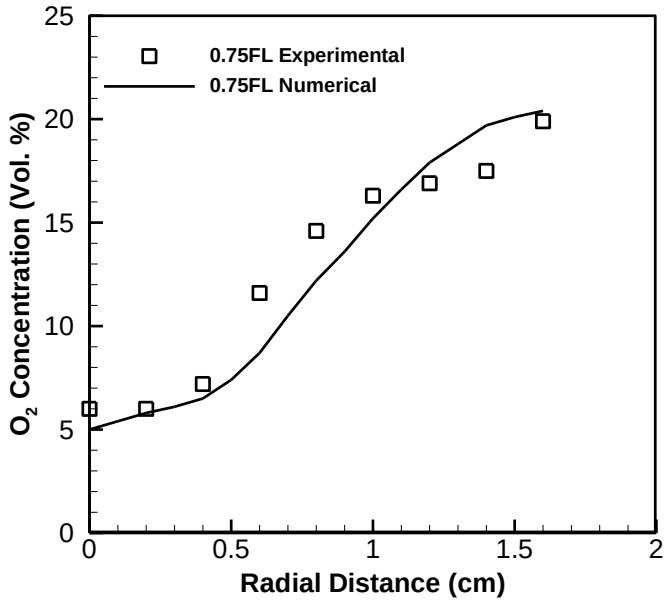

Fig. 224: O_2 concentration profiles for methyl decanoate + n–heptane flame at 0.75 FL at Φ=1.2

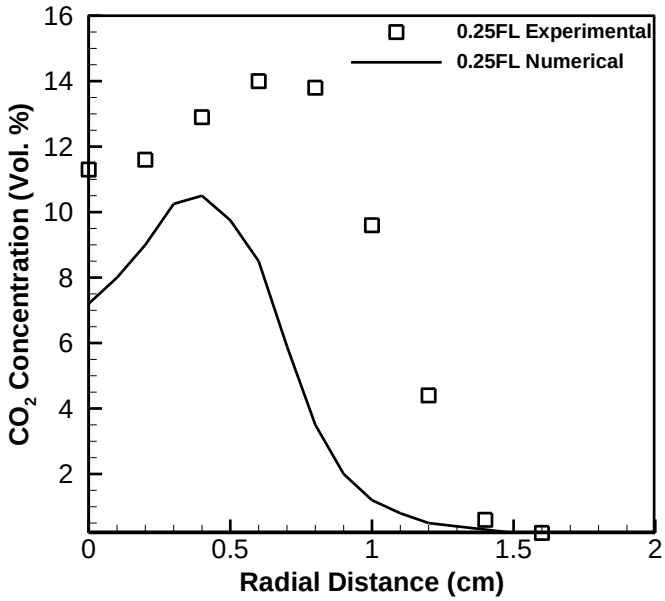

Fig. 225: CO_2 concentration profiles for methyl decanoate + n–heptane flame at 0.25 FL at Φ=1.2

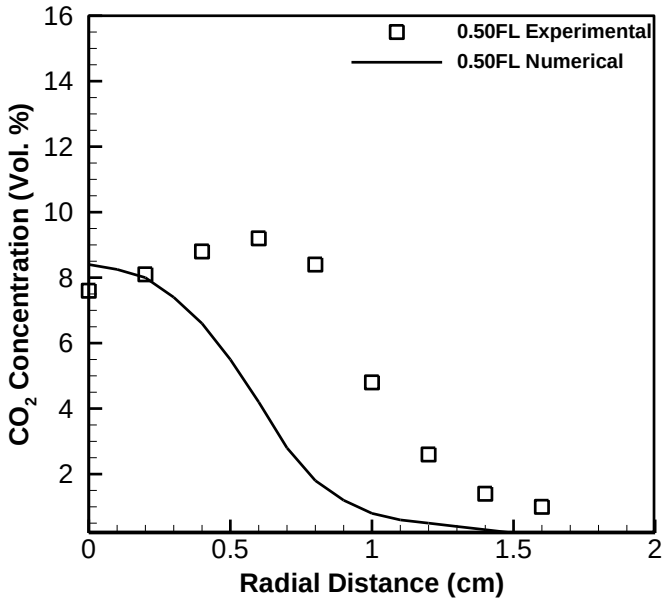

Fig. 226: CO_2 concentration profiles for methyl decanoate + n–heptane flame at 0.50 FL at Φ=1.2

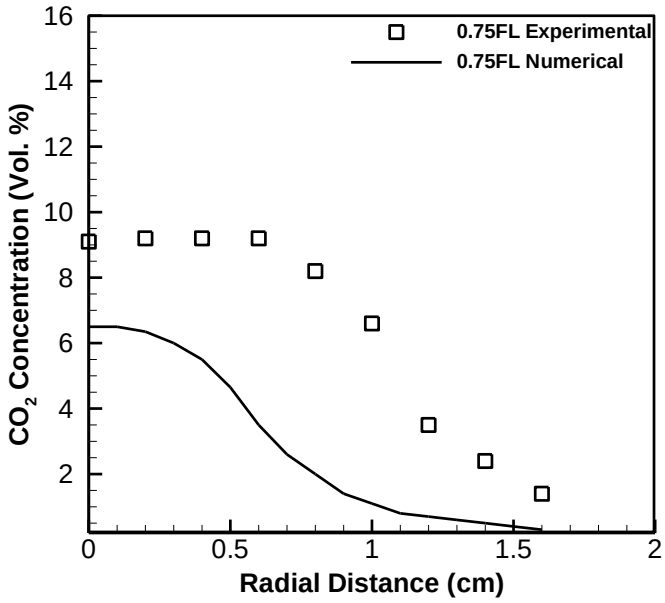

Fig. 227: CO_2 concentration profiles for methyl decanoate + n–heptane flame at 0.75 FL at Φ=1.2

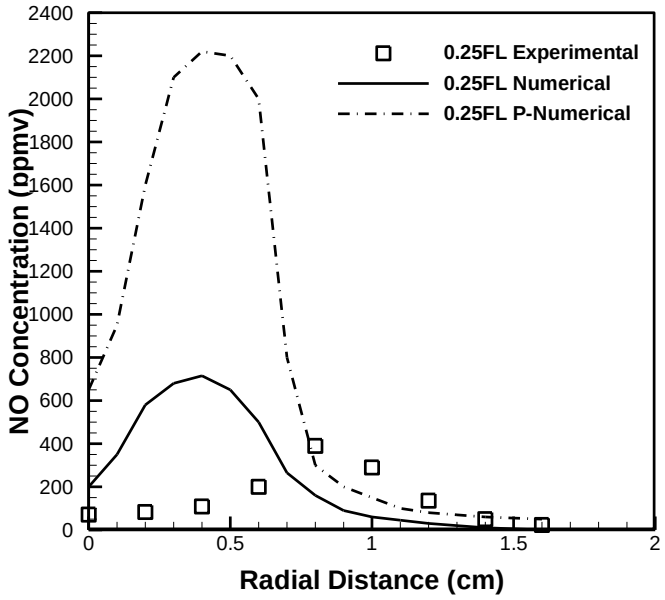

Fig. 228: NO concentration profiles for methyl decanoate + n–heptane flames at 0.25FL at Φ=1.2

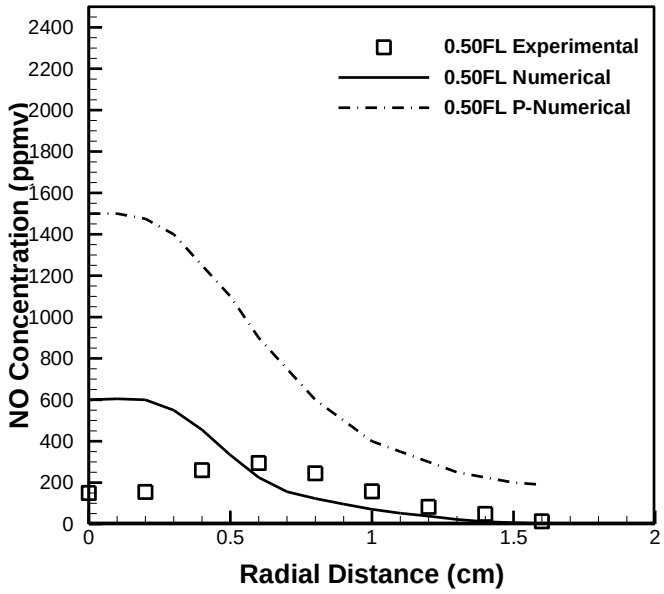

Fig. 229: NO concentration profiles for methyl decanoate + n–heptane flame at 0.50 FL at Φ=1.2

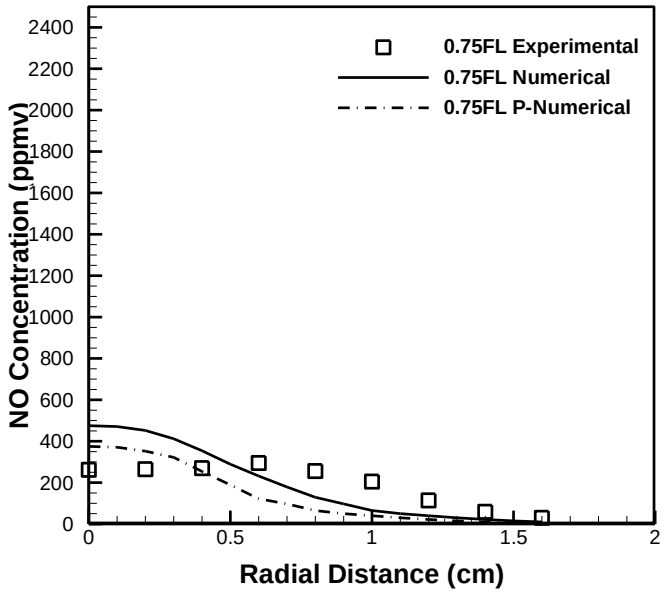

Fig. 230: NO concentration profiles for methyl decanoate + n–heptane flame at 0.75 FL at Φ=1.2

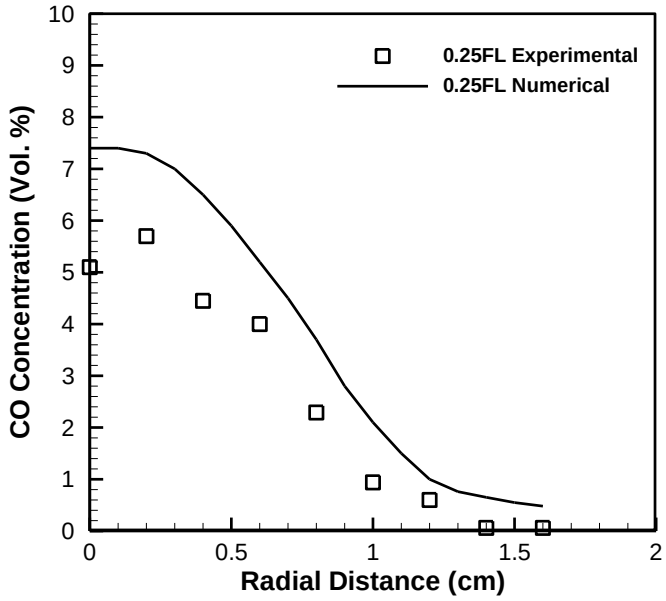

Fig. 231: CO concentration profiles for methyl decanoate + n–heptane flame at 0.25 FL at Φ=1.2

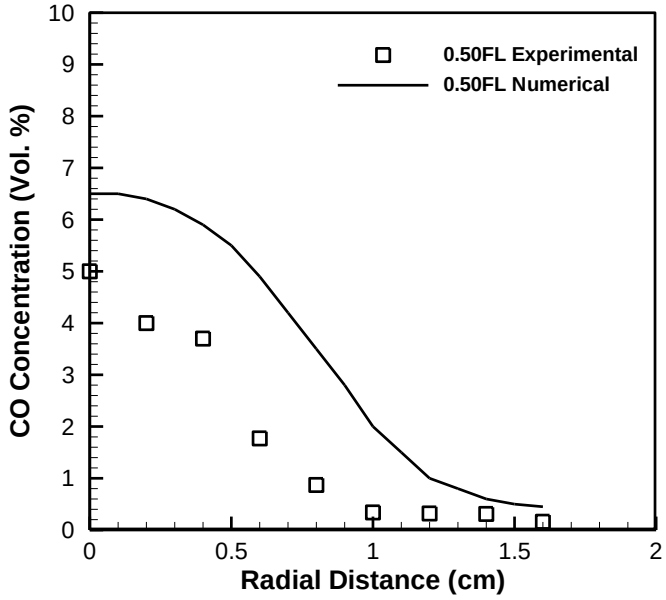

Fig. 232: CO concentration profiles for methyl decanoate + n–heptane flame at 0.50 FL at Φ=1.2

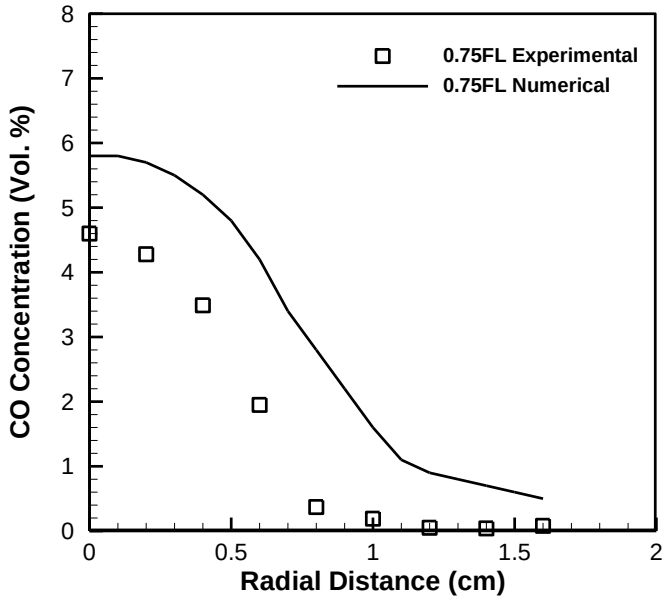

Fig. 233: CO concentration profiles for methyl decanoate + n–heptane flame at 0.75 FL at Φ=1.2

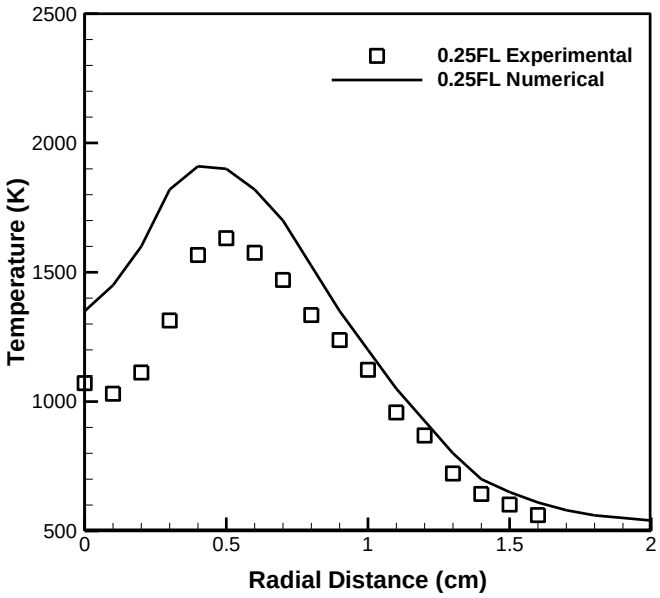

Fig. 234: Temperature profiles for n – heptane flame at 0.25 FL at Φ=2

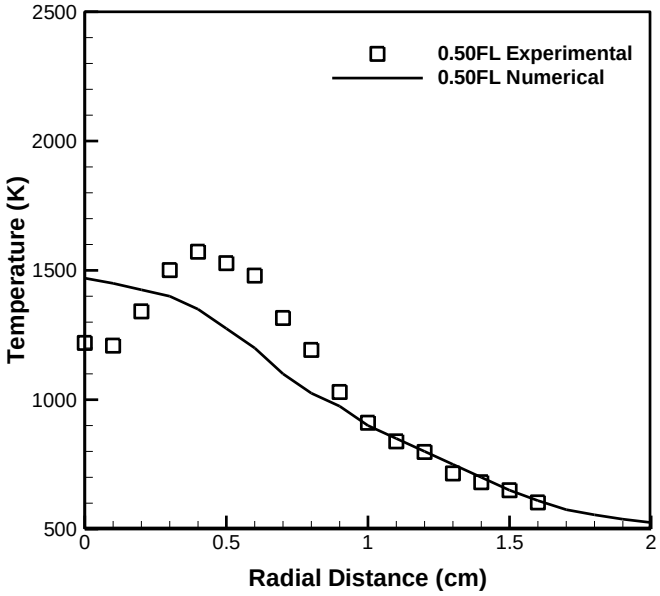

Fig. 235: Temperature profiles for n – heptane flame at 0.50 FL at Φ=2

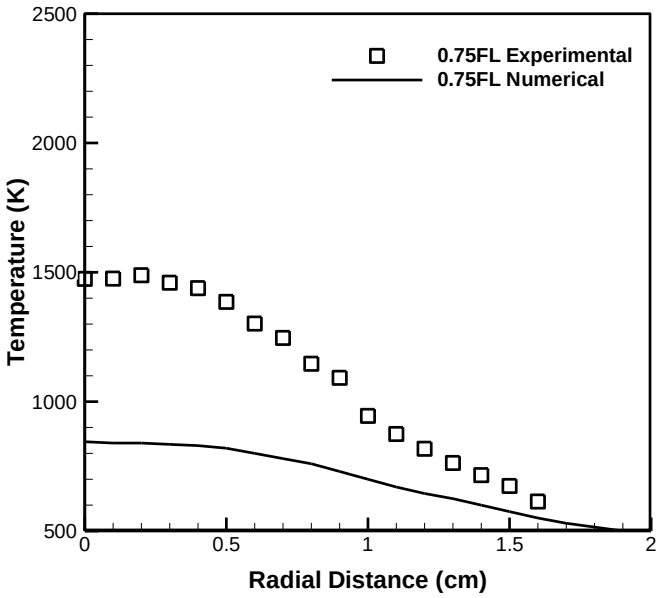

Fig. 236: Temperature profiles for n – heptane flame at 0.75 FL at Φ=2

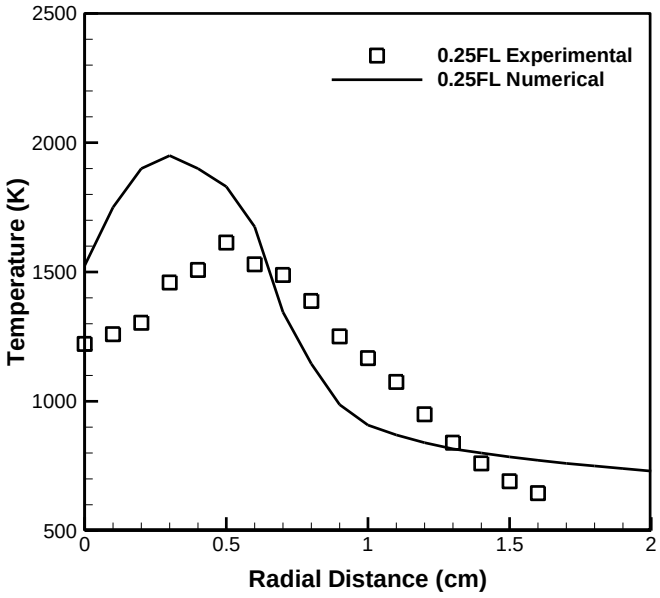

Fig. 237: Temperature profiles for methyl decanoate flame at 0.25 FL at Φ=2

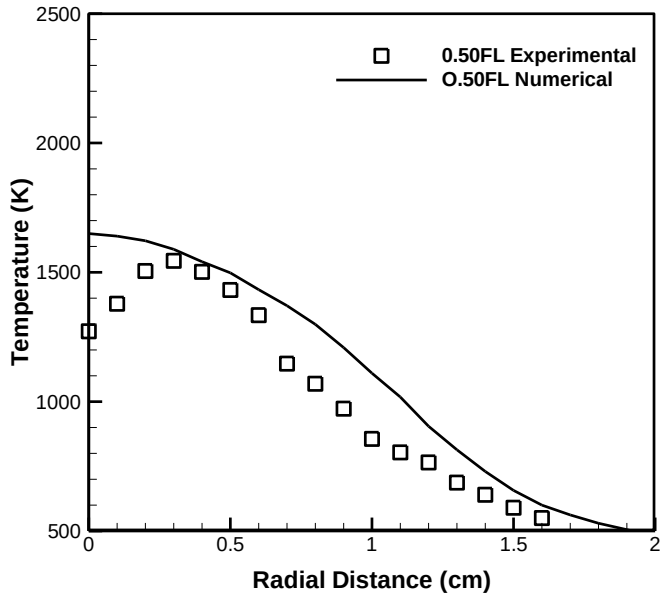

Fig. 238: Temperature profiles for methyl decanoate flame at 0.50 FL at Φ=2

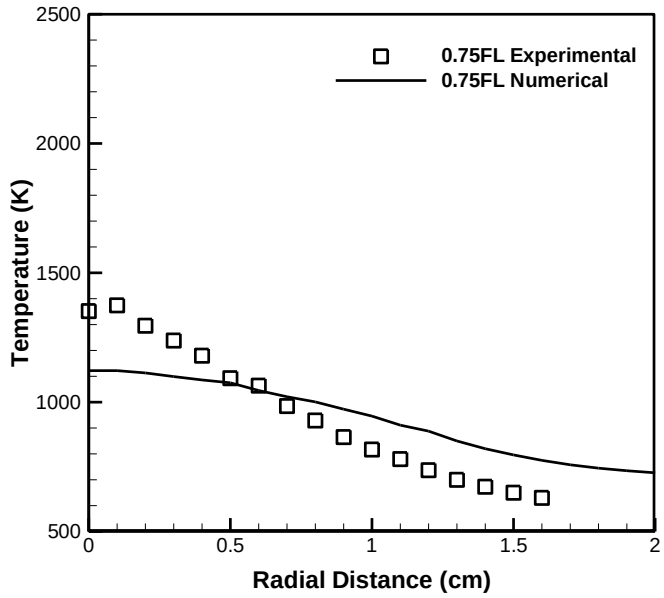

Fig. 239: Temperature profiles for methyl decanoate flame at 0.75 FL at Φ=2

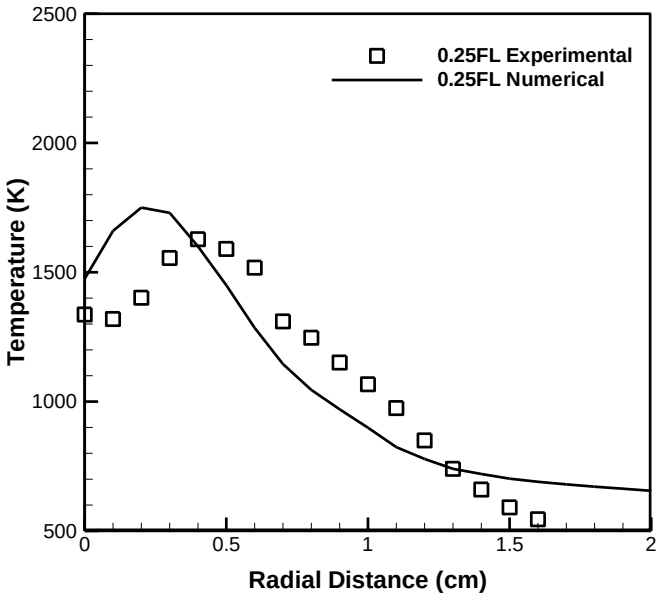

Fig. 240: Temperature profiles for methyl decanoate+n-heptane flame at 0.25 FL at Φ=2

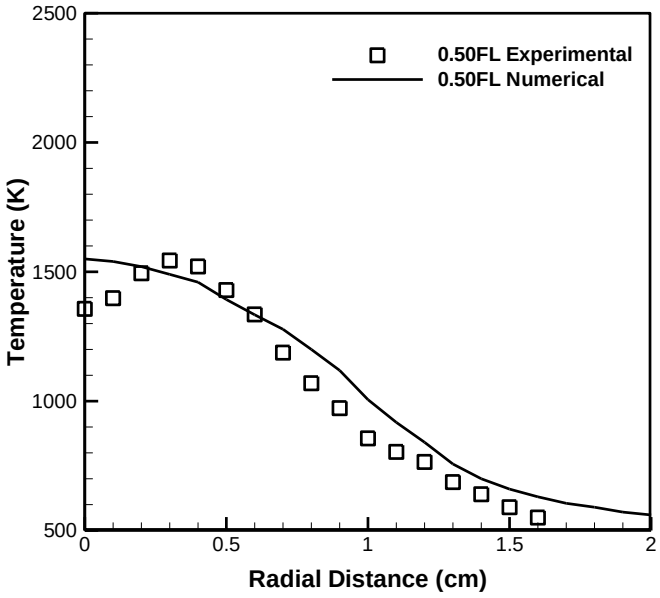

Fig. 241: Temperature profiles for methyl decanoate+n-heptane flame at 0.50 FL at Φ=2

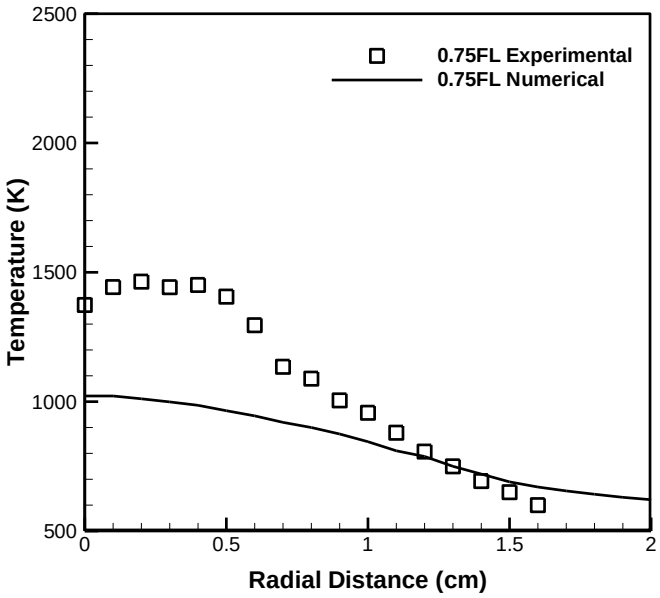

Fig. 242: Temperature profiles for methyl decanoate+n-heptane flame at 0.75 FL at Φ=2

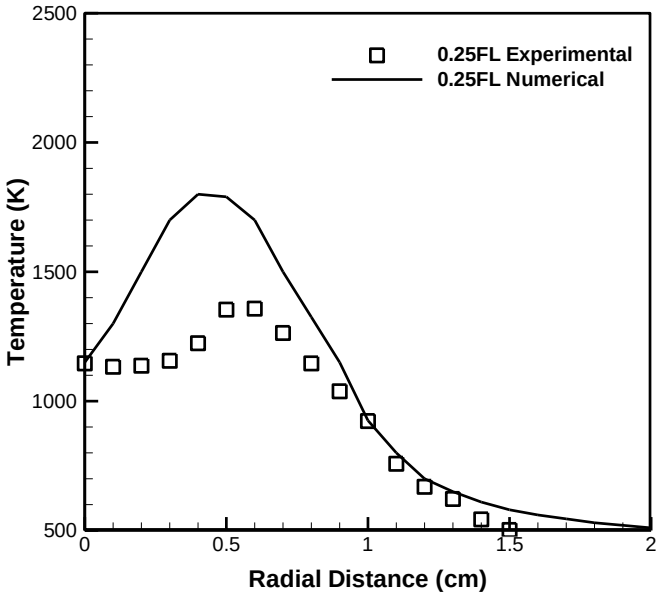

Fig. 243: Temperature profiles for n-heptane flame at 0.25 FL at Φ=3

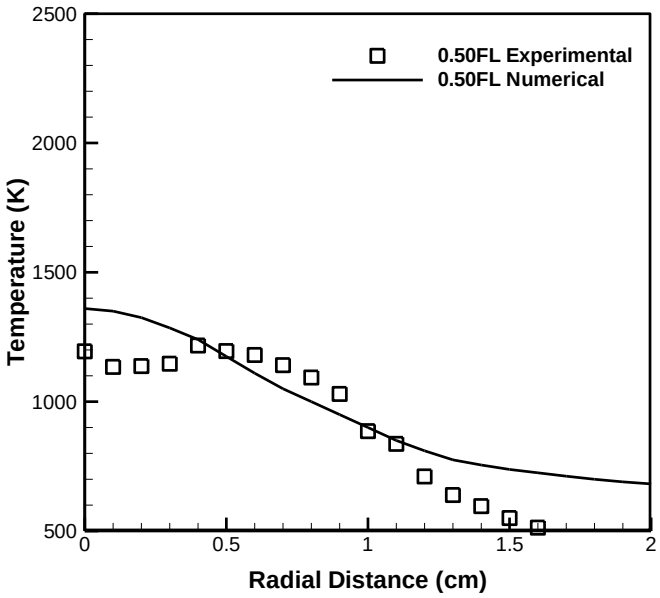

Fig. 244: Temperature profiles for n-heptane flame at 0.50 FL at Φ=3

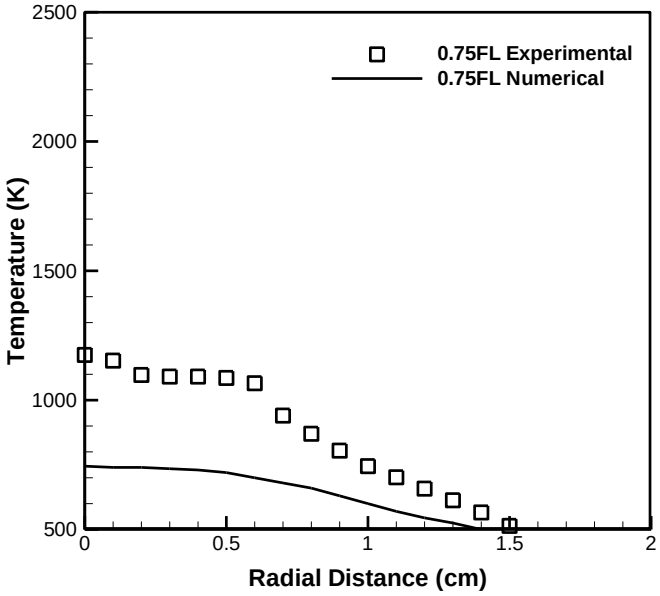

Fig. 245: Temperature profiles for n-heptane flame at 0.75 FL at Φ=3

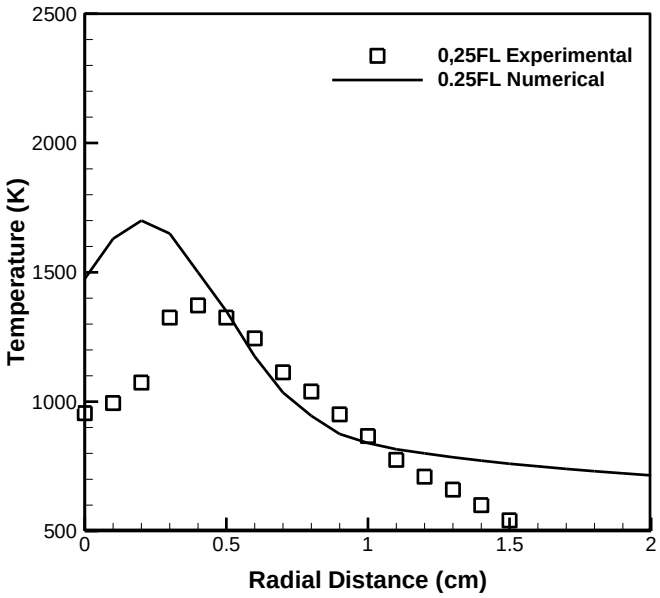

Fig. 246: Temperature profiles for methyl decanoate flame at 0.25 FL at Φ=3

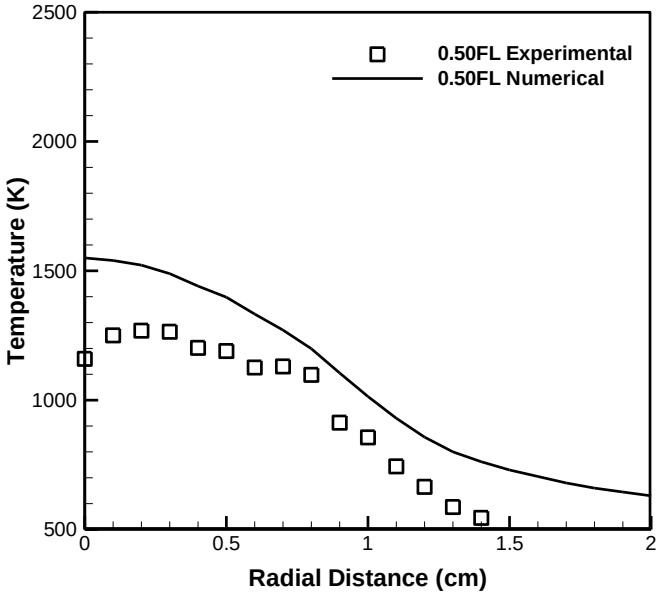

Fig. 247: Temperature profiles for methyl decanoate flame at 0.50 FL at Φ=3

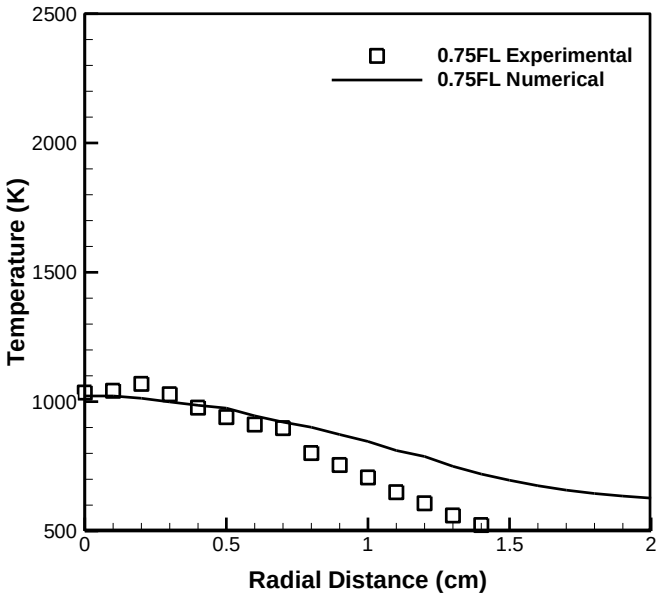

Fig. 248: Temperature profiles for methyl decanoate flame at 0.75 FL at Φ=3

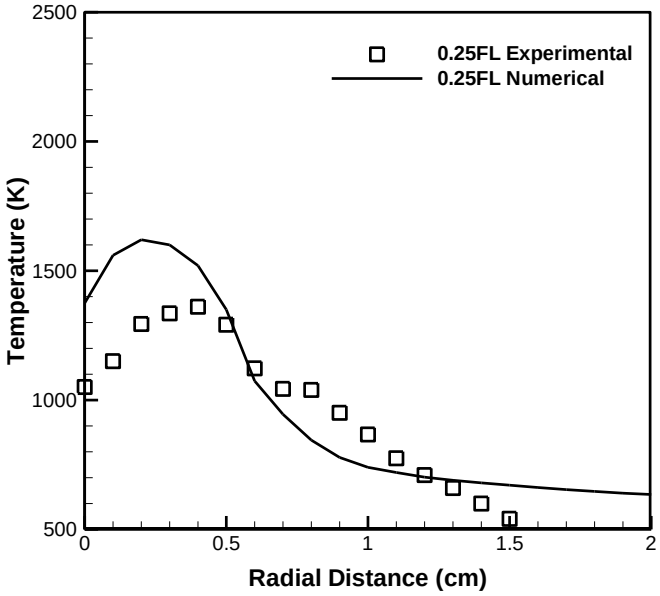

Fig. 249: Temperature profiles for methyl decanoate+n-heptane flame at 0.25 FL at Φ=3

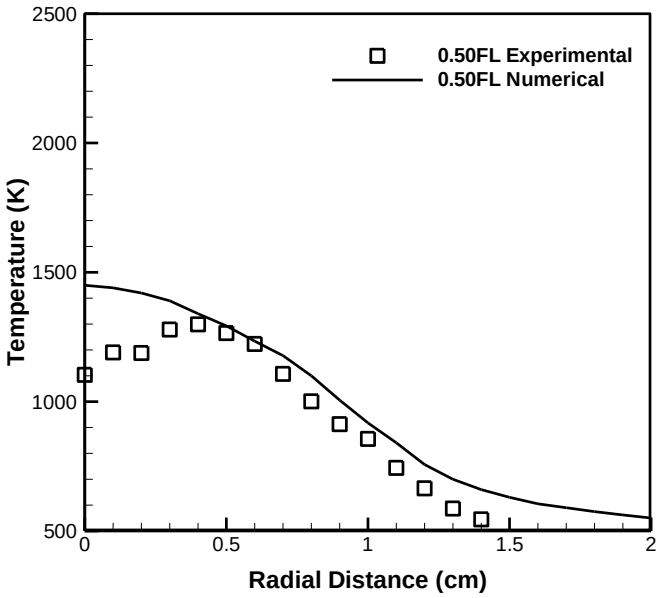

Fig. 250: Temperature profiles for methyl decanoate+n-heptane flame at 0.50 FL at Φ=3

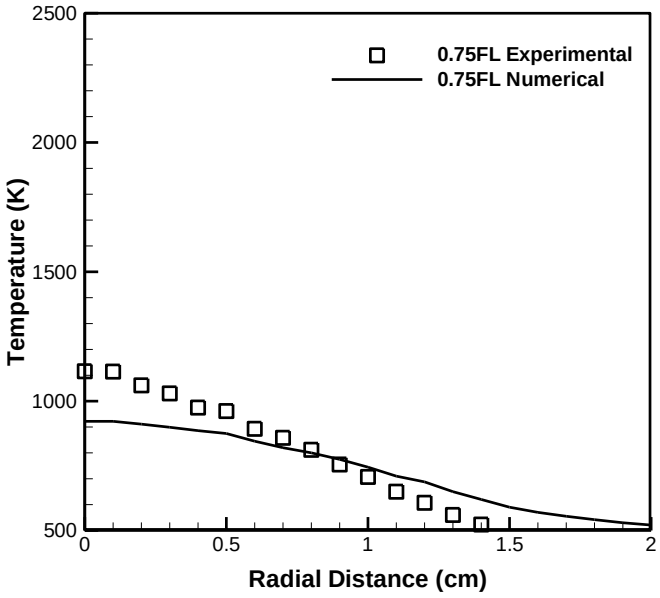

Fig. 251: Temperature profiles for methyl decanoate+n-heptane flame at 0.75 FL at Φ=3

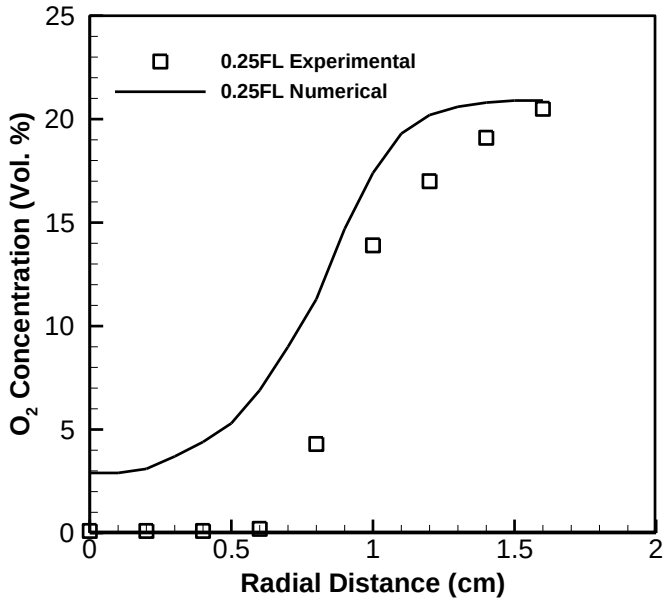

Fig. 252: Oxygen concentration profiles for n – heptane flame at 0.25 FL at Φ=2

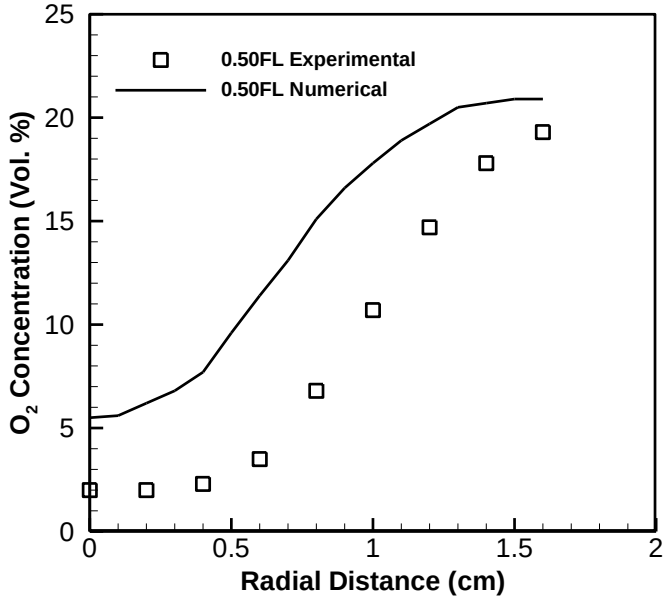

Fig. 253: Oxygen concentration profiles for n – heptane flame at 0.50 FL at Φ=2

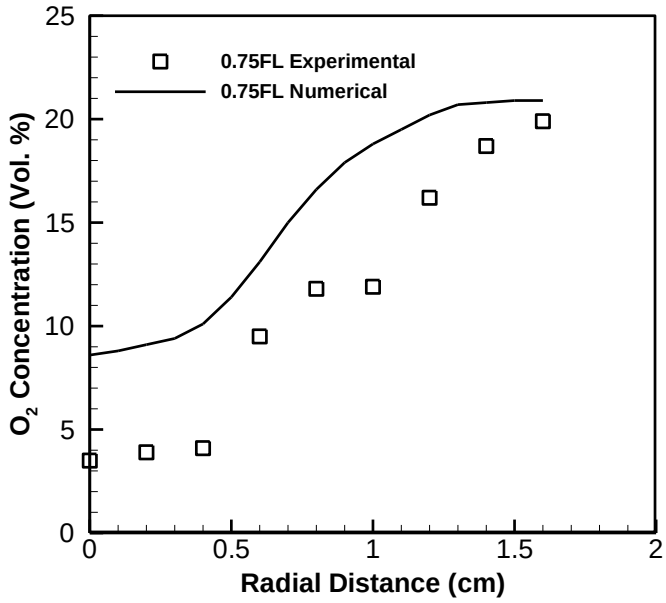

Fig. 254: Oxygen concentration profiles for n – heptane flame at 0.75 FL at Φ=2

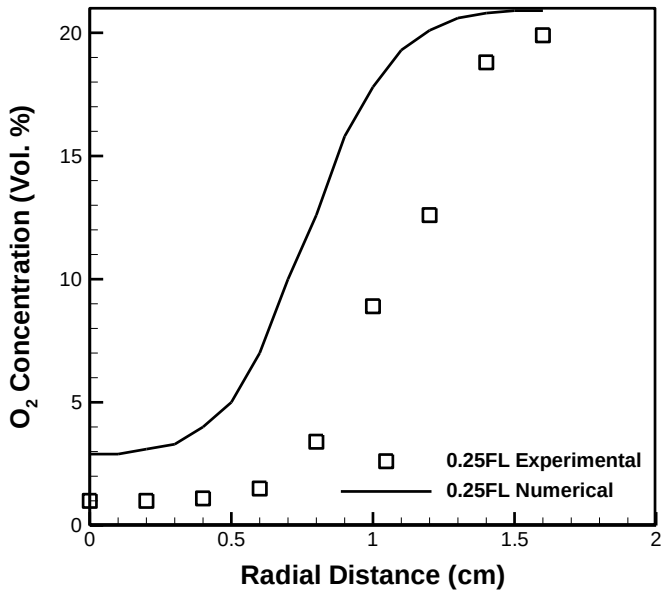

Fig. 255: Oxygen concentration profiles for methyl decanoate flame at 0.25 FL at Φ=2

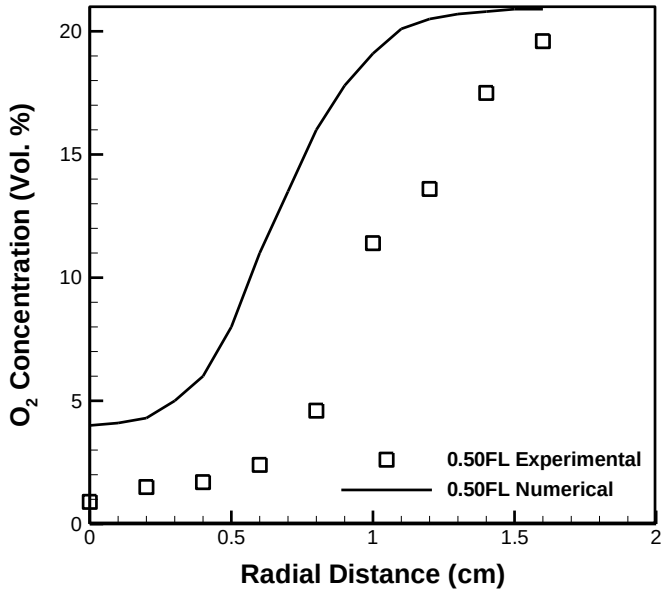

Fig. 256: Oxygen concentration profiles for methyl decanoate flame at 0.50 FL at Φ=2

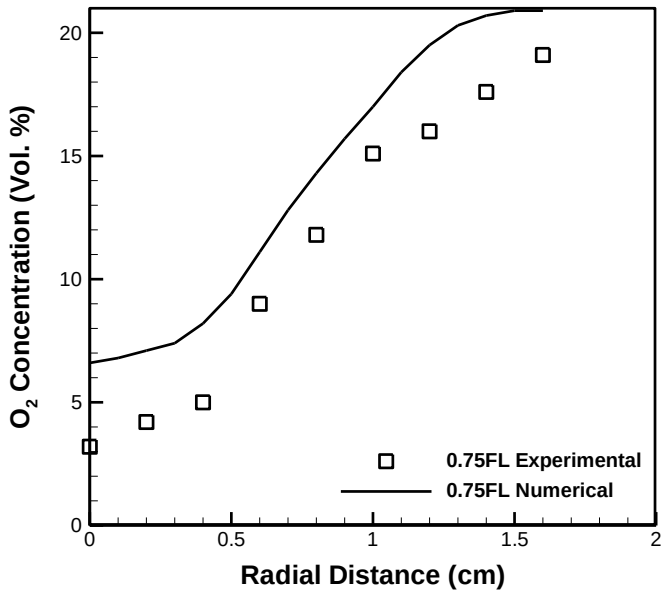

Fig. 257: Oxygen concentration profiles for methyl decanoate flame at 0.75 FL at Φ=2

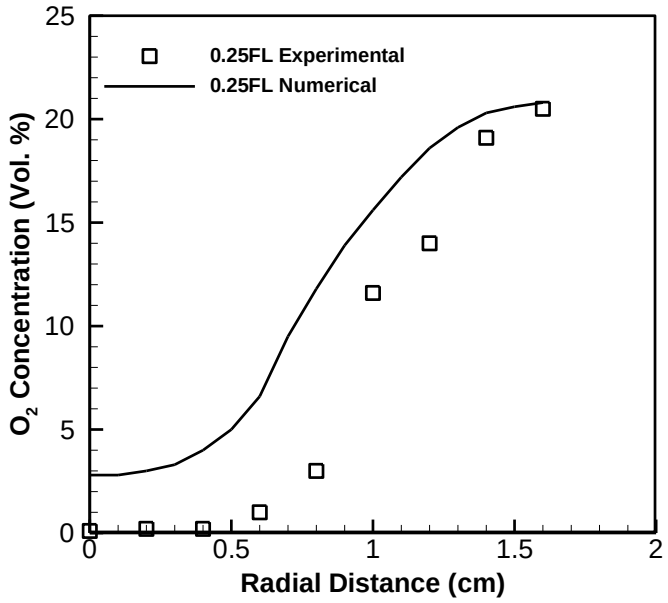

Fig. 258: O_2 concentration profiles for methyl decanoate+n-heptane flame at 0.25 FL at Φ=2

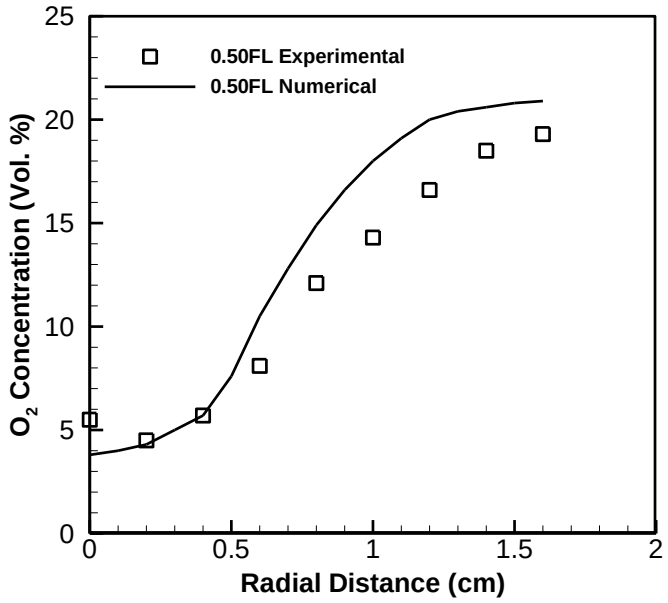

Fig. 259: O_2 concentration profiles for methyl decanoate+n-heptane flame at 0.50 FL at Φ=2

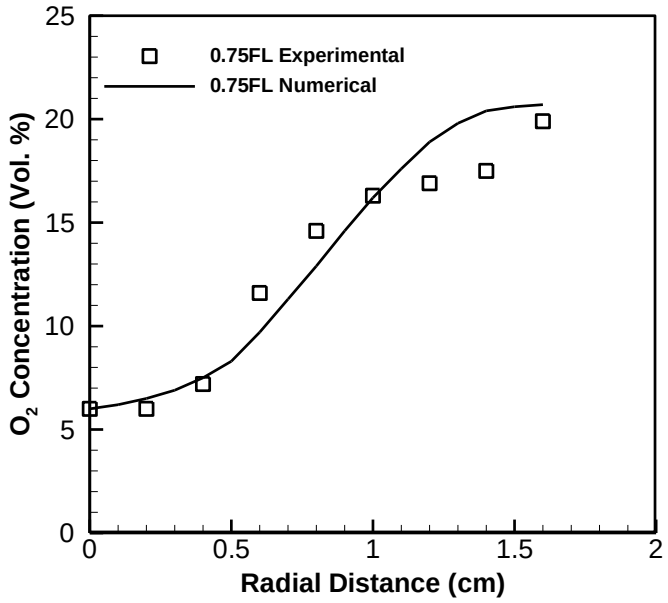

Fig. 260: O_2 concentration profiles for methyl decanoate+n-heptane flame at 0.75 FL at Φ=2

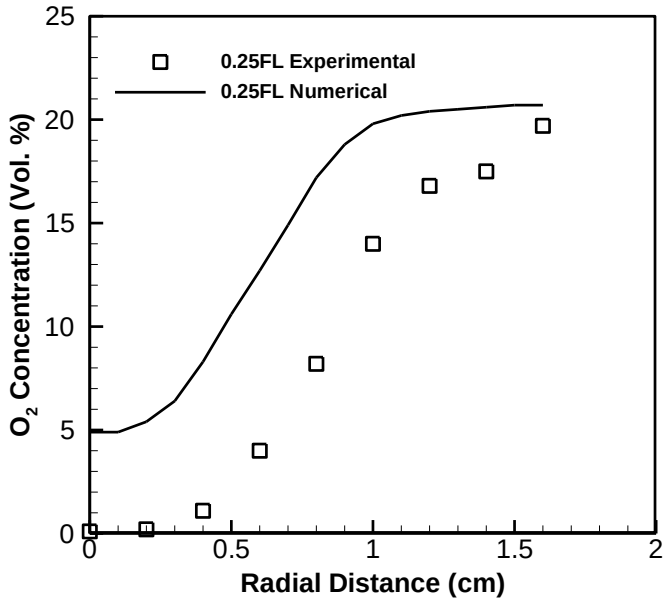

Fig. 261: O_2 concentration profiles for n-heptane flame at 0.25 FL at Φ=3

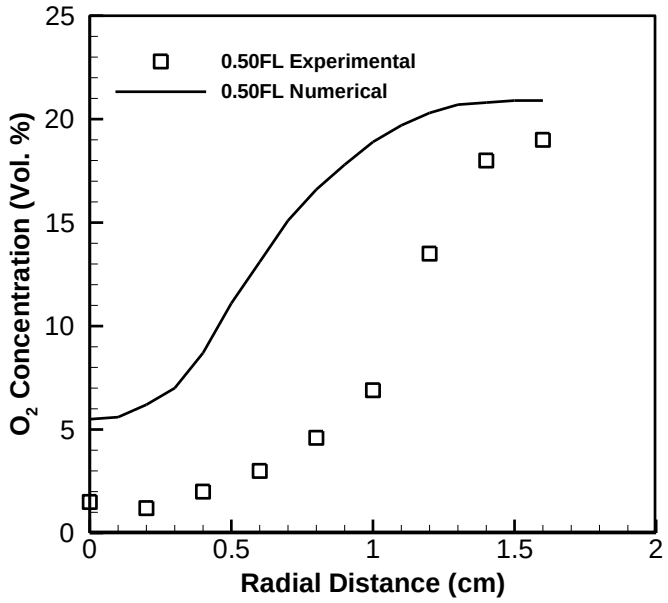

Fig. 262: O_2 concentration profiles for n-heptane flame at 0.5 FL at Φ=3

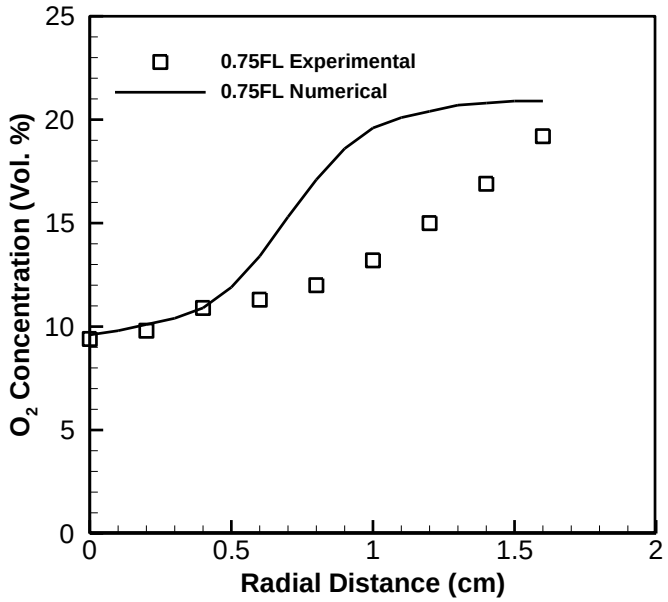

Fig. 263: O_2 concentration profiles for n-heptane flame at 0.75 FL at Φ=3

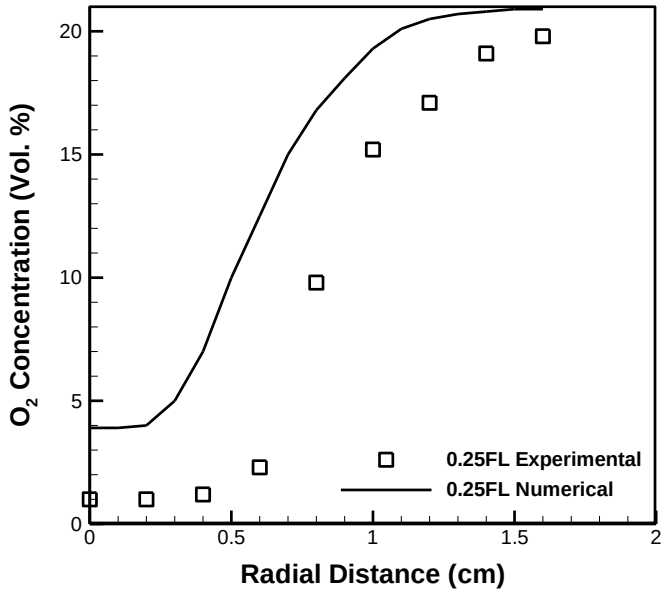

Fig. 264: O_2 concentration profiles for methyl decanoate flame at 0.25 FL at Φ=3

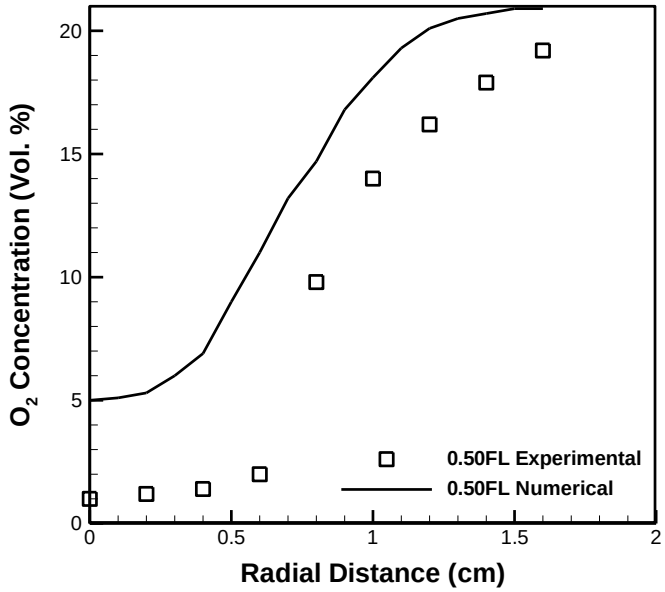

Fig. 265: O_2 concentration profiles for methyl decanoate flame at 0.5 FL at Φ=3

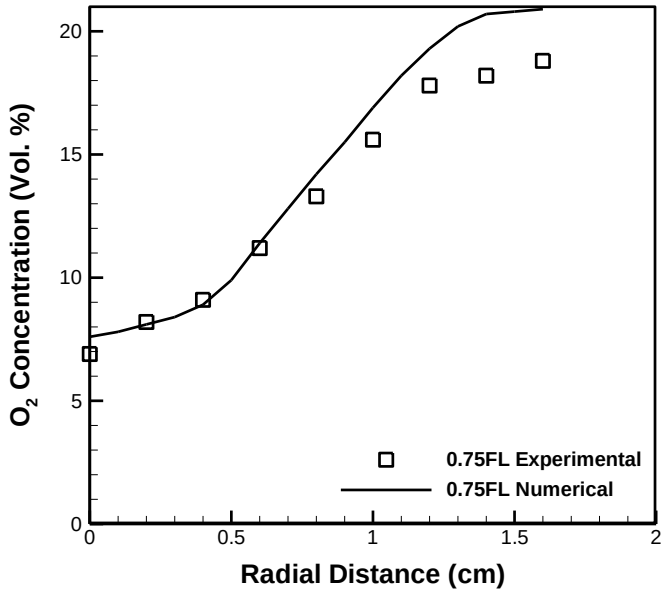

Fig. 266: O_2 concentration profiles for methyl decanoate flame at 0.75 FL at Φ=3

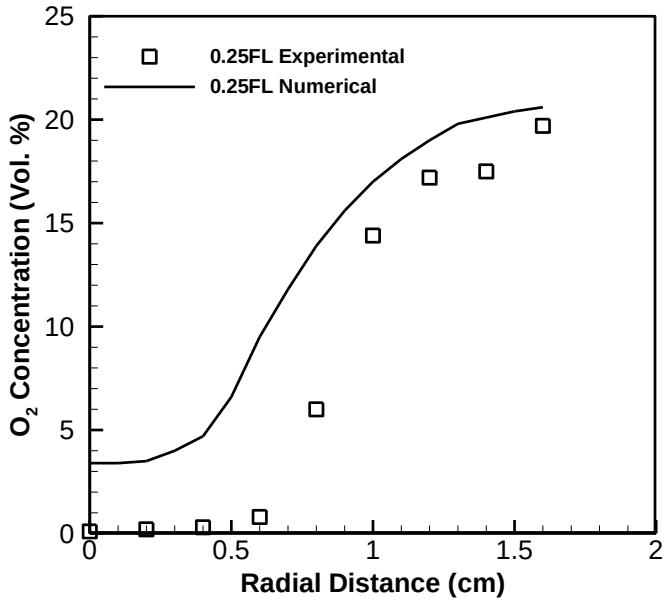

Fig. 267: O_2 concentration profiles for methyl decanoate+n-heptane flame at 0.25 FL at Φ=3

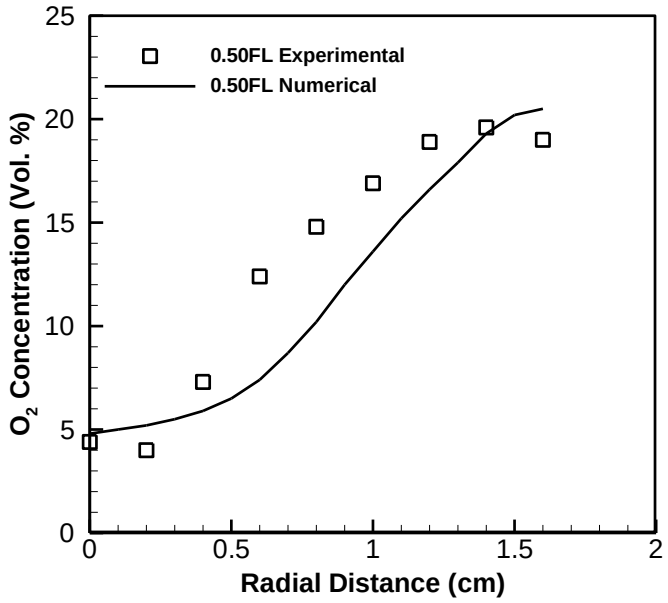

Fig. 268: O_2 concentration profiles for methyl decanoate+n-heptane flame at 0.5 FL at Φ=3

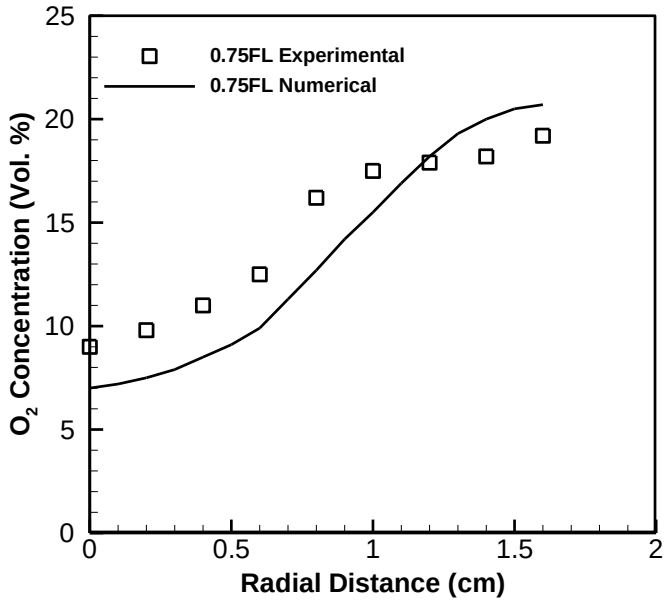

Fig. 269: O_2 concentration profiles for methyl decanoate+n-heptane flame at 0.75 FL at Φ=3

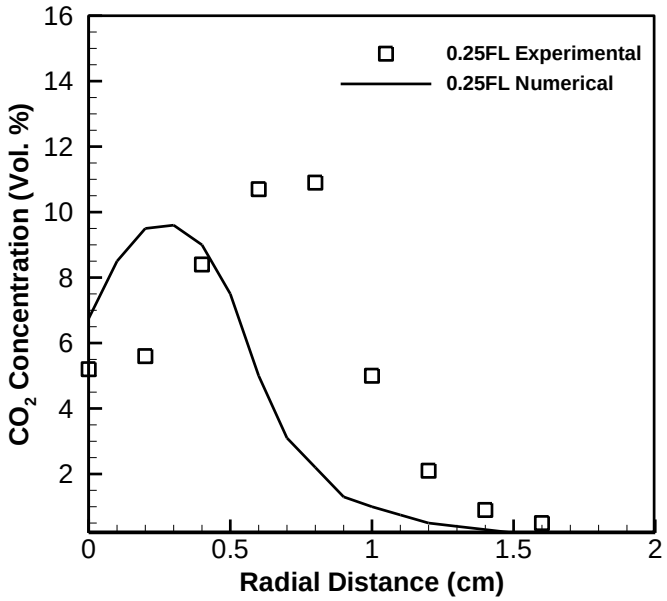

Fig. 270: CO_2 concentration profiles for n-heptane flame at 0.25 FL at Φ=2

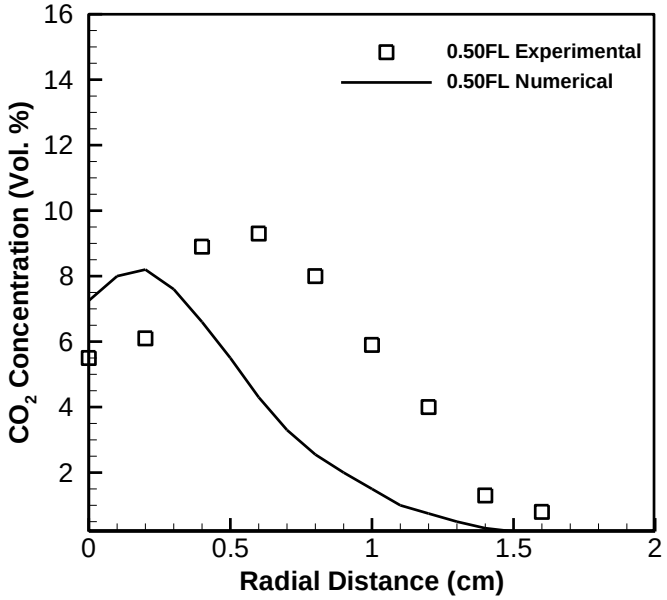

Fig. 271: CO_2 concentration profiles for n-heptane flame at 0.5 FL at Φ=2

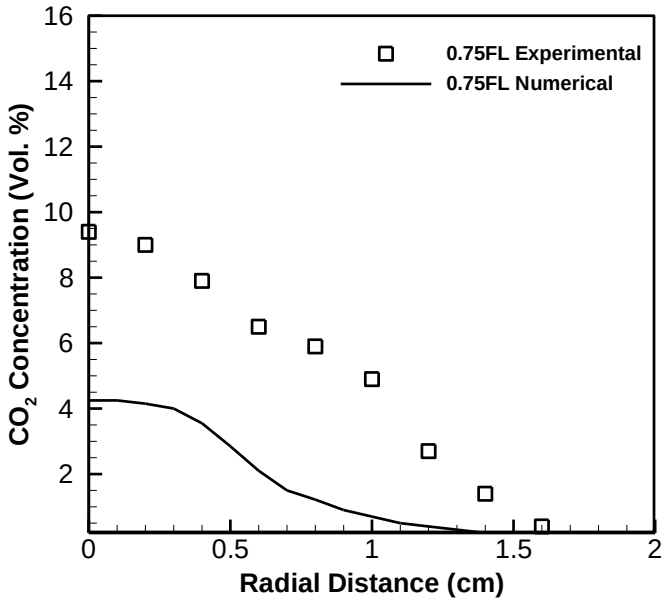

Fig. 272: CO_2 concentration profiles for n-heptane flame at 0.75 FL at Φ=2

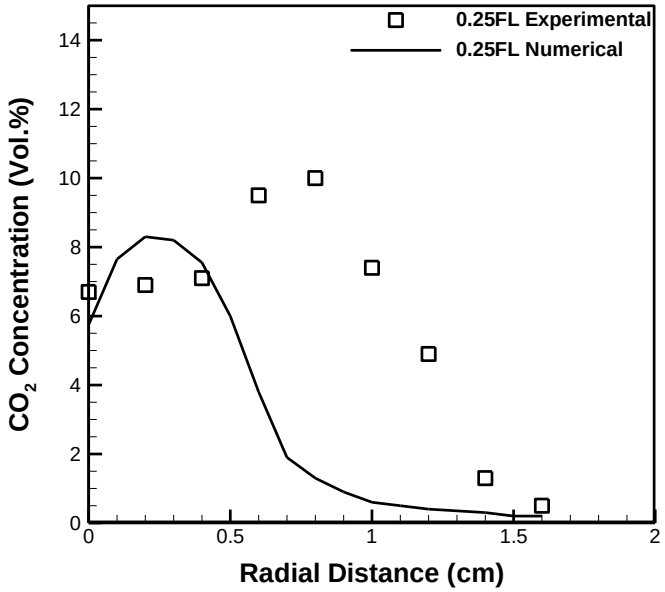

Fig. 273: CO_2 concentration profiles for methyl decanoate flame at 0.25 FL at Φ=2

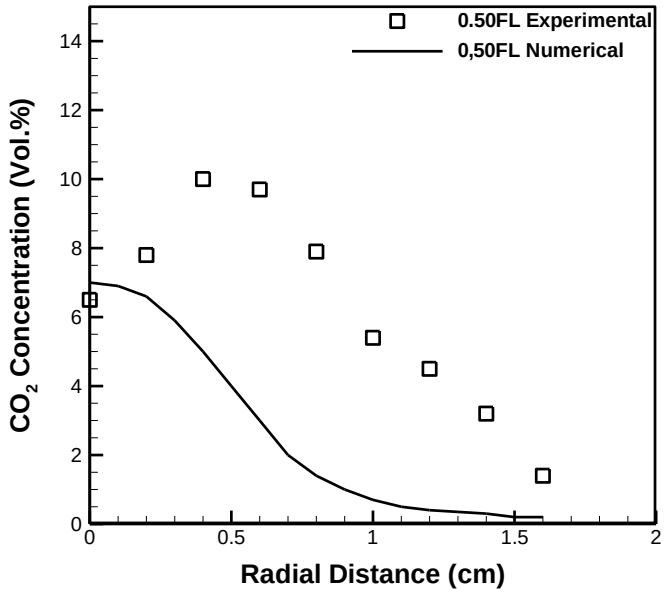

Fig. 274: CO_2 concentration profiles for methyl decanoate flame at 0.5 FL at Φ=2

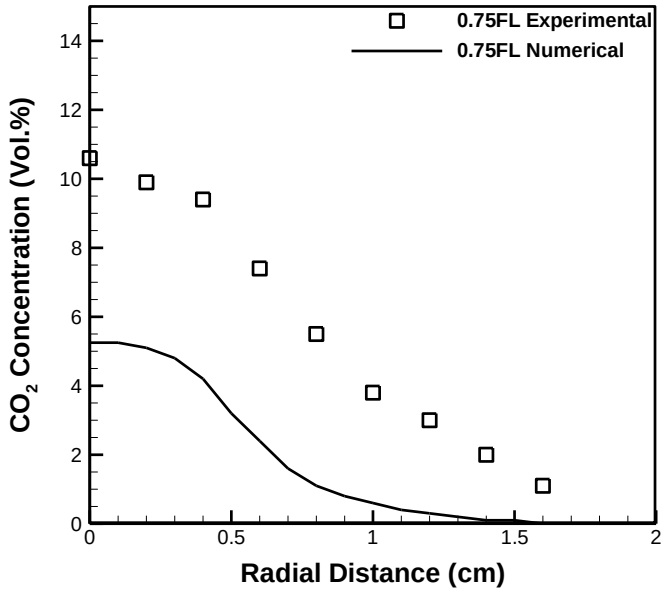

Fig. 275: CO_2 concentration profiles for methyl decanoate flame at 0.75 FL at Φ=2

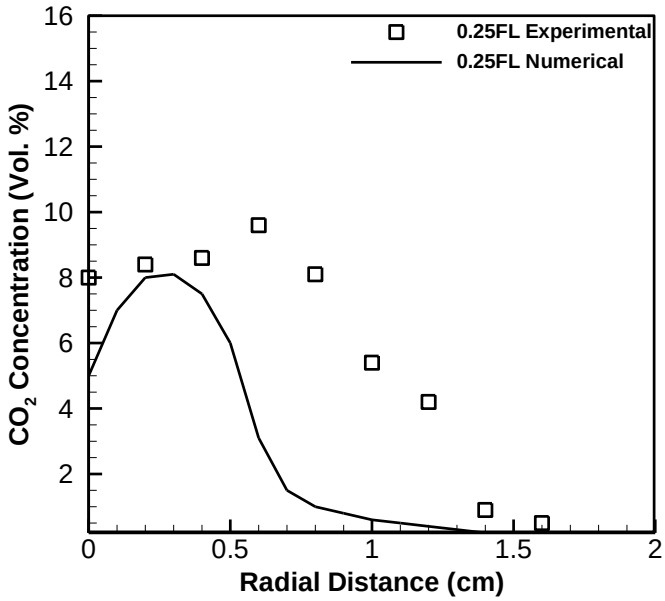

Fig. 276: CO_2 concentration profiles for methyl decanoate+n-heptane flame at 0.25 FL at Φ=2

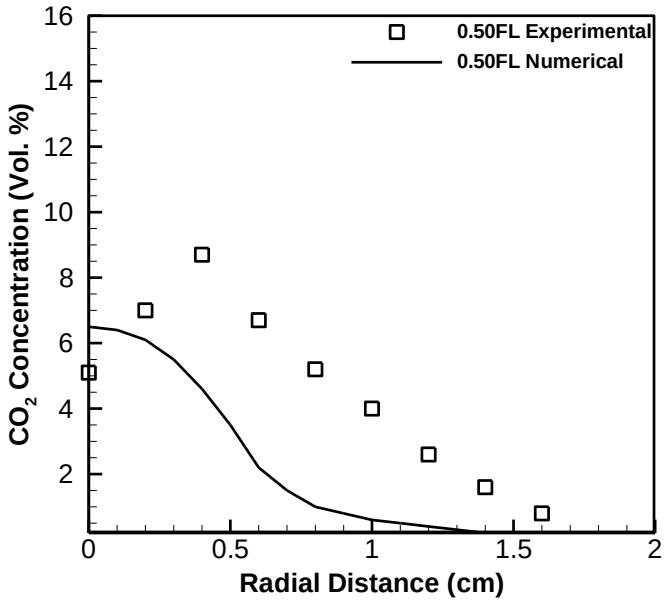

Fig. 277: CO_2 concentration profiles for methyl decanoate+n-heptane flame at 0.5 FL at Φ=2

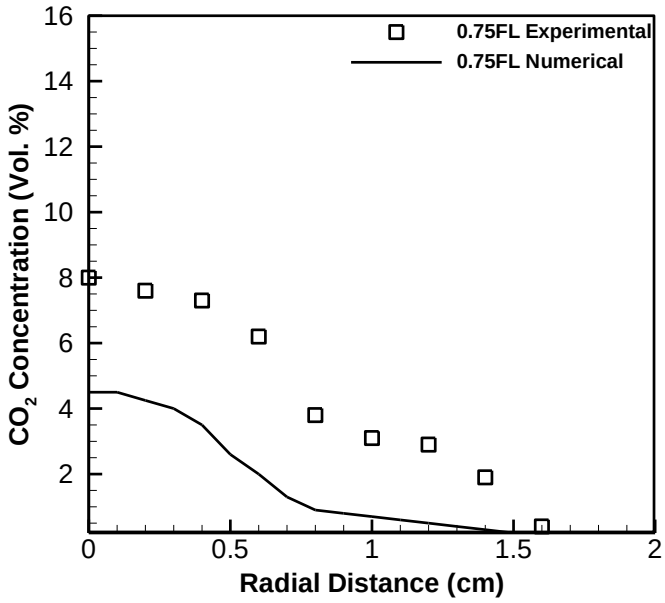

Fig. 278: CO_2 concentration profiles for methyl decanoate+n-heptane flame at 0.75 FL at Φ=2

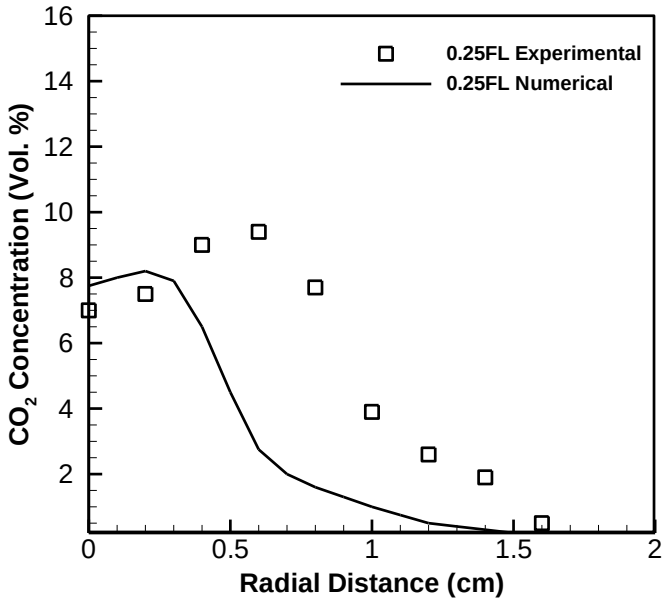

Fig. 279: CO_2 concentration profiles for n-heptane flame at 0.25 FL at Φ=3

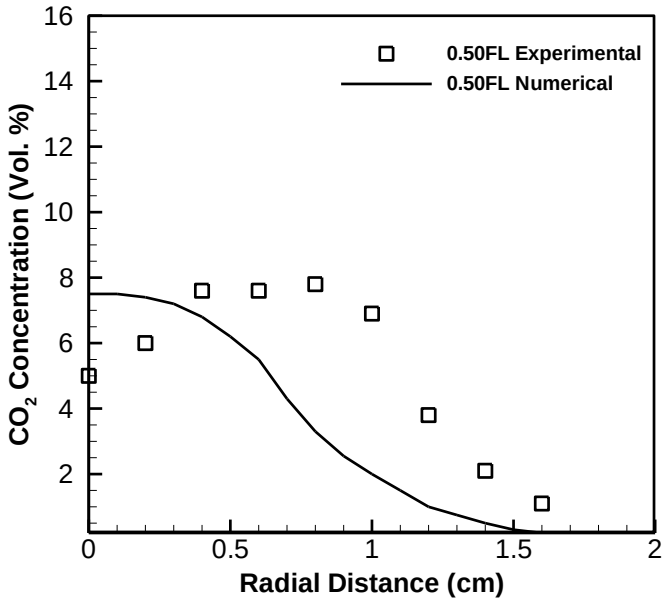

Fig. 280: CO_2 concentration profiles for n-heptane flame at 0.5 FL at Φ=3

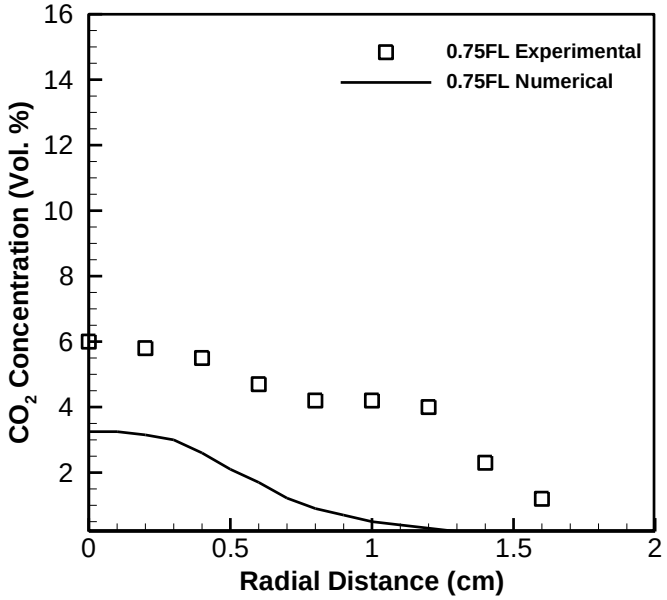

Fig. 281: CO_2 concentration profiles for n-heptane flame at 0.75 FL at Φ=3

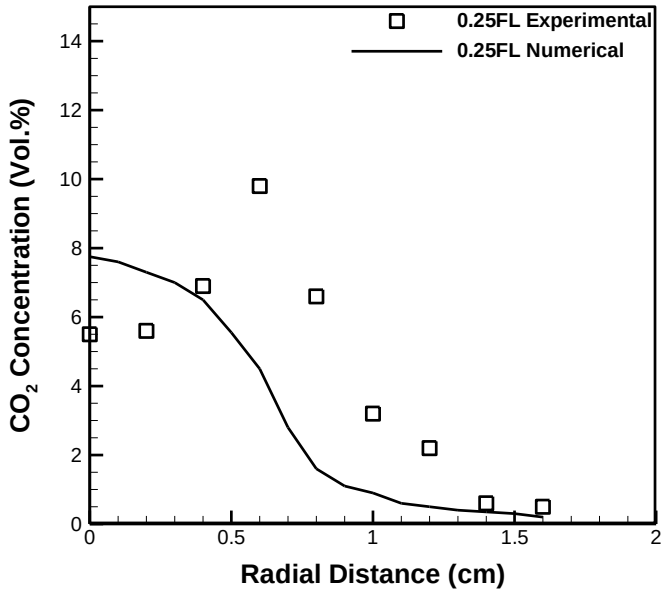

Fig. 282: CO_2 concentration profiles for methyl decanoate flame at 0.25 FL at Φ=3

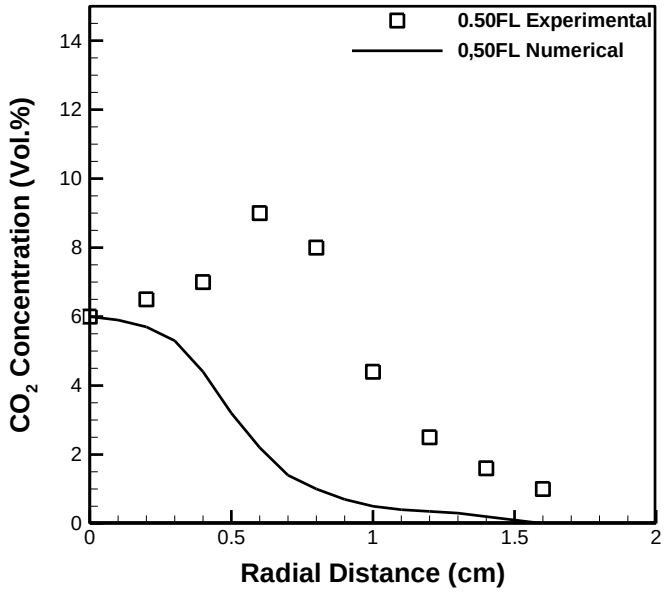

Fig. 283: CO_2 concentration profiles for methyl decanoate flame at 0.5 FL at Φ=3

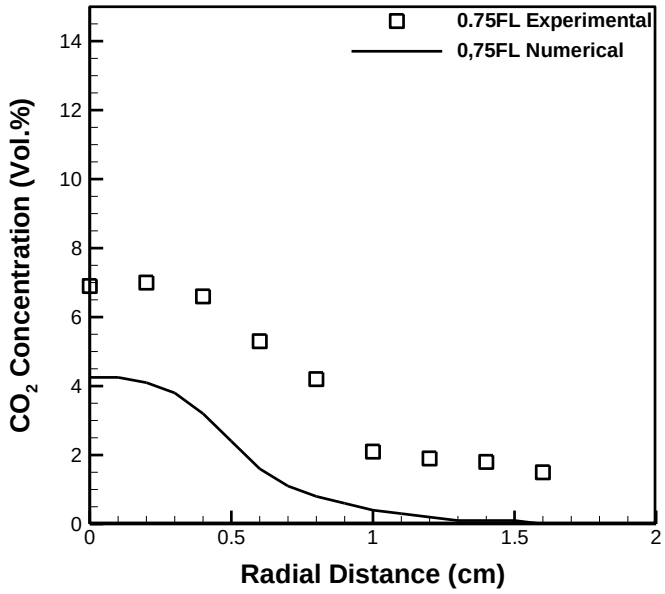

Fig. 284: CO_2 concentration profiles for methyl decanoate flame at 0.75 FL at Φ=3

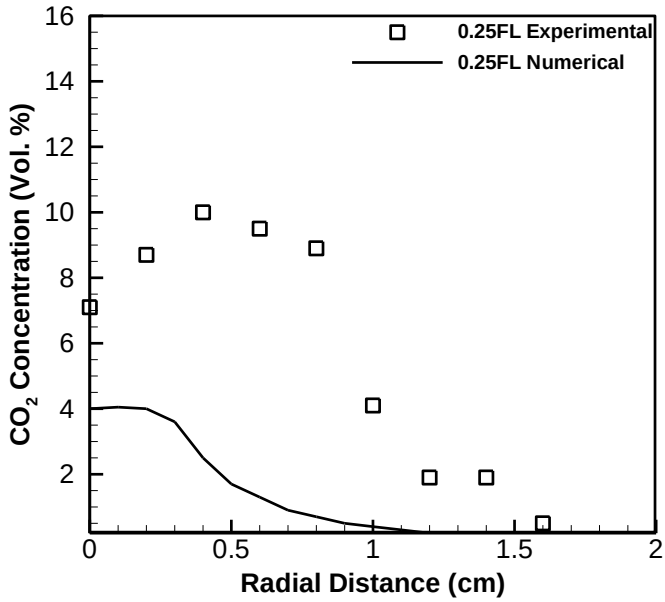

Fig. 285: CO_2 concentration profiles for methyl decanoate+n-heptane flame at 0.25 FL at Φ=3

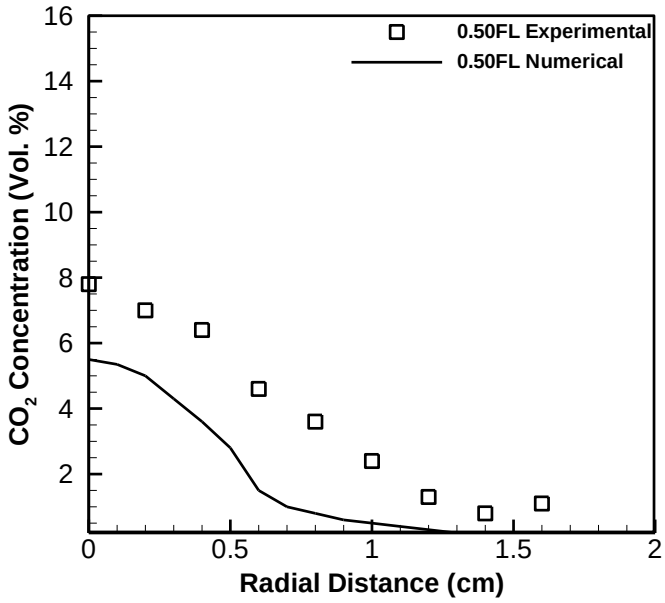

Fig. 286: CO_2 concentration profiles for methyl decanoate+n-heptane flame at 0.5 FL at Φ=3

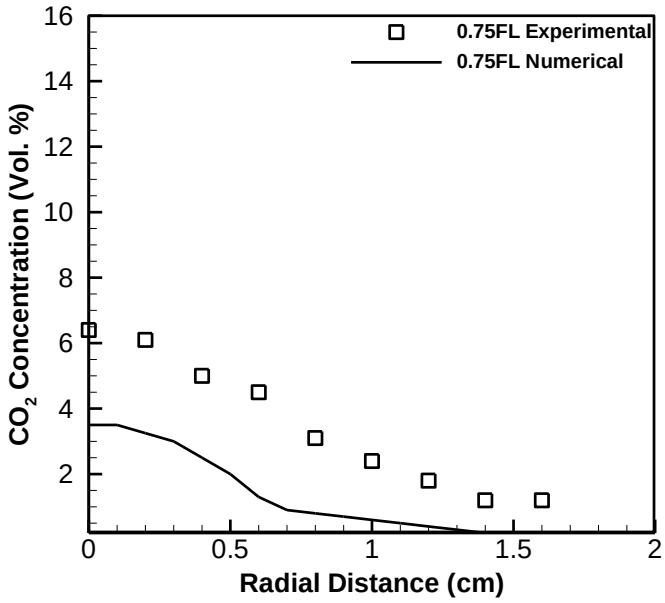

Fig. 287: CO_2 concentration profiles for methyl decanoate+n-heptane flame at 0.75 FL at Φ=3

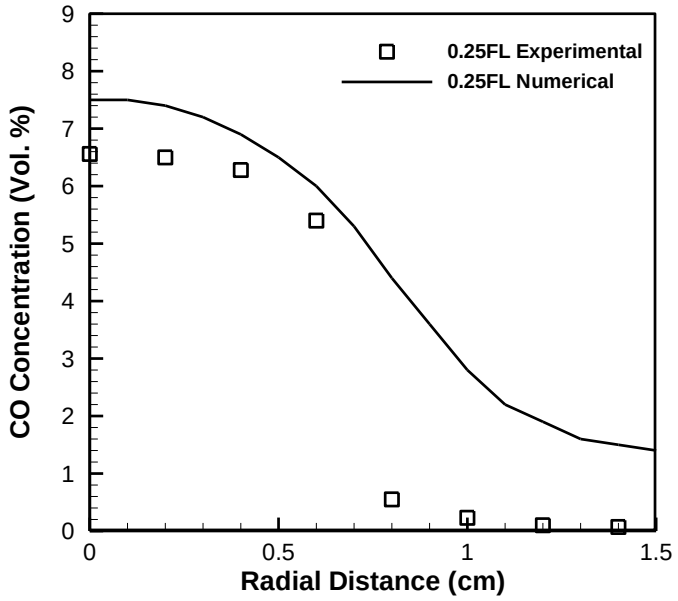

Fig. 288: CO concentration profiles for n-heptane flame at 0.25 FL at Φ=2

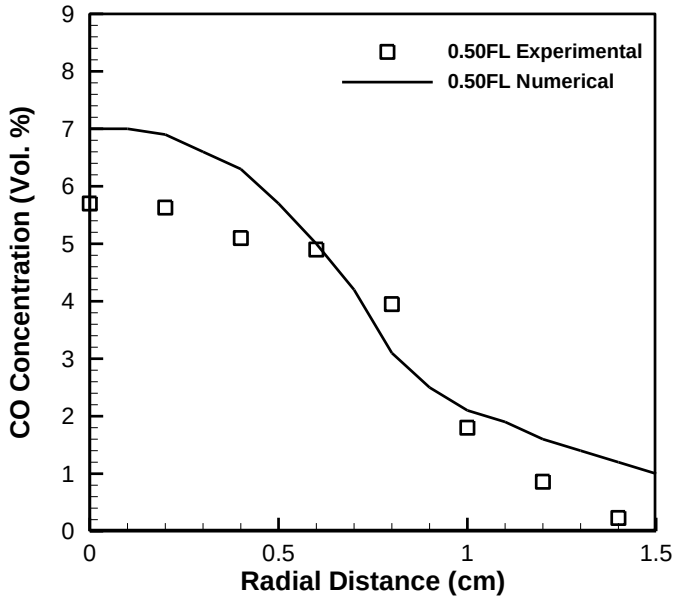

Fig. 289: CO concentration profiles for n-heptane flame at 0.5 FL at Φ=2

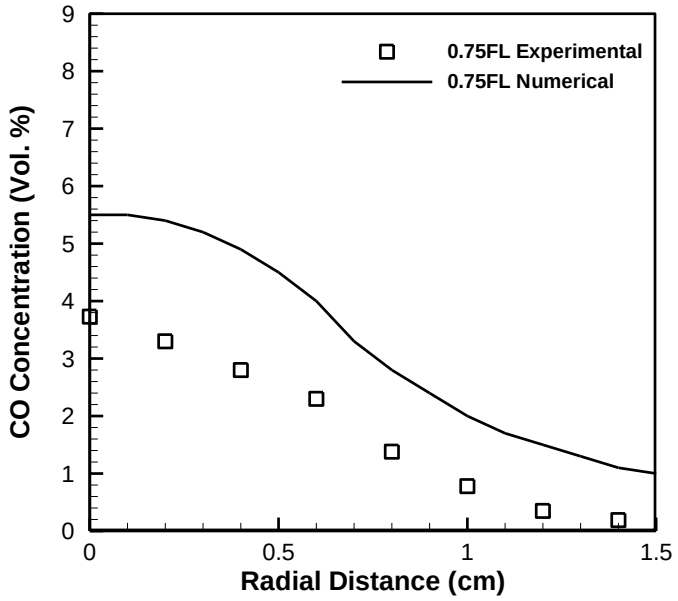

Fig. 290: CO concentration profiles for n-heptane flame at 0.75 FL at Φ=2

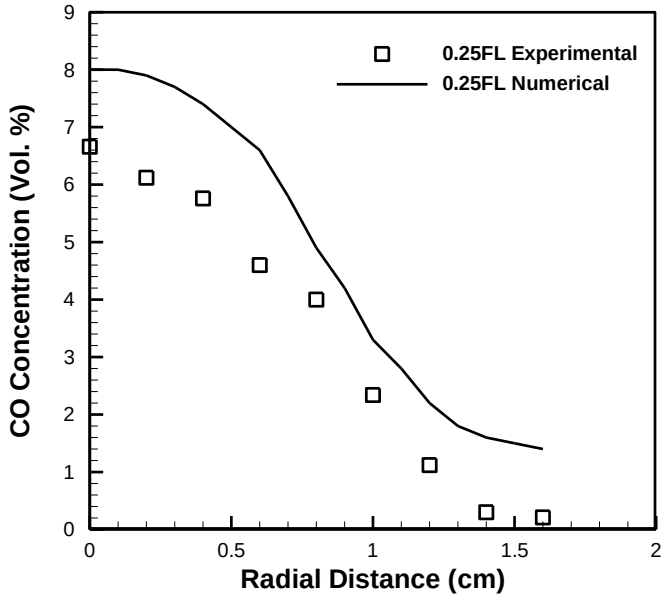

Fig. 291: CO concentration profiles for methyl decanoate flame at 0.25 FL at Φ=2

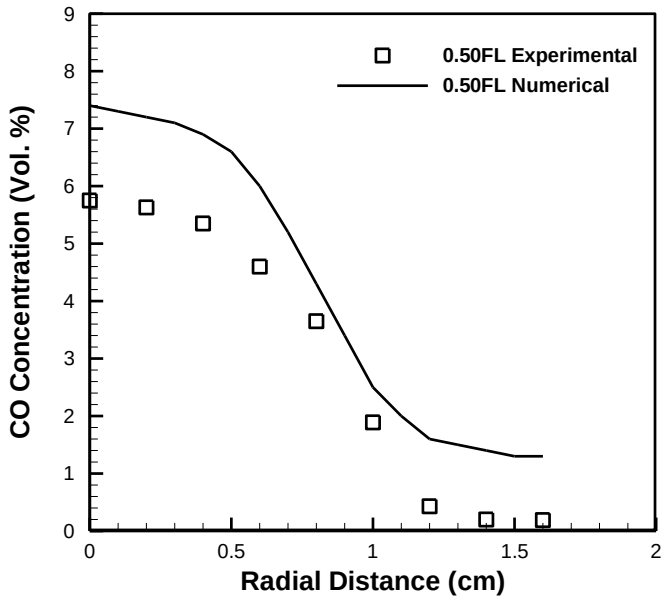

Fig. 292: CO concentration profiles for methyl decanoate flame at 0.5 FL at Φ=2

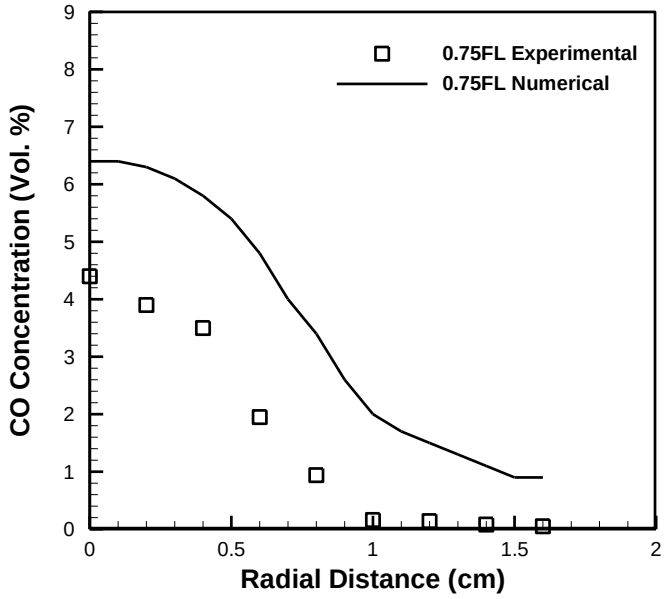

Fig. 293: CO concentration profiles for methyl decanoate flame at 0.75 FL at Φ=2

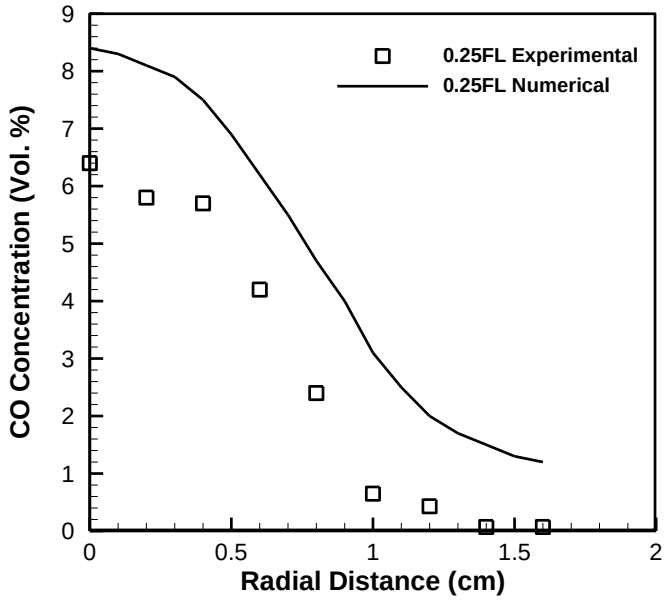

Fig. 294: CO concentration profiles for methyl decanoate+n-heptane flame at 0.25 FL at Φ=2

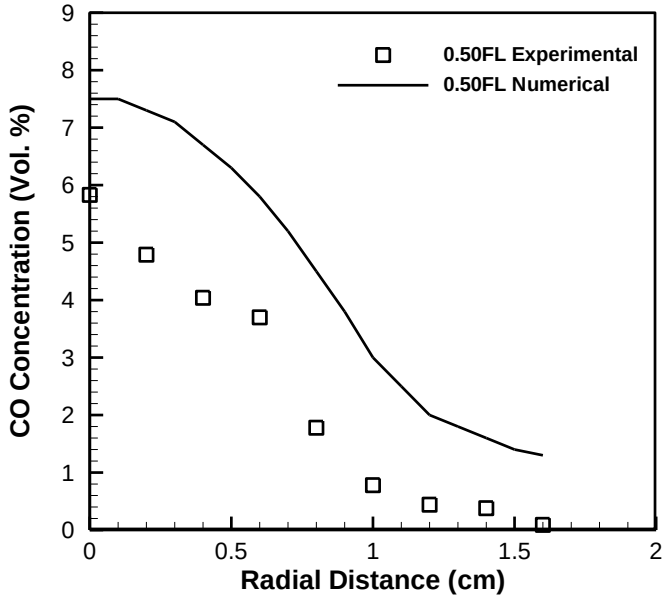

Fig. 295: CO concentration profiles for methyl decanoate+n-heptane flame at 0.5 FL at Φ=2

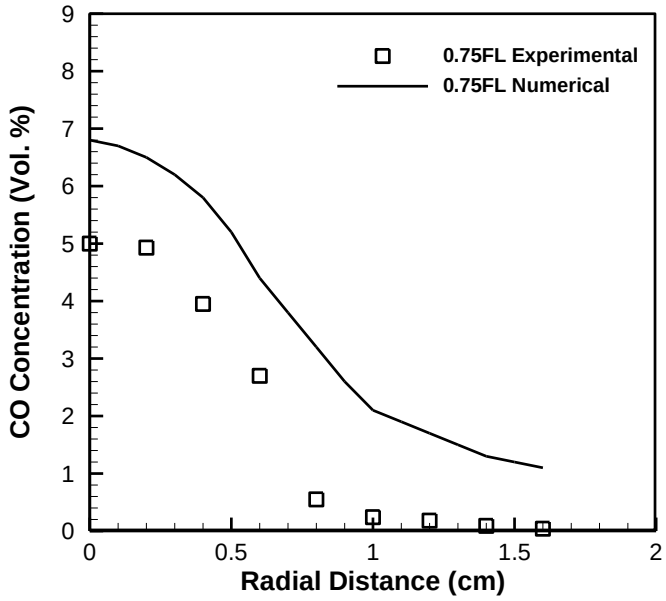

Fig. 296: CO concentration profiles for methyl decanoate+n-heptane flame at 0.75 FL at Φ=2

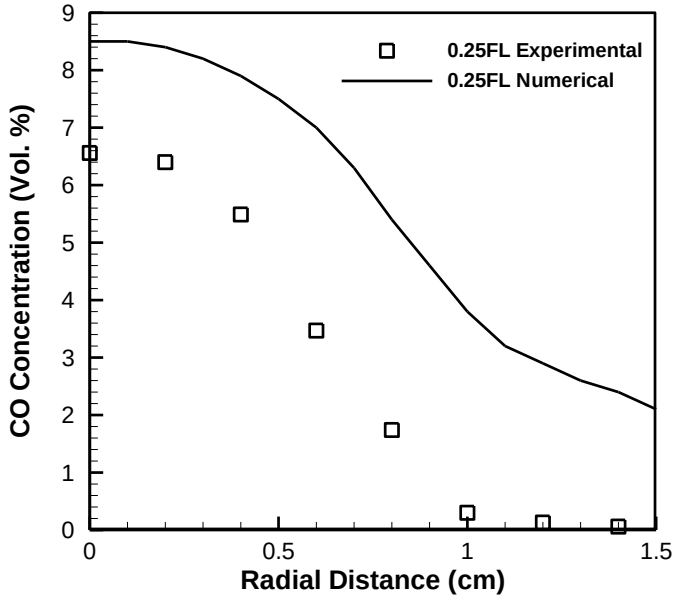

Fig. 297: CO concentration profiles for n-heptane flame at 0.25 FL at Φ=3

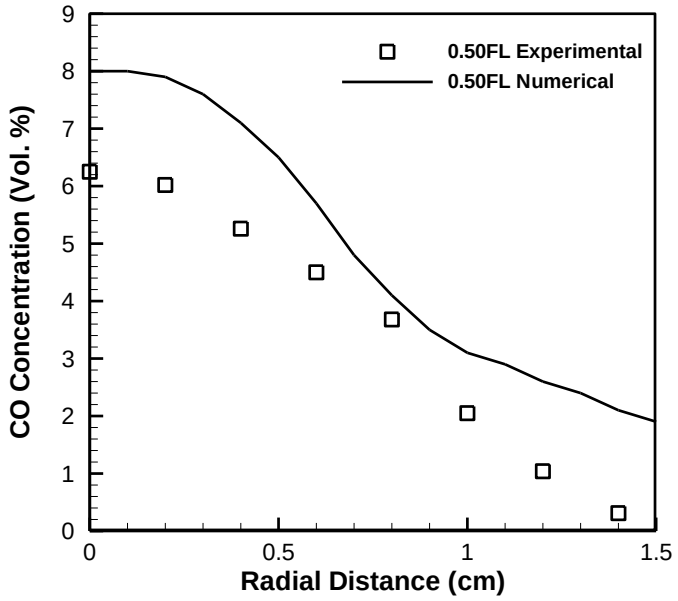

Fig. 298: CO concentration profiles for n-heptane flame at 0.5 FL at Φ=3

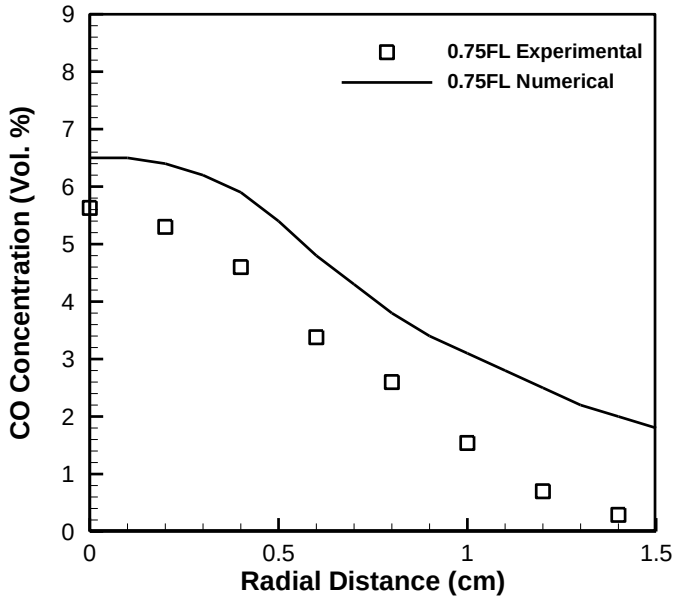

Fig. 299: CO concentration profiles for n-heptane flame at 0.75 FL at Φ=3

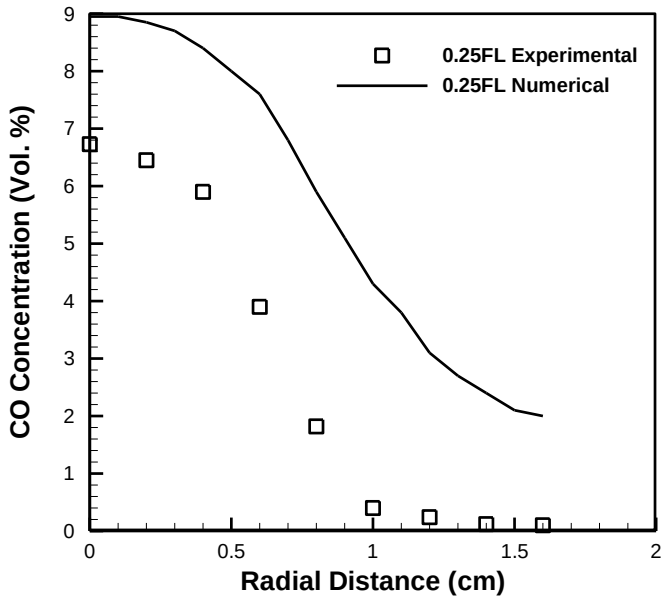

Fig. 300: CO concentration profiles for methyl decanoate flame at 0.25 FL at Φ=3

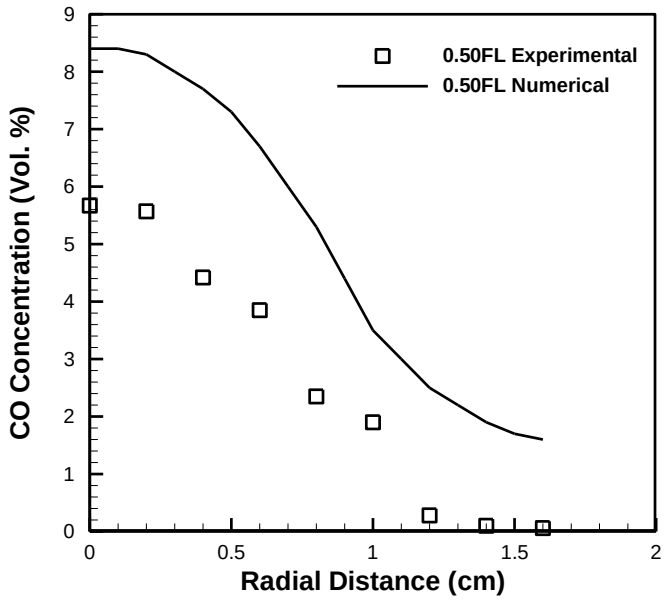

Fig. 301: CO concentration profiles for methyl decanoate flame at 0.5 FL at Φ=3

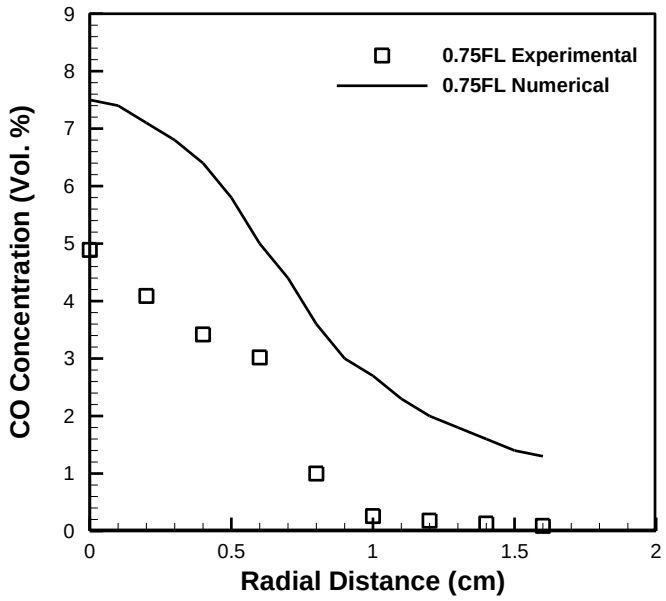

Fig. 302: CO concentration profiles for methyl decanoate flame at 0.75 FL at Φ=3

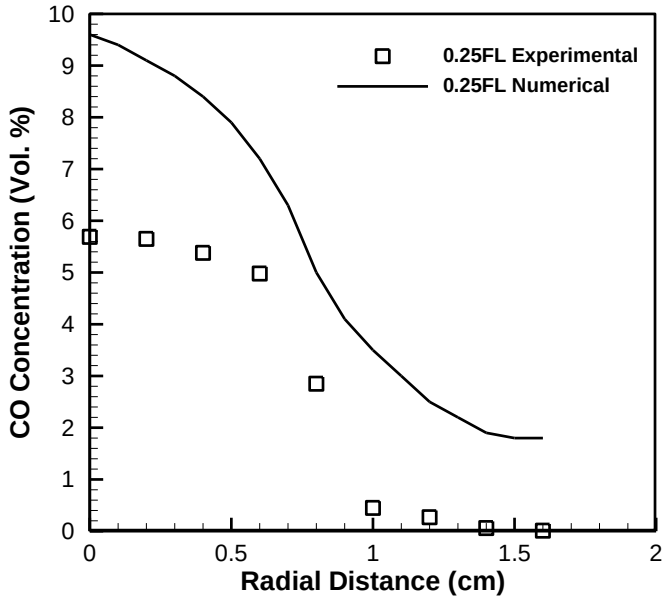

Fig. 303: CO concentration profiles for methyl decanoate+n-heptane flame at 0.25 FL at Φ=3

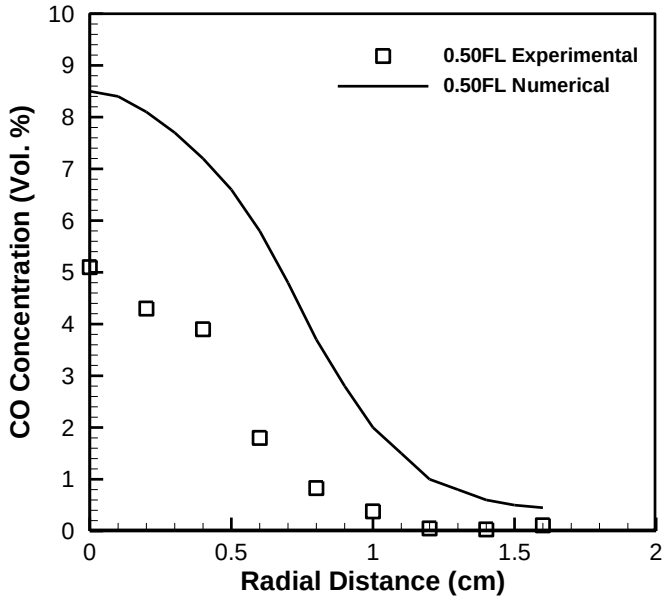

Fig. 304: CO concentration profiles for methyl decanoate+n-heptane flame at 0.5 FL at Φ=3

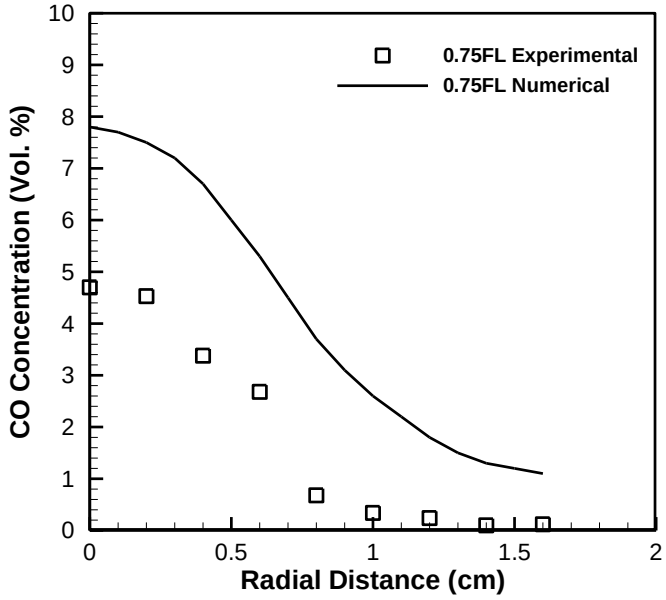

Fig. 305: CO concentration profiles for methyl decanoate+n-heptane flame at 0.75 FL at Φ=3

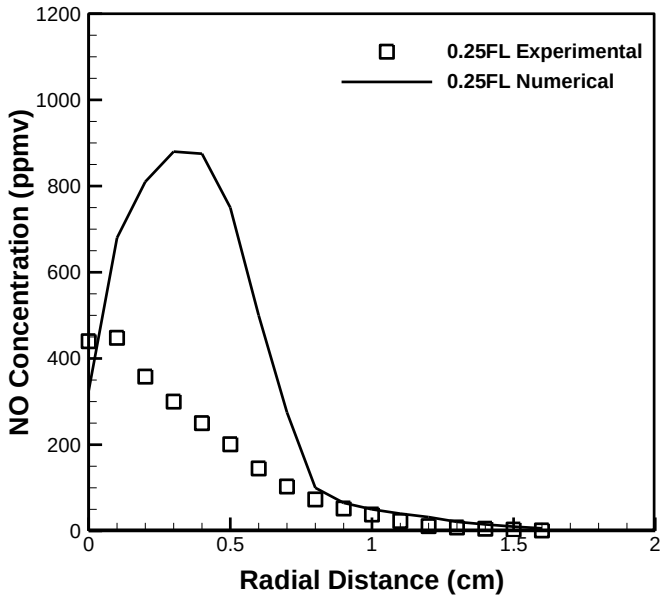

Fig. 306: NO concentration profiles for n-heptane flame at 0.25 FL at Φ=2

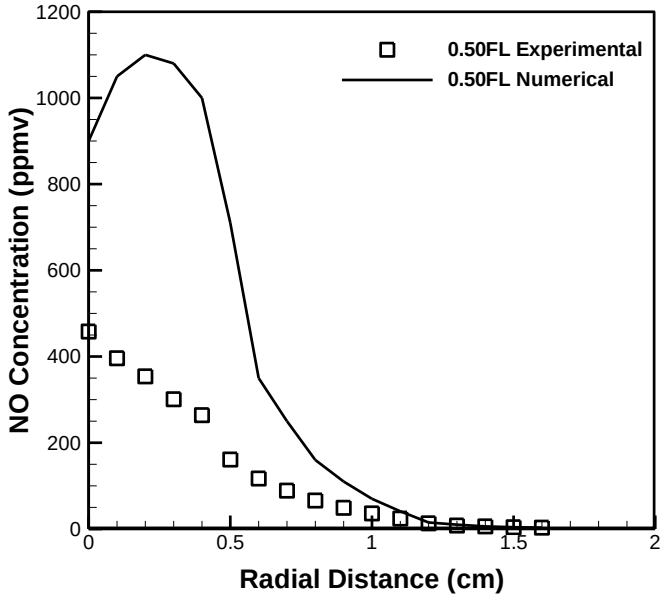

Fig. 307: NO concentration profiles for n-heptane at 0.5 FL at Φ=2

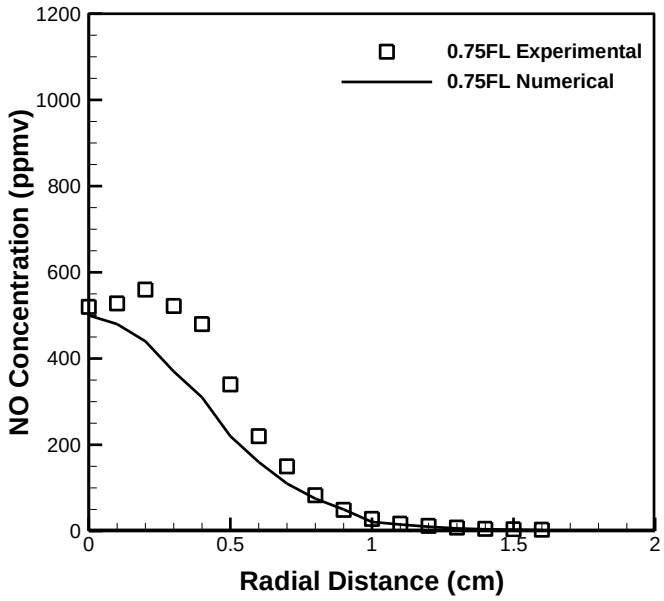

Fig. 308: NO concentration profiles for n-heptane flame at 0.75 FL at Φ=2

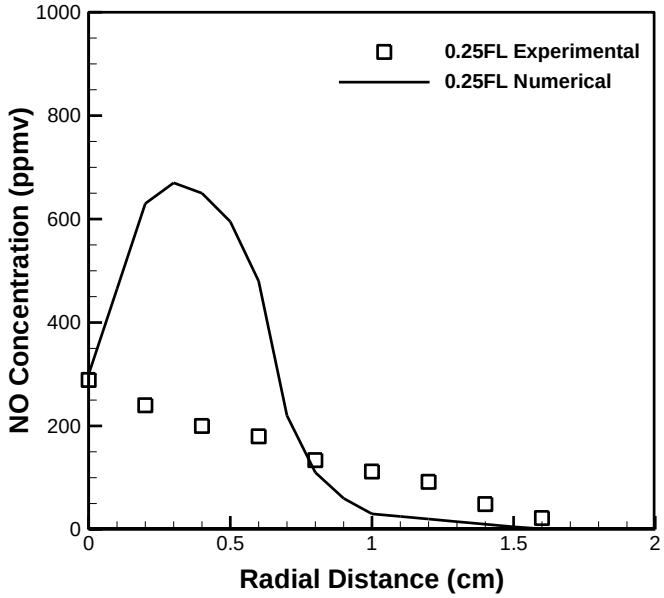

Fig. 309: NO concentration profiles for methyl decanoate flame at 0.25 FL at Φ=2

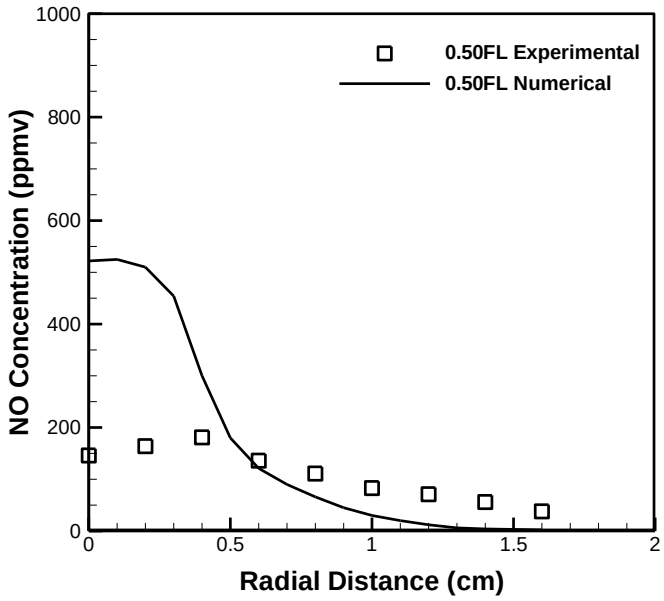

Fig. 310: NO concentration profiles for methyl decanoate flame at 0.5 FL at Φ=2

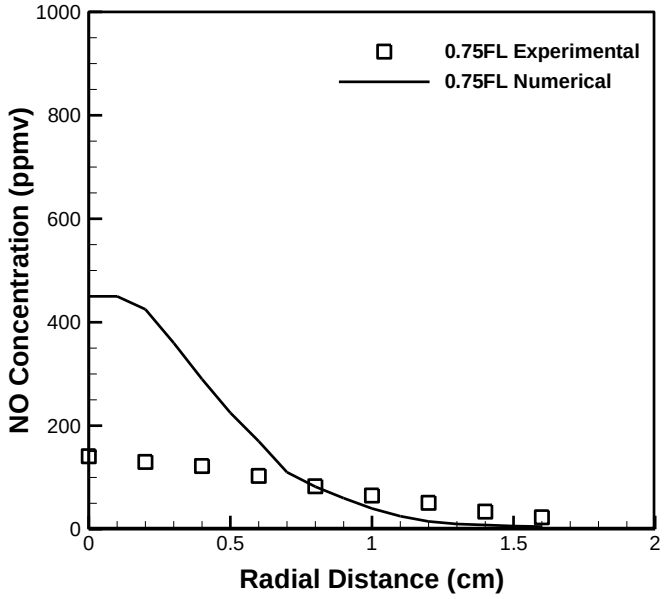

Fig. 311: NO concentration profiles for methyl decanoate flame at 0.75 FL at Φ=2

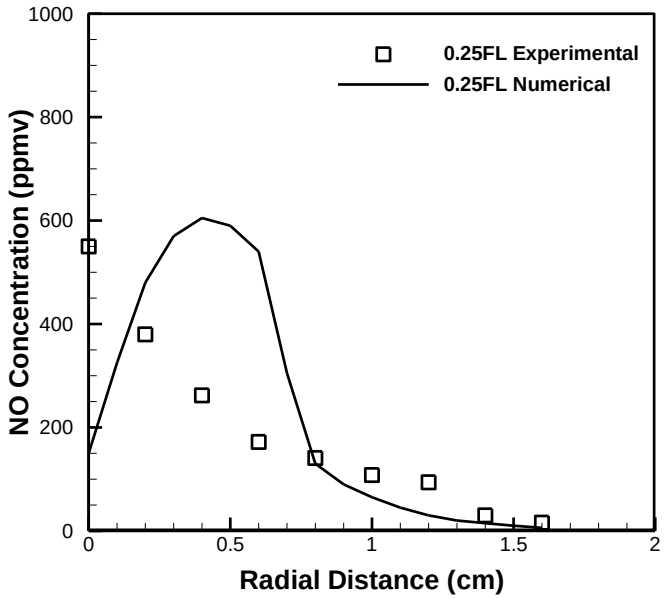

Fig. 312: NO concentration profiles for methyl decanoate+n-heptane flame at 0.25 FL at Φ=2

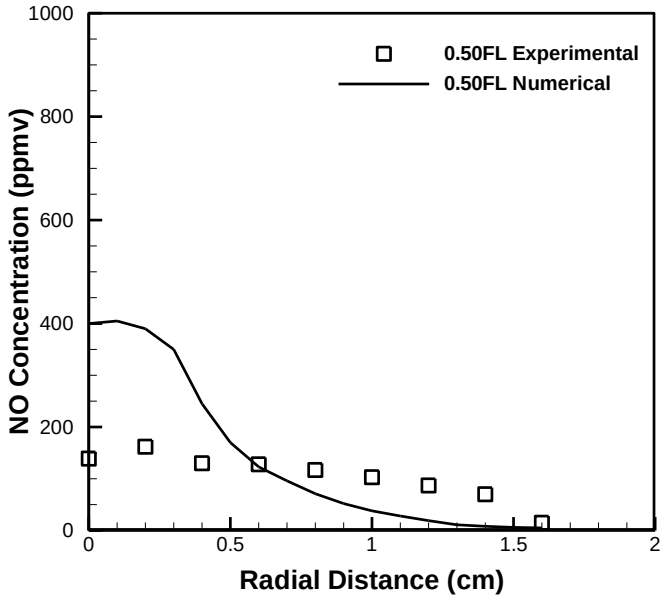

Fig. 313: NO concentration profiles for methyl decanoate+n-heptane flame at 0.5 FL at Φ=2

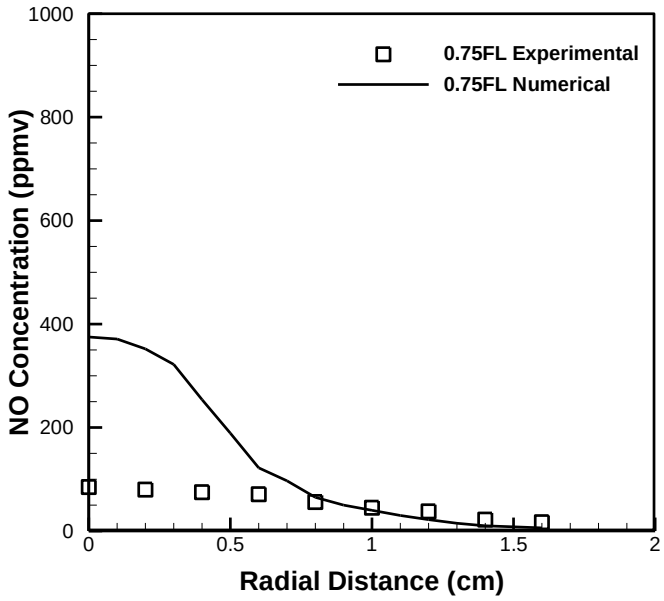

Fig. 314: NO concentration profiles for methyl decanoate+n-heptane flame at 0.75 FL at Φ=2

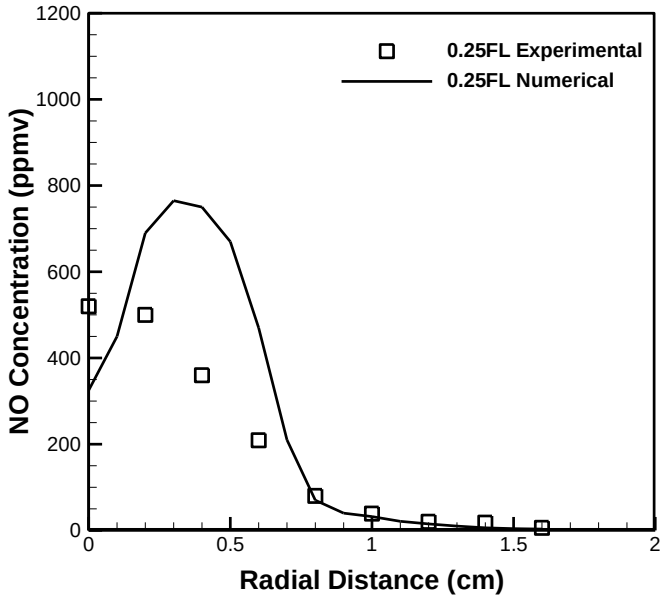

Fig. 315: NO concentration profiles for n-heptane flame at 0.25 FL at Φ=3

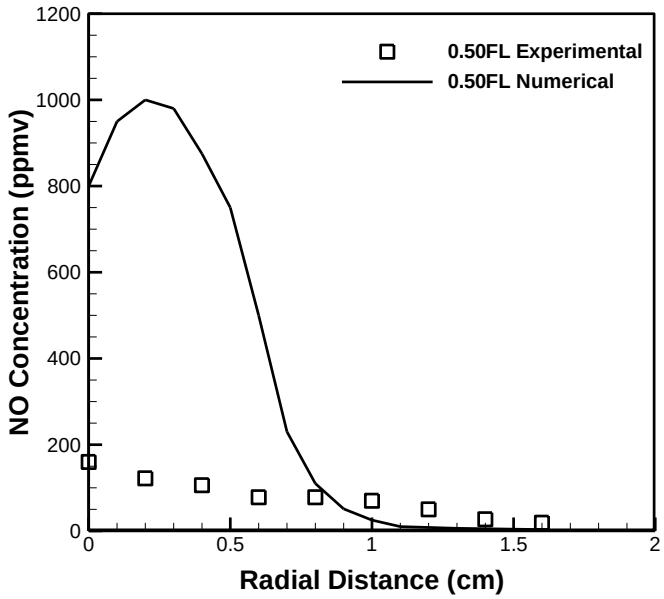

Fig. 316: NO concentration profiles for n-heptane flame at 0.5 FL at Φ=3

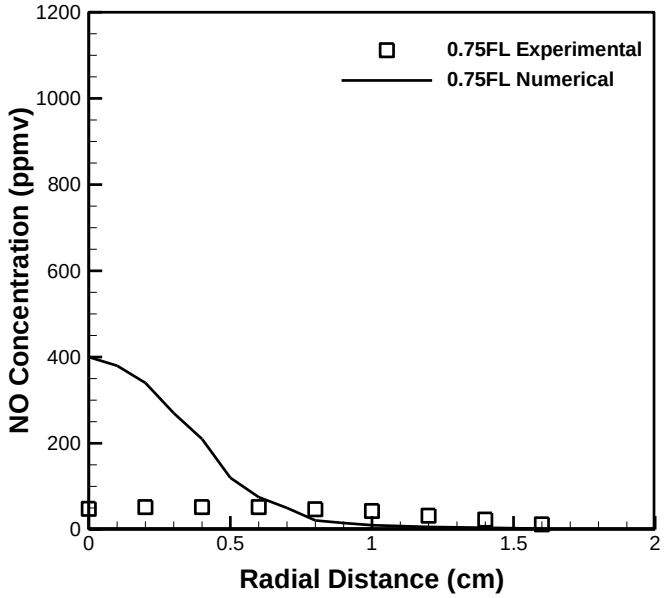

Fig. 317: NO concentration profiles for n-heptane flame at 0.75 FL at Φ=3

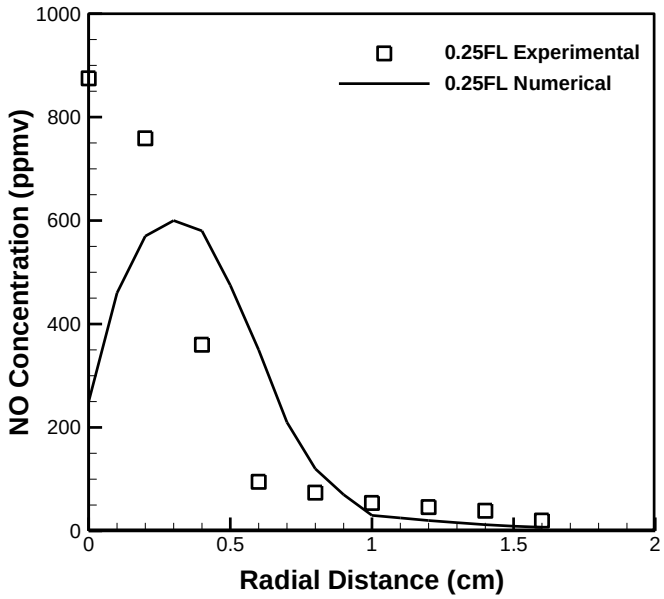

Fig. 318: NO concentration profiles for methyl decanoate flame at 0.25 FL at Φ=3

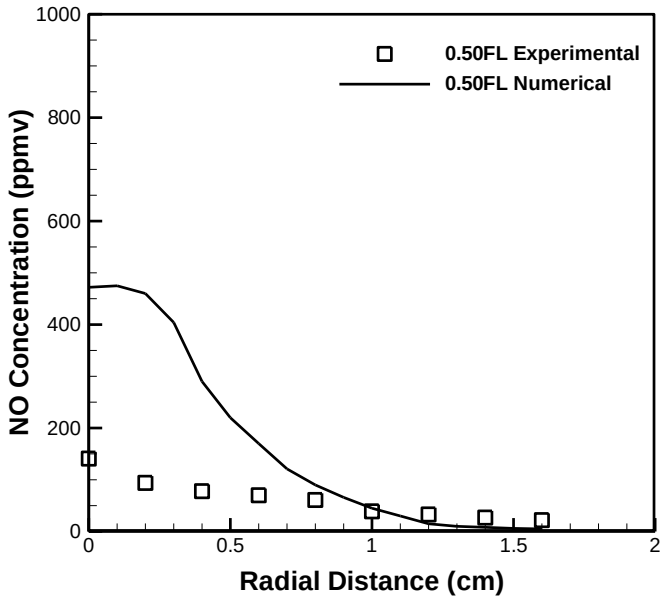

Fig. 319: NO concentration profiles for methyl decanoate flame at 0.5 FL at Φ=3

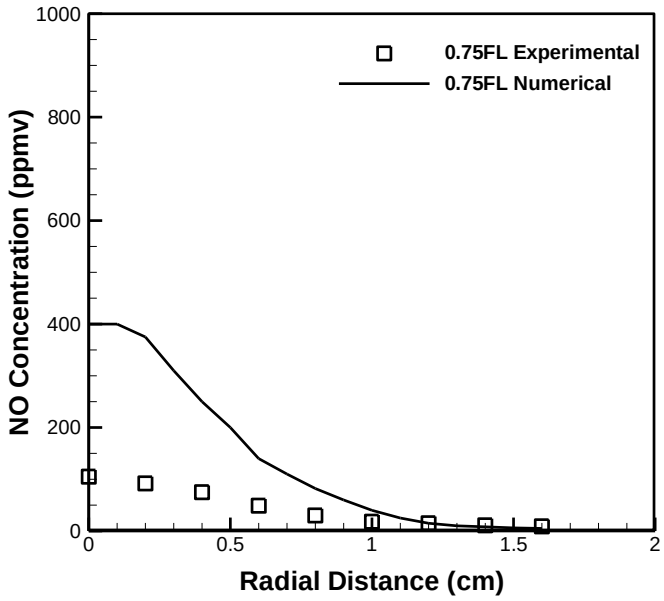

Fig. 320: NO concentration profiles for methyl decanoate flame at 0.75 FL at Φ=3

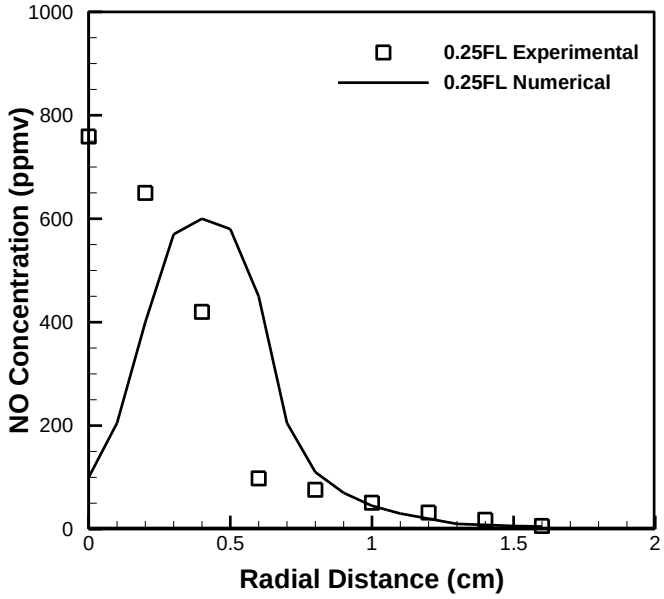

Fig. 321: NO concentration profiles for methyl decanoate+n-heptane flame at 0.25 FL at Φ=3

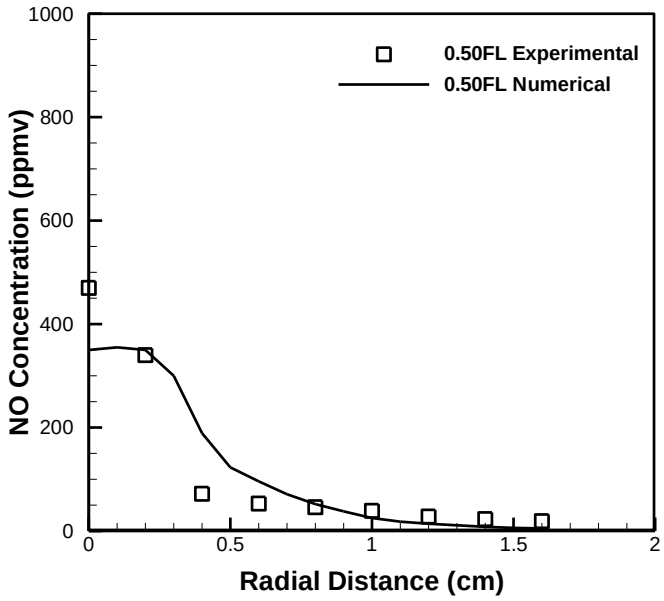

Fig. 322: NO concentration profiles for methyl decanoate+n-heptane flame at 0.5 FL at Φ=3

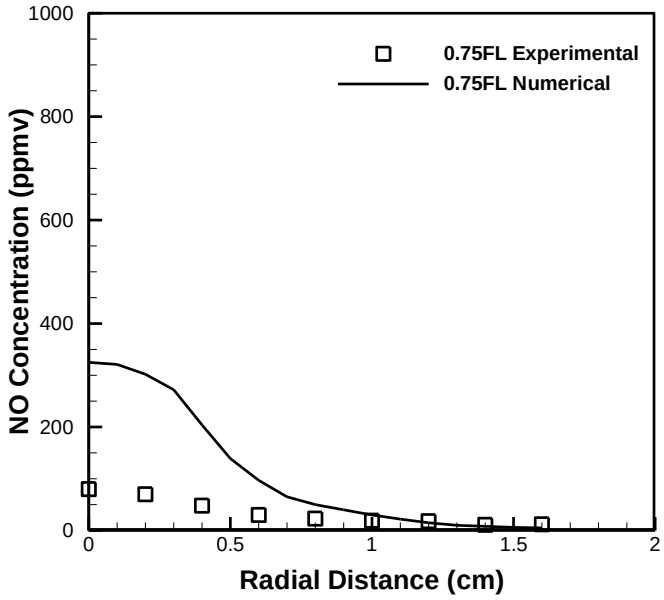

Fig. 323: NO concentration profiles for methyl decanoate+n-heptane flame at 0.75 FL at Φ=3

Chapter 7
Summary and Conclusions

The increasing demand of petroleum fuels has resulted in a fast depletion of the natural petroleum resources and has sparked interest in the development of alternate fuels. Biofuels, such as CME and SME, are viable alternatives to petroleum fuels, particularly for transportation. Their sources are renewable, locally grown, and free of sulfur and are carbon-neutral. Blends of CME/SME and diesel can be readily used in current automobiles with minimal modifications. The use of such biofuels currently accounts for less than 1% of the total fuel consumption in the USA and Europe; in addition to cost considerations, the lack of detailed knowledge of the combustion behavior of biofuel blends is a deterring factor in the widespread use of these fuels.

Reported studies of exhaust emissions of diesel engines when operated on neat transesterified biofuels and their blends with diesel fuel showed a reduction in CO, smoke and PM, along with an increase in NO. Also, an increase in fuel consumption was observed due to the slightly lower energy content of biofuels compared to petroleum fuels. A number of fuel properties (viscosity, heating value, density and cetane number), as well as engine operating conditions have been shown to affect emissions from engines using biofuels.

The objective of this study was to clarify controversies and discrepancies in literature and define the cause(s) of soot and NO_x formation in the flames of biofuel blends on a chemical basis. In order to investigate the primary mechanism(s) that contribute to soot and NOx formation and their interactions for the six biofuel blends on a chemical basis alone, the equivalence ratio was varied and its effects were studied on

the formation of soot and NO_x. The chemical aspect of the combustion of the fuels was decoupled from the physical. The variables measured included: global emission indices, global radiation fraction of heat release, inflame temperature, inflame species concentration, soot volume fraction, and the concentration of OH and CH radicals.

Numerical analysis with surrogate fuels (n-heptane and methyl decanoate) was performed with FLUENT software to predict temperature and concentration fields to substantiate the experimental results.

The following conclusions were drawn:

(a) For all fuel blends tested, the flame length decreased and the color changed from blue to blue-yellow as the equivalence ratio was increased from $\Phi = 1.2$ to $\Phi = 7$, indicating higher degree of combustion close to stoichiometric air-fuel ratio.

(b) The radiative heat fraction and the CO emission index significantly increased with increasing equivalence ratio showing increased tendency of the flames to produce soot at higher equivalence ratios due to incomplete combustion. The NO_x emissions decreased and the CO emissions increased as the equivalence ratio was increased from $\Phi = 1.2$ to $\Phi = 7$ for all fuels tested.

(c) A decrease in radiative heat fraction and the emission index of CO was observed as the volume percentage of CME and SME was increased in their respective blends An increase in the emission index of NO_x and a decrease in the CO emission index were observed as the volume percentage of CME and SME was increased in their respective blends. The presence of the fuel-bound oxygen was attributed to these observations.

(d) Peak temperatures occurred in the near-burner region (0.25 F_L) and reached a maximum at $\Phi = 1.2$. The temperatures were within experimental uncertainties, and did not significantly vary among fuel blends. At $\Phi = 3$ and 7, higher soot concentrations transferred heat away from the flame resulting in lower measured flame temperatures.

(e) The peak values of soot volume fraction occurred in the mid-burner and far-burner regions of the flames at high equivalence ratios $\Phi = 3$ and 7. The presence of more soot in these regions transferred heat away from the flame, thus resulting in lower flame temperatures compared to those in the near-burner region.

(f) As the equivalence ratio was increased, the flame radiative fraction of heat release increased significantly, indicating that burning soot primarily contributed to the flame radiation at these conditions. Although quantitative differences existed, the trends were similar in flames of biofuel-diesel blends and the pure fuel flames.

(g) Close to stoichiometric conditions, all fuels demonstrated similar distribution of inflame concentration of NO showing resemblance with temperature profiles. As the volume percentage of biofuel was increased in the blend, the NO emissions increased. NO formation at this condition was attributed to the thermal mechanism. At fuel rich conditions, the measured values of NO did not correlate with the peak measured temperatures.

(h) In order to determine the dominant route of soot and NOx formation in flames of the six biofuel blends, PLIF measurements of OH and CH radicals were carried

out. At Φ = 1.2, flames from all fuels produced peak OH concentration fields and peak temperatures. Also, it was observed that residence time increased with NO_x concentration. These results indicated the dominance of the thermal (Zeldovich) mechanism for all fuels at this condition.

(i) At fuel rich conditions, it was found that the population of OH radicals was low in the flames of all fuels, but significant CH radical concentrations were detected in all the flames, with the maximum population occurring in the CME B25 fuel flame. The presence of high concentrations of CH measured in the regions of peak NOx indicate that NOx formation is primarily through the Fenimore mechanism, rather than the thermal mechanism, at fuel-rich conditions.

(j) The results of the OH concentration and the soot concentration for all fuels tested at Φ = 1.2 condition shows that, OH radical dominated the soot oxidation process.

(k) Numerical model for the combustion of laminar flames of n-heptane, methyl decanoate and their blend was successfully developed. From the comparison, the experimental and numerical temperature and O_2 concentration profiles had shown a good agreement in most cases.

(l) Model predictions for the CO concentration compared to the experimental results for all fuels were within experimental uncertainties. All the results showed that the numerical flame was shorter and narrower than the experimental flame. This was mainly due to the rapid reaction assumption in the numerical

model and the presence of soot in the experimental flame that was ignored in the numerical model

(m) Based on experimental results, NO concentration was predicted to be higher for the n-heptane compared to methyl decanoate at every location. Experimental and the numerical model values for temperature profiles showed that n-heptane and biodiesel blend surrogate produced results within experimental uncertainties and met the criteria for the formation of NO by the Zeldovich mechanism.

Recommendations

(a) The present laminar flame results can be used as elemental blocks of modeling the turbulent flames in practical devices, such as engines.

(b) This study only reveals the part of soot formation process. In order to complete the whole picture, the soot production part needs to be investigated.

(c) Other alternative fuels such as bio-oils, ethanol and their blends with diesel and gasoline can be tested with the current experimental set-up.

(d) Current study focused on the fuel rich conditions. Future studies can focus on fuel lean conditions

(e) Effects of soot formation and radiative losses from the flame were neglected in the current numerical model which can be considered in further numerical analysis.

References

Agarwal, A., "Biofuels (alcohols and biodiesel) Applications as Fuels for Internal Combustion Engines," *Progress in Energy and Combustion Science*, 2007, Vol. 33, pp. 233-271.

Buyukkaya, E., "Effects of Biodiesel on a DI Diesel Engine Performance, Emission and Combustion Characteristics," *Fuel*, 2010, Vol. 89, pp. 3099-3105.

Canakci, M. and Van Gerpen, J., "Comparison of Engine Performance and Emissions for Petroleum Diesel Fuel, Yellow grease Biofuel and Soybean oil Biofuel," *Transactions of the ASABE*, 2003, Vol. 46, No. 4, pp. 937–944.

Chinthamony, S., "Structure of Gas Jet Diffusion Flames from an Elliptic Burner in an Elliptic Co-Flow," *Master's Thesis*, 2005, School of Aerospace and Mechanical Engineering, University of Oklahoma, Norman, OK.

Dhamale, N., Goepfert, B., Parthasarathy, R., and Gollahalli, S., "Combustion Properties of Turbulent Canola Methyl Ester and Diesel Flames" *48th AIAA Aerospace Sciences Meeting*, 2010, AIAA-2010-1354.

Dooley, S., Curran, H.J., and Simmie, J.M., "Autoignition Measurements and a Validated Kinetic Model for the Biodiesel Surrogate, Methyl Butanoate," *Combustion and Flame*, 2008, Vol. 153, pp. 2-32.

Durbin, T., Collins, J., Norbeck, J. and Smith, M., "Effects of Biofuel, Biofuel Blends, and a Synthetic Diesel on Emissions from Light Heavy-Duty Diesel Vehicles," *Environmental Science and Technology*, 2000, Vol. 34, No. 3, pp. 349-355.

Fernando, S., Hall, C., and Jha, S., "NO_x Reduction from Biodiesel Fuels," Energy and Fuels, 2006, Vol. 20, pp. 376-382.

Fisher, E., Pitz, W., Curran, H., and Westbrook, C., "Detailed Chemical Kinetic Mechanisms for Combustion of Oxygenated Fuels," *Proceedings of the Combustion Institute*, 2000, The Combustion Institute, Vol. 28, PA, pp. 1579-1586.

Fontaras, G., Kousoulidou, M., Karavalakis, G., Tzamkiozis, T., Pistikopoulos, P., Ntziachristos, L., Bakeas, E., Stournas, S., Samaras, Z., "Effects of low concentration biodiesel blend application on modern passenger cars. Part 1: Feedstock impact on regulated pollutants, fuel consumption and particle emissions," *Environmental Pollution*, 2010, Vol. 158, pp. 1451-1460.

Giakoumis, E., Rakopoulos, C., Dimaratos, A., and Rakopoulos, D., "Exhaust Emissions of Diesel Engines Operating Under Transient Conditions with Biodiesel Fuel Blends," *Progress in Energy and Combustion Science*, 2012, Vol. 38, pp. 691-715.

Graboski, M., and McCormick, R., "Combustion of Fat and Vegetable Oil Derived Fuels in Diesel Engines," *Progress in Energy and Combustion Science*, 1998, Vol. 24, pp. 125-164.

Graboski, M., McCormick, R., and Alleman, T., "The Effect of Biofuel Composition on Engine Emissions from a DDC Series 60 Diesel Engine," *National Renewable Energy Limited Report*, 2003, NREL/SR-510-31461.

Gumus, M., Sayin, C., and Canakci, M., "The Impact of Fuel Injection Pressure on the Exhaust Emissions of a Direct Injection Diesel Engine Fueled with Biodiesel-Diesel Fuel Blends," *Fuel*, 2012, Vol. 95, pp. 486-494.

Hanson, R., "Combustion Diagnostics: Planer Image Techniques," *Twenty-First Symposium (International) on Combustion*, The Combustion Institute, 1986, PA, pp.1677-1691.

Herbinet, O., Pitz, W., and Westbrook, C., "Detailed Chemical Kinetic Oxidation Mechanism for a Biodiesel Surrogate," *Combustion and Flame*, 2008, pp. 507-528.

Herbinet, O., Pitz, W., and Westbrook, C., "Detailed Chemical Kinetic Mechanism for the Oxidation of a Biodiesel Fuels Blend Surrogate," *Combustion and Flame*, 2010, pp. 893-908.

Hariharan, P., "An Experimental Study on Elliptic Turbulent Partially Premixed Propane / Hydrogen / Air Flames with and without Co-Flow Air," *Master's Thesis*, School of Aerospace and Mechanical Engineering, University of Oklahoma, Norman, OK.

Jha, S., Fernando, S., and Filipto, S., "Flame Temperature Analysis of Biodiesel Blends and Components," *Fuel*, 2008, Vol. 87, pp. 1982-1988.

Karabektas, M., "The Effects of Turbocharger on the Performance and Exhaust Emissions of a Diesel Engine Fuelled with Biodiesel," *Renewable Energy*, 2009, Vol. 34, pp. 989-993

Kitamura, T., Ito, T., Senda, J., and Fujimoto, H., "Detailed Chemical Kinetic Modeling of Diesel Spray Combustion with Oxygenated Fuels", *SAE Paper*, 2001, Paper No. 1262, pp.1-20.

Kuo, K., Principles of Combustion, John Wiley and Sons, 1986, New York.

Labeckas, G. and Slavinskas, S., "The Effect of Rapeseed Oil Methyl Ester on Direct Injection Diesel Engine Performance and Exhaust Emissions," *Energy Conversion & Management*, 2006, 47, pp. 1954-1967.

Love, N., "Effects of Equivalence Ratio and Iodine Number on NO_x emissions from the flames of the Biofuels and Hydrocarbons," *Ph. D. Dissertation*, 2009, School of Aerospace and Mechanical Engineering, University of Oklahoma, Norman, Oklahoma.

Love, N., Parthasarathy, R., and Gollahalli, S., "A Method for the Rapid Characterization of Combustion Properties of Liquid Fuels Using a Tubular Burner," *ASME International Mechanical Engineering Congress and Exposition*, 2007, Paper No. 42112.

Love N., Parthasarathy, R., and Gollahalli, S., "Rapid Characterization of Radiation and Pollutant Emissions of Biofuel and Hydrocarbon Liquid Fuels," *Journal of Energy Resources Technology*, 2009, Vol. 131, Paper No. 012202, pp. 1-9.

Love, N., Parthasarathy, R., and Gollahalli, S., "Effect of Iodine Number on NOx Formation in Laminar Flames of Oxygenated Biofuels," *International Journal of Green Energy*, Vol. 6, 2009, pp. 323-332.

Lujan, J., Bermudez, V., Tormos, B., and Pla, B., "Comparative analysis of a DI Diesel Engne Fuelled with Biodiesel Blends During the European MVEG-A Cycle: Performance and Emissions (II)," *Biomass and Bioenergy*, 2009, Vol. 33, pp. 948-956.

Ma F., and Hanna M., "Biodiesel production: a review," *Bio resource Technology*, 1999, Vol. 70, pp. 1-15.

McCormick, R., Graboski, M., Alleman, T. and Herring, A., "Impact of Biofuel Source Material and Chemical Structure on Emissions of Criteria Pollutants from a Heavy-Duty Engine," *Environmental Science and Technology*, 2001, 35, pp. 1742-1747.

Mueller C., Boehman A., and Martin G., "An Experimental Investigation of the Origin of Increased NOx Emissions when Fuelling a Heavy-Duty Compression–Ignition Engine with Soy Biodiesel," *SAE*, 2009, SAE technical paper no. 2009-01-1792.

Muralidharan, K., Vasudevan, D., and Sheeba, K., "Performance, Emission and Combustion Characteristics of Biodiesel Fuelled Variable Compression Ratio Engine," *Energy*, 2011, Vol. 36, pp. 5385-5393.

Neoh, K., Howard, J., and Sarofim, A., "Effect of Oxidation on the Physical Structure of Soot," *Twenty Symposium (International) on Combustion*, 1984, The Combustion Institute, PA, pp. 951-957.

Olikara, C., and Borman, G., "A Computer Program for Calculating Properties of Equilibrium Combustion Products with Some Applications to I.C. Engines," *SAE*, 1975, *SAE* Paper 750468.

Ozener, O., Yuksek, L., Ergenc, A., and Ozkan, M., "Effects of Soybean Biodiesel on a DI Diesel Engine Performance, Emission and Combustion Characteristics," *Fuel*, 2013, *Article in Press.* http://dx.doi.org/10.1016/j.fuel.2012.10.081

Pahl, G., "Biodiesel: Growing a new energy economy," *Chelsea Green Publishing Company*, 2008, 2nd Edition.

Reid, K., "Bioheat: Biofuel oil in focus – Part 1," *Fuel Oil News*, 2007.

Schumacher, L., Marshall, W., Krahl J., Wetherell, W. and Grabowski, M., "Biofuel Emissions Data from Series 60 DDC Engines," *Transactions of the ASABE*, 2001, Vol. 44, No. 6, pp. 1465–1468.

Sivathanu, Y., and Faeth, G., "Generalized State Relationships for Scalar Properties in Non-Premixed Hydrocarbon/Air Flames," *Combustion and Flame*, 1990, Vol. 82, pp. 211-230.

Szybist, J., McFarlane, J., and Bunting, B., "Simulation of Biodiesel Blends HCCI in a Modified Hatz Diesel Engine", 2008, SAE 2007-01-4010.

Szybist, J., Boehman, A., Taylor, J., and McCormick, R., "Evaluation of formulation strategies to eliminate the biofuel NOx effect", *Fuel Processing Technology*, 2005, Vol. 86, pp. 1109-1126.

Szybist, J., Kirby, S., and Boehman, A., "NO_x Emissions of Alternative Diesel Fuels: A Comparative Analysis of Biofuel and FT Diesel," *Energy Fuels*, 2005, Vol. 19, No. 4, pp 1484–1492.

Sun, J., Caton, J. and Jacobs, T., "Oxides of Nitrogen Emissions from Biodiesel-fuelled Diesel Engines," *Progress in Energy and Combustion Science*, 2010, Vol. 36, pp. 677-695.

Tamhane, A., "Statistics and Data Analysis," *Prentice-Hall, Inc.*, 2000.

Tat, M., and Van Gerpen, J., "Fuel property effects on biofuel," *ASAE Annual Meeting*, 2003, Paper No. 036034.

Turns, S., "An Introduction to Combustion: Concepts and Applications," *McGraw-Hill Inc.*, 2000, 2nd Edition.

Tyson K., "Biodiesel Handling and Use Guidelines," Retrieved January 7, 2010, *US Departm,ent of Energy National Renewable Energy Laboratory*, http://www.nrel.gov/docs/fy06osti/40555.pdf, 2004, NREL/TP-580-30004.

United States Department of Energy, "Annual Energy Review 2011," *DOE/EIA-0384(2011)*, 2012.

United States Energy Information Administration, "Short-term energy outlook," 2013, pp. 1-2.

United States Environmental Protection Agency, "A Comprehensive Analysis of Biofuel Impacts on Exhaust Emissions," *Draft Technical Report*, 2002, EPA420-P-02-001.

Wang, W., Lyons, D., Clark, N., and Gautam, M., "Emissions from Nine Heavy Trucks Fueled by Diesel and Biofuel Blends without Engine Modification," *Environmental Science and Technology*, 2000, 34, pp. 933-939.

Weiss, G., Chen, J., and Buchholz, B., "A Numerical Investigation into the Anomalous Slight NOx Increase When Burning Biofuel: A New _Old_ Theory," *Fuel Processing Technology*, 2007, pp. 659–667.

Xue, J., Grift, T., and Hansen, A., "Effect of Biodiesel on Engine Performances and Emissions," *Renewable and Sustainable Energy Reviews*, 2011, Vol. 15, pp. 1098-1116.

Yagi, S., and Iino, H., "Radiation from Soot Particles in Luminous Flames," *Eighth International Symposium on Combustion*, 1962, The Combustion Institute, PA, pp. 288-293.

Appendix A
Sample Calculations

Stoichiometric Equations:

$$C_xH_{2y}O_{2z} + a\,(O_2 + 3.76N_2) \rightarrow xCO_2 + y\,H_2O + (3.76a)\,N_2$$

$$a = x + \frac{y}{2} - z$$

$$AF_{stoic} = \frac{a(32 + 3.76 \cdot 28)}{12x + 2y + 32z}$$

For diesel fuel ($C_{14.4}H_{24.9}$):

$$a = 14.4 + \frac{12.45}{2} - 0 = 20.625$$

$$AF_{stoic} = \frac{20.625(32 + 3.76 \cdot 28)}{12 \cdot (14.4) + 24.9 + 32 \cdot (0)} = 14.32$$

For CME ($C_{19}H_{36}O_2$):

$$a = 19 + \frac{18}{2} - 1 = 27$$

$$AF_{stoic} = \frac{27(32 + 3.76 \cdot 28)}{12 \cdot (19) + 36 + 32 \cdot (1)} = 12.52$$

For CME B75:

Mole Fraction for CME in CME B75= 0.69

Mole fraction for Diesel in CME B75= 0.31

({0.69 * $C_{19}H_{36}O_2$ + 0.31 * $C_{14.4}H_{24.9}$} = $C_{17.52}H_{32.42}O_{1.35}$)

$C_{17.52}H_{32.42}O_{1.35}$ + 118.819 (0.79N_2 + 0.21O_2) → 17.522 CO_2 + 93.867 N_2 + 16.212 H_2O

$$AF_{Stoic} = \frac{3426.74}{200.13 + 64.19} = 12.964$$

Jet Exit Velocity of Burner:

$$u_{exit} = \frac{\dot{m}_{mix}}{\rho_{mix} \cdot A_{Exit}} = \frac{\dot{m}_{air} + \dot{m}_{fuel}}{\rho_{mix} \cdot A_{Exit}}$$

Given:

$\dot{m}_{air} = 4.2 \text{ x } 10^{-5} \text{ kg/s}$ $\qquad$ $\rho_{mix} = 0.66 \text{ kg/m}^3$

$\dot{m}_{fuel} = 1.99 \text{ x } 10^{-5} \text{ kg/s}$ $\qquad$ $A_{Exit} = \frac{\pi \cdot 0.0095^2}{4} = 7.09 \text{ x } 10^{-5} \text{ m}^2$

$$u_{exit} = \frac{\left(4.2 \text{ x } 10^{-5}\right) + \left(1.99 \text{ x } 10^{-5}\right)}{0.66 \cdot \left(7.09 \text{ x } 10^{-5}\right)} = 1.32 \text{ m/s}$$

Flame temperature correction:

Due to radiative, and conductive heat losses the temperature read from the thermocouple bead was less than the true flame temperatures. Thus it was necessary to correct for these losses. This was done with the use of the energy balance equation for the thermocouple bead presented below (Jha et al., 2008, Hariharan, 2004, Chinthamony, 2005).

$$h\, A_b \left(T_g - T_b\right) = \frac{k_w\, A_w \left(T_b - T_\infty\right)}{L} + \sigma \varepsilon A_b \left(T_b^4 - T_\infty^4\right)$$

where;

A_b = Surface area of the bead = πd^2 = 1.256E-07 m

A_w = Cross-sectional area of the thermocouple wires = $\frac{\pi (\text{wire diameter})^2}{4}$

= 1.266E-08 m

h = Convective heat transfer coefficient between the thermocouple bead and surrounding gases

h = 0.8 x $Re^{0.25}$ x k/bead dia = 269.53 W/m^2K

k_w = Thermal conductivity of the thermocouple wire

L = Length of the thermocouple wire = 0.3 m

T_b = Uncorrected thermocouple bead temperature = 1015 K

T_g = True flame temperature

T_∞ = Cold junction temperature or room temperature

σ = Stefan-Boltzmann constant = 5.67E-08 W/m^2K^4

ε = Emissivity of the thermocouple bead wire = 0.22

Emission Index Calculation:

$$EI_{NO} = \left(\frac{\chi_{NO}}{\chi_{CO} + \chi_{CO_2}} \right) \left(\frac{N \cdot MW_{NO}}{MW_f} \right) \cdot 1000$$

Given:

Concentration of NO = 27 ppm

Concentration of CO_2 = 0.9 %

Concentration of CO = 8 ppm

MW_f = 296 kg/kmol MW_{CO} = 28 kg/kmol

MW_{NO} = 30 kg/kmol MW_{CO_2} = 44 kg/kmol

N = Number of moles of carbon in a mole of fuel = 19

$$\chi_{NO} = \frac{27}{1 \text{ x } 10^6} = 2.7 \text{ x} 10^{-5}$$

$$\chi_{CO_2} = \frac{0.9}{100} = 0.009$$

$$\chi_{CO} = \frac{8}{1 \text{ x } 10^6} = 8 \text{ x } 10^{-6}$$

$$EI_{NO} = \left(\frac{2.7 \text{ x} 10^{-5}}{\left(8 \text{ x } 10^{-6}\right) + \left(0.009\right)} \right) \left(\frac{19 \cdot 30}{296} \right) \cdot 1000 = 5.77 \frac{g_{NO}}{kg_{\text{fuel burnt}}}$$

Soot volume fraction calculations:

The volumetric soot concentration measurement was done with the use of the relationship from the application of Beer's Law and Mie's theory.

$$f_v = \frac{-\ln\left(\frac{I_o}{I_s}\right)\cdot\lambda}{k_\lambda \cdot \delta}$$

where;

I_s = Incident laser intensity

I_o = Attenuated laser intensity

k_λ = Spectral extinction coefficient based on the refractive indices of the soot

λ = He:Ne laser wavelength

δ = Flame thickness

Using the equation for soot volume fraction for diesel fuel at $\Phi = 7$ along the centerline.

Fuel = CME B75

I_s = 1.26 mW

I_o = 1.3 mW

δ = 2.2E-02 m

λ = 633 nm

k_λ = 4.16

$$f_v = -\ln\left(\frac{1.3}{1.26}\right)\cdot\frac{633\,x\,10^{-9}}{4.16\cdot 0.027} = 2.00\,E-7$$

Radiative Fraction of Heat Released:

$$F = \frac{4\pi \ell^2 \cdot q_{corrected}}{\dot{m} \cdot LHV_{fuel}}$$

$$q_{corrected} = q_{total} - q_{back}$$

Each test was run for time duration of 3 minutes with a sampling rate of 2 Hz, allowing the heat flux to reach a steady value. The data was averaged over this sample time. Next, after the flame was extinguished the background radiation (q_{back}) was obtained and used for correction of the total radiation ($q_{corrected}$). Some sample values obtained for CME at $\Phi = 7$ are presented here for the calculation.

q_{total}	= 157.5 W/m^2	q_{back}	= 85.7 W/m^2
ℓ	= 50 cm	$\dot{m}$	= 2.35 x 10^{-5} kg/s
LHV	= 37.4 MJ/kg		

$$q_{corrected} = 157.5 - 85.7 = 71.8 \text{ W/m}^2$$

$$F = \frac{4\pi (0.5)^2 \cdot (71.8)}{(2.35 \text{ x } 10^{-5}) \cdot (37.4 \text{ x } 10^{6})} = 0.26$$

Appendix B
Uncertainty Calculations

Experimental measurements were reported as m ± w (95% confidence level) where m was the best estimate of the measurement, w was the uncertainty in the measurement, implying that when the experiment was repeated, 19 out of 20 times (95%) the measurement lied within the range m ± w. Note that w had the same units as m.

Errors in Experiments

Error in experimentation is called uncertainty.

Precision (random) and bias (fixed) errors were calculated and presented in the figures of this report as error bars. The precision error was statistically determined based on the sample size and standard deviation of the data points. Bias error was also found based on the calibration error or least count of the instrument used, typically 0.1 – 1% of the full scale value. The overall uncertainty (ω) can be expressed mathematically as:

$$\omega = \sqrt{P^2 + B^2}$$

where P is the precision and B the bias error of the measurements. The precision error was calculated based on the following:

$$P = t_{\alpha/2} \frac{S_x}{\sqrt{n}}$$

where S_x represents the standard deviation of the data points, n is the number of data points, and $t_{\alpha/2}$ the student's t-distribution value for a 95% confidence interval. Typical $t_{\alpha/2}$ values are presented below.

n =	υ =	$t_{\alpha/2}$ for a 95% confidence interval
3	2	4.303
4	3	3.182
5	4	2.776
6	5	2.571
7	6	2.447
8	7	2.365
9	8	2.306

Precision errors were much larger than corresponding bias errors and accounted for most of the uncertainty in the present study. For this reason the measurements were repeated 5 to 9 times and instruments calibrated before use each day. For some cases where multiple uncertainties were present, as in the calculation of the Emission Index, the errors were propagated. Below is a sample of how the error was propagated for the Emission Index of NO.

$$\delta EI_{NO} = \sqrt{\left(\frac{\partial EI_{NO}}{\partial \chi_{NO}}\delta\chi_{NO}\right)^2 + \left(\frac{\partial EI_{NO}}{\partial \chi_{CO}}\delta\chi_{CO}\right)^2 + \left(\frac{\partial EI_{NO}}{\partial \chi_{CO_2}}\delta\chi_{CO_2}\right)^2}$$

where;

$$EI_{NO} = \left(\frac{\chi_{NO}}{\chi_{CO} + \chi_{CO_2}} \right) \left(\frac{N \cdot MW_{NO}}{MW_f} \right)$$

$$\frac{\partial EI_{NO}}{\partial \chi_{NO}} = \left(\frac{1}{\chi_{CO} + \chi_{CO_2}} \right) \left(\frac{N \cdot MW_{NO}}{MW_f} \right)$$

$$\frac{\partial EI_{NO}}{\partial \chi_{CO}} = -\left(\frac{\chi_{NO}}{\left(\chi_{CO} + \chi_{CO_2}\right)^2} \right) \left(\frac{N \cdot MW_{NO}}{MW_f} \right)$$

$$\frac{\partial EI_{NO}}{\partial \chi_{CO_2}} = -\left(\frac{\chi_{NO}}{\left(\chi_{CO} + \chi_{CO_2}\right)^2} \right) \left(\frac{N \cdot MW_{NO}}{MW_f} \right)$$

$\delta\chi_{NO}$ = Overall uncertainty (ω) associated with the NO measurements

$\delta\chi_{CO}$ = Overall uncertainty (ω) associated with the CO measurements

$\delta\chi_{CO_2}$ = Overall uncertainty (ω) associated with the CO_2 measurements

The uncertainty associated with the Emission Index of NO is then expressed as:

$$EI_{NO} \pm \delta EI_{NO}$$

Appendix C
Nomenclature

AF	Air to fuel ratio
c_p	Specific heat at constant pressure
D	Binary mass diffusion coefficient
EI	Emission index
f_v	Soot volume fraction
E	Total energy
E_i	Activation energy
F	Radiative fraction of heat released
FL	Visible Flame Length
f_v	Soot Volume Fraction
G	Gibb's function
g	Gravity
g_k	Partial molar Gibb's function
h	Enthalpy of formation
I_o	Attenuated laser intensity
I_s	Incident laser intensity
K	Total number of species
k	Thermal conductivity
k_{fi}	Forward rate constant
k_{ri}	Reverse rate constant
k_λ	Spectral extinction coefficient

ℓ	Distance from flame centerline to pyrheliometer
LHV	Lower heating value
$\dot{m}$	Mass flow rate of liquid fuel
$\dot{m}_o$	Mass through flow rate
MW	Molecular weight
N	Number of carbon atoms
N_k	Number of moles
N_o	Number of chemical species
P	Static pressure
$q_{background}$	Background radiation
$q_{corrected}$	Corrected total radiation
q_{total}	Total flame radiation
R	Universal gas constant
R_r	Source energy due to chemical reaction
Re	Reynolds number
u	Bulk velocity
S	Net rate of production of species by chemical reaction
t	Time
T	Temperature
Y	Mass fraction
χ	Mole fraction
δ	Flame thickness
Φ	Equivalence ratio

η	Real part of soot refractive index
κ	Imaginary part of soot refractive index
λ	Wavelength
μ	Dynamic viscosity
ρ	Density
τ	Stress tensor
υ	Velocity vector
ω	molar rate of production
BBO	Beta Barium Borate
CME	Canola methyl ester
CME B25	25% by volume of Canola methyl ester in Diesel
CME B50	50% by volume of Canola methyl ester in Diesel
CME B75	75% by volume of Canola methyl ester in Diesel
FDO	Frequency doubler option
ICCD	Intensified charged coupled device
OPO	Optical Parametric Oscillator
PLIF	Planar Laser Induced Fluorescence
PLII	Planar Laser Induced Incandescence
SME	Soy methyl ester
SME B25	25% by volume of Canola methyl ester in Diesel
SME B50	50% by volume of Canola methyl ester in Diesel
SME B75	75% by volume of Canola methyl ester in Diesel